NEUTRON STUDIES ON MAGNETS WITH FRUSTRATED ARCHITECTURES

NEUTRON STUDIES ON RARE-EARTH AND DOUBLE PEROVSKITE MAGNETIC OXIDES WITH FRUSTRATED TETRAHEDRAL ARCHITECTURES

By DALINI D. MAHARAJ, Hon. B. Sc. , M. Sc.

A Thesis Submitted to the School of Graduate Studies in Partial Fulfilment of the Requirements for the Degree Doctor of Philosophy

DOCTOR OF PHILOSOPHY (2020)
McMaster University Hamilton, Ontario (Physics and Astronomy)
TITLE: Neutron Studies on Rare-earth and Double Perovskite Magnetic Oxides with Frustrated Tetrahedral Architectures
AUTHOR: Dalini D. Maharaj, Hon. B.Sc. (University of Toronto), M.Sc. (McMaster University)
SUPERVISOR: Professor Bruce D. Gaulin
NUMBER OF PAGES: ix, 123

Lay Abstract

This thesis describes the investigation of the novel magnetic properties of the insulating oxides, $Yb_2Ti_2O_7$, La_2LiOsO_6, La_2LiRuO_6, Ba_2CaOsO_6, Ba_2MgOsO_6 and Ba_2ZnOsO_6. $Yb_2Ti_2O_7$ belongs to the family of compounds called, the rare-earth titanates $R_2Ti_2O_7$, while the remaining compounds are members of the double perovskite family, $A_2BB'O_6$. In particular, we seek to understand the nature of the interactions between electrons, which are responsible for stabilizing exotic magnetic phases exhibited by these materials.

The introductory parts of this thesis are presented in Chapters 1, 2 and 3. First, an elementary theoretical description of the origin of magnetism in crystalline materials is provided in Chapter 1. Chapter 2 describes the strength of utilizing neutron scattering and x-ray diffraction techniques in the study of magnetic oxides. Finally, Chapter 3 provides a full description of the specific neutron instruments which were utilized to study the materials in this thesis.

The first thesis topic explored in Chapter 4 addresses how weak imperfections in the crystal structure of $Yb_2Ti_2O_7$ can cause it to exhibit drastically different magnetic properties. In the pentultimate chapter of this thesis, our experimental findings of the noncubic double perovskites La_2LiOsO_6 and La_2LiRuO_6 are presented in Chapter 5. Here we investigate whether these noncubic double perovskites behave differently from cubic compounds like Ba_2YOsO_6 and Ba_2YRuO_6. This study is important as the cubic systems, Ba_2YOsO_6 and Ba_2YRuO_6, were found to display unexpected magnetic properties based on pre-existing theoretical descriptions for these magnetic oxides. This particular study highlights whether these anomalous properties are only

present in compounds with highly symmetric cubic structures. Finally, we discuss the magnetic properties of Ba_2CaOsO_6, Ba_2MgOsO_6 and Ba_2ZnOsO_6 in Chapter 7 and identify a novel octupolar ordered magnetic phase. These experimental findings are unprecedented, as this phase has never before been identified in d electron magnets.

Abstract

Magnetic frustration is the underpinning theme to all of the magnetic oxide systems explored in this dissertation. The materials studied in this thesis belong to two topical families of interest in modern condensed matter physics, namely, the rare-earth titanates $R_2Ti_2O_7$ and the double perovskites $A_2BB'O_6$. Although the dominant interactions driving the magnetic ground states in each of these systems are different, both systems feature magnetic ions arranged on 3-D tetrahedral architectures with the rare-earth, R, ion in $R_2Ti_2O_7$ forming a network of corner-sharing tetrahedra, and the magnetic B' ion in $A_2BB'O_6$ forming a network of edge-sharing tetrahedra. Three distinctive results arising from research performed during my PhD candidacy are each presented in Chapters 4 through 6. Chapter 1 provides the theoretical background necessary to understand the numerous crystalline systems studied in this thesis. Chapter 2 explains the necessity of utilizing neutron scattering and x-ray experiments to tease out the key signatures which were essential to formulating the conclusions made in each study.

Chapter 4 involves a study of the widely known quantum spin liquid candidate, $Yb_2Ti_2O_7$ and the effect of "stuffing" on its ground state anisotropy. This study was motivated by the following burning question which arose from my previous Master's thesis work which involved a crystal-field study of $Yb_2Ti_2O_7$, "Is there any effect, of intentional stuffing in $Yb_2Ti_2O_7$, on the description of the ground state anisotropy of the Yb^{3+} ion?" Two stuffed powder samples of $Yb_{2+x}Ti_{2-x}O_{7-x/2}$ with compositions x = 0.08 and x = 0.12 were studied with time-of-flight (TOF) inelastic neutron scattering (INS) methods. This highly sensitive crystal-field study revealed the presence of

additional crystal-field levels associated with the Yb^{3+} ions at its nominal site, but in the presence of oxygen deficient environment, and at the Ti-site. Based on fits to the crystal-field schemes found for these stuffed $Yb_2Ti_2O_7$ ions, it was found that the anisotropy of Yb^{3+} ions at these two defective sites is Ising like, compared with the XY like anisotropy which they possess at their nominal site.

Chapter 5 also follows naturally from an inelastic neutron scattering experiment performed as part of my Master's thesis work on the cubic $5d^3$ double perovskite Ba_2YOsO_6. Previous studies of cubic Ba_2YOsO_6 and Ba_2YRuO_6 revealed the development of spin gaps concomitant with the formation of magnetic Bragg peaks associated with the magnetic long-range order of both systems below their respective transition temperatures. These studies brought into question the origin of the spin gaps as none are expected for orbitally quenched d^3 systems. These original studies proposed that spin-orbit coupling is the source of anisotropy in these systems as showcased by the relative sizes of the spin gaps. The inelastic neutron scattering study presented here addresses whether this property also occurs in the monoclinic d^3 systems La_2LiRuO_6 and La_2LiOsO_6. Our inelastic neutron scattering investigation confirmed the presence of the spin gap in these monoclinic d^3 double perovskites and showed that the monoclinic systems also order into a type I AF magnetic structure. Remarkably, it was found that although geometric frustration is relieved in the monoclinic lattices, these systems still showed dramatically suppressed transition temperatures and displayed smaller spin gaps. This study provides an important benchmark in understanding the role and importance of geometric frustration and spin-orbit coupling in these d^3 magnets. In addition, this study speaks to general trends in d^3 double perovskite magnets.

The final study presented in this thesis in Chapter 6 highlights the most original aspect of my PhD thesis studies. A study of a series of three Os^{6+} containing d^2 double perovskites - Ba_2CaOsO_6, Ba_2ZnOsO_6 and Ba_2MgOsO_6 - was conducted and employed inelastic neutron scattering, neutron diffraction and x-ray synchrotron diffraction methods. Ba_2CaOsO_6 and Ba_2MgOsO_6 were previously thought to host a type I antiferromagnetic ground state based on heat capacity, magnetization and muon spin relaxation experiments. Chapter 6 describes in detail, our experimental findings which refute the previously held notion that Ba_2MgOsO_6 and Ba_2CaOsO_6 are antiferromagnets and that Ba_2ZnOsO_6 possesses a distinct magnetic ground state from

these two compounds. Our inelastic neutron scattering measurements highlighted the development of spin gaps in all three d^2 magnets below their transition temperatures. Unlike the d^3 case however, the evolution of these spin gaps were not accompanied by the growth of magnetic Bragg reflections at the corresponding wavevector where the spin gap excitations occur. To reconcile the behaviour in these three cubic d^2 systems, a theoretical description was formulated and it accounted for spin-orbit effects and an effective crystal-field effect on the two-electron ground state multiplet. In this framework, these d^2 systems are found to enter a novel octupolar ordered ground state. This is the first example of its realization in d-electron systems and a full account of this theory is provided in the Appendix.

Acknowledgements

The research presented within this thesis is a result of many long hours of work and personal sacrifice. However, the contributions and support of my mentors, colleagues, friends and family were central to my success. I would like to take this opportunity to recognize those who have been a positive influence during my graduate career.

First and foremost, I would like to extend my heartfelt gratitude to my PhD supervisor, Bruce Gaulin, for his unwavering support during my program. Bruce has also provided me with sound advice and has presented me with many unique opportunities to participate in and organize academic events, worldwide, enabling me to improve my professional skills.

Bruce and I have been fortunate to work with Arun Paramekanti. His dedication to research helped us to forge a productive and synergistic collaboration. My immense gratitude goes out to Arun for his profound contributions to our research. I would like to express my special thanks to my committee members, Graeme Luke and Maikel Rheinstädter. I appreciate the insightful perspectives which Graeme shared during our committee meetings. Also, the meticulous and constructive feedback which Maikel has provided me with has improved the professional quality of my work.

My graduate experience at McMaster University has been an enriching learning experience. I am extremely grateful to have worked with Hanna Dabkowska, Antoni Dabkowski, Marek Kiela and Casey Marjerrison, who channelled their wealth of experience, knowledge, technical expertise to assist me with sample preparation and characterization in the crystal growth and x-ray labs. I was also fortunate to have

the diligent co-working support of my lab-mates, Gabriele Sala, Edwin Kermarrec, Connor Buhariwalla, Jonathan Gaudet and Kyle Ma, during many demanding neutron scattering experiments.

I would like to express my deepest appreciation for the guidance and round-the-clock support of the lead instrument scientists, Matthew Stone, Alexander Kolesnikov and Clemens Ritter. Your input and feedback in the preparation of manuscripts made each research paper that much more robust.

I would like to extend my sincere thanks to my friends, Andrea Vargas, John Hartley, Noémie De Vuyst, and Ryan Plestid for always believing in me. They have been important sounding boards when I was faced with challenges during the course of my PhD degree.

The successful completion of my dissertation would not have been possible without the unfaltering support of my parents and my brother, Ravi Maharaj. Their spiritual guidance and love have provided me with the strength to see through every moment in life. Finally, I would like to thank my loving fiancé, James Kim for being a source of an immeasurable amount of support, patience and kindness.

Contents

List of Figures

List of Abbreviations and Symbols

Abbreviations

AF Antiferromagnetic

DP Double perovskite

FCC Face-centred cubic

GS Ground state

INS Inelastic neutron scattering

NN Nearest neighbour

RE Rare-earth

SOC Spin-orbit coupling

TM Transition metal

Fundamental Constants

c	Speed of light in vacuum	$299,792,458\,m/s$
h	Planck constant	$6.626\,070\,15 \times 10^{-34}\,J \cdot s$
$a.u.$	Atomic mass unit	$1.660\,539066\,60\,(50) \times 10^{-27}\,kg$

μ_N	Spin magnetic moment	$5.050\,783\,7461\,(15) \times 10^{-27}\, J \cdot T^{-1}$
μ_B	Bohr magneton	$9.274009994(57)\ \times\ 10^{-24}\, J\ \cdot\ T^{-1}$
m_e	Electron mass	$9.1093837015(28)\ \times\ 10^{-31}\, kg$

Declaration of Academic Achievement

- **Chapter 4:** is based on
  G. Sala, D. D. Maharaj, M. B. Stone, H. A. Dabkowska, and B. D. Gaulin, *Crystal field excitations from Yb^{3+} ions at defective sites in highly stuffed $Yb_2Ti_2O_7$*, Phys. Rev. B **97**, 224409 (2018).

  D. D. Maharaj grew the stuffed $Yb_2Ti_2O_7$ crystals with composition, x = 0.08 and x = 0.12, under the supervision and guidance of H. A. Dabkowska.

  G. Sala and D. D. Maharaj were responsible for the characterization and preparation of the two samples for the time-of-flight inelastic neutron scattering experiments performed at SEQUOIA. G. Sala and D. D. Maharaj performed the experiment at SEQUOIA and analyzed the inelastic neutron scattering data. G. Sala performed the crystal-field calculations and the Monte Carlo simulations.

  G. Sala performed the neutron powder diffraction experiment at POWGEN and did the Rietveld structural refinements of the neutron diffraction data sets.

  G. Sala, D. D. Maharaj and B, D. Gaulin were the lead authors of the manuscript. B. D. Gaulin provided edits to the entire manuscript, and contributed significantly to the writing of the introduction. D. D. Maharaj made all of the figures except for Figs. 7, which was made by G. Sala.

- **Chapter 5:** is based on
  D. D. Maharaj, G. Sala, C. A. Marjerrison, M. B. Stone, J. E. Greedan, and B. D. Gaulin, *Spin gaps in the ordered states of $La_2LiXO_6 (X = Ru, Os)$ and*

their relation to the distortion of the cubic double perovskite structure in $4d^3$ and $5d^3$ magnets, Phys. Rev. B **98**, 104434 (2018).

C. A. Marjerrison prepared the powder samples of La_2LiOsO_6 and La_2LiRuO_6, and characterized the samples. D. D. Maharaj and G. Sala performed the inelastic neutron scattering measurements at SEQUOIA.

D. D. Maharaj performed the analysis of the inelastic neutron scattering data sets and conducted the SpinW calculations. D. D. Maharaj and B. D. Gaulin were the lead authors on the manuscript. D. D. Maharaj made all of the figures.

- **Chapter 6:** is based on
  D. D. Maharaj, A. Paramekanti, G. Sala, M. B. Stone, E. Kermarrec, C. Ritter, F. Fauth, C. A. Marjerrison, J. E. Greedan, and B. D. Gaulin. *Multipolar vs Néel Order in Cubic $5d^2$ double perovskites*, Phys. Rev. Let. **124**, 087206 (2020).

  C. A. Marjerrison synthesized Ba_2CaOsO_6. Dalini D. Maharaj synthesized Ba_2MgOsO_6 and Ba_2ZnOsO_6 under the supervision of C. A. Marjerrison.

  D. D. Maharaj and G. Sala performed the inelastic neutron scattering experiments on Ba_2MgOsO_6 and Ba_2ZnOsO_6. G. Sala carried out the inelastic neutron scattering experiment on Ba_2CaOsO_6. D. D. Maharaj and C. Ritter did the experiments at D20. F. Fauth conducted the x-ray synchrotron experiment at CELLS.

  C. Ritter assisted D. D. Maharaj with Rietveld refinements on the data sets obtained from both the neutron and x-ray diffraction experiments. D. D. Maharaj conducted the FULLPROF calculations for the estimated upper bound on the magnetic moments in Ba_2CaOsO_6, Ba_2MgOsO_6 and Ba_2ZnOsO_6.

  A. Paramekanti developed the theory for octupolar order in d^2 double perovskites, which is presented in even more detail in the Appendix.

  D. D. Maharaj, B. D. Gaulin and A. Paramekanti contributed equally to the authorship of manuscript.

  D. D. Maharaj made the figures which present the results obtained from the neutron and x-ray diffraction experiments. Figures obtained from theoretical calculations were made by A. Paramekanti.

- **Appendix** is based on
  A. Paramekanti, D. D. Maharaj and B. D. Gaulin. *Octupolar order in d-orbital Mott insulators*, Phys. Rev. B 101, 054439 (2020).

  A. Paramekanti fully developed the theory for octupolar order in d electron magnets.

  D. D. Maharaj and B. D. Gaulin provided the experimental context and results for these studies.

  A. Paramekanti was the lead author of the manuscript. D. D. Maharaj and B. D. Gaulin assisted with edits to the manuscript.

Dedicated to my loving and supportive parents

1 Introduction to Magnetism in Insulating Oxides

> "The behaviour of large and complex aggregations of elementary particles, it turns out, is not to be understood in terms of a simple extrapolation of the properties of a few particles. Instead, at each level of complexity entirely new properties appear, and the understanding of the new behaviors requires research which I think is as fundamental in its nature as any other. — *Phillip W. Anderson*"

Unpaired electrons give rise to magnetic phenomena in crystalline materials because they each possess spin (s = 1/2) and they also possesses orbital angular momentum, which also contributes to the magnetism of the ion. Spin is an intrinsic quantum mechanical property of electrons which has fundamental implications for the behaviour of interacting electrons in materials.[1] The orbital moment can be understood in classical terms, as arising from from the orbital motion of charged electrons around atomic nuclei.[2] The macroscopic Maxwell's equations and the Dirac equation can be utilized to develop a theoretical description of electrons in solids, from which a quantum theory of magnetism can be obtained. These procedures are provided in Ref. [1] in Chapters 1 and 2. It is ultimately a challenging task to obtain exact solutions to the many body problems which arise from these methods. This fact highlights one of the core difficulties involved in developing a quantum theory of magnetism. When it is appropriate however, it is useful to describe magnetic systems in terms of localized

[1] For example, in a many electron system, the total wavefunction must be antisymmetric under exchange of any two electrons.

[2] The motion of charged particles generates a magnetic field which is perpendicular to both the current and attractive (Coulomb) force between the electron and nucleus, which keeps the electron in orbital motion.

moments. Utilizing this approach aids in the development of *spin Hamiltonians* for systems which involve different types of interactions between the magnetic ions.

On this note, this chapter will provide the necessary background to understand the spin Hamiltonians for all materials studied in this thesis. To develop this idea, first, magnetic properties of a collection of non-interacting ions, shall be discussed. Following this, various interaction terms which appear in the spin Hamiltonians for the materials studied in the thesis will be discussed. Finally a short review of each of the materials will be provided.

1.1 Non-Interacting Magnetic Moments

To discuss magnetism arising from a collection of identical, non-interacting ions, we first introduce the *magnetic susceptibility*, χ. The magnetic susceptibility is a measure of the magnetization density, M, of a material when it is subject to an external magnetic field, H. The magnetic susceptibility can be computed as follows $\chi = \partial M/\partial H$ where the magnetization M is defined as,

$$M(H,T) = \sum_n \frac{M_n(H)e^{-E_n/k_BT}}{\sum_n e^{-E_n/k_BT}}, \tag{1.1}$$

and $M_n(H) = -\frac{1}{V}\frac{\partial E_n(H)}{\partial H}$ [2]. The susceptibility aids one to clearly distinguish magnetic materials from nonmagnetic materials when their response to the application of an external field is measured. When an ion is placed in an external field $\vec{H} = H\hat{z}$, the Hamiltonian of the ion is shifted by, $\Delta\mathcal{H}_{mag}$ which is given by,

$$\Delta\mathcal{H}_{mag} = \mu_B(\boldsymbol{L} + \boldsymbol{S}) \cdot \boldsymbol{H} + \frac{e^2H^2}{8mc^2} \cdot (x^2 + y^2), \tag{1.2}$$

where $\boldsymbol{L}$ is the total electronic orbital angular momentum, and $\boldsymbol{S}$ is the sum of the spins of the electrons in the system. The degeneracy of the electronic levels is split when an external magnetic field is applied. These energy shifts can be computed using second order perturbation theory [3]. If the eigenvalues of the atom in the ground state are E_n, the perturbed energies are given by $E_{n'} = E_n + \Delta E_n$, where the energy shifts ΔE_n can be computed using,

$$\Delta E_n = \mu_B \boldsymbol{H} \cdot \langle n| \boldsymbol{L} + g_0 \boldsymbol{S} |n\rangle + \sum_{n \neq n'} \frac{|\langle n| \mu_B \boldsymbol{H} \cdot (\boldsymbol{L} + g_0 \boldsymbol{S}) |n'\rangle|^2}{E_n - E_{n'}} + \frac{e^2}{8mc^2} H^2 \langle n| \sum_i (x_i^2 + y_i^2) |n\rangle . \tag{1.3}$$

Clearly, knowledge of the ground state wavefunctions, $\{|n\rangle\}$, of the ion is key to determining the matrix elements in Equation (1.3). To determine the total J, L and S which characterize the state of the ion, it is essential to determine which electron levels are occupied. Hund's rules provide a guideline for determining the order of electronic filling of the atomic orbitals. The essence of Hund's rules are summarized in the following three points.

1. Maximize S_z – The n electrons are placed in the $2(2l+1)$ levels such that the total spin is maximized. This conditions satisfies the Pauli exclusion principle which describes the tendency for electrons to avoid each other. For less than or equal to half filling of atomic levels ($n \leq 2l+1$), the electron levels are singly occupied and are characterized by different values of l_z. For greater than half filling, electrons occupy the electron levels with opposite spin. This condition must be satisfied as electrons cannot occupy the same quantum mechanical state, otherwise, the Pauli exclusion principle will be violated.
2. The total orbital angular momentum L of the first occupied state has the largest value. Thus, the first electron will occupy the level with characterized by l_z which corresponds to the maximum value of l. For half or total occupation of the electron levels, $L = 0$.
3. The total J is determined to take the values $|L+S|$ or $|L-S|$ for more than half-filling ($n \geq 2l+1$) or less than half-filling ($n \leq 2l+1$).

Armed with this information, it is now possible to determine the energy shifts, and hence susceptibilities for a collection of non-interacting atoms or ions.

Many naturally occurring materials exhibit weak magnetism as their constituent ions or atoms contain *saturated* electronic levels which do not overlap with each other significantly.[3] In these materials, the electron levels are completely occupied and

[3]Saturated electronic levels refer to the case in which the electronic levels are fully occupied.

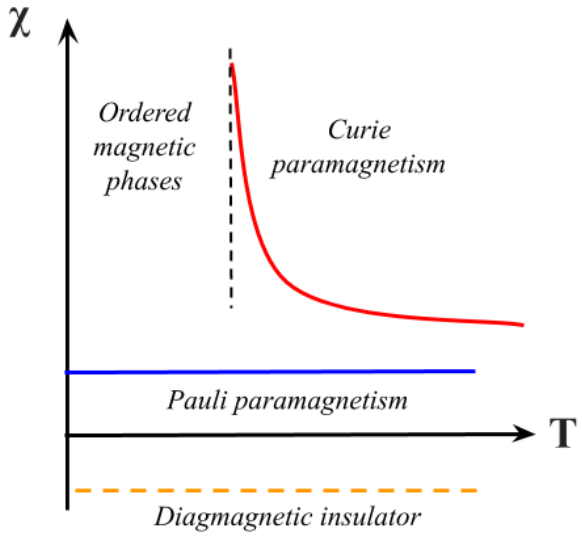

Figure 1.1: The susceptibilities of different types of materials are shown in this schematic.

Hund's rules dictate that the ion has no orbital or spin angular momentum. Therefore, the first and third terms in Equation (1.3) vanish as $J|0\rangle = S|0\rangle = L|0\rangle = 0$. The third term on the other hand, makes a very small contribution to the field induced shift. Following the definition of the susceptibility stated earlier,

$$\chi = -\frac{e^2}{6mc^2}\frac{N}{V}\langle 0|\sum_i r_i^2|0\rangle\,. \tag{1.4}$$

This value of χ is small, negative and temperature independent because it is a quantum mechanical property of the ion [4]. The negative value reflects the response of the orbital currents which can be thought of in terms of the classical Lenz's law. The response of the orbital currents to external field H directly opposes it. This property is referred to as *Larmor diamagnetism* and is exhibited by nonmagnetic materials when subjected to a field H, as shown in Figure 1.1. It is temperature independent since the excited states are at least a few eV away, leaving them unpopulated. Next, we would like to investigate specifically, the response of a collection of ions which possess partially filled orbitals respond to the application of an external field H. There are

two cases worth distinguishing for this discussion.

The first case is realized when the electron shells are one electron short of being half-filled leaving the total angular momentum $J = 0$. In this case, the first term in Equation (1.3) will vanish, like in the case with filled shells. However, the second term need not vanish leaving two contributions to the magnetic susceptibility. The sign of the second term is opposite to the Larmor diamagnetic contribution and is termed, the *Van Vleck paramagnetic* susceptibility. This contribution favours alignment of the moments with the external magnetic field. Therefore, the total susceptibility exhibited by ions with one electron short of being half-filled will be dictated by the balance between the Larmor diamagnetic and Van-Vleck paramagnetic terms.

More importantly, the second case involves ions with $J \neq 0$. Strong paramagnetism is observed in these materials and arises from the first term in Equation (1.2). This term tends to dominate the second and third terms in Equation (1.3), and we are left to evaluate only the first term. This contribution can be efficiently computed via clever use of the Wigner-Eckhart theorem.[4] Using this approach converts the matrix element to,

$$\begin{aligned} \langle JLSJ_z|\, \boldsymbol{L} + g_0 \boldsymbol{S}\, |JLSJ_z\rangle = \langle JLSJ_z|\, g(JLS)\boldsymbol{J}\, |JLSJ_z\rangle \quad \text{where,} \\ g(JLS) = \frac{3}{2} + \frac{1}{2}\left[\frac{S(S+1) - L(L+1)}{J(J+1)}\right]. \end{aligned} \tag{1.5}$$

The strength of the coupling of the total angular momentum of the ion to the external magnetic field can be expressed as $\mu = -g(JLS) \cdot \mu_B \cdot J$. The resulting susceptibility reflects the strengthening of this paramagnetism with decreasing temperature according to,

$$\chi = \frac{N}{V}\frac{(g\mu_B)^2}{3}\frac{J(J+1)}{k_B T} \tag{1.6}$$

where $k_B T >> g\mu_B H$. This inverse relation is known as *Curie's law*. Physically, when the external field H is applied, the degeneracy of the electronic levels is removed. Paramagnetism has the effect of reducing the statistical disorder of the spin orientations where instead, the spins preferably align with the direction of the external field H.

[4] A derivation of the Wigner-Eckhart theorm is provided in [5].

This effect is therefore opposed by thermal disorder. This behaviour is a signature of systems with a *permanent moment*.

We now make special mention that the susceptibilities discussed hitherto arise from quantum mechanical properties of the atom [4]. There are some materials which fail to exhibit the expected paramagnetic behaviour down to very low temperatures, and instead show a spontaneous magnetization at low temperatures. These materials also retain a non-zero magnetization even when the external field is removed. We must then question the origin and mechanism for the generation of spontaneous magnetization in some materials. Up until this point, we have spoken to the magnetic properties of isolated ions. Herein lies our answer − spontaneous magnetization is generated by a macroscopic spatial ordering of the magnetic moments which occurs due to the interactions between them.

1.2 Prelude to Magnetic Order in Crystalline Materials

In this section, we return to address the origins of spontaneous magnetization in materials at low temperatures. It was previously mentioned that Curie's law applies at only very high temperatures. The description which was developed for M in Section 1.1 therefore cannot explain spontaneous magnetization at low temperatures. Ultimately, the interactions between the magnetic moments in crystalline materials that are responsible for generating low temperature magnetic long-range ordered phases.

To understand how this arises, consider the statistical free-energy F of an arrangement of spins which interact with each other. The free energy can be expressed in terms of the internal energy, U, of the system when it is at equilibrium at temperature T, with entropy S. The entropy is a measure of the level of disorder any statistical system. The free energy is given by[5],

$$F = U - TS. \tag{1.7}$$

There are two cases we can distinguish, the very high and low temperature limits in relation to the internal energy of the system. At very high temperatures, the entropic

[5]See for example, Ref. [6].

contribution (TS) dominates. Physically in a magnetic spin system, this is realized as the highly disordered, paramagnetic phase wherein the spins are free to point in any spatial direction as shown in Figure 1.2, preserving the $3D$ rotational symmetry of the spin orientation. However, if the system achieves thermodynamic equilibrium at a temperature T such that $k_B T < U$, the internal energy of the system dominates. As the interactions between the spins in the system are a measure of this internal energy, the behaviour of the spins in the magnetic system are driven by U. This results in the generation of a long-range ordered magnetic state wherein the rotational symmetry of the spins is broken, and the magnetic interactions between the spins pin the orientations of the spins in a specific direction. Therefore, the interaction which drives magnetic order in such systems, must be on the energetic scale $\sim k_B T_C$ of the ordering temperature, T_C.

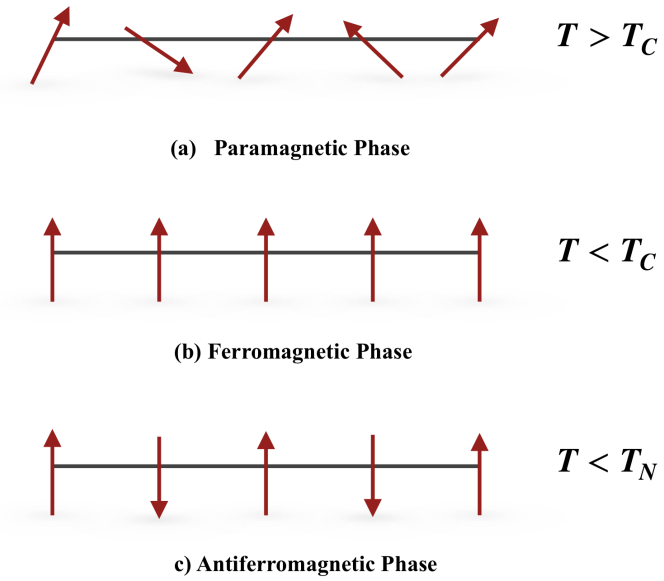

Figure 1.2: This schematic shows the paramagnetic, ferromagnetic and antiferromagnetic phases represented in a 1-D spin chain.

The most simple case of magnetic order can be demonstrated with a 1-D spin chain as shown in Figure 1.2 (b.). This demonstrates *ferromagnetic* ordering of spins wherein the magnetic moments align parallel to each other. A similar phenomenon exists wherein nearest neighbour moments align antiparallel to each other. This ordered phase is referred to as the *antiferromagnetic* phase as shown in Figure 1.2 (c.). The temperatures at which ferromagnetic and anti-ferromagnetic ordering occur are

referred to as the Curie (T_C) and Néel (T_N) temperatures, respectively.

In the study of magnetic systems, experimentalists plot the inverse magnetic susceptibility, which is obtained from measurements of the susceptibility, at high temperatures. In this high temperature limit, the paramagnetic behaviour driven by thermal disorder dominates. The high temperature data can be utilized to perform a linear fit to obtain the *Curie-Weiss* constant θ_{CW} by utilizing the relation,

$$\chi = \frac{C}{T - \theta_{CW}}. \tag{1.8}$$

θ_{CW} is a phenomenological scale which takes account of interactions between the spins [7]. When a linear fit of the plot of $1/\chi$ is performed, θ_{CW} is the value of intercept. When $\theta_{CW} > 0$, this is usually indicative of net ferromagnetic interactions while $\theta_{CW} < 0$ represents net anti-ferromagnetic interactions (see Figure 1.3). Furthermore, the energy scale of the interactions is proportional to size of $|\theta_{CW}|$.

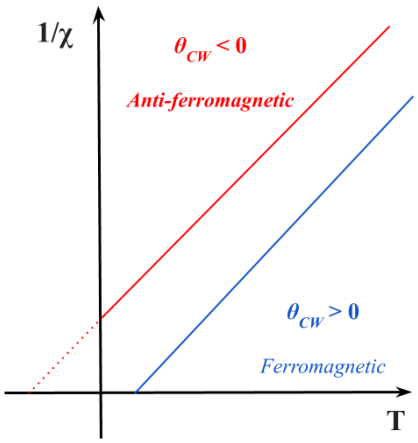

Figure 1.3: This schematic shows how the Curie-Weiss temperature θ_{CW} is obtained from a plot of the inverse susceptibility $1/\chi$, as a function of temperature T.

Now that we have considered two simple cases of conventional magnetic order and are able to identify them experimentally, it is important to understand the mechanisms which yield magnetic order. The next section is dedicated to a description of typical magnetic interactions which can stabilize magnetic order.

1.3 Magnetic Interactions

Exchange Interaction

The mechanism for conventional magnetic order in crystalline systems is the *exchange interaction*. The exchange interaction arises from a combination of the Coulomb interaction between electrons from neighbouring magnetic sites, and the Pauli exclusion principle [4]. This is most easily demonstrated and appreciated by considering the hydrogen molecule problem which was first considered by Heitler and London in 1927 [8]. A more accurate theoretical description of this procedure can be found in Ref. [1].[6] The Hamiltonian of the system is given by,

$$\begin{aligned}\mathcal{H} = &\frac{\hbar^2}{2m}\left(\boldsymbol{p_1^2} + \boldsymbol{p_2^2}\right) + \frac{e^2}{4\pi\epsilon_0}\frac{1}{|\boldsymbol{r_1} - \boldsymbol{r_2}|} \\ &- \frac{e^2}{4\pi\epsilon_0}\left[\frac{1}{|\boldsymbol{r_1} - \boldsymbol{R_1}|} + \frac{1}{|\boldsymbol{r_1} - \boldsymbol{R_2}|} + \frac{1}{|\boldsymbol{r_2} - \boldsymbol{R_2}|} + \frac{1}{|\boldsymbol{r_2} - \boldsymbol{R_1}|}\right],\end{aligned} \tag{1.9}$$

where $\{\boldsymbol{r_i}, \boldsymbol{p_i}\}$ represent the positions and momenta of the two electrons. $\boldsymbol{R_i}$ denotes the positions of the protons in the nuclei of the hydrogen atoms which are assumed to remain fixed. We note that $\mathcal{H}$ is symmetric under exchange of the positions of the electrons ($\boldsymbol{r_1} \leftrightarrow \boldsymbol{r_2}$). As a result the spatial part of the electron wavefunctions are either even or odd with respect to this transformation. This means that,

$$\psi(\boldsymbol{r_1}, \boldsymbol{r_1}) = \pm\psi_{\pm}(\boldsymbol{r_1}, \boldsymbol{r_2}). \tag{1.10}$$

We denote the energies corresponding to each of these wavefunctions are $E_{\pm}$. The Pauli exclusion principle requires that the total wavefunction (the product of the spin and spatial wavefunctions) is anti-symmetric under exchange. Thus the total two-electron wavefunction can either be a spin singlet state ($S = 0$) viz.,

[6] In the discussion to follow, the ground state of the two electron system is found to be the low spin i.e. $S = 0$ state. However, a more theoretical treatment (as given in Ref. [1]) gives the energy eigenfunctions of the singlet and triplet states with respect to the self-energy of the charge distribution. It is found that the singlet state possesses a higher energy than the triplet state. Hence, the triplet (high-spin) state is the ground state. This is the origin of Hund's first rule of maximum multiplicity.

$$\Psi_{tot,+} = \frac{1}{\sqrt{2}}(|\uparrow\downarrow\rangle - |\downarrow\uparrow\rangle)\psi_{+}(\boldsymbol{r_1}, \boldsymbol{r_1}), \tag{1.11}$$

or a triplet state ($S = 1$) with three components (m = -1, 0 1) given by,

$$\Psi_{tot,-} = \begin{cases} |\uparrow\uparrow\rangle\, \psi_{-}(\boldsymbol{r_1}, \boldsymbol{r_1}) \\ |\downarrow\downarrow\rangle\, \psi_{-}(\boldsymbol{r_1}, \boldsymbol{r_1}) \\ \frac{1}{\sqrt{2}}(|\uparrow\downarrow\rangle + |\downarrow\uparrow\rangle)\psi_{-}(\boldsymbol{r_1}, \boldsymbol{r_1}). \end{cases}$$

The ground state of the molecule is the spin singlet ($S = 1$) state and it is separated by from the first excited state (the $S = 1$ triplet state) by $\Delta E = E_{+} - E_{-}$. An effective Hamiltonian, $\mathcal{H}_{spin}$, can be used to represent the total two electron system. We represent this effective Hamiltonian in terms of $\boldsymbol{S_1} \cdot \boldsymbol{S_2}$ and note that $\boldsymbol{S}^2 = (\boldsymbol{S_1} + \boldsymbol{S_2})^2$ implies that,

$$\boldsymbol{S_1} \cdot \boldsymbol{S_2} = \frac{1}{2}(\boldsymbol{S}^2 - \boldsymbol{S_1}^2 - \boldsymbol{S_2}^2). \tag{1.12}$$

For two spin 1/2 particles, this results in

$$\boldsymbol{S_1} \cdot \boldsymbol{S_2} = \frac{1}{2}\boldsymbol{S}^2 - \frac{3}{4}. \tag{1.13}$$

Therefore the operator $\boldsymbol{S_1} \cdot \boldsymbol{S_2}$ has the eigenvalues $-\frac{3}{4}$ and $\frac{1}{4}$ corresponding to the S = 0 (low spin) and S = 1 (high spin) cases, respectively. The spin Hamiltonian can be expressed in terms of the singlet-triplet splitting as,

$$\mathcal{H}_{spin} = \frac{1}{4}(E_{+} + 3E_{-}) - (E_t - E_{-})\boldsymbol{S_1} \cdot \boldsymbol{S_2}. \tag{1.14}$$

If the zero-point energy of the system is defined as $\frac{1}{4}(E_{+} + 3E_{-})$ this leaves,

$$\begin{aligned} \mathcal{H}_{spin} &= -(E_{+} - E_{-})\boldsymbol{S_1} \cdot \boldsymbol{S_2} \\ &= -\mathscr{J}\, \boldsymbol{S_1} \cdot \boldsymbol{S_2}, \end{aligned} \tag{1.15}$$

where $\mathscr{J}$ is the exchange energy. Therefore, a parallel alignment of spins is favoured

if $\mathscr{J} > 0$, but an anti-parallel arrangement is preferred if $\mathscr{J} < 0$. The latter case is realized for the hydrogen molecule.

It must be emphasized that the original Hamiltonian on the other hand, does not contain any spin dependent terms. The effective spin Hamilton $\mathcal{H}_{spin}$ merely accounts for the Coulomb interaction between the electrons. Encoded in the exchange constant $\mathscr{J}$ is the magnitude and strength of this interaction. Therefore, the size of this energy is on the scale of kinetic and Coloumb energies and can therefore account for Curie temperatures associated with magnetic long range ordered states.

A model based on the exchange interaction has been developed for magnetic insulators. This model is referred to as the *Heisenberg* Hamiltonian, though, it was originally introduced by Dirac in 1928. In this framework, only the exchange between nearest neighbouring ions are accounted for. The Hamiltonian has the form,

$$\mathcal{H} = -\mathscr{J} \sum_{\langle \boldsymbol{R}\boldsymbol{R'} \rangle} \boldsymbol{S_R} \cdot \boldsymbol{S_{R'}} + 2\mu_B \boldsymbol{B} \cdot \sum_{\boldsymbol{R}} \boldsymbol{S_R}, \tag{1.16}$$

where $\boldsymbol{R}$ are the positions of the magnetic ions and $\boldsymbol{S_R}$ are the spin operators corresponding to the magnetic ions at position $\boldsymbol{R}$. The size of the exchange constant $\mathscr{J}$ depends on the degree of overlap between electronic orbitals of neighbouring ions.

Dipolar Interaction

One of the simplest interactions that might come to mind is the *dipolar interaction*, which is the interaction between magnetic moments. The dipolar potential between two magnetic moments $\boldsymbol{m_1}$ and $\boldsymbol{m_2}$ which are separated by distance $\boldsymbol{r}$ is given by,

$$V(\boldsymbol{r}) = \frac{\mu_0}{4\pi r^3}\Big[\boldsymbol{m_1} \cdot \boldsymbol{m_2} - \frac{3}{r^2}(\boldsymbol{m_1} \cdot \boldsymbol{r})(\boldsymbol{m_2} \cdot \boldsymbol{r})\Big]. \tag{1.17}$$

A simple order of magnitude calculation leads to an estimate of $V(\boldsymbol{r})/k_B \sim 0.1\,K$. When compared with Curie temperatures, which are on the order of about $\sim 100 - 1000\,K$, it is clear that dipolar interactions do not give rise to ferromagnetic order. Indeed, dipolar interactions are very weak and only become important in novel systems where conventional magnetic order is dramatically suppressed due to the effect of magnetic frustration or because the exchange coupling itself is weak, as it is for rare

earth based magnets.[7]

Superexchange Interaction

In insulating solids, the typical interatomic spacings of active magnetic sites are too large for there to be significant overlap between valence orbitals. As a result, the exchange interaction cannot be the predominant mechanism for magnetic exchange in these materials. The magnetic interactions are instead, mediated by nonmagnetic cations in the system. Double perovskite antiferromagnets of the form $A_2BB'O_6$ provide a clear example of materials in which the exchange between the magnetic B' sites are mediated by the nonmagnetic O^{2-} sites. One straightforward instance of this involves the exchange between p-orbitals of O^{2-} at the corners of two neighbouring octahedrally coordinated transition metal cations within the $Fm\bar{3}m$ structure. For purely illustrative purposes, consider the exchange pathway between two d^3 Cr^{3+} ions as shown in Figure 1.4.

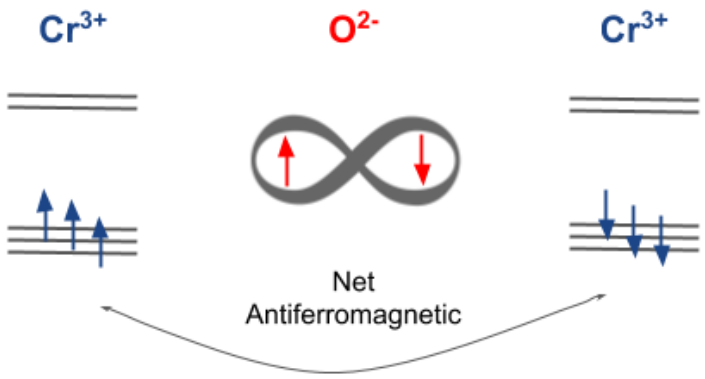

Figure 1.4: The superexchange pathway for Cr^{3+} in the double perovskite lattice is shown, where the electrons from the p-orbital of the nonmagnetic O^{2-} anion mediates antiferromagentic exchange between neighbouring Cr^{3+} ions.

The two electrons within the p orbitals of the O^{2-} ion must possess opposite spin, in accordance with the Pauli exclusion principle (condition #1). Each of these electrons occupies the empty e_g orbital of one of the two d ions involved in the

[7] See more details in Section 1.5.

magnetic interaction.[8] The three unpaired electrons in the t_{2g} levels of the Cr^{3+} ion naturally align with the electron in the e_g level due to Hund's first rule (condition #1). When conditions #1 and #2 are combined, the electrons are thus polarized and couple separately to the Cr^{3+} cations. The net result is that the electrons on the neighbouring Cr^{3+} sites align anti-parallel to each other, generating net anti-ferromagnetic interactions. The previously described superexchange mechanism follows the well established guidelines known as the Goodenough-Kanamori rules [9, 10]. This concludes the introduction to magnetic interactions in insulating solids. To explore further magnetic interactions mechanisms the reader is encouraged to refer to books by White [1], Ashcroft & Mermin [2] and Alloul [4], which provide an excellent overview of magnetism. The next section includes an overview of sources of magnetic anisotropy. Magnetic anisotropy plays an essential role in describing magnetic ground states in insulating oxides.

1.4 Magnetic Anisotropy

Generally speaking, magnetic anisotropy arises due to the influence of spin-orbit coupling (SOC) and the crystal-electric field (CEF). These terms introduce corrections to the electronic energy levels of atoms and ultimately, influence the magnetic ground state properties. Below, we discuss the origin of these two effects. Then we address the specific forms of the anisotropic contributions to the spin Hamiltonians which apply to the crystal systems investigated in this thesis.

1.4.1 Crystal electric field

First we consider a prominent term which needs to be considered in the spin Hamiltonians of virtually all transition metal oxides and rare-earth oxides. The *crystal electric field* (CEF) describes the electric field which is experienced by a magnetic ion within its local environment in a crystalline lattice. The magnetic ion can interact with the electrons of these nonmagnetic elements via an electrostatic Coulomb potential. The strength of CEF effects directly depends on which electronic levels the unpaired electrons in the magnetic ion occupy. Comparing d-electron systems with f-electron systems, CEF effects are expected to be stronger in the former case as d orbitals are

[8] See Section 1.4.1 to understand how t_{2g} and e_g levels are formed from d levels in octahedral environments.

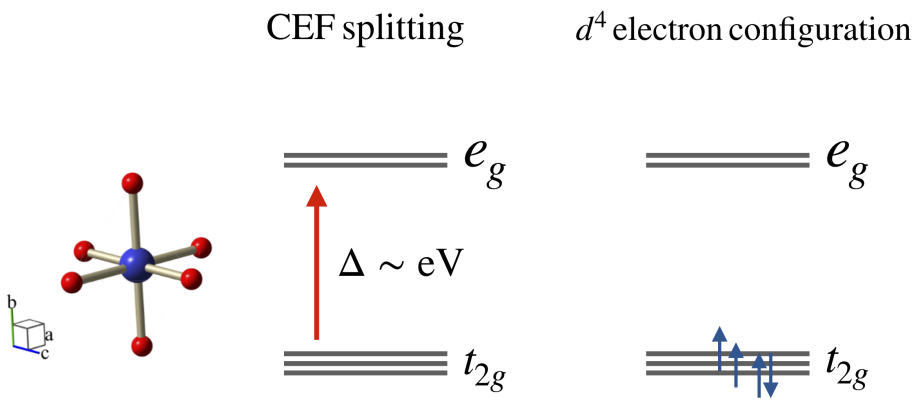

Figure 1.5: The local environment of the B' site is shown in this figure. In addition, the splitting of the d-electron levels at the B' site into a ground state t_{2g} triplet and excited e_g triplet is shown. The order the electron filling for a d^4 electron system is also illustrated as an example.

more spatially extended than the f-orbitals. The CEF splits the degeneracy of the energy levels which the unpaired electrons occupy, altering the electron configuration of the ion. This effect is accounted for as a perturbation to the spin Hamiltonian.

We shall use the example of $A_2BB'O_6$ to illustrate one commonly observed CEF splitting, where the B' ion is occupied by a d electron ion. The B' site is octahedrally coordinated to six oxygen atoms as shown in Figure 1.5. The crystal-electric field of this environment splits the d levels into a ground state triplet and an excited state doublet, which are collectively referred to as the t_{2g} and e_g levels, respectively. The gap, Δ, between these orbitals is on the order of electronvolts (eV). To highlight the influence of the crystal-field on the order of electron filing, we shall consider a four electron system as shown in Figure 1.5. As the energy barrier Δ is huge, the fourth electron pairs with one of the electrons in the t_{2g} levels as this configuration more energetically favourable than if it were to singly occupy the e_g level.

The crystal electric field Hamiltonian

It is appropriate to use a point-charge calculation to estimate describe the electrostatic CEF potential because, in this framework, the potential satisfies Laplace's equation, and can be expressed in terms of spherical harmonics [4]. The general form of the CEF potential $V(\boldsymbol{r}, \theta, \phi)$ is given by,

$$V(\boldsymbol{r},\theta,\phi) = \sum_{L'}\sum_{M'} A_{L'}^{M'} r^{L'} Y_{L'}^{M'}(\theta,\phi). \tag{1.18}$$

The number of terms which need to be included in the expansion is greatly reduced because many terms vanish due to orthogonality of the spherical harmonics and symmetry considerations which depend on the details of the magnetic ion in the local CEF [4]. The problem for magnetic ions in cubic CEFs has additionally been solved by Hutchings [11]. The terms in the expansion obtained for magnetic ions in cubic CEFs have also been re-expressed in terms of the so-called *Stevens operators* which are a function of the orbital angular momentum operators total L and L_z [12]. The resulting crystal-field Hamiltonian $\mathcal{H}_{CEF}$ reflects the point symmetry of the magnetic ion in the lattice.

To illustrate this concept, we shall consider the rare-earth ion, Yb^{3+}, in the pyrochlore structure with $Fm\overline{3}m$ symmetry as shown in Figure 1.6. The Yb^{3+} ion is surrounded by eight oxygen ions (O^{2-}) and has D_{3d} point symmetry as shown in Figure 1.6. The O^{2-} ions from the co-ordination environment interact with the magnetic ion via the electrostatic Coloumb potential $V(\boldsymbol{r},\theta,\phi)$. The applicable CEF Hamiltonian for $Yb_2Ti_2O_7$ given symmetry considerations on the pyrochlore lattice is,

$$\mathcal{H}_{CEF} = B_2^0\hat{O}_2^0 + B_4^0\hat{O}_4^0 + B_4^3\hat{O}_4^3 + B_6^0\hat{O}_6^0 + B_6^3\hat{O}_6^3 + B_6^6.\hat{O}_6^6. \tag{1.19}$$

The CEF parameters can be accurately determined by performing neutron spectroscopic measurements. [9]

1.4.2 Spin-orbit interaction

The spin-orbit interaction arises from the coupling between the spin and orbital angular momenta of an ion. The contribution of spin-orbit coupling (SOC) is only significant in systems containing heavy magnetic ions. To understand the mechanism of this interaction, consider the relative motion of the magnetic ionic nuclei with respect to the rest frame of the electrons which preside in the ionic orbitals. The electrons' spins couple to the magnetic field which is generated by the positively charged nucleus, via

[9] Section 2.3.2.3 provides a description for identifying CEFs in an inelastic neutron scattering experiment.

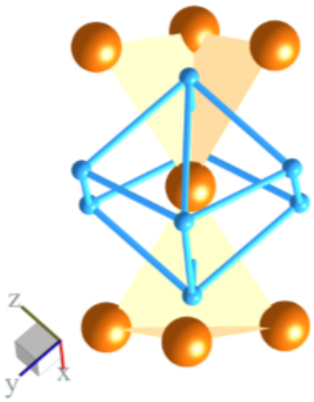

Figure 1.6: This schematic shows the Yb^{3+} ion in the presence of the local oxygen environment in the $Yb_2Ti_2O_7$ lattice. Permission to use photo obtained from Dalini. D. Maharaj, Master's Thesis, McMaster University [18].

a Zeeman interaction. The spin-orbit interaction, $\mathcal{H}_{SOC}$, can be expressed as,

$$\mathcal{H}_{SOC} = \lambda \boldsymbol{L} \cdot \boldsymbol{S}, \tag{1.20}$$

where λ relates strength of the spin-orbit interaction and is explicitly given by $\lambda = -\frac{e\hbar^2}{4m^2c^2}\frac{1}{r}\frac{\partial V}{\partial r}$. The strength of the spin-orbit interaction roughly scale as Z^2 for heavy ions [13].

Spin-orbit coupling manifests itself in the form of anisotropic exchange interactions or single-ion anisotropy. Therefore, systems based on $4d$, $4f$ and $5d$ ions are expected to display strong anisotropy as they possess substantial spin and orbital momenta. In the case of the double perovskite magnets studied in this thesis, La_2LiOsO_6 and La_2LiRuO_6, these forms of anisotropy are considered in two separate spin Hamiltonians which were utilized to model the low lying excitation spectra obtained from inelastic neutron scattering measurements. These anisotropic terms have the form,

$$\begin{aligned} \mathcal{H} &= -D\sum_i S_{i,x}^2 \qquad (\textbf{single}-\textbf{ion anisotropy}) \text{ and} \\ \mathcal{H} &= -K_1\sum_{NN} S_{i,x}S_{j,x} \quad (\textbf{anisotropic exchange}), \end{aligned} \tag{1.21}$$

where the parameters D and K describe the strength of single-ion anisotropy and

anisotropic exchange.

Turning our attention to $Yb_2Ti_2O_7$, it is a well-known fact that anisotropic exchange interactions and the Dzyaloshinskii Moriya (DM) interaction are important elements of its spin Hamiltonian. These interactions can be collectively expressed as,

$$\mathcal{H} = \frac{1}{2}\sum_{ij} J_{ij}^{\mu\nu} S_i^{\mu} S_j^{\nu} - \mu_B H^{\mu} \sum_i g_i^{\mu\nu} S_i^{\nu}, \tag{1.22}$$

where μ and ν refer to the global x, y, z coordinates and i and j refer different sublattices on the tetrahedron [14].

1.5 Frustrated Magnetism

Magnetic frustration has been a hotbed for new and exciting research in the field of condensed matter physics. At the core of this research field is the study of competing interactions and/or the effect of lattice geometries which preclude conventional magnetic order via the exchange interaction, which was introduced in Section 1.3. As geometric frustration is of key relevance to the magnetic systems studied in this thesis, we shall only consider this manifestation of magnetic frustration. In geometrically frustrated magnets, all bond interactions in the system cannot be simultaneously satisfied. In such a scenario, the ground state (GS) is highly degenerate paving way for weaker interactions, such as dipolar interactions, and anisotropies to dictate the nature of the magnetic GS. For example ferromagmetic interactions with local Ising like anisotropy can lead to a highly frustrated spin ice state in the rare-earth compounds $Dy_2Ti_2O_7$ and $Ho_2Ti_2O_7$ [15].

For illustrative purposes, we shall consider a formal definition of geometric frustration. Consider two spins which with exchange interactions characterized by $\mathscr{J}$ as given in Equation (1.15). It is clear that for most lattices hosting spins with ferromagnetic exchange interactions, the GS of the lattice is trivial as all pairwise ferromagnetic interactions between each spin can be satisfied. However, the scenario is not straightforward in the case of spins with near neighbour (NN) AF exchange interactions. The geometry of the lattice will dictate the spins are able to align anti-parallel to its neighbour. Lattices containing for example, triangular motifs, have a GS degeneracy for this reason. Indeed, the first pioneering work was led by Wannier in 1950 which

involved a study of AF Ising spins on the triangular lattice [16]. Generally speaking, if there is no spin system configuration wherein the individual NN spin interactions cannot be all satisfied at once, the system is frustrated.

To generalize this notion to other lattices in 2-D and 3-D, we must first consider the elementary cell comprising it. For example the elementary cell of the face-centred cubic lattice is a tetrahedron formed by four triangular plaquettes. If J_{ij} denotes the exchange between two spins on one plaquette, following the definition of Toulouse [17], the plaquette is frustrated if the frustration parameter P is negative. P is defined as the product of all J_{ij} around the entire plaquette with,

$$P = \prod_{<i,j>} sign(J_{i,j}).$$

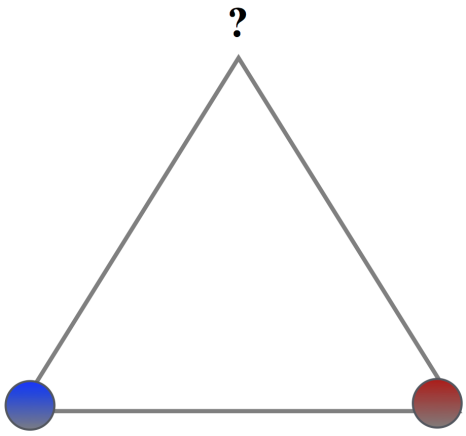

Figure 1.7: This schematic shows the frustrated triangular. The red dots represent $|\uparrow\rangle$ and blue dots represent $|\downarrow\rangle$. The double gray bar represents $J > 0$ and single-bars represent $J < 0$. Permission to use photo obtained from Dalini. D. Maharaj, Master's Thesis, McMaster University [18].

Figure 1.7 illustrates one of the frustrated triangular plaquettes which make up the tetrahedron, which is the elementary cell of the $R_2Ti_2O_7$ and $A_2BB'O_6$ magnetic sublattices. It is obvious that the product P is negative, hence, the FCC lattice with NN AF interactions is frustrated.

The tetrahedron is the building block for two archetypical frustrated lattices. The first case involves networks of corner-sharing tetrahedra as realized in the family of rare-earth titanates as shown in Figure 1.8. Early theoretical studies by Reimers

et al demonstrated that the high degree of frustration associated with this lattice precludes order at any non-zero temperature [19]. The cubic double perovskites (DPs) of the form $A_2BB'O_6$ provide an example for the second frustrated lattice based on tetrahedral architectures. Here, the magnetic lattice forms a network of edge-sharing tetrahedra as shown in Figure 1.8. The DPs are very widely studied due to the rich phase diagrams which have been produced for these systems [20–22]. The remainder of this chapter is dedicated to describing the magnetism exhibited by magnetic systems belonging to these two families.

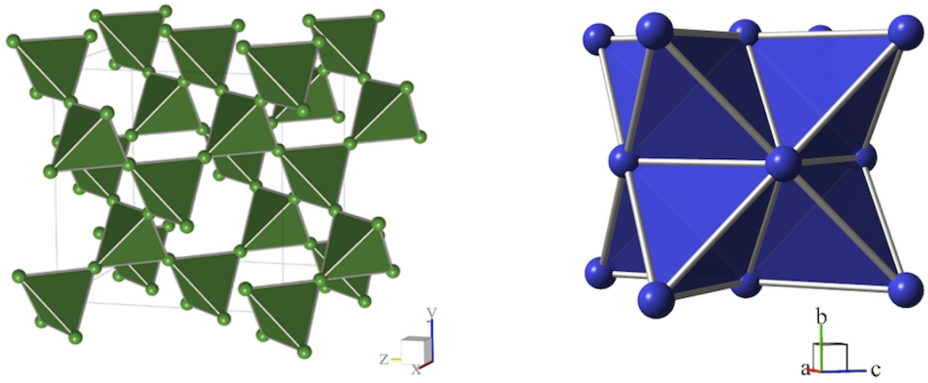

Figure 1.8: The frustrated networks of (a) corner-sharing tetrahedra (b) edge-sharing tetrahedra in the $R_2Ti_2O_7$ and $A_2BB'O_6$ crystal systems are shown in this illustration. Permission to use photo obtained from Dalini. D. Maharaj, Master's Thesis, McMaster University [18].

1.6 Introduction to the Materials Studied

1.6.1 The quantum spin ice candidate $Yb_2Ti_2O_7$

The rare-earth titanate (RET) pyrochlores have the general formula, $R_2Ti_2O_7$, where the R site is occupied by a rare-earth (RE) ion and the family of materials have cubic $Fd\bar{3}m$ symmetry. The R and Ti ions independently form networks of corner-sharing tetrahedra as shown in Figure 1.9. It is a well-known fact that the major factors which influence the nature of the ground state in these compounds are single-ion anisotropy, which is dictated by the crystal-field splitting of the f electron levels of the R^{3+} ion, dipolar interactions, and anisotropic exchange interactions [14]. The reader is encouraged to refer to excellent review articles which provide a comprehensive overview

of the numerous exotic ground states observed across this series as a result of the fine balance between these effects [23, 24].

One unique property of $Yb_2Ti_2O_7$ which distinguishes it from its other rare-earth counterparts is that it hosts net ferromagnetic interactions, as highlighted by its positive Curie-Weiss constant of $\sim +0.49\,K - +0.75\,K$ [25–28].[10] From this perspective, $Yb_2Ti_2O_7$ provides an important benchmark in systematic studies of the RET compounds. $Yb_2Ti_2O_7$ is demonstrably highly frustrated indeed as its ground state has been shown to exhibit strong sample dependence. Below, a short review of studies on $Yb_2Ti_2O_7$ is provided for context, but a comprehensive review can be found in Ref. [14].

Initial studies of powder samples of $Yb_2Ti_2O_7$ revealed a sharp anomaly at $\sim 240\,mK$ in heat capacity measurements [25, 26]. Although low temperature anomalies which appear in specific heat measurements could signal magnetic order, μSR studies conducted by Hodges *et al* provided no evidence for long-range magnetic order [30]. Later neutron scattering investigations confirmed the absence of long-range order in $Yb_2Ti_2O_7$ [31, 32]. In direct contrast, Yasui *et al* performed a neutron scattering investigation on single-crystals of $Yb_2Ti_2O_7$, finding evidence for magnetic ordering of Yb^{3+} moments in $Yb_2Ti_2O_7$ [33]. The varied reported low temperature behaviour of $Yb_2Ti_2O_7$ created some controversy surrounding the nature of the ground state of $Yb_2Ti_2O_7$. A later study involved a "tour de force" effort to unambiguously determine the exchange parameters of the anisotropic spin Hamiltonian of $Yb_2Ti_2O_7$ from inelastic neutron scattering measurements performed on single-crystals grown by the optical float-zone method [31, 34]. The outcome of this major piece of research classified $Yb_2Ti_2O_7$ as a quantum spin-ice candidate [34].

All these studies taken into consideration highlight the fragile nature of $Yb_2Ti_2O_7$'s ground state. Questions subsequently arose regarding the quality/stoichiometry of single-crystal samples, as detailed specific heat investigations yielded qualitatively different results for single-crystals versus powder samples.[11] Powder samples typically show a sharp anomaly at $240\,mK$ alongside a broad hump at $2\ K$ [28, 35]. Single-crystal samples on the other hand, show a broad hump [28, 35]. Rare-earth titanates

[10] Different values of θ_{CW} have been reported for $Yb_2Ti_2O_7$ as given by Refs. [25–27]. The strong dependence of θ_{CW} arises from the non-linearity of the inverse susceptibility and this matter is explored in detail in Refs. [26, 29].

[11] See Refs. [28, 35] for more details.

grown by the optical float zone method are known to experience a light degree of "stuffing" at the Ti^{4+} site [28], as shown in Figure 1.9.

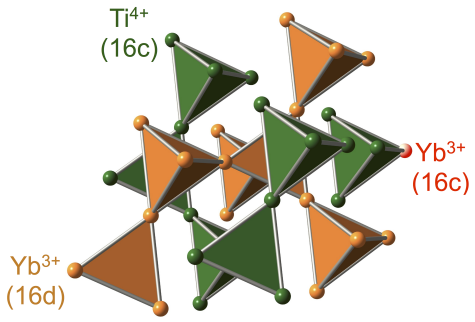

Figure 1.9: The interpenetrating networks of magnetic Yb^{3+} ions and nonmagnetic Ti^{4+} ions in $Yb_2Ti_2O_7$ are shown. The stuffed Yb^{3+} ions on the Ti^{4+} site is demonstrated in red. Reprinted figure from article Physical Review B, 97, 224409 (2018) with permission from Dalini D. Maharaj. Copyright 2020 by the American Physical Society.

This effect of stuffing could account for the variability in the GS of $Yb_2Ti_2O_7$ as stuffing introduces an additional nearest neighbour bond for the stuffed ions [28]. The result is that the stuffed Yb^{3+} ions would have different exchange pathways from the ions which are located at the nominal position, by virtue of their differing local oxygen environments. This would consequently influence the size and potentially, the sign of the exchange. One particular property that could be directly studied to probe the influence of stuffing in $Yb_2Ti_2O_7$ is the crystal-field scheme. The size and anisotropy of the magnetic moments in $Yb_2Ti_2O_7$ at the A and B sites can be directly determined from a measurement of the crystal-field levels at each site. To this end a study of the crystal-field levels in $Yb_2Ti_2O_7$ was conducted by Gaudet *et al* [36]. To investigate the potential effect of stuffing, a crushed single crystal sample, with stuffing on the $\sim$ 2% level, was investigated in parallel. No additional CEF levels associated with the anisotropy of the B site Yb^{3+} ions were experimentally measured. However, a first-principles calculation of the CEF splitting of the $4f$ levels of Yb^{3+} at B site demonstrated that the local environment would generate an Ising-like anistropy there [36]. This motivated our spectroscopic study of the crystal-field levels in two "highly" stuffed samples crystal single-crystal samples of $Yb_2Ti_2O_7$. More details can be found in Chapter 4.

1.6.2 Frustrated double perovskite magnets

Cubic rock-salt ordered double perovskites have the chemical formula $A_2BB'O_6$ [37]. When $A_2BB'O_6$ systems host net anti-ferromagnetic correlations between magnetic ions at the B' site, one of the hallmark architectures of frustration is realized (see Section 1.5). Many such systems containing heavy $4d$ and $5d$ ions at the B' have been widely studied because of the plethora of exotic ordered states which have been predicted due to the interplay of magnetic frustration and strong spin-orbit effects [20–22, 38].

The monoclinic d^3 double perovskites - La_2LiRuO_6 & La_2LiOsO_6

Investigations of the cubic d^3 double perovskites, Ba_2YRuO_6 and Ba_2YOsO_6 provide the context and motivation for the study of the monoclinic systems, La_2LiRuO_6 & La_2LiOsO_6. Inelastic neutron scattering investigations of Ba_2YRuO_6 and Ba_2YOsO_6 showed the development of spins gaps of size ~ 4 and 15 meV below their respective T_N's of 36 K and 69 K [39, 40]. This is unexpected for a d^3 electron configuration as Hund's rules dictate that the orbital moment would be quenched (see Figure 1.10). Furthermore, neutron powder diffraction studies found that both materials were found to develop type I AF order below their respective T_N's. There were a few important takeaways from the original studies which were performed by Carlo *et al* and Kermarrec *et al* [39, 40]. The size of the spin gap was found to correlate with the Néel transition temperature T_N and the spin-orbit parameter λ. Another feature of Ba_2YRuO_6 and Ba_2YOsO_6 is that the ordered moment of the Os^{5+} ions is significantly less than that is expected for a $S = 3/2$ system. Hybridization of the magnetic d orbitals and the oxygen orbitals has been argued to be the primary mechanism for this reduced moment [40]. The most important conclusion however, relates to the origin of the spin gap. The source of anisotropy in these systems has been attributed to the effect of anisotropic exchange interactions which arise due to spin-orbit coupling. Evidence for this is displayed size of the spin gaps in Ba_2YOsO_6 and Ba_2YOsO_6, which increase with the strength of spin-orbit coupling λ of the magnetic ions osmium and ruthenium ions [40].

The study of La_2LiRuO_6 & La_2LiOsO_6 provide a helpful point of reference for these studies and conclusions drawn from them for the following reasons. First, we consider that La_2LiRuO_6 and La_2LiOsO_6 are monoclinic systems which deviate only slightly from perfect cubic symmetry. The naïve position is that slight distortions

to the frustrated magnetic lattice might relieve magnetic frustration. It is also of interest to discern whether the spin gaps observed in cubic Ba_2YOsO_6 and Ba_2YRuO_6 apply to these non-cubic systems. The differences or similarities among the cubic and non-cubic systems enable one to hone in on the interactions of relevance in these novel d^3 systems.

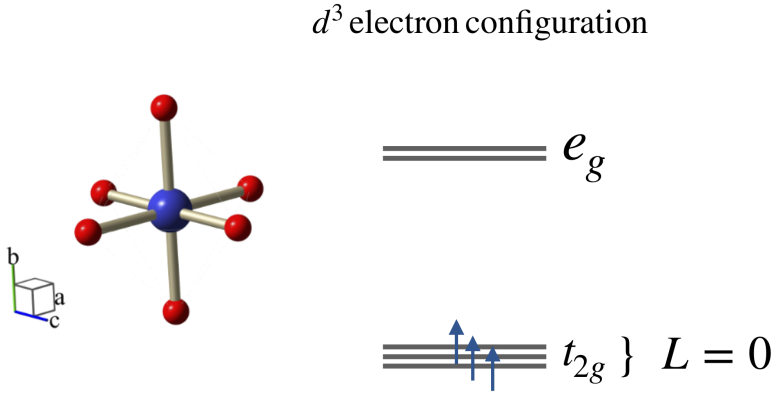

Figure 1.10: The electron filling for a d^3 magnetic ion in the presence of an octahedral crystal-field is shown.

The cubic d^2 double perovskites - Ba_2MOsO_6 (M = Zn, Mg & Ca)

A microscopic model was developed, at the mean-field level, for cubic rock-salt ordered d^2 double perovskites with strong spin-orbit coupling by Chen *et al* [21]. The complex phase diagram obtained from this model predicted the existence of a two-sublattice quadrupolar ordered phase with a vicinal antiferromagnetic (AFM100) phase [21]. As Ba_2CaOsO_6, Ba_2MgOsO_6, and Ba_2ZnOsO_6 are all cubic systems based on the heavy $5d^2$ Os^{6+} ion, these systems were investigated to understand their placement within this phase diagram. In addition, study of d^2 systems aids in the understanding of systematic behaviour and influence of spin-orbit coupling in relation to other $5d^n$ systems across the transition metal series.

Heat capacity, μSR, neutron diffraction and magnetization studies were performed by Thompson *et al* and Marjerrison *et al* on Ba_2CaOsO_6, Ba_2MgOsO_6, and Ba_2ZnOsO_6 [41, 42]. The first study involving Ba_2CaOsO_6 concluded the development of AF long-range order below the Neél temperature of $T_N \sim 50\,K$. These conclusions were made primary on the basis of specific heat studies and μSR studies which demonstrated the development of zero-longitudinal-field oscillations, indicative of magnetic long-range

order [41]. Marjerrison *et al* arrived at the same conclusions for Ba_2MgOsO_6 based on a combination of magnetization, specific heat and μSR. From a qualitative point of view, Ba_2MgOsO_6 and Ba_2CaOsO_6 were found to exhibit very similar properties and share similar Néel temperature of $T_N = 50K$. On the other hand, the μSR study of Ba_2ZnOsO_6 revealed the development of damped oscillations below its transition temperature of $T_N \sim 30\,K$. The authors concluded here, that the μSR lineshape indicated that Ba_2ZnOsO_6 remains in a complex partially ordered, partially dynamic state below 30 K [42].

To contribute to deeper understanding of these DPs, we conducted inelastic neutron scattering studies, and high intensity powder diffraction on Ba_2CaOsO_6, Ba_2MgOsO_6 and Ba_2ZnOsO_6. Inelastic neutron scattering studies would help confirm the similarity and differences noted among Ba_2CaOsO_6, Ba_2MgOsO_6 and Ba_2ZnOsO_6. The neutron powder diffraction studies were pursued at a high intensity diffraction instrument to aid in finding evidence for magnetic order in Ba_2CaOsO_6 and Ba_2MgOsO_6.

Bibliography

[1] Robert White. *Quantum Theory of Magnetism*. 3rd ed. Springer-Verlag Berlin Heidelberg, 2007.

[2] N.W. Ashcroft and N.D. Mermin. *Solid State Physics*. Holt, Rinehart and Winston, 1976, pp. 644–645.

[3] Eugen Merzbacher. *Quantum Mechanics*. 3rd ed. Wiley, 1998.

[4] Henri Alloul. *Introduction to the Physics of Electrons in Solids*. Springer-Verlag Berlin Heidelberg, 2011, pp. 231–273.

[5] Kurt Gottfried. *Quantum Mechanics: Fundamentals*. Vol. 1. W.A. Benjamin, Inc., 1966, pp. 302–304.

[6] John Berlinsky and Brooks Harris. *Statistical Mechanics: An Introductory Graduate Course*. 1st ed. Springer International Publishing, 2019.

[7] Piers Coleman. *Introduction to Many-Body Physics*. 1st ed. Cambridge University Press, 2015.

[8] W. Heitler and F. London. "Wechselwirkung neutraler Atome und homöopolare Bindung nach der Quantenmechanik". In: *Zeitschrift für Physik* 44 (1927), pp. 455–472.

[9] John B. Goodenough. "Theory of the Role of Covalence in the Perovskite-Type Manganites $[\mathrm{La}, M(\mathrm{II})]\mathrm{MnO}_3$". In: *Phys. Rev.* 100 (1955), pp. 564–573.

[10] Junjiro Kanamori. "Superexchange interaction and symmetry properties of electron orbitals". In: *Journal of Physics and Chemistry of Solids* 10 (1959), pp. 87–98.

[11] M. T. Hutchings. *Solid State Physics: Advances in Research and Applications*. Vol. 16. Academic Press, 1964, pp. 227–257.

[12] K. W. H. Stevens. "Matrix elements and operator equivalents connected with the magnetic properties of rare earth ions." In: *Proc. Roy. Soc. A* 654 (1952), p. 209.

[13] K. V. Shanavas, Z. S. Popović, and S. Satpathy. "Theoretical model for Rashba spin-orbit interaction in d electrons". In: *Phys. Rev. B* 90 (2014), p. 165108.

[14] K. A. Ross. "Neutron Scattering Studies of the Quantum Spin Ice Material $Yb_2Ti_2O_7$". PhD thesis. McMaster University, 2012.

[15] Steven T. Bramwell and Michel J. P. Gingras. "Spin Ice State in Frustrated Magnetic Pyrochlore Materials". In: *Science* 294 (2001), pp. 1495–1501.

[16] G. H. Wannier. "Antiferromagnetism. The Triangular Ising Net". In: *Phys. Rev.* 79 (1950), pp. 357–364.

[17] G. Toulouse. In: *Commun. Phys.* 2 (1977).

[18] D. D. Maharaj. "Neutron Scattering of the Frustrated Magnets Ba_2YOsO_6 and $Yb_2Ti_2O_7$". MA thesis. McMaster University, 2015.

[19] J. N. Reimers, A. J. Berlinsky, and A.-C. Shi. "Mean-field approach to magnetic ordering in highly frustrated pyrochlores". In: *Phys. Rev. B* 43 (1991), pp. 865–878.

[20] Gang Chen, Rodrigo Pereira, and Leon Balents. "Exotic phases induced by strong spin-orbit coupling in ordered double perovskites". In: *Phys. Rev. B* 82 (2010), p. 174440.

[21] Gang Chen and Leon Balents. "Spin-orbit coupling in d^2 ordered double perovskites". In: *Phys. Rev. B* 84 (2011), p. 094420.

[22] William Witczak-Krempa, Gang Chen, Yong Baek Kim, and Leon Balents. "Correlated Quantum Phenomena in the Strong Spin-Orbit Regime". In: *Annual Review of Condensed Matter Physics* 5 (2014), pp. 57–82.

[23] Jason S. Gardner, Michel J. P. Gingras, and John E. Greedan. "Magnetic pyrochlore oxides". In: *Rev. Mod. Phys.* 82 (2010), pp. 53–107.

[24] Alannah M. Hallas, Jonathan Gaudet, and Bruce D. Gaulin. "Experimental Insights into Ground-State Selection of Quantum XY Pyrochlores". In: *Annual Review of Condensed Matter Physics* 9 (2018), pp. 105–124.

[25] H.W.J. Blöte, R.F. Wielinga, and W.J. Huiskamp. "Heat-capacity measurements on rare-earth double oxides $R_2Ti_2O_7$". In: *Physica* 43 (1969), pp. 549–568.

[26] S. T. Bramwell, M. N. Field, M. J. Harris, and I. P. Parkin. "Bulk magnetization of the heavy rare earth titanate pyrochlores - a series of model frustrated magnets". In: *Journal of Physics: Condensed Matter* 12 (1999), pp. 483–495.

[27] J. A. Hodges, P. Bonville, A. Forget, M. Rams, K. Królas, and G. Dhalenne. "The crystal field and exchange interactions in $Yb_2Ti_2O_7$". In: *Journal of Physics: Condensed Matter* 13 (2001), pp. 9301–9310.

[28] K. A. Ross, Th. Proffen, H. A. Dabkowska, J. A. Quilliam, L. R. Yaraskavitch, J. B. Kycia, and B. D. Gaulin. "Lightly stuffed pyrochlore structure of single-crystalline $Yb_2Ti_2O_7$ grown by the optical floating zone technique". In: *Phys. Rev. B* 86 (2012), p. 174424.

[29] H. B. Cao, A. Gukasov, I. Mirebeau, and P. Bonville. "Anisotropic exchange in frustrated pyrochlore $Yb_2Ti_2O_7$". In: *Journal of Physics: Condensed Matter* 21 (2009), p. 492202.

[30] J. A. Hodges, P. Bonville, A. Forget, A. Yaouanc, P. Dalmas de Réotier, G. André, M. Rams, K. Królas, C. Ritter, P. C. M. Gubbens, C. T. Kaiser, P. J. C. King, and C. Baines. "First-Order Transition in the Spin Dynamics of Geometrically Frustrated $Yb_2Ti_2O_7$". In: *Phys. Rev. Lett.* 88 (2002), p. 077204.

[31] K. A. Ross, J. P. C. Ruff, C. P. Adams, J. S. Gardner, H. A. Dabkowska, Y. Qiu, J. R. D. Copley, and B. D. Gaulin. "Two-Dimensional Kagome Correlations and Field Induced Order in the Ferromagnetic XY Pyrochlore $Yb_2Ti_2O_7$". In: *Phys. Rev. Lett.* 103 (2009), p. 227202.

[32] J. S. Gardner, G. Ehlers, N. Rosov, R. W. Erwin, and C. Petrovic. "Spin-spin correlations in $Yb_2Ti_2O_7$: A polarized neutron scattering study". In: *Phys. Rev. B* 70 (2004), p. 180404.

[33] Yukio Yasui, Minoru Soda, Satoshi Iikubo, Masafumi Ito, Masatoshi Sato, Nobuko Hamaguchi, Taku Matsushita, Nobuo Wada, Tetsuya Takeuchi, Naofumi Aso, and Kazuhisa Kakurai. "Ferromagnetic Transition of Pyrochlore Compound $Yb_2Ti_2O_7$". In: *Journal of the Physical Society of Japan* 72 (2003), pp. 3014–3015.

[34] Kate A. Ross, Lucile Savary, Bruce D. Gaulin, and Leon Balents. "Quantum Excitations in Quantum Spin Ice". In: *Phys. Rev. X* 1 (2011), p. 021002.

[35] A. Yaouanc, P. Dalmas de Réotier, C. Marin, and V. Glazkov. "Single-crystal versus polycrystalline samples of magnetically frustrated $Yb_2Ti_2O_7$: Specific heat results". In: *Phys. Rev. B* 84 (2011), p. 172408.

[36] J. Gaudet, D. D. Maharaj, G. Sala, E. Kermarrec, K. A. Ross, H. A. Dabkowska, A. I. Kolesnikov, G. E. Granroth, and B. D. Gaulin. "Neutron spectroscopic study of crystalline electric field excitations in stoichiometric and lightly stuffed $Yb_2Ti_2O_7$". In: *Phys. Rev. B* 92 (2015), p. 134420.

[37] P. W. Anderson. "Resonating valence bonds: A new kind of insulator?" In: *Materials Research Bulletin* 8 (1973), pp. 153–160.

[38] Naoya Iwahara, Veacheslav Vieru, and Liviu F. Chibotaru. "Spin-orbital-lattice entangled states in cubic d^1 double perovskites". In: *Phys. Rev. B* 98 (2018), p. 075138.

[39] J. P. Carlo, J. P. Clancy, K. Fritsch, C. A. Marjerrison, G. E. Granroth, J. E. Greedan, H. A. Dabkowska, and B. D. Gaulin. "Spin gap and the nature of the $4d^3$ magnetic ground state in the frustrated fcc antiferromagnet Ba_2YRuO_6". In: *Phys. Rev. B* 88 (2013), p. 024418.

[40] E. Kermarrec, C. A. Marjerrison, C. M. Thompson, D. D. Maharaj, K. Levin, S. Kroeker, G. E. Granroth, R. Flacau, Z. Yamani, J. E. Greedan, and B. D. Gaulin. "Frustrated fcc antiferromagnet Ba_2YOsO_6: Structural characterization, magnetic properties, and neutron scattering studies". In: *Phys. Rev. B* 91 (2015), p. 075133.

[41] C. M. Thompson, J. P. Carlo, R. Flacau, T. Aharen, I. A. Leahy, J. R. Pollichemi, T. J. S. Munsie, T. Medina, G. M. Luke, J. Munevar, S. Cheung, T. Goko, Y. J. Uemura, and J. E. Greedan. "Long-range magnetic order in the 5d2 double

perovskite Ba_2CaOs_6: comparison with spin-disordered Ba_2YRe_6". In: *Journal of Physics: Condensed Matter* 26 (2014), p. 306003.

[42] C. A. Marjerrison, C. M. Thompson, A. Z. Sharma, A. M. Hallas, M. N. Wilson, T. J. S. Munsie, R. Flacau, C. R. Wiebe, B. D. Gaulin, G. M. Luke, and J. E. Greedan. "Magnetic ground states in the three Os^{6+} ($5d^2$) double perovskites Ba_2MOsO_6 ($M = \mathrm{Mg}, \mathrm{Zn}, \mathrm{and\,Cd}$) from Néel order to its suppression". In: *Phys. Rev. B* 94 (2016), p. 134429.

2 Neutron & X-ray Scattering Theory

> "When I conceived the first basic ideas of wave mechanics in 1923–24, I was guided by the aim to perform a real physical synthesis, valid for all particles, of the coexistence of the wave and of the corpuscular aspects that Einstein had introduced for photons in his theory of light quanta in 1905. — *Louis de Broglie*"

2.1 Historical Perspective

Neutron and x-ray scattering methods are extremely powerful tools utilized in the study of the structural and magnetic properties of complex condensed matter systems. These techniques had remarkable beginnings as Nobel Prizes were awarded to the pioneering scientists who either first showcased their utility in the investigation of materials, or made ground breaking theoretical predictions which strongly influenced their development. Max von Laue was awarded the Nobel Prize in Physics in 1914 for demonstrating the diffraction of x-rays using crystals [1]. One year later, the father-son duo, W. H. Bragg and W. L. Bragg, later showed how crystals could be uniquely identified using x-ray diffraction [2], leading to the explosion of the field of crystallography.

Later in 1932, an exciting era began in the realm of physics marking the advent of the "mysterious" new theory, quantum mechanics, which had serious implications for fundamental concepts underpinning classical mechanics. Key principles were established including, the concept of spin in real particles, the Pauli Exclusion principle

and the Heisenberg uncertainty principle. Consequently, there were huge ramifications for the theoretical description of matter in the sub-field of condensed matter physics. In tandem with the emergence of quantum mechanics, Louis de Broglie demonstrated the wave nature of electrons in 1929 [3] and Clinton Joseph Davisson and George Paget Thomson demonstrated the diffraction of electrons by crystals [4]. It is no surprise that following the discovery of the neutron by Chadwick in 1932 did physicists also begin to conceive of neutron diffraction experiments.

The study of magnetic materials with neutron scattering was first proposed by Bloch [5] given the neutron's ability to interact with magnetic degrees of freedom through its spin. The first triumphant neutron scattering study of magnetic systems followed, and was conducted by Shull and Smart who directly measured the anti-ferromagnetic phase in MnO [6]. Before that time, magnetic properties were only indirectly probed through other techniques, e.g. detecting Curie points and specific heat anomalies.

Armed with these new perspectives provided by experimental scattering methods, theorists were challenged to develop new frameworks to describe solid state systems. Rich phase diagrams were produced for simple magnetic spin systems, thereby egging on experimentalists to produce samples which could approximately represent these simple spin systems in reality. The experiments which followed therefore provided a direct challenge to the new status quo of quantum physics, and its accuracy in describing condensed matter systems. Since then, many theories have been corrected, and exotic magnetic phases have been realized, accelerating materials innovation.

The remainder of this chapter briefly touches on neutron and x-ray diffraction techniques, highlighting their complementarity, and provides a solid description of neutron scattering theory. A rigorous description of x-ray scattering is omitted as neutron scattering is the principle technique which I used during my thesis studies. The discussion below is largely guided by a books written by Furrer [7, 8], Ashcroft & Mermin [9], Squires [10] and Lovesey [11]. The reader is encouraged to reference these books for detailed information as this account seeks to provide only the necessary details required to understand the contents of this thesis.

2.2 Principles of X-ray and Neutron Diffraction

A scattering formalism for both x-rays and neutrons can be developed in parallel. A typical scattering experiment setup is shown in Figure 2.1. The scattering experiment comprises a radiation source (neutron or x-ray) of fixed energy, a sample for investigation and a detector. During a scattering experiment, the scattering intensity is measured as a function of the energy (ϵ) and momentum ($\boldsymbol{\kappa}$) exchanged with the sample, and scattering angle are measured. Broadly speaking, we can distinguish two types of scattering, namely, elastic ($\epsilon = 0$) and inelastic scattering $\epsilon \neq 0$. We shall first consider elastic scattering of x-rays and neutrons from crystalline structure.

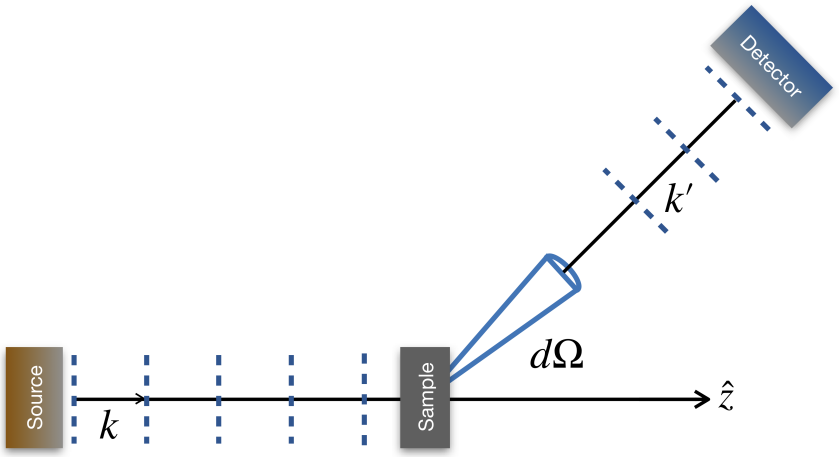

Figure 2.1: A typical scattering experiment involves a source of neutrons or x-rays incident upon a sample. The intensity scattered in a particular direction of solid angle $d\Omega$ is measured with the use of an appropriate detector.

Elastic scattering of neutrons and x-rays can be utilized for the determination of crystal structures via diffraction. This is possible since typical atomic spacings in crystals are comparable to the wavelength of neutrons and x-rays. The diffraction pattern obtained from a diffraction experiment can be predicted based on the symmetries of the structure. The easiest way to illustrate diffraction in crystals is through Bragg's law of diffraction as shown in Figure 2.2. The atoms in the crystal form planes of diffraction, with fixed spacing d. These planes are referred to as Miller planes and are collectively indexed by $\{hkl\}$. hkl indexes the reciprocal lattice vector $\boldsymbol{\tau_{hkl}}$ which is perpendicular to family of Miller planes $\{hkl\}$ [1]. A diffraction maximum is obtained

[1] See Ref. [9] for an explanation of reciprocal space, applied to crystallography.

for a given set of planes, $\{hkl\}$, if the x-rays or neutrons undergo elastic scattering at an angle 2θ. The relationship between the scattering angle 2θ, d_{hkl} and λ is,

$$\lambda = 2d_{hkl} \sin\theta_{hkl}. \tag{2.1}$$

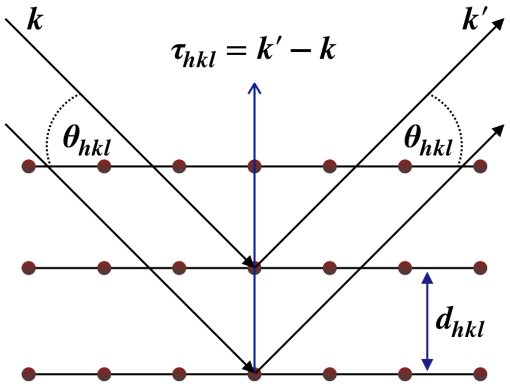

Figure 2.2: A schematic of Bragg's law is shown with the incident radiation, at an angle θ, on a family of Miller planes indexed by the reciprocal lattice vector $\boldsymbol{\tau_{hkl}}$. The von Laue condition is satisfied and constructive interference of the radiation produces a diffraction maximum.

The von Laue condition for successful diffraction of x-rays/neutrons is that the momentum transfer $\boldsymbol{\kappa}$ must be a reciprocal lattice vector $\boldsymbol{\tau_{hkl}}$, i.e. $\boldsymbol{\kappa} = \boldsymbol{\tau_{hkl}}$. Therefore, a diffraction data set will contain diffraction maxima occurring at different hkl corresponding to a reciprocal lattice vector $\boldsymbol{\tau_{hkl}}$ perpendicular to the planes of symmetry related atoms. Bragg's description, though simple, fails to account for the difference in intensities of the diffraction maxima. A more rigorous treatment of neutron and x-ray scattering is required to tease out this information.

We shall proceed to do so by first utilizing the *Born approximation* and assume that the incident x-ray photons/neutrons are free particles and that their wavefunctions can be described in terms of plane waves. For simplicity, assume that the incident x-ray/neutron waves propagate in the Cartesian $\hat{z}$ direction. The form of ψ_0 for the incident plane wave is, $\psi_0 = e^{i(kz-\omega t)}$, where $\omega = 2\pi/T$ and $k = 2\pi/\lambda$. ω, k and z represent the angular frequency, wavevector and Cartesian co-ordinate of the direction of propagation of the wave, respectively. The x-ray/neutron has a well defined energy E according to the relation $E = \hbar\omega$ where $\hbar = \frac{h}{2\pi}$ is the reduced Planck's constant. For both the x-ray and neutron cases, ψ_0 are solutions to the Schrödinger's equation

for a free particle with energy E.[2].

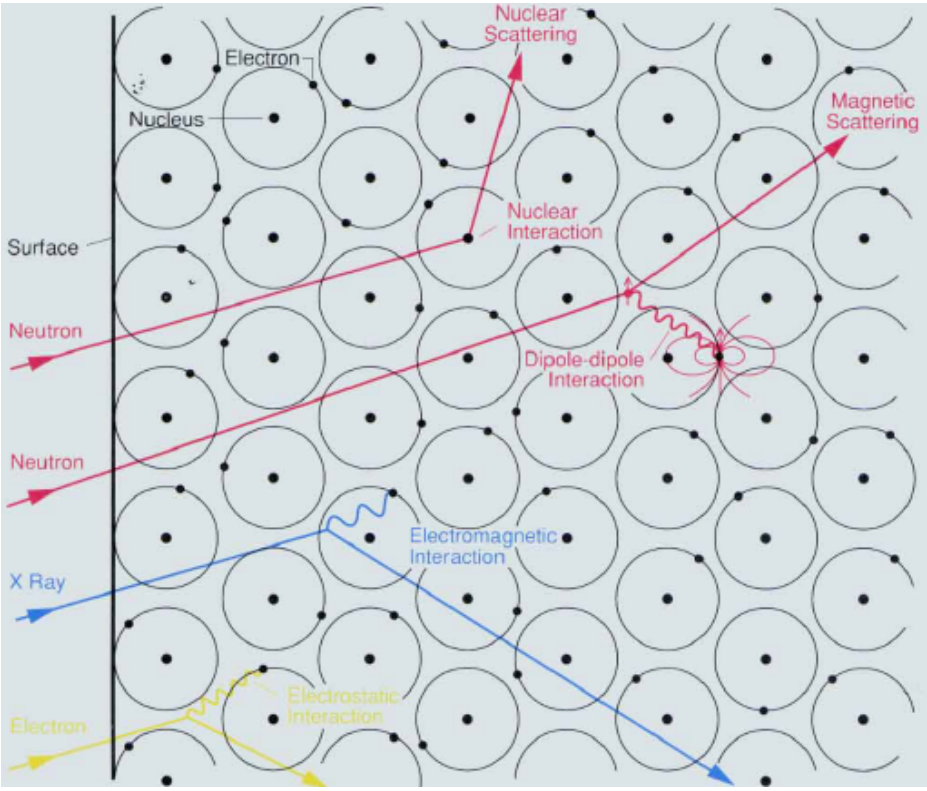

Figure 2.3: The scattering mechanisms of x-rays and neutrons with matter are pictorially demonstrated. Reprinted figure from lecture notes Neutron Scattering - A Primer and permission was obtained from Prof. Roger Pynn to reuse this image.

When the x-rays or neutrons encounter the scattering species, they are subject to an interaction potential. X-rays are sensitive to the electric fields produced by the electron density of atoms, as shown in Figure 2.3. Neutrons on the other hand, undergo direct or hard scattering with the nuclei as they are massive, uncharged particles.[3][4] This is also shown in Figure 2.3. Thereafter, the beam of x-rays or neutrons are scattered off into different directions. The scattered wavefunction is given by, $\psi_s = -\frac{b}{r}\,\psi_0$, where b is the scattering length. b depends on the interaction potential between the photon

[2]The form of Schödinger's equation varies distinctly for neutrons and x-rays because the former can be treated in the non-relativisitic limit where the rest mass energy mc^2 is much larger than the kinetic energy E while the photon has zero rest mass and is always in the super-relativisitic limit [12]

[3]The term "massive particle" refers to those particles which have real, non-zero, rest mass e.g. electrons, neutrons and protons. A photon, on the other hand, is not a massive particle.

[4]Neutrons also interact with the spins degrees of freedom of the unpaired electrons in the scattering species, as shown in Figure 2.3.

and electron density (x-ray case), and the neutron and scattering nuclei (neutron case). We seek to describe elastic scattering of the x-rays or neutrons due to this interaction potential, where the energy of a given x-ray photon or neutron remains the same, while the wavevector can change.

Consider the current of particles per second, incident on the sample I_0, being scattered within solid angle $d\Omega$, into a current I_s. The definition of the differential cross-section, yields,

$$I_s = I_0 \frac{d\sigma}{d\Omega} d\Omega. \tag{2.2}$$

I_s and I_0 can be represented in terms of the wavefunctions for the incident and scattered waves, ψ_0 and ψ_s. An equivalent form for Eq. 2.8 can be rewritten in terms of ψ_0 and ψ_s with,

$$k' \, \psi_s^* \, \psi_s \, r^2 \, d\Omega = k \, \psi_0^* \, \psi_0 \, d\Omega \, \frac{d\sigma}{d\Omega}. \tag{2.3}$$

In the limit of large distances, take $\psi_s \rightarrow -b \, e^{ikr}/r$, where b can in general, be dependent on the scattering angle. Applying $k = k'$ and orthonormality of ψ_0 to Equation (2.8), the differential cross-section becomes,

$$\frac{d\sigma}{d\Omega} = bb^*. \tag{2.4}$$

b can be evaluated from first-order perturbation theory using the interaction potential of the x-rays or neutrons with matter, as a weak perturbation to the free-particle Hamiltonian.

In crystals, the electron density distribution and arrangement of nuclei are periodically arranged. As such, we can naively expect that the interaction potential of the x-ray photons or neutrons with the crystal can be mathematically described in terms of periodic function which can be decomposed into a Fourier series. The Fourier series decomposition occurs at nodes $\boldsymbol{\tau}$ which are reciprocal lattice vectors of the crystal structure. We use $\widetilde{V}(\boldsymbol{\tau})$ and $\widetilde{\rho}(\boldsymbol{\tau})$ to denote the Fourier transform of the potentials due to the nuclear scattering centre, $V(\mathbf{r})$ (neutron case) and electron density, $\rho(\mathbf{r})$ (x-ray case), respectively. Without proof, we further assert that (i) the diffraction

intensity, and (ii) the scattering length b is proportional to $V(\mathbf{r})$ (neutron case) and electron density, $\rho(\mathbf{r})$ (x-ray case). In the end, the total scattering turns out to be a superposition of the individual contributions of each hkl reflection where we call each contribution, the form factor $F_{\boldsymbol{\tau}}$. $F_{\boldsymbol{\tau}}$ is given by,

$$F_{\boldsymbol{\tau}} = \sum_{\text{unit cell}} b_i \cdot e^{-2\pi i \boldsymbol{\tau}\cdot\mathbf{r}_i} \cdot e^{-W_i} \,(\text{neutron}), \tag{2.5}$$

and

$$F_{\boldsymbol{\tau}} = \sum_{\text{unit cell}} f_{at,i}(\boldsymbol{\tau}) \cdot e^{-2\pi i \boldsymbol{\tau}\cdot\mathbf{r}_i} \cdot e^{-W_i} \,(\text{X}-\text{rays}). \tag{2.6}$$

The common factor e^{-W_i} which appears in both equations is called the Debye-Waller factor[5] which is a temperature dependent term which is related to the mean square displacement $\langle u^2 \rangle$ of the atoms within the lattice about their equilibrium positions via $W_i = 8\pi^2 \frac{\sin^2(\theta)}{\lambda^2} \cdot \langle u^2 \rangle$. This factor suppresses the scattered intensity for high temperatures and for high order reflections (or equivalently, reflections with small d_{hkl}). In neutron diffraction, b_i refers to a scattering length equal to $\frac{2m}{4\pi\hbar^2}V(\boldsymbol{\tau})$. In x-ray diffraction $f_{at,i}$ is the atomic scattering factor or form factor for an atom i at position r_i. f_{at} is defined as,

$$f_{at}(\boldsymbol{\tau}) = \int \rho(\mathbf{r}) e^{i\boldsymbol{\tau}\cdot\mathbf{r}} d^3\mathbf{r}, \tag{2.7}$$

where $Z = \int \rho(\mathbf{r})\, d^3\mathbf{r}$ is the atomic number Z, representing the total number of electrons in the atom.

There are a key points that need to clarified from the discussion above.

- The total scattering measured for either the neutron or x-ray case scales with the form factor squared.
- The x-ray form factor stated in Equation (2.7), represents only the real component of the scattering. It is the form factor arising from only elastic scattering processes, or *Thomson scattering*. The imaginary contribution is referred to as the *anomalous dispersion* correction term, δf. This term is of significance when

[5]The Debye Waller factor accounts for the attenuating effect of lattice vibrations on the scattering strength (see Ref. [14]).

the photon energy is tuned to that of an absorption edge of an atom.[6]

- The neutron form factor stated in Equation (2.5) relates the scattering strength arising from nuclear scattering only. Neutrons also interact with spin degrees of freedom in matter. Refer to Section 2.3 for the full scattering function of neutrons with matter.
- The geometric features of Bragg diffraction are encoded within the physical and mathematical periodic structure of the interaction potentials $V(\mathbf{r})$ and $\rho(\mathbf{r})$. The scattering intensities both have the information regarding the crystalline structure encoded in them.

Clearly, neutron and x-ray diffraction experiments can be conducted to obtain information about the structure of matter. However, the next section is dedicated to highlighting their complementarity, showing the strength of utilizing both techniques, in spite of this fundamental similarity.

2.2.1 Complementary Probes: X-ray vs Neutron Diffraction

So far, this chapter has explained the similar utility of neutron and X-ray diffraction methods. This section shall proceed to motivate the use of each technique, which aids in motivating their respective uses in Chapter 6. We shall first consider that neutrons and X-rays coming from their sources have energies on the order of $\sim$ 1 MeV and $\sim$ 1- 100 keV, respectively. Although neutron energies are huge, their motion can be "moderated" or slowed because they are massive particles. The speed of X-rays on the other hand, cannot be manipulated in this manner. Neutron energies can be moderated to the $\sim$ meV level, and be utilized in scattering experiments to investigate elementary excitations of condensed matter systems - such as phonons and magnons - which are also on that energy scale. Another direct consequence of neutrons having mass is that it is possible to conduct time-of-flight[7] scattering experiments with neutrons. As will be discussed in Chapter 3, this is a very powerful technique for the measurement of lattice and spin dynamics.

It is possible for neutrons to probe spin dynamics in crystals as they possess spin.

[6] When this condition is met, a resonance effect is created such that the change of the phase of the photon is different from exactly π and the magnitude of the form factor is somewhat different from the case in which the photon energy is away from the absorption edge.

[7] Refer to Chapter 3 for details on time-of-flight scattering techniques.

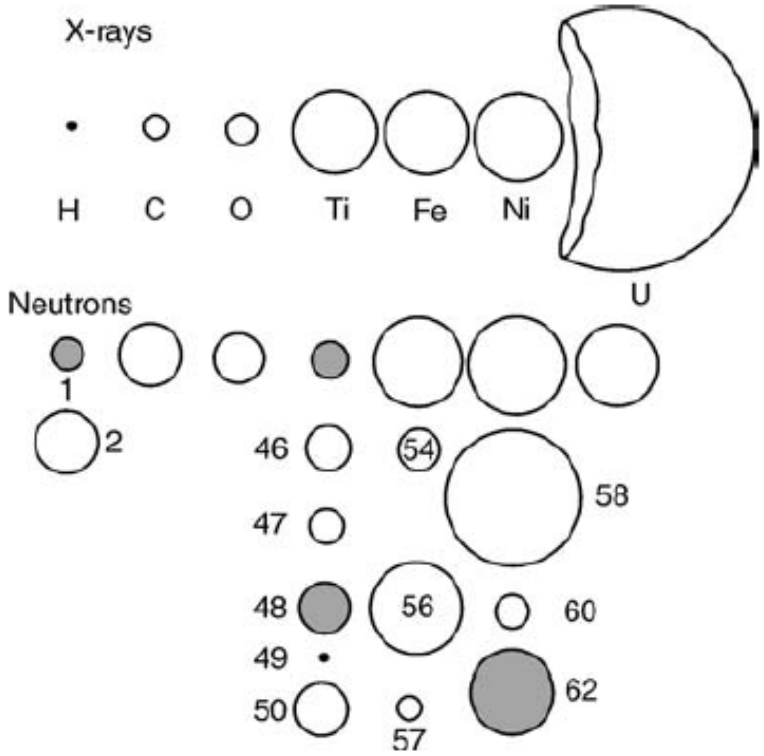

Figure 2.4: The comparison of the variability of the scattering cross-section with atomic size for neutrons and x-rays are represented in this schematic. The radii of the circles are proportional to the scattering amplitude, b. Shaded circles represent negative values of b. Reprinted from Neutron Scattering from Magnetic Materials, 1st Edition, Tapan Chatterji, Page. 12, Copyright 2020, with permission from Elsevier.

This permits neutrons to interact directly with magnetic degrees of freedom in matter. Measuring inelastic processes in a neutron scattering experiment enables the direct measure of magnetic excitations of the system being investigated.[8]

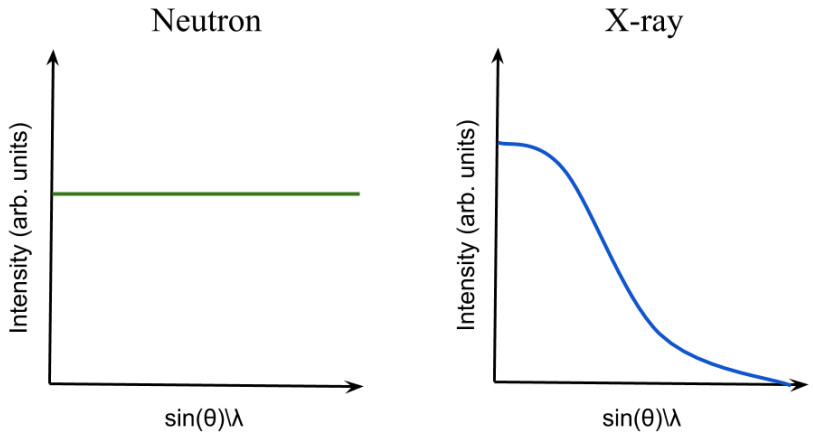

Figure 2.5: The comparison of the θ dependence of the scattering length b_i (for the neutron case) and the atomic factor $f_{a,i}$ (for the x-ray case) are pictorially represented.

Another feature of neutron and x-ray scattering can be highlighted by inspection of the form factors. The form factor for x-rays depends directly on the electron density in the sample. Hence, the strength of $\rho(\boldsymbol{\tau})$ is directly related to the atomic number Z. In contrast, the interaction potential $V(\boldsymbol{\tau})$ between neutrons and nuclei results from the strong nuclear force. All isotopes of the same atom do not have the same scattering length b as it is dependent on the spin state of the atom.[9] Hence it turns out that the nuclear scattering cross-section for neutrons from a given sample is not systematically related to the size of the atom as it is in the case of x-ray scattering, as seen in Figure 2.4. Another clear difference between the form factors for x-rays and the nuclear contribution to neutron scattering is that the of the form factor of x-rays depends on θ while b is a constant, as shown in Figure 2.5. In the neutron case, the scattering length b can be characterized by this single parameter as the scattering is nearly point-like, containing only s-wave components, and is therefore isotropic. This is a result of the fact that the range of the nucleus-neutron interaction is ($\sim 10^{-13}\, cm$)

[8]The neutron scattering intensity from nonmagnetic versus magnetic excitations are discernible due to their differing and opposite $|Q|$ dependence. Refer to Section 2.3 for more details.

[9]The size and sign of b is determined from neutron refraction experiments as b^2 is obtained in neutron scattering experiments.

and is smaller than the wavelength of thermal neutrons.

It is clear from the previous discussion that x-rays diffraction is not a sensitive to the positions of low Z elements like oxygen and hydrogen. On the other hand, neutron scattering is able to provide this information, as oxygen and hydrogen have large coherent neutron scattering lengths. Another disadvantage of the Z dependence of x-ray scattering arises in the study of compounds containing a mix of two or more high Z atoms where the contrast is low. Neutrons can be utilized to contrast two or more atomic species with similar atomic number provided that their scattering lengths are distinct from each other. It was also mentioned that the neutron scattering length b is different for isotopes of the same element. This property can be exploited in the study of biological materials in neutron scattering experiments. A technique called contrast variation is employed wherein specific hydrogen containing functional groups or molecules can be selectively deuterated by substituting hydrogen with deuterium. As hydrogen and deuterium have very different neutron scattering lengths of -3.74 fm and 6.67 fm respectively, this improves contrast of these targeted functional groups or molecules within the sample without altering their chemical behaviour.

The final detail which will be discussed relates to a practical consequence in scattering experiments using x-rays versus neutrons. This can be appreciated by considering Figure 2.6, which shows two Bragg peaks, one from a neutron diffraction data set and the other from an x-ray diffraction data set. The stark difference between the linewidths of the Bragg peaks of the neutron diffraction data compared with the x-ray synchrotron data can be clearly seen. The angular resolution of the synchrotron x-ray scattering data is typically many times better than the corresponding neutron diffraction data on the same material. This difference can be appreciated by accounting for the brightness of neutron sources compared with x-ray synchrotron sources. The brightness of neutron and x-ray sources characterizes the flux and divergence of the beams which they are capable of producing. X-ray synchrotron sources produce high flux photon beams ($\sim 10^{24}$ photons $s^{-1}\,m^2$) which are also highly coherent, with divergences of $\sim 0.01 \times 0.1\,mrad^2$. As a result, very high spatial resolutions are achievable in x-ray synchrotron diffraction experiments. In contrast, neutron scattering is an intensity limited technique in which the flux of neutron beams produced at neutron sources are a factor $\sim 10^{13}$ lower and have large divergences of $\sim 10 \times 10\,mrad^2$. The comparatively low brilliance of neutron sources makes it difficult to focus neutron

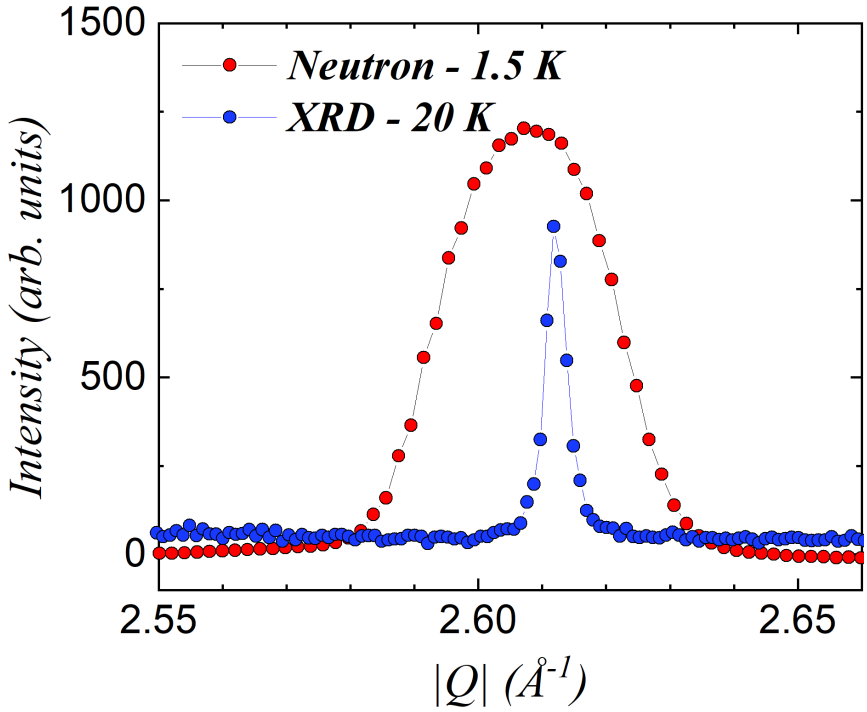

Figure 2.6: A comparison of the same nuclear Bragg peak of Ba_2CaOsO_6 from neutron and synchrotron x-ray data are shown. Reprinted figure from article Physical Review Letters 124, 087206 (2020) with permission from Dalini D. Maharaj. Copyright 2020 by the American Physical Society.

beams without compromising the neutron intensity upon the sample.

Consideration of all these details makes it easy to envision how x-ray and neutrons can be used in a complementary manner. Typically, high resolution structural determination is first performed with x-ray diffraction and neutron diffraction can be used for (i) improving contrast between different atomic species in samples (ii) determination of magnetic structures. Neutron scattering on the other hand, is an extremely powerful tool. Although there are cutting-edge techniques being developed at synchrotron sources, e.g. resonant inelastic x-ray scattering, neutron scattering is still the go-to method of probing magnetic excitations in materials.

2.3 Neutron Scattering Theory

The mathematical quantities which directly map to measurables in an inelastic neutron scattering experiment are defined in the bullet points below. To visualize the physical meaning of these definitions, consider the scattering of a neutron beam, with incident flux Φ, from a scattering centre. The neutrons are detected thereafter, with a detector positioned in the direction θ, ϕ, away from the scattering centre.

- The partial differential cross-section, $\frac{d^2\sigma}{d\Omega dE'}$, is defined as the number of neutrons scattered per second into a small solid angle in the direction θ, ϕ, with final energy in the window E and $E + dE'$. In this case, the final energy is analyzed.
- The differential cross-section, $\frac{d\sigma}{d\Omega}$, corresponds to the case where the final neutron energy is not analyzed in the experiment. It is therefore defined as the number of neutrons scattered per second into a small solid angle in the direction θ, ϕ. It is related to the partial differential cross-section by, $\frac{d\sigma}{d\Omega} = \int_0^\infty (\frac{d^2\sigma}{d\Omega dE'}) dE'$.
- The total scattering cross-section, σ_{tot}, refers to the total number of neutrons scattered per second, relative to the incident flux Φ, i.e. $\sigma_{tot} =$ (total number of neutrons scattered per second)$/\Phi$. Returning to the case of elastic scattering outlined in Section 2.2, we obtain the total nuclear scattering from the differential cross-section in Equation (2.8), through the relation, $\sigma_{tot} = \int \frac{d\sigma}{d\Omega} d\Omega = 4\pi b^2$.

A good starting point for a complete theoretical description of neutron scattering is nuclear scattering. The results obtained from Section 2.3.1 will provide a good foundation for magnetic neutron scattering, which is discussed afterwards in Section 2.3.2.

2.3.1 Nuclear Scattering

We now proceed to develop the form of the equations by utilizing an expression for the scattering rate, $W_{k,\lambda\to k',\lambda'}$. The scattering rate is number of transitions per second associated with the change in the eigenstate of the total scattering system[10] from $\{k,\lambda\}$ to $\{k',\lambda'\}$ after the neutron interacts with the scattering centre via potential V. k and k' refer to the incident and scattered wavevectors of the neutron while λ and λ' describe the change in the quantum state of the scattering centre.[11] The differential cross-section is directly related to $W_{k,\lambda\to k'\lambda'}$ by the following relation,

$$\left(\frac{d\sigma}{d\Omega}\right)_{\lambda\to\lambda'} = \frac{1}{\Phi}\frac{1}{d\Omega}\sum_{k' \text{ in } \mathrm{d}\Omega} W_{k,\lambda\to k',\lambda'}. \tag{2.8}$$

The summation is taken over all scattering processes where the scattered neutron wavevector, k', lies in the solid angle θ, ϕ and k, λ, λ' are fixed. The summation over $W_{k,\lambda\to k',\lambda'}$ is Fermi's golden rule,[12] and it can be expressed in terms of the density of states, $\rho_{k'}$ and the transition matrix element of V (for a transition to occur between the initial state $|k,\lambda\rangle$ and final state $|k',\lambda'\rangle$ of the scattering system), as,

$$W_{k,\lambda\to k',\lambda'} = \frac{2\pi}{\hbar}\rho_{\mathbf{k}'}|\left\langle \boldsymbol{k}'\lambda'\right| V\left|\boldsymbol{k}\lambda\right\rangle|^2. \tag{2.9}$$

The density of states $\rho_{k'}$ is the number of momentum states in $d\Omega$ per unit energy range for neutrons in the state k'. The transition matrix element $\left\langle \boldsymbol{k}'\lambda'\right| V\left|\boldsymbol{k}\lambda\right\rangle$ is given by,

$$\left\langle \boldsymbol{k}'\lambda'\right| V\left|\boldsymbol{k}\lambda\right\rangle = \int \psi^*_{\boldsymbol{k}'}\,\chi^*_{\boldsymbol{k}'}\,V\,\psi_{\boldsymbol{k}}\,\chi_{\boldsymbol{k}}\,d\mathbf{R}\,d\mathbf{r} \tag{2.10}$$

where $d\mathbf{R} = d\mathbf{R_1}d\mathbf{R_2}...d\mathbf{R_N}$. Each $d\mathbf{R}_i$ is an infinitesimal volume element for the i^{th} nucleus and $d\mathbf{r}$ is an infinitesimal volume element for the neutron. A clear consequence of Fermi's golden rule in Equation (2.9) is that for fixed k, λ and λ', the transition probability is only significant for a small range of $|\boldsymbol{k}'|$ corresponding to the conservation

[10] Total scattering system refers to the neutron and the scattering centre.

[11] It is important to note that the polarization state of the neutron is not accounted for. We can omit this property for the experiments performed for this thesis work as they do not involve polarization analysis.

[12] A derivation of Fermi's golden rule can be found in Merzbacher, (1970), Chapter 18.[13]

of energy for the entire scattering system. This value of $\boldsymbol{k}'$ is the appropriate value to place at the right-hand side of Equation (2.9).

The integral in Equation (2.10) can be manipulated into a manageable form. Box normalization of the neutron wavefunction gives $\psi_{\boldsymbol{k}} = \frac{1}{\sqrt{Y}} e^{i\boldsymbol{k}\cdot\mathbf{r}}$[9]. Applying this alongside the relation, $\rho_{\boldsymbol{k}'} = \frac{Y}{(2\pi)^3} k' \frac{m}{\hbar^2} d\Omega$, Equation (2.10) becomes,

$$\langle \boldsymbol{k}'\lambda' | \, V \, | \boldsymbol{k}\lambda \rangle = \frac{1}{Y} \int e^{-i\mathbf{k}'\cdot\mathbf{r}} \, \chi^*_{\lambda'} \, V \, e^{i\mathbf{k}\cdot\mathbf{r}} \, \chi_\lambda \, d\mathbf{R} \, d\mathbf{r}. \tag{2.11}$$

To simplify notation, rewrite the last line as $\langle \boldsymbol{k}'\lambda' | \, V \, | \boldsymbol{k}\lambda \rangle / Y$ so that the neutron wavefunction is $e^{i\boldsymbol{k}\cdot\mathbf{r}}$. We now proceed to solve for the partial differential cross-section $\frac{d^2\sigma}{dE' d\Omega}$. Utilizing the flux of the neutrons[13] as $\Phi = \frac{1}{Y}\frac{\hbar}{m}k$ along with $\rho_{k'}$, Equation (2.9) and Equation (2.11), we obtain,

$$\left(\frac{d\sigma}{d\Omega}\right)_{\lambda\to\lambda'} = \frac{k'}{k}\left(\frac{m}{2\pi\hbar^2}\right)^2 | \, \langle \boldsymbol{k}'\lambda' | \, V \, | \boldsymbol{k}\lambda \rangle \, |^2, \tag{2.12}$$

where $\left(\frac{d\sigma}{d\Omega}\right)_{\lambda\to\lambda'}$ is the cross-section for neutrons being scattering into $d\Omega$ in the direction $\boldsymbol{k}'$. Since $\boldsymbol{k}$, λ and λ' are all fixed, the conservation of energy dictates that energy of the scattered neutrons must be the same. Denoting the initial and final energy of the neutron as E and E' and the initial and final energy of the scattering centre as E_λ and $E_{\lambda'}$, energy conservation dictates that,

$$E + E_\lambda = E' + E_{\lambda'}. \tag{2.13}$$

Therefore the energy distribution of the scattered neutron can be expressed as a δ-distribution and the differential cross-section is,

$$\left(\frac{d^2\sigma}{d\Omega dE'}\right)_{\lambda\to\lambda'} = \frac{k'}{k}\left(\frac{m}{2\pi\hbar^2}\right)^2 | \, \langle \boldsymbol{k}'\lambda' | \, V \, | \boldsymbol{k}\lambda \rangle \, |^2 \, \delta(E_\lambda - E_{\lambda'} + E - E'). \tag{2.14}$$

It is easy to see this since we can track back to the original expression for $\frac{d\sigma}{d\Omega}$ by

[13]The neutron density, from box normalization, is $\frac{1}{Y}$. The flux, Φ, is simply the product of the neutron density and the velocity $v = \frac{\hbar k}{m}$.

integrating over dE' and using the fact that, $\int \delta(E_\lambda - E_{\lambda'} + E - E')\, dE' = 1$.

In order to completely evaluate any of these cross-sections, we require the potential V. Without loss of generality, we assume that the potential V is the sum of the potential from each atomic nucleus. Denote the potential due to the i^{th} nucleus as $V_i(\mathbf{r} - \mathbf{R_i})$ such that,

$$V = \sum_i V_i(\mathbf{r} - \mathbf{R_i}). \tag{2.15}$$

By applying a change of variables to the integral $\langle \boldsymbol{k}'\lambda'| V |\boldsymbol{k}\lambda\rangle$ using $\mathbf{x_i} = \mathbf{r} - \mathbf{R_i}$, the integral becomes

$$\begin{aligned} |\langle \boldsymbol{k}'\lambda'| V |\boldsymbol{k}\lambda\rangle| &= \sum_i \int \chi^*_{\lambda'} e^{-i\mathbf{k}'\cdot(\mathbf{x_i}+\mathbf{R_i})} V_i(\mathbf{x_i}) \chi_\lambda e^{i\mathbf{k}\cdot(\mathbf{x_i}+\mathbf{R_i})}\, d\mathbf{R}\, d\mathbf{x_i} \\ &= \sum_i V_i(\boldsymbol{\kappa}) \langle \lambda'| e^{i\boldsymbol{\kappa}\cdot R_i} |\lambda\rangle . \end{aligned} \tag{2.16}$$

The Fourier transform $V_i(\boldsymbol{\kappa})$ of the potential V_i of the i^{th} nucleus appears in Equation (2.16) where,

$$V_i(\boldsymbol{\kappa}) = \int V_i(\mathbf{x_i}) e^{i\boldsymbol{\kappa}\cdot x_i} d\mathbf{x_i} \tag{2.17}$$

and $\boldsymbol{\kappa} = \boldsymbol{k} - \boldsymbol{k'}$ is the scattering vector.

Case: Scattering Due to Single Nucleus

It is instructive to first consider $\langle \boldsymbol{k}'\lambda'| V |\boldsymbol{k}\lambda\rangle$ and $\frac{d\sigma}{d\Omega}$ for a single nucleus and apply those results to the current case involving N nuclei. With $i = 1$ and $R_1 = 0$ in Equation (2.16), this leads to,

$$\begin{aligned} \langle \boldsymbol{k}'\lambda'| V |\boldsymbol{k}\lambda\rangle &= \int \chi^*_\lambda \chi_\lambda\, d\mathbf{R_1} \int V(\mathbf{r}) e^{i\boldsymbol{\kappa}\cdot r}\, d\mathbf{r} \text{ and} \\ &= \int V(\mathbf{r})\, e^{i\boldsymbol{\kappa}\cdot r}\, d\mathbf{r}, \end{aligned} \tag{2.18}$$

since χ_λ is normalized. Inserting this into Equation (2.12) yields,

$$\left(\frac{d\sigma}{d\Omega}\right) = \left(\frac{m}{2\pi\hbar^2}\right)^2 \left| \int V(\mathbf{r}) e^{i\boldsymbol{\kappa}\cdot r}\, d\mathbf{r} \right|^2. \tag{2.19}$$

The potential $V(\mathbf{r})$ can be expressed as $V(\mathbf{r}) = a\delta(\mathbf{r})$ since it is short ranged, where a is a real constant and $\delta(\mathbf{r})$ is the Dirac δ-distribution with the property $\int_{\text{allspace}} \delta(\mathbf{r})\, d\mathbf{r} = 1$. Applying this form of $V(\mathbf{r})$ to Equation (2.19) yields,

$$\left(\frac{d\sigma}{d\Omega}\right) = \left(\frac{m}{2\pi\hbar^2}\right)^2 a^2. \tag{2.20}$$

However, since $\frac{d\sigma}{d\Omega} = b^2$, this implies that, $a = \frac{2\pi\hbar^2}{m} b$, and the potential

$$V(\mathbf{r}) = \frac{2\pi\hbar^2}{m} b\delta(\mathbf{r}). \tag{2.21}$$

This potential is known as the *Fermi pseudopotential*, and we shall use this form to describe the interaction potential between the neutron and a given atomic nucleus.

Case: Scattering Due to N Nuclei

Returning to the previous case involving N scattering centres, the potential due to the i^{th} nucleus is denoted as $V_i(\mathbf{x_i}) = \frac{2\pi\hbar^2}{m} b_i \delta(\mathbf{x_i})$. The Fourier transform of $V_i(\mathbf{x_i})$ is then,

$$V_i(\boldsymbol{\kappa}) = \frac{2\pi\hbar^2}{m} b_i. \tag{2.22}$$

Inserting this into the partial differential cross-section in Equation (2.14), we are left with,

$$\left(\frac{d^2\sigma}{d\Omega dE'}\right)_{\lambda\to\lambda'} = \frac{k'}{k} \Big| \sum_i b_i \, \langle\lambda'|\, e^{i\boldsymbol{\kappa}\cdot R_i} \,|\lambda\rangle \, \Big|^2 \delta(E_\lambda - E_{\lambda'} + E - E'). \tag{2.23}$$

It is useful to insert the integral representation of the δ-distribution expressed in time

domain.[14] The integral is,

$$\delta(E_\lambda - E_{\lambda'} + E - E') = \frac{1}{2\pi\hbar}\int_{-\infty}^{\infty} e^{i(E_{\lambda'}-E_\lambda)t/\hbar}\, e^{-i\omega t}\, dt, \tag{2.24}$$

where $w = (E - E')/\hbar$. Furthermore the matrix element appearing in Equation (2.23) is a sum over N values. Therefore the square of the matrix element can be expressed as a sum of N^2 terms which have the form,

$$b_i^* b_i \left\langle\lambda\right| e^{i\boldsymbol{\kappa}\cdot\boldsymbol{R_i'}} \left|\lambda\right\rangle^* \left\langle\lambda'\right| e^{i\boldsymbol{\kappa}\cdot\boldsymbol{R_i}} \left|\lambda\right\rangle. \tag{2.25}$$

Therefore Equation (2.23) can be expressed as follows,

$$\begin{aligned}\left(\frac{d^2\sigma}{d\Omega dE'}\right)_{\lambda\to\lambda'} &= \frac{k'}{k}\sum_{i\,i'} b_i\, b_i'\, \left\langle\lambda\right| e^{i\boldsymbol{\kappa}\cdot R_i'} \left|\lambda'\right\rangle\, \left\langle\lambda'\right| e^{i\boldsymbol{\kappa}\cdot R_i} \left|\lambda\right\rangle \\ &\quad\times \frac{1}{2\pi\hbar}\int_{-\infty}^{\infty} e^{i(E_{\lambda'}-E_\lambda)t/\hbar}\, e^{-i\omega t}\, dt, \\ &= \frac{k'}{k}\frac{1}{2\pi\hbar}\sum_{i\,i'} b_i\, b_i' \int_{-\infty}^{\infty} \left\langle\lambda\right| e^{-i\boldsymbol{\kappa}\cdot\boldsymbol{R_i'}} \left|\lambda'\right\rangle \\ &\quad\times \left\langle\lambda'\right| e^{i\hat{H}t/\hbar}\, e^{i\boldsymbol{\kappa}\cdot\boldsymbol{R_i}}\, e^{-i\hat{H}t/\hbar} \left|\lambda\right\rangle\, e^{-i\omega t}\, dt.\end{aligned} \tag{2.26}$$

Note that the Hamiltonian of the total scattering system appears as $\hat{H}$ where E_λ and $E_{\lambda'}$ are eigenvalues of $\hat{H}$ corresponding to the eigenfunctions $|\lambda\rangle$ and $|\lambda'\rangle$.[15]

Equation (2.26) is the partial differential cross-section corresponding to the transition of the scattering system from state λ to a specific state λ'. In a neutron scattering experiment however, the measured partial differential cross-section does not distinguish specific final states. Hence we must find an expression which will give the total $\frac{d^2\sigma}{d\Omega dE'}$. A statistical approach is required wherein $\left(\frac{d^2\sigma}{d\Omega dE'}\right)_{\lambda\to\lambda'}$ is summed over all final states while λ is kept fixed, and the resulting expression, averaged over all λ. The first step is conducted by using the relation $\sum_{\lambda'} \langle\lambda| A |\lambda'\rangle\, \langle\lambda'| B |\lambda\rangle = \langle\lambda| AB |\lambda\rangle$.

[14] The integral representation of the delta distribution can get found in Appendix A of Ref. [10].

[15] It can be easily shown (through a series expansion) that $e^{iE_\lambda t/\hbar}$ (or $e^{iE_{\lambda'}t/\hbar}$), is equivalent to $e^{i\hat{H}t/\hbar}$.

This yields,

$$\begin{aligned}\sum_{\lambda'}\left(\frac{d^2\sigma}{d\Omega dE'}\right)_{\lambda\to\lambda'} &= \frac{k'}{k}\frac{1}{2\pi\hbar}\sum_{ii'} b_i\, b'_i \int_{-\infty}^{\infty} e^{-i\omega t} \\ &\times \sum_{\lambda'} \langle\lambda|\, e^{-i\boldsymbol{\kappa}\cdot\boldsymbol{R'_i}}\,|\lambda'\rangle\ \langle\lambda'|\, e^{i\hat{H}t/\hbar}\, e^{i\boldsymbol{\kappa}\cdot\boldsymbol{R_i}}\, e^{-i\hat{H}t/\hbar}\ |\lambda\rangle\ dt, \\ &= \frac{k'}{k}\frac{1}{2\pi\hbar}\sum_{ii'} b_i\, b'_i \int_{-\infty}^{\infty} e^{-i\omega t} \\ &\times \langle\lambda|\, e^{-i\boldsymbol{\kappa}\cdot\boldsymbol{R'_i}} e^{i\hat{H}t/\hbar}\, e^{i\boldsymbol{\kappa}\cdot\boldsymbol{R_i}}\, e^{-i\hat{H}t/\hbar}\ |\lambda\rangle\ dt.\end{aligned} \tag{2.27}$$

To perform the average, we must multiply equation Equation (2.27) by the probability p_λ, that the scattering system is in the state λ, and then sum over λ. p_λ is given by,

$$p_\lambda = \frac{1}{Z} e^{-E_\lambda \beta} \text{ where} \tag{2.28}$$

$Z = \sum_\lambda e^{-E_\lambda\beta}$, is the partition function, $\beta = \frac{1}{k_B T}$ is the Bose factor and T is the temperature of the scattering system. Simultaneously applying the time-dependent Heisenberg operator corresponding to the position coordinate, $\mathbf{R_i}(t) = e^{i\hat{H}t/\hbar}\mathbf{R_i}e^{-i\hat{H}t/\hbar}$, the final result is,

$$\frac{d^2\sigma}{d\Omega dE'} = \frac{k'}{k}\sum_{ii'} b_i\, b'_i \frac{1}{2\pi\hbar}\int_{-\infty}^{\infty} \langle e^{i\boldsymbol{\kappa}\cdot\boldsymbol{R'_i(0)}} e^{i\boldsymbol{\kappa}\cdot\boldsymbol{R_i(t)}}\rangle \times\ e^{-i\omega t}\, dt, \tag{2.29}$$

where we have invoked the notation for the thermal average of an operator $\hat{A}$ as $\langle\hat{A}\rangle = \sum_\lambda \langle\lambda|\,\hat{A}\,|\lambda\rangle$.

In Section 2.2.1, it was highlighted that the scattering length b of a single element can vary depending on (i) the isotope of the atom, and/or (ii) the spin state of the nucleus, if it posses one. We shall now fully account for these factors when considering the form of the total partial differential cross-section. To start, we consider that the scattering system contains a single element with each atom having a scattering length b_i, which occurs with relative frequency f_i such that.

$$\sum_i f_i = 1 \tag{2.30}$$

Therefore, we expect that the average value of b for the scattering system is,

$$\bar{b} = \sum_i f_i b_i. \tag{2.31}$$

and the average value of b^2 is,

$$\overline{b^2} = \sum_i f_i b_i^2. \tag{2.32}$$

If we consider that the scattering system is comprised of a large number of nuclei whose scattering lengths are not correlated, we can assume that the cross-section is the cross-section averaged over all the systems. The cross-section is then given by,

$$\begin{aligned} \frac{d^2\sigma}{d\Omega dE'} &= \frac{k'}{k}\frac{1}{2\pi\hbar}\sum_{i\,i'}\overline{b_i\,b_i'}\int_{-\infty}^{\infty}\langle i',i\rangle\, e^{-i\omega t}\,dt, \text{ where} \\ \langle i',i\rangle &= \langle e^{i\boldsymbol{\kappa}\cdot\boldsymbol{R_i'(0)}}e^{i\boldsymbol{\kappa}\cdot\boldsymbol{R_i(t)}}\rangle. \end{aligned} \tag{2.33}$$

The value of $\overline{b_i\,b_i'}$ depends on whether it refers to the the same nucleus with $i = i'$, or different nuclei with $i \neq i'$. For those two cases we have,

$$\begin{aligned} \overline{b_{i'}b_i} &= (\bar{b})^2,\ i \neq i', \\ \overline{b_{i'}b_i} &= (\overline{b^2}),\ i = i'. \end{aligned} \tag{2.34}$$

Substituting this into the Equation (2.29), we are left with,

$$\begin{aligned} \frac{d^2\sigma}{d\Omega dE'} &= \frac{k'}{k}\frac{1}{2\pi\hbar}(\bar{b})^2\sum_{\substack{i\,i' \\ i\neq i'}}\int_{-\infty}^{\infty}\langle i',i\rangle\, e^{-i\omega t}\,dt + \frac{k'}{k}\frac{1}{2\pi\hbar}\overline{b^2}\sum_i\int_{-\infty}^{\infty}\langle i',i\rangle\, e^{-i\omega t}\,dt, \\ &= \frac{k'}{k}\frac{1}{2\pi\hbar}(\bar{b})^2\sum_{i\,i'}\int_{-\infty}^{\infty}\langle i,i\rangle\, e^{-i\omega t}\,dt + \frac{k'}{k}\frac{1}{2\pi\hbar}\{\overline{b^2} - (\bar{b})^2\}\sum_i\int_{-\infty}^{\infty}\langle i,i\rangle\, e^{-i\omega t}\,dt. \end{aligned} \tag{2.35}$$

In this current form, the total scattering is separated into two contributions, namely

coherent $\frac{d^2\sigma}{d\Omega dE'}\Big|_{coh}$ and incoherent $\frac{d^2\sigma}{d\Omega dE'}\Big|_{inc}$ scattering, which are given by,

$$\begin{aligned}
\frac{d^2\sigma}{d\Omega dE'}\bigg|_{coh} &= \frac{k'}{k}\,\frac{1}{2\pi\hbar}\,(\bar{b})^2 \sum_{i\,i'} \int_{-\infty}^{\infty} \langle i', i\rangle\, e^{-i\omega t}\, dt, \\
&= \frac{\sigma_{coh}}{4\pi}\,\frac{k'}{k}\,\frac{1}{2\pi\hbar} \sum_{i\,i'} \int_{-\infty}^{\infty} \langle i', i\rangle\, e^{-i\omega t}\, dt, \\
\frac{d^2\sigma}{d\Omega dE'}\bigg|_{inc} &= \frac{k'}{k}\,\frac{1}{2\pi\hbar}\,\{\overline{b^2} - (\bar{b})^2\} \sum_{i} \int_{-\infty}^{\infty} \langle i, i\rangle\, e^{-i\omega t}\, dt, \\
&= \frac{\sigma_{inc}}{4\pi}\,\frac{k'}{k}\,\frac{1}{2\pi\hbar} \sum_{i} \int_{-\infty}^{\infty} \langle i, i\rangle\, e^{-i\omega t}\, dt.
\end{aligned} \tag{2.36}$$

As presented above, the coherent scattering represents the correlations of the position of the same nucleus at different times and the correlations of the positions of different nuclei at different times [10]. Coherent scattering is the source of interference effects, for example, diffraction. The incoherent scattering refers to the correlations between the positions of the same nucleus at different times. Physically, incoherent scattering corresponds to scatterings which arises from the random distribution of the deviations of the scattering lengths from their mean value. Therefore, it is the term which needs to be added to the coherent scattering, to obtain the true scattering of the system.

Now to obtain the value of f_i, the spin state of the nucleus needs to be accounted for. If the nucleus has spin I, then the spin-neutron system has the value $I + \frac{1}{2}$ or $I - \frac{1}{2}$. Let b^+ and b^- denote the scattering lengths corresponding to the two spin values with $I + \frac{1}{2}$ or $I - \frac{1}{2}$, respectively. The number of states associated with each of the spin states is $2(I + \frac{1}{2}) + 1 = 2I + 2$ and $2(I - \frac{1}{2}) + 1 = 2I$, respectively. If the nuclei have randomly oriented spins and the neutrons are unpolarized, all spin states are equally likely. Therefore, the weights of f^+ and f^- corresponding to the nuclei with scattering lengths b^+ and b^- are,

$$\begin{aligned}
f^+ &= \frac{I+1}{2I+1}, \text{ and} \\
f^- &= \frac{I}{2I+1}, \text{ respectively.}
\end{aligned} \tag{2.37}$$

Hence, the average scattering length $\bar{b}$ is given by,

$$\bar{b} = \frac{1}{2I+1}\{(I+1)b^{+} + Ib^{-}\}. \tag{2.38}$$

2.3.1.1 Coherent Nuclear Scattering

Two key examples of coherent scattering, Bragg scattering and phonon scattering, shall be presented in this short section. The reader is encouraged to reference *Introduction to the Theory of Thermal Neutron Scattering* by Squires [10] for full background on the development of the equations presented here. The objective of this section is to highlight how Bragg's law can be obtained from this scattering formalism, and the description for one-phonon scattering.

The cross-sections outlined in the sections below require a description for the motions of the atoms undergoing simple harmonic motion. Previously, the instantaneous position of the l^{th} nucleus was denoted as $\mathbf{R}_l(t)$. Their positions will now be expressed in terms of their equilibrium positions, $\mathbf{l}$, and displacement away from equilibrium, $\mathbf{u_l}(t)$ by $\mathbf{R}_l(t) = \mathbf{u_l}(t) + \mathbf{l}$. $\mathbf{u_l}(t)$ is a superposition of the normal modes of the lattice of N nuclei.

Part A: Bragg's Law

The total coherent elastic scattering for a crystal lattice containing N nuclei is given by,

$$\left.\frac{d^2\sigma}{d\Omega dE'}\right|_{coh\,el} = \frac{\sigma_{coh}}{4\pi}\,\frac{k'}{k}\,\frac{N}{2\pi\hbar}\,e^{\langle U^2\rangle}\sum_{l} e^{i\boldsymbol{\kappa}\cdot\boldsymbol{l}}\int_{-\infty}^{\infty} e^{-i\omega t}\,dt, \tag{2.39}$$

where $U = -\boldsymbol{\kappa}\cdot\boldsymbol{u_0}(t)$. As noted earlier, the infinite integral appearing in Equation (2.41) can be expressed in terms of a δ-distribution as follows,

$$\int_{-\infty}^{\infty} e^{-i\omega t}dt = 2\pi\delta(\omega) = 2\pi\hbar\delta(\hbar\omega). \tag{2.40}$$

Since $\hbar\omega = 0$ is the change in energy of the neutron, the scattering is elastic and $|\boldsymbol{k}| = |\boldsymbol{k'}|$. This yields,

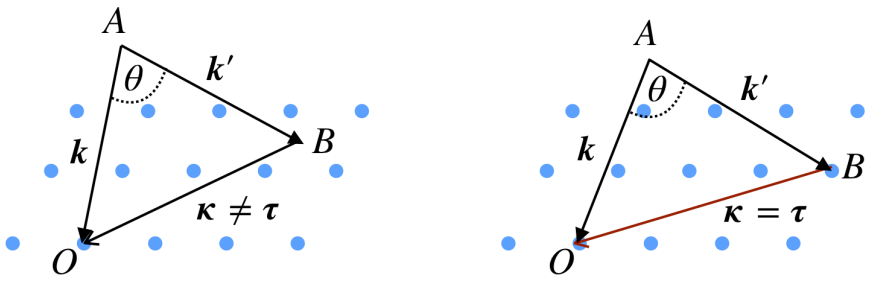

Figure 2.7: A representation of Bragg's law in reciprocal space. (a.) Coherent Bragg scattering does not occur if $\boldsymbol{\kappa} \neq \boldsymbol{\tau}$ (b.) Coherent Bragg scattering occurs when $\boldsymbol{\kappa} = \boldsymbol{\tau}$.

$$\left.\frac{d^2\sigma}{d\Omega dE'}\right|_{coh\,el} = \frac{\sigma_{coh}}{4\pi} N\, e^{\langle U^2\rangle} \sum_l e^{i\boldsymbol{\kappa}\cdot\boldsymbol{l}}\, \delta(\hbar\omega). \tag{2.41}$$

Integrating $\left.\frac{d^2\sigma}{d\Omega dE'}\right|_{coh\,el}$ over the final energy, E', we are left with the differential cross-section,

$$\left.\frac{d\sigma}{d\Omega}\right|_{coh\,el} = \frac{\sigma_{coh}}{4\pi} N\, e^{\langle U^2\rangle} \sum_l e^{i\boldsymbol{\kappa}\cdot\boldsymbol{l}}. \tag{2.42}$$

Using the reciprocal lattice vector to rewrite the lattice sum, the differential cross-section becomes,

$$\left.\frac{d\sigma}{d\Omega}\right|_{coh\,el} = \frac{\sigma_{coh}}{4\pi} N \frac{(2\pi)^3}{v_0} e^{(-2W)} \sum_{\boldsymbol{\tau}} \delta(\boldsymbol{\kappa} - \boldsymbol{\tau}). \tag{2.43}$$

where $2W = -\langle U^2\rangle = \langle\{\boldsymbol{\kappa}\cdot\boldsymbol{u_0}\}(0)\}^2\rangle$ is the *Debye Waller Factor* which was introduced earlier in Section 2.2. It is clear from Equation (2.43) that scattering only occurs at $\boldsymbol{\kappa} = \boldsymbol{k} - \boldsymbol{k'} = \boldsymbol{\tau}$. $\boldsymbol{k}$ and $\boldsymbol{k'}$ are represented by the edges AO and AB, of the scattering triangle. This condition can be represented schematically as shown in Figure 2.7. The scattering is elastic when $AO = AB$ and coherent if point B corresponds to a point in reciprocal space. Only for special values of θ and specific orientations (in the case of a single-crystal), can B coincide with a reciprocal lattice point. The scattering triangle is an isoceles triangle with $OB = \boldsymbol{\tau}$ satisfying the geometric condition,

$$\boldsymbol{\tau} = 2k \sin\left(\frac{1}{2}\theta\right). \tag{2.44}$$

$\boldsymbol{\tau}$ is a vector perpendicular to a family of Miller planes and has magnitude

$$\boldsymbol{\tau} = n\frac{2\pi}{d}, \tag{2.45}$$

where d is the spacing of the planes and n is an integer. Since $k = \frac{2\pi}{\lambda}$, we are left with,

$$n\lambda = 2d \sin\left(\frac{1}{2}\theta\right), \tag{2.46}$$

which is in essence, an equivalent form of Bragg's law.

Part B: One-phonon scattering

The total single-phonon coherent scattering partial differential cross-section is,

$$\begin{aligned}\left.\frac{d^2\sigma}{d\Omega dE'}\right|_{coh\,1\,ph} &= \frac{\sigma_{coh}}{4\pi}\frac{k}{k'}\frac{1}{4\pi M}e^{-2W}\sum_l e^{i\boldsymbol{\kappa}\cdot l}\sum_s \frac{(\boldsymbol{\kappa}\cdot e_s)^2}{\omega_s} \\ &\times \int_{-\infty}^{\infty}\left[e^{i(\mathbf{q}.\mathbf{l}-\omega_{st})}\langle\, n_s+1\,\rangle + e^{i(\mathbf{q}\cdot\mathbf{l}-\omega_{st})}\langle n_s\rangle\right]e^{-i\omega t}dt.\end{aligned} \tag{2.47}$$

This total cross-section includes the sum over all single-photon emission processes and single-phonon annihilation processes, where $\mathbf{q}$ represents the wavevector of the phonon modes. The first term involving $\langle n_s + 1\rangle$, corresponds to the contribution resulting from single-phonon emission processes. The second term which includes $\langle n_s\rangle$, relates single-phonon annihilation processes. Utilizing the equivalence of the infinite integral over t to the delta distribution and summing over $\mathbf{l}$, we have the total cross-section, due to one-phonon emission processes,

$$\begin{aligned}\left.\frac{d^2\sigma}{d\Omega dE'}\right|_{+1\,ph} &= \frac{\sigma_{coh}}{4\pi}\frac{k}{k'}\frac{(2\pi)^3}{v_0}\frac{1}{2M}e^{-2W}\sum_s\sum_{\boldsymbol{\tau}}\frac{(\boldsymbol{\kappa}\cdot\boldsymbol{e_s})^2}{\omega_s}\langle n_s+1\rangle \\ &\times\ \delta(\omega-\omega_s)\delta(\boldsymbol{\kappa}-\boldsymbol{q}-\boldsymbol{\tau}),\end{aligned} \tag{2.48}$$

and one-phonon annihilation processes,

$$\left.\frac{d^2\sigma}{d\Omega dE'}\right|_{-1\,ph} = \frac{\sigma_{coh}}{4\pi}\frac{k}{k'}\frac{(2\pi)^3}{v_0}\frac{1}{2M}e^{-2W}\sum_s\sum_{\boldsymbol{\tau}}\frac{(\boldsymbol{\kappa}\cdot\boldsymbol{e_s})^2}{\omega_s}\langle n_s\rangle \times \delta(\omega+\omega_s)\delta(\boldsymbol{\kappa}+\boldsymbol{q}-\boldsymbol{\tau}). \tag{2.49}$$

The delta distributions which appear in each of Equation (2.48) and Equation (2.49) provide the conditions for one-phonon scattering.

First, we consider the phonon emission case and extend the conclusions obtained therein to the phonon annihilation case. For a one-phonon emission process, we require that $\omega = \omega_s$ and $\boldsymbol{\kappa} = \boldsymbol{\tau} + \boldsymbol{q}$. This implies that the change in energy of the neutron is $E - E' = \hbar\omega_s$. Therefore, the neutron must lose energy equivalent to $\hbar\omega_s$, corresponding to the s^{th} phonon mode. The neutron loses kinetic energy to excite that particular mode, such that,

$$\frac{\hbar^2}{2m}(\boldsymbol{k^2} - \boldsymbol{k'^2}) = \hbar\omega_s. \tag{2.50}$$

The change in wavevector $\boldsymbol{k} - \boldsymbol{k'}$ must be related to the wavevector of the normal mode $\mathbf{q}$ by,

$$\boldsymbol{k} - \boldsymbol{k'} = \boldsymbol{\tau} + \boldsymbol{q}. \tag{2.51}$$

This equation can be viewed in terms of conservation of momentum. Equation (2.51) relates the change in momentum of the neutron to the momentum imparted to the crystal. Conversely, for the phonon annihilation case, $\frac{\hbar^2}{2m}(\boldsymbol{k'^2} - \boldsymbol{k^2}) = \hbar\omega_s$ represents that the neutron absorbs energy equivalent to $\hbar\omega_s$, thereby annihilating the s^{th} phonon mode.

We make two final remarks to conclude this section. First, we consider the limiting case of the expectation values of $\langle n_s + 1\rangle$ and $\langle n_s\rangle$ as $T \to 0$. Performing this limit yields, $\langle n_s + 1\rangle \to 1$ and $\langle n_s\rangle \to 0$. This means that at low temperatures the likelihood of destroying a phonon mode is zero, since, we expect the occupation of each phonon mode in the ground state of the crystal, to be zero. On the other hand, the likelihood of inducing an excitation is unity, as the lattice phonon modes

are in their ground state and can be excited. The second remark highlights a more qualitative feature of inelastic neutron scattering due to phonons. The cross-section in Equation (2.48) has a $\boldsymbol{\kappa}^2$ dependence. This implies that the neutron scattering intensity of phonon scattering increases as $\boldsymbol{\kappa}^2$ with increasing $|\boldsymbol{\kappa}|$.

2.3.2 Magnetic Scattering

To formulate the theory for magnetic scattering of neutrons, we shall modify the form of $\frac{d^2\sigma}{d\Omega dE'}$ in Equation (2.14), which was developed for nuclear scattering. There are two important considerations to account for when modifying this equation. First, the interaction potential V is now due to the dipolar interaction between the incident neutron and unpaired electrons in the system. If the field generated by a single unpaired electron is $\mathbf{B}$, this interaction potential can be characterized by,

$$\begin{aligned} V_n &= -\mu_n \cdot \mathbf{B}, \\ &= -\frac{-\mu_0}{4\pi}\gamma\mu_N 2\mu_B \sigma \cdot (\mathbf{W_S} + \mathbf{W_L}), \end{aligned} \tag{2.52}$$

where W_L and W_S are the contributions due to the orbital motion and spin of the electron, respectively. As neutrons interact with the spin degrees-of-freedom of the unpaired electrons, they are able change the spin state of the scattering system during a scattering event. This leads us to our second adjustment to Equation (2.14), where we must now label the quantum state of the scattering system by $|k\sigma\lambda\rangle$, where σ denotes the spin state of the scattering system. The cross-section for a scattering process which changes the spin state of the scattering system from $|k\sigma\lambda\rangle$ to $|k'\sigma'\lambda'\rangle$ is,

$$\left(\frac{d^2\sigma}{d\Omega dE'}\right)_{\sigma\lambda\to\sigma'\lambda'} = \frac{k'}{k}\left(\frac{m}{2\pi\hbar^2}\right)^2 |\left\langle k'\sigma'\lambda'\right| V_m \left|k\sigma\lambda\right\rangle|^2 \delta(E_\lambda - E_{\lambda'} + \hbar\omega). \tag{2.53}$$

Evaluation of the matrix element involving V_m is lengthy and omitted for simplicity, and the reader is encourage to refer to Squires for details[10]. Explicit evaluation of the matrix element in equation Equation (2.53) yields,

$$\left(\frac{d^2\sigma}{d\Omega dE'}\right)_{\sigma\lambda\to\sigma'\lambda'} = (\gamma r_0)^2 \frac{k'}{k} |\left\langle \sigma'\lambda' \right| \sigma \cdot \mathbf{Q}_\perp \left| \sigma\lambda \right\rangle|^2 \delta(E_\lambda - E_{\lambda'} + \hbar\omega), \tag{2.54}$$

where $\mathbf{Q}_\perp$ is the vector projection of $\mathbf{Q}$ onto the plane perpendicular to $\hat{\boldsymbol{\kappa}}$.[16] The operator $\mathbf{Q}(\boldsymbol{\kappa})$ is related to the Fourier transform $\mathbf{M}(\boldsymbol{\kappa})$, of the magnetization density of the system, $\mathbf{M}(\mathbf{r})$, and is defined by,

$$\begin{aligned} \mathbf{Q} &= \mathbf{Q_S} + \mathbf{Q_L} \\ &= -\frac{1}{2\mu_B} \boldsymbol{M}(\boldsymbol{\kappa}). \end{aligned} \tag{2.55}$$

Investigation of the detailed form of $\mathbf{Q}_\perp$ appearing in the matrix element in Equation (2.54),

$$\mathbf{Q}_\perp = \sum_i e^{i\boldsymbol{\kappa}\cdot\boldsymbol{r_i}} \{\hat{\boldsymbol{\kappa}} \times (\boldsymbol{s_i} \times \hat{\boldsymbol{\kappa}}) + \frac{i}{\hbar\kappa}(\boldsymbol{p_i} \times \hat{\boldsymbol{\kappa}})\}, \tag{2.56}$$

allows one to note an important difference between nuclear scattering and magnetic scattering. In the nuclear case, the contribution from the i^{th} species to the matrix element in the cross-section is related to the scattering length through $b_i e^{i\kappa\cdot r_i}$. This highlights the short-range nature of the neutron-nucleus interactions. In the case of magnetic scattering, the contribution from the i^{th} species is complicated in comparison and is given by, $-\gamma r_0 \cdot \left\{\hat{\kappa} \times (\mathbf{s_i} \times \hat{\kappa}) + \frac{\mathbf{i}}{\hbar\kappa}(\mathbf{p_i} \times \hat{\kappa})\right\} e^{i\boldsymbol{\kappa}\cdot\boldsymbol{r_i}}$. This form reflects the long-range nature of the neutron-nucleus magnetic interaction and the fact that the dipole-dipole interaction for the spin and the dipole-current interaction for the orbital motion are non-central forces [10].

As described previously in the case of nuclear scattering, the sum and average over the final states must be performed on equation Equation (2.54) in order to obtain the experimentally measured quantity, $\frac{d^2\sigma}{d\Omega dE'}$. To this end, the generalized total cross-section is given by,

[16] Recall that $\hat{\kappa}$ is the unit vector corresponding the scattering vector $\boldsymbol{\kappa}$.

$$\begin{aligned}\frac{d^2\sigma}{d\Omega dE'} &= (\gamma r_0)^2 \frac{k'}{k} \sum_{\alpha\beta} (\delta_{\alpha\beta} - \hat{\kappa}_\alpha \hat{\kappa}_\beta) \\ &= \times \sum_{\lambda\lambda'} p_\lambda \left\langle \lambda \right| Q_\alpha^+ \left| \lambda' \right\rangle \left\langle \lambda' \right| Q_\beta \left| \lambda \right\rangle \delta(E_\lambda - E_{\lambda'} + \hbar\omega).\end{aligned} \tag{2.57}$$

For simplicity, can first consider a special case of Equation (2.65) where we probe scattering arising from a Bravais crystal containing a single magnetic ion with quenched orbital angular momentum i.e. $L = 0$. In this case the cross-section is due to **spin-only** scattering which is given by,

$$\begin{aligned}\frac{d^2\sigma}{d\Omega dE'} &= (\gamma r_0)^2 \frac{k'}{k} \sum_{\alpha\beta} (\delta_{\alpha\beta} - \hat{\kappa}_\alpha \hat{\kappa}_\beta) \sum_{l'\,d'} \sum_{l\,d} F^*_{d'}(\boldsymbol{\kappa}) F_d(\boldsymbol{\kappa}) \\ &\times \sum_{\lambda\lambda'} p_\lambda \left\langle \lambda \right| e^{-i\boldsymbol{\kappa}\cdot \boldsymbol{R}_{\boldsymbol{l'\,d'}}} S^\alpha_{l'\,d'} \left| \lambda' \right\rangle \\ &\times \left\langle \lambda' \right| e^{i\boldsymbol{\kappa}\cdot \boldsymbol{R}_{\boldsymbol{l\,d}}} S^\beta_{l\,d} \left| \lambda \right\rangle \delta(E_\lambda - E_{\lambda'} + \hbar\omega).\end{aligned} \tag{2.58}$$

The operator $\mathbf{R_{l\,d}}$ refers to the position of the l^{th} scattering species presiding in the d^{th} unit cell and $S^\beta_{l\,d}$ refers to the β component of the 3D spin operator of atomic species at $\mathbf{R_{l\,d}}$. In this equation, the factor $F_d(\boldsymbol{\kappa})$ is referred to as the **magnetic form factor** and is directly related to the magnetization density, $\boldsymbol{M(\kappa)}$ by,

$$\boldsymbol{M(\kappa)}/\mu_B = g\mathbf{S}f(\boldsymbol{\kappa}), \tag{2.59}$$

where $g = 2$. If the unpaired spin state is described a radial wavefunction, then $f(\boldsymbol{\kappa})$ reduces to,

$$f(\boldsymbol{\kappa}) = \int_0^\infty dr\, r^2\, j_0(\kappa\, r) |\Phi(r)|^2 \equiv \left\langle\, j_0 \,\right\rangle. \tag{2.60}$$

$\left\langle\, j_0 \,\right\rangle$ is the spherical Bessel function of order $n = 0$. The $|Q|$ dependence of the form-factor is reflected by this spherical Bessel function, and it follows that the strength of magnetic scattering decreases with increasing $|Q|$. In this way, magnetic and nuclear scattering can be distinguished from one another. This statement also applies to

scattering due to both spin ($\boldsymbol{S}$) and orbital ($\boldsymbol{L}$) moments. The form-factor in this case is,

$$M(\boldsymbol{\kappa})/\mu_B = 2\langle\, j_0 \,\rangle \mathbf{S} + (\langle\, j_0 \,\rangle + \langle\, j_2 \,\rangle)\mathbf{L}, \tag{2.61}$$

provided that $|Q|$ is much smaller than the inverse of the mean radius of the wave function for the unpaired electrons [11].

However, specific forms of the form factor apply when considering materials containing transition metal ions or rare-earth ions. First we consider transition metal ions containing partially filled d-orbitals. The large size of the crystal-field splitting generated due to the coordination environment of the transition metal makes orbital currents -that is, transitions of electrons between different d orbitals on the same site- unfavourable. Nevertheless, these sites still contain a small orbital moment, which causes the Landé g-factor to be slightly different from the spin-only value, 2. In this case, the parametrization given in Equation (2.60) can be maintained with the following modification for $f(\boldsymbol{\kappa})$,

$$f(\boldsymbol{\kappa}) = \langle\, j_0 \,\rangle + \frac{g-2}{2}\langle\, j_2 \,\rangle \quad (\textbf{transition metal}). \tag{2.62}$$

On the other hand, rare-earth ions typically contain an unquenched orbital moment and the form-factor must account for the total angular momentum $\mathbf{J}$. Therefore the factor $g\mathbf{S}$ must be replaced by $g\mathbf{J}$ where $g = g_L + g_S$ with,

$$\begin{aligned} g_L &= \frac{J(J+1) - L(L+1) + S(S+1)}{J(J+1)}, \quad \text{and} \\ g_S &= \frac{J(J+1) + L(L+1) - S(S+1)}{2J(J+1)}. \end{aligned} \tag{2.63}$$

Therefore, the resulting form-factor for a rare-earth ion with an unquenched orbital moment is,

$$f(\boldsymbol{\kappa}) = \langle\, j_0 \,\rangle + \frac{g_L}{g}\langle\, j_2 \,\rangle \quad (\textbf{rare earth}). \tag{2.64}$$

Extensive work has been done to determine the magnetic form-factors for an array of ions and can be obtained from Brown [15] and Kobayashi [16].

We shall proceed to specific contributions Equation (2.65) to illustrate the ways in which different magnetic phenomena can be identified in a neutron scattering experiment. Before we proceed to outline specific cases of Equation (2.65), it is desirable to express the cross-section, in terms of time-dependent operators as it was previously done for the nuclear scattering case. To this end, consider the time-dependent cross-section described by,

$$\begin{aligned}\frac{d^2\sigma}{d\Omega dE'} = \frac{(\gamma r_0)^2}{2\pi\hbar}\frac{k'}{k}\sum_{\alpha\beta}(\delta_{\alpha\beta}-\hat{\kappa}_\alpha\hat{\kappa}_\beta)\sum_{l'd'\,ld}\frac{1}{4}g_{d'}g_d\,F^*_{d'}(\boldsymbol{\kappa})\,F_d(\boldsymbol{\kappa}) \\ \times\int_\infty^\infty \langle\, e^{-i\boldsymbol{\kappa}\cdot\boldsymbol{R_{l'd'}(0)}}\,e^{i\boldsymbol{\kappa}\cdot\boldsymbol{R_{ld}}(t)}\rangle\langle\, S^\alpha_{l'd'}(0)S^\beta_{ld}(t)\,\rangle\, e^{-i\omega\,t}\,dt,\end{aligned} \tag{2.65}$$

An important feature that can be deduced from this form of the cross-section is that magnetic scattering has directional dependence, due to the tensor $(\delta_{\alpha\beta}-\hat{\kappa}_\alpha\hat{\kappa}_\beta)$. The magnetic components which are perpendicular to the momentum transfer, $\boldsymbol{\kappa}$, or equivalently, the scattering plane, are probed in a neutron scattering experiment. If for example, a system exhibits magnetic order along the direction $\hat{\boldsymbol{\eta}}$, then the directional dependence is characterized by the expression $1-(\hat{\boldsymbol{\kappa}}\cdot\hat{\boldsymbol{\eta}})^2$ [17]. Lastly, it is clear that the magnetic scattering is dependent on the magnetic fluctuation of the scattering system, reflecting a parallel to the nuclear case in which the scattering is dependent on the density fluctuation.

For a Bravais lattice, we have instead

$$\begin{aligned}\frac{d^2\sigma}{d\Omega dE'} = \frac{(\gamma r_0)^2}{2\pi\hbar}\frac{k'}{k}\,N\{\frac{1}{2}gF(\boldsymbol{\kappa})\}^2\sum_{\alpha\beta}(\delta_{\alpha\beta}-\hat{\kappa}_\alpha\hat{\kappa}_\beta)\sum_l e^{i(\boldsymbol{\kappa}\cdot\boldsymbol{l})} \\ \times\int_\infty^\infty \langle\, e^{-i\boldsymbol{\kappa}\cdot\boldsymbol{u_0}(0)}e^{i\boldsymbol{\kappa}\cdot\boldsymbol{u_l}(t)}\rangle\langle\, S^\alpha_0(0)S^\beta_{l'}(t)\,\rangle\, e^{-i\omega\,t}\,dt,\end{aligned} \tag{2.66}$$

where $\boldsymbol{u}_l(t)$ is the displacement of nucleus l from its equilibrium position. This equation contains the correlation function for the atomic co-ordinates. Therefore, magnetic scattering is not only influenced by the magnetic behaviour of the scattering system,

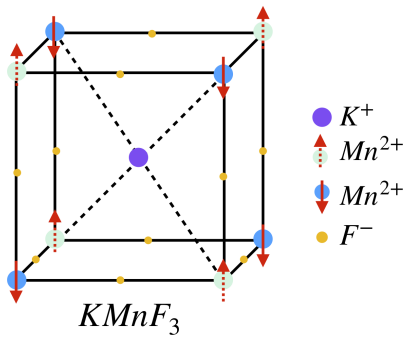

Figure 2.8: The simple antiferromagnetic structure of KMn_3 is shown.

but it also characterized by the positions and dynamics of the crystalline structure.

2.3.2.1 Elastic Scattering from Simple Antiferromagnetic Structures

The antiferromagnetic phase is an ordered magnetic state which is realized in a crystal system when nearest neighbouring ions have long-range ordered, antiparallel aligned magnetic moments. The magnetic structure of an antiferromagnet can be decomposed into two magnetic sublattices, A and B, each defined by a network of spins which are oriented in the same direction but anti-parallel to the network of spins in the other sublattice. To illustrate this concept, consider the simple antiferromagnetic

structure of $KMnF_3$ as shown in Figure 2.8a.). If we denote $\hat{\boldsymbol{\eta}}$ as the direction in which the sublattice A spins are oriented, and we took the average of the magnetic moment over the nuclear unit cell, then $\langle S \rangle = 0$, as there are as many spins oriented in the $+\hat{\boldsymbol{\eta}}$ direction as there are in the $-\hat{\boldsymbol{\eta}}$ direction. Instead, it is useful to perform this sum over sublattice A alone, and we redefine $\langle S \rangle = 0$ as the *staggered magnetization*. The staggered magnetization is performed over the magnetic unit cell/sublattice, instead of the total nuclear unit cell and we utilize this definition to calculate the cross-section for a single domain and treat the crystal as non-Bravais. From Equation (2.65), we can evaluate

$$\sum_{ll'} e^{i(\boldsymbol{\kappa}\cdot(\boldsymbol{l}-\boldsymbol{l'}))} \langle S^{\eta}_{l'} \rangle \langle S^{\eta}_{l} \rangle = \langle S^{\eta} \rangle^2 N_m \sum_{A} e^{i\boldsymbol{\kappa}\cdot\boldsymbol{l}} \sum_{d} \sigma_d \, e^{i\boldsymbol{\kappa}\cdot\boldsymbol{d}}, \tag{2.67}$$

where $N_m (= \frac{1}{2}N)$ is the number of magnetic unit cells in the crystal, $\sigma_d = +1$ for magnetic sublattice A and $\sigma_d = +1$ for magnetic sublattice B. As the crystal structure

is periodic,

$$\sum_{A} e^{i\boldsymbol{\kappa}\cdot\boldsymbol{l}} = \frac{(2\pi)^3}{v_{0m}} \sum_{\boldsymbol{\tau}_m} \delta(\boldsymbol{\kappa} - \boldsymbol{\tau}_m), \tag{2.68}$$

where ($v_0 m = 2v_0$) is the volume of the magnetic unit cell and τ_m is a vector in the magnetic reciprocal lattice. Finally, we integrate over E' to evaluate the cross-section for a simple antiferromagnetic structure with sublattices A and B present. This leads to,

$$\left(\frac{d\sigma}{d\Omega}\right)_{el} = (\gamma r_0)^2 \, N_m \frac{(2\pi)^3}{v_{0m}} \sum_{\boldsymbol{\tau}_m} |F_M(\boldsymbol{\tau}_m)|^2 \, e^{-2W} \, \{1 - (\hat{\boldsymbol{\tau}} \cdot \hat{\boldsymbol{\eta}})^2_{av}\} \delta(\boldsymbol{\kappa} - \boldsymbol{\tau}_m), \tag{2.69}$$

where $F_M = \frac{1}{2} \langle S^{\eta} \rangle \, F(\boldsymbol{\tau}_m) \sum_d \sigma_d \, e^{i\boldsymbol{\tau_m}\cdot\boldsymbol{d}}$. This implies that elastic magnetic scattering occurs at magnetic reciprocal lattice vectors. Referring to the simple case of $KMnF_3$, sublattice A has a face-centred cubic magnetic unit cell. On the other hand, the reciprocal lattice would be simple cubic, if all Mn^{2+} ions were treated equally. Therefore, elastic magnetic scattering and nuclear Bragg scattering, in most cases, occur at distinct momentum transfers, $\boldsymbol{\kappa}$, allowing one to distinguish nuclear scattering from magnetic scattering. In a typical magnetic structure determination study with neutrons, the material is typically investigated above and below the Néel transition temperature, T_N. Only below T_N, the magnetic peaks are present and can be distinguished from the nuclear Bragg peaks by comparing against diffraction data above T_N. Thereafter, magnetic structures can be determined and refined using programs such as *FULLPROF* [18].

2.3.2.2 Spin Waves

A spin-wave is an elementary excitation of an ordered spin system. We shall consider the simplest case involving a linear spin chain of N moments with spacing a, which host near neighbour ferromagnetic coupling. The Hamiltonian describing the direct exchange between the ions is given by,

$$\mathcal{H} = -2J \sum_i \boldsymbol{S_i} \cdot \boldsymbol{S_{i+1}}, \tag{2.70}$$

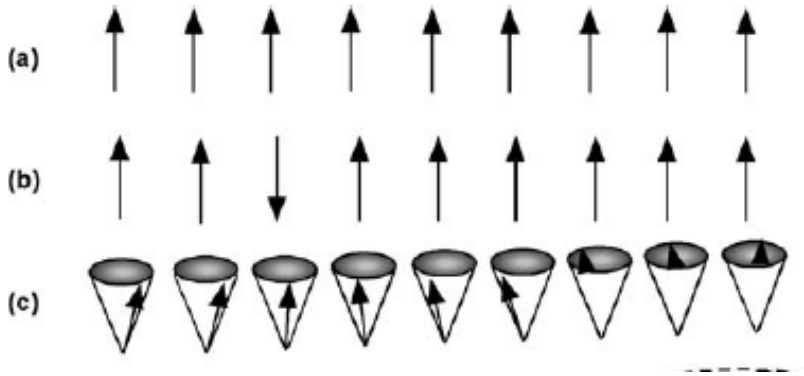

Figure 2.9: (a) The ferromagnetic ground state is shown. (b) One possible excitation of the ferromagnetic state involving one flipped spin is shown. The energetic cost is too great for this state to be physically realized. (b) The collective disturbance of the spin chain results in the generation of a magnon, as shown. Reprinted from Neutron Scattering from Magnetic Materials, 1st Edition, Tapan Chatterji, Page. 19, Copyright 2020, with permission from Elsevier.

where $J < 0$. The most simple excitation of this system involves a collective excitation of the spins, which is referred to as a magnon and is schematically shown in Figure 2.9. This is in contrast to the case where an individual spin is flipped. However, the energy cost is greater than that involved with generating a *magnon*. Magnons posses a quantized value, and can be compared to phonons which are normal modes associated with the motions of the atoms within the crystalline structure. In the same way, a magnon is a normal mode of the coupled spin system whose energy $E = \hbar\omega$ and wave vector $\boldsymbol{\kappa}$ are given by,

$$\hbar\omega = 4\,J\,S\,(1 - \cos(\kappa a)). \tag{2.71}$$

in the low energy limit, $\kappa a \lll 1$, $1 - \cos(\kappa a) \simeq \frac{1}{2}(ka)^2$. Therefore the dispersion in the low energy goes as,

$$\hbar\omega \simeq 2\,J\,S\,a^2\,\kappa^2 = D\,\kappa^2 \tag{2.72}$$

where D is the spin wave stiffness constant. For an antiferromagnetic spin chain, the dispersion relation is,

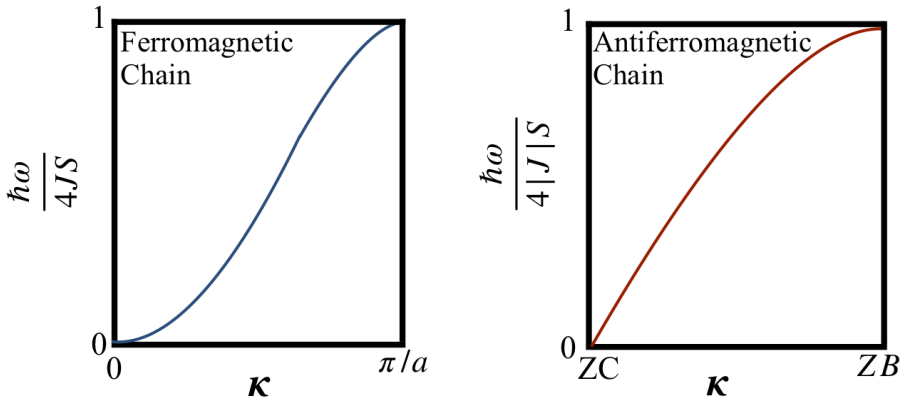

Figure 2.10: The low $\boldsymbol{\kappa}$ dispersions for a $1D$ (a) ferromagnetic, and (b) antiferromagnetic spin chain with nearest neighbour spacing a is shown. ZC and ZB denote zone centre and zone boundary, respectively.

$$\hbar\omega = 4\,|J|\,S\,sin(\kappa a). \tag{2.73}$$

The low energy limit for the antiferromagnetic spin chain is,

$$\hbar\omega \simeq 4\,J\,S\,a\,\kappa. \tag{2.74}$$

Hence the dispersion relations for a ferromagnet and for an antiferromagnet are distinguishable based on their $\boldsymbol{\kappa}$ dependence as shown in Figure 2.10. Note that in these figures, at $|\boldsymbol{\kappa}| = 0$, the scattering intensity is zero. It should be noted that depending on the physics involved in the crystal system, additional factors such as single-ion anisotropy or anisotropic exchange interactions can generate gaps in this excitation spectrum. To conclude this discussion, the cross-section for one-magnon creation, processes is,

$$\begin{aligned}\left(\frac{d^2\sigma}{d\Omega dE'}\right)_{m,+1} &= \frac{k}{k'}(\gamma\, r_0)^2\,\frac{(2\pi)^3}{2N_m\,v_0}\,\frac{g^2S}{4}(1+\hat{\boldsymbol{\kappa}}_z^2)\,f^2(\boldsymbol{\kappa})e^{-2W} \\ &\times \sum_{\boldsymbol{\tau}\boldsymbol{\kappa}} \langle\, n_\kappa + 1\rangle\,\delta(\boldsymbol{\kappa}-\boldsymbol{k}-\boldsymbol{\tau})\delta[E-\hbar\omega(\boldsymbol{k})],\end{aligned} \tag{2.75}$$

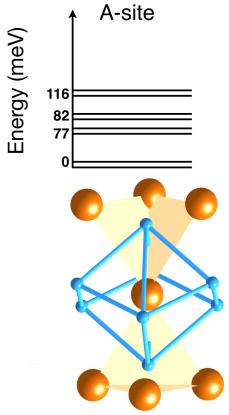

Figure 2.11: The $4f$ levels of Yb^{3+} are split into four doublets due to the crystal-field effect which is generated by the local oxygen environment.

and for one-magnon annihilation processes it is,

$$\left(\frac{d^2\sigma}{d\Omega dE'}\right)_{m,-1} = \frac{k}{k'}(\gamma\, r_0)^2\, \frac{(2\pi)^3}{2N_m\, v_0}\, \frac{g^2 S}{4}(1+\hat{\boldsymbol{\kappa}}_z^2)\, f^2(\boldsymbol{\kappa}) e^{-2W} \times \sum_{\boldsymbol{\tau}\boldsymbol{\kappa}} \langle\, n_\kappa \rangle\, \delta(\boldsymbol{\kappa}+\boldsymbol{k}-\boldsymbol{\tau})\delta[E+\hbar\omega(\boldsymbol{k})]. \tag{2.76}$$

2.3.2.3 Crystal-field Excitations

Crystal electric fields (CEFs) are fields which are generated due to the local environment surrounding magnetic species in a crystalline lattice. For simplicity, we shall consider crystal electric fields which are on the energy scale of thermal neutrons ($\sim$ 1-100 meV), such as those realized in the rare-earth titanates. The valence electrons in rare-earth ions occupy the $4f$ electronic levels. As the rare-earth atoms are subject to electric fields generated generated by the local oxygen environment, shown in Figure 2.11, the degeneracy of the $4f$ levels split. The example shown in Figure 2.11 applies to $Yb_2Ti_2O_7$, where the $4f$ levels get split into four doublets. In a thermal neutron scattering experiment at low temperatures, it is possible to excite the ground state electrons to the excited levels. At high temperatures, the excited states become thermally occupied, and it is possible to observe additional transitions between the excited levels. It is also possible for a neutron to de-excite an electron from an excited stated to a lower lying crystal field level. These transitions manifest themselves as

resonance peaks at particular energy transfers E. Information provided by inelastic neutron scattering experiments regarding the intensities of the resonance peaks is invaluable. First, the resonance peaks can be labelled as a CEF as the neutron scattering intensity should agree with the expectations for the transition matrix elements between the corresponding CEF levels. Accurate determination of the transition matrix elements and measurements of the energy eigenvalues of the CEFs aid in determination of the size and anisotropy of the ground state moment. The cross-section for crystal-electric field excitations between level n to m is given by,

$$\frac{d^2\sigma}{d\Omega dE'} = N\left(\frac{1}{2}\,g\,r_0\right)F^2(\boldsymbol{\kappa})e^{-2W(\boldsymbol{\kappa})}\rho_{\Gamma_n}\sum_{\alpha}\left(1-\frac{Q_\alpha^2}{Q^2}\right)|\langle\Gamma_m|J_\alpha|\Gamma_n\rangle|^2 \\ \delta(\hbar\omega + E_{\Gamma_n} - E_{\Gamma_m}). \tag{2.77}$$

We seek to obtain a form of Equation (2.77) which can be applied to polycrystalline materials. The factor $|\langle\Gamma_m|J_\alpha|\Gamma_n\rangle|^2$ becomes,

$$|\langle\Gamma_m|J_\perp|\Gamma_n\rangle|^2 = \frac{2}{3}\sum_{\alpha}|\langle\Gamma_m|J_\alpha|\Gamma_n\rangle|^2 \tag{2.78}$$

where $J_\perp$ is the component of the total angular momentum perpendicular to the scattering vector[8]. The matrix elements for rare-earth atoms in cubic crystal-fields has been tabulated by Birgenau[19]. One notable feature of Equation (2.77) is that the $\boldsymbol{\kappa}$ dependence of the inelastic scattering from the CEFs is contained solely in the square of the magnetic form factor, $F_M(\boldsymbol{\kappa})$. This is unsurprising as the excitations arise from single-ion effects. Another consequence is that, if CEFs are measured as a function of $\boldsymbol{\kappa}$, they will manifest as dispersionless features.

Bibliography

[1] Max von Laue. "Eine quantitative Prüfung der Theorie für die Interferenzerscheinungen bei Röntgenstrahlen". In: *Annalen der Physik* 346 (1913), pp. 989–1002.

[2] W. L. Bragg. "The diffraction of short electromagnetic waves by a crystal". In: *Proc. Cambridge Phil. Soc., 1913* 17 (1913), pp. 43–57.

[3] Louis De Broglie. "Recherches sur la théorie des Quanta". In: *Ann. Phys.* 10 (1925), pp. 22–128.

[4] George Paget Thomson. "The diffraction of electrons by single crystals". In: *Proceedings of the Royal Society of London. Series A, Containing Papers of a Mathematical and Physical Character* 133 (1931), pp. 1–25.

[5] F. Bloch. "On the Magnetic Scattering of Neutrons". In: *Phys. Rev.* 50 (1936), pp. 259–260.

[6] C. G. Shull and J. Samuel Smart. "Detection of Antiferromagnetism by Neutron Diffraction". In: *Phys. Rev.* 76 (1949), pp. 1256–1257.

[7] A. Furrer. *Neutron Scattering in Novel Materials: Proceedings of the Eighth Summer School on Neutron Scattering, Zuoz, Switzerland, 5-11 August 2000*. World Scientific, 2000.

[8] "Neutron Scattering in Condensed Matter Physics". In: *Neutron Scattering in Condensed Matter Physics*, pp. i–xiv.

[9] N.W. Ashcroft and N.D. Mermin. *Solid State Physics*. Holt, Rinehart and Winston, 1976, pp. 644–645.

[10] G. L. Squires. *Introduction to the Theory of Thermal Neutron Scattering*. 3rd ed. Cambridge University Press, 2012.

[11] S. W. Lovesey. *Theory of neutron scattering from condensed matter. Vol. 1. Nuclear scattering*. 1984.

[12] J. Baruchel. *Neutron and synchrotron radiation for condensed matter studies: Theory, instruments and methods*. Vol. 1. Neutron and Synchrotron Radiation for Condensed Matter Studies. Springer-Verlag, 1993.

[13] Eugen Merzbacher. *Quantum Mechanics*. 3rd ed. Wiley, 1998.

[14] P. Debye. "Interferenz von Röntgenstrahlen und Wärmebewegung". In: *Annalen der Physik* 348 (1913), pp. 49–92.

[15] P. J. Brown. *International Tables for Crystallography vol. C*. 2nd ed. Kluwer Academic Publishers, 1999, p. 450.

[16] Kohjiro Kobayashi, Tatsuya Nagao, and Masahisa Ito. "Radial integrals for the magnetic form factor of $5d$ transition elements". In: *Acta Crystallographica Section A* 67 (2011), pp. 473–480.

[17] Tapan Chatterji. "Chapter 1 - Magnetic Neutron Scattering". In: *Neutron Scattering from Magnetic Materials*. Ed. by Tapan Chatterji. Amsterdam: Elsevier Science, 2006, pp. 1–24.

[18] J. Rodriguez-Carvajal. "Recent advances in magnetic structure determination by neutron powder diffraction". In: *Physica B* 192 (1993), p. 55.

[19] R. J. Birgeneau. "Transition probabilities for f-electron J-multiplets in cubic crystal fields". In: *Journal of Physics and Chemistry of Solids* 33 (1972), pp. 59–68.

3 Neutron Scattering Techniques

3.1 Neutron Production

3.1.1 Neutrons from a reactor source

The Institut Laue Langevin (ILL) is one of the world centres for neutron research. At the ILL, neutron production is driven by a reactor source which has a power of $58MW$. The reactor is capable of producing a continuous neutron flux of 1.5×10^{15} neutrons$\cdot\, cm^{-2} \cdot\, s^{-1}$. Neutrons are produced via nuclear fission of ^{235}U nuclei. The nuclear reaction is activated with thermal neutrons, and the result is the generation of 2.5 fast neutrons and the release of 180 MeV of energy. The process can be described as,

$$n_{thermal} +^{235} U \;\rightarrow\; 2\,\text{fission fragments} + 2.5 n_{fast} + 180 MeV. \tag{3.1}$$

In a critical assembly, the reaction is self-sustaining where 1 neutron triggers another fission process and approximately 1.5 neutrons are available for experimental use, although some of this may be absorbed in other material [1].

To contain this reaction for neutron production, a pool-reactor arrangement is employed at the ILL, as shown in Figure 3.1. There is one fuel rod in the ILL's reactor core and it contains $\sim 8.57\,kg$ of highly enriched (93%) uranium as fuel. The control rods are used to control the nuclear reaction and are made of boron as it has a huge

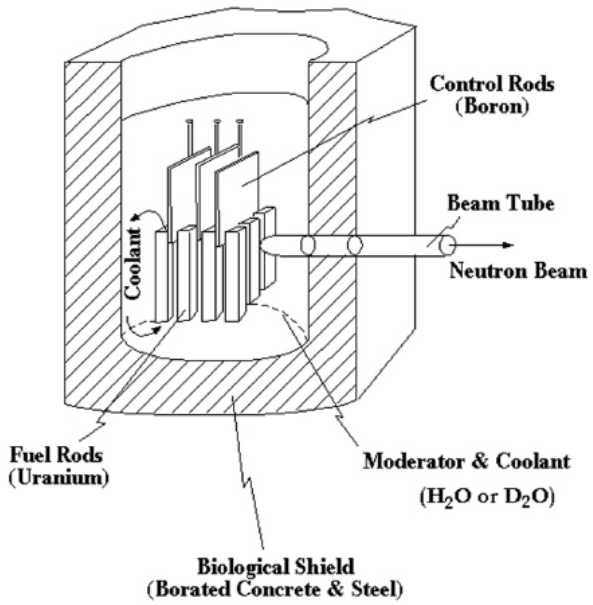

Figure 3.1: The most important elements encompassing the function of a pool-type nuclear reactor are schematically shown. This figure was reprinted from Page 3.1-5 of the Neutron Data Booklet (Ref. [1]). Permission was obtained from Colin Carlile to reuse this figure. Copyright 2020 by OCP Imprints.

neutron absorption cross-section of 3835(9) *barns*.[1] In this layout, the reactor core is surrounded by a reflector vessel filled with D_2O, and beyond this vessel, the pool is filled with H_2O. D_2O and H_2O *moderate* or slow the fast neutrons from the nuclear reaction to thermal energy scales.[2] Finally, the massive shielding, which is comprised of borated concrete and steel, hugs the entire assembly and provides protection to scientists and instruments from harmful radiation exposure. The beam tubes shown in Figure 3.1 are used to deliver the neutrons to the instruments.

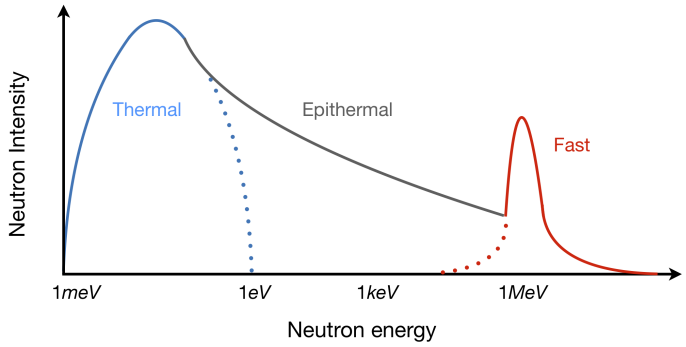

Figure 3.2: The profile of the neutron flux emanating from a typical nuclear reactor is shown.

The distribution of the output neutron flux from the reactor, as a function of neutron energy, is shown in Figure 3.2. The “fast neutrons" which immediately emerge from the core have energies between 1-2 MeV. The *epithermal* region is comprised of neutrons with energies of $\sim$ $200meV$ to $0.5MeV$. These neutrons are subject to slowing as they undergo elastic collisions with the moderating material. The *thermal* energy region represents the neutrons which have energy $<$ 200 meV and are achieving thermal equilibrium with the moderator. For fast neutrons to be moderated to thermal energies, they undergo $\sim$ 16 collisions in H_2O and $\sim$ 29 collisions in D_2O to be thermalized.

To optimize the flux at the neutron energy required, the noses of the beam tubes are located just outside the core. When fast neutrons escape the core, they are moderated by the surrounding D_2O are are trapped by the reflector vessel. In this region of maximum flux, additional moderators are placed to provide a broad

[1] 1 *barn* is equivalent to $10^{-24}\,cm^2$

[2] H_2O and D_2O are good moderators of neutrons as the hydrogen nuclei have a high neutron scattering cross-section. Also, as the hydrogen nuclei share a similar mass to the neutron mass, elastic scattering processes between these two particles permit efficient retardation of the neutron energy.

spectrum of energies for different instruments. One of the moderators provides a hot source, and it is composed of a block of graphite (at 2770 K). Two of the moderators provide cold and ultra-cold neutrons. A 25 *litre* tank of liquid deuterium (at 20 K) is utilized for these two sources. The three thermal neutron tubes are optimally placed to face the reflector vessel. The neutron tubes or, guides, are designed to transmit neutrons (i.e. low absorption) to distances as far as 40-150 m away from the reactor source without a significant loss in intensity.

3.1.2 Neutrons via spallation

The Spallation Neutron Source (SNS), which is located at Oak Ridge National Laboratory is a pulsed neutron source. Neutrons are generated via spallation of an appropriate material - referred to as a target- with a high-energy, pulsed, ion beam. At the SNS, the power delivered to the target is 1.4 MW. The neutron bunches coming from the target each contain roughly 10^{14} neutrons, have a duration of $1\mu\, s$ and are produced at a rate of 60 Hz.

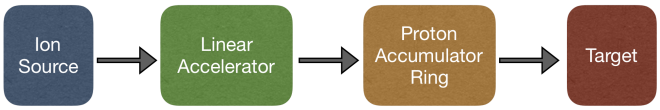

Figure 3.3: The different steps involved in neutron production at a pulsed source are shown.

A schematic, showing the different stages and components of this neutron production process is shown in Figure 3.3. The ion source produces H^- ions of energy 2.5 MeV and forms them into pulses. The pulsed H^- beam travels to the linear accelerator (or, linac) where the ions are accelerated to about 1 GeV. The pulsed ions are then transmitted to the proton accumulator ring, where the ion bunches, are intensified before being delivered to the target.

Shorter and more intense ion bunches are produced as the accumulator ring is equipped with a stripper foil which removes two electrons from each H^- ion, resulting in the generation of a short and sharp pulsed H^+ ion beam profile for the spallation process. The pulsed ion beam is then directed toward a liquid mercury target for neutron generation. When a single mercury atom is bombarded by the high energy

proton beam, 20 to 30 neutrons are “spalled". These neutrons are then moderated to the required energies and are directed with neutron guides to the instruments.

3.2 Two-axis technique at *D20*

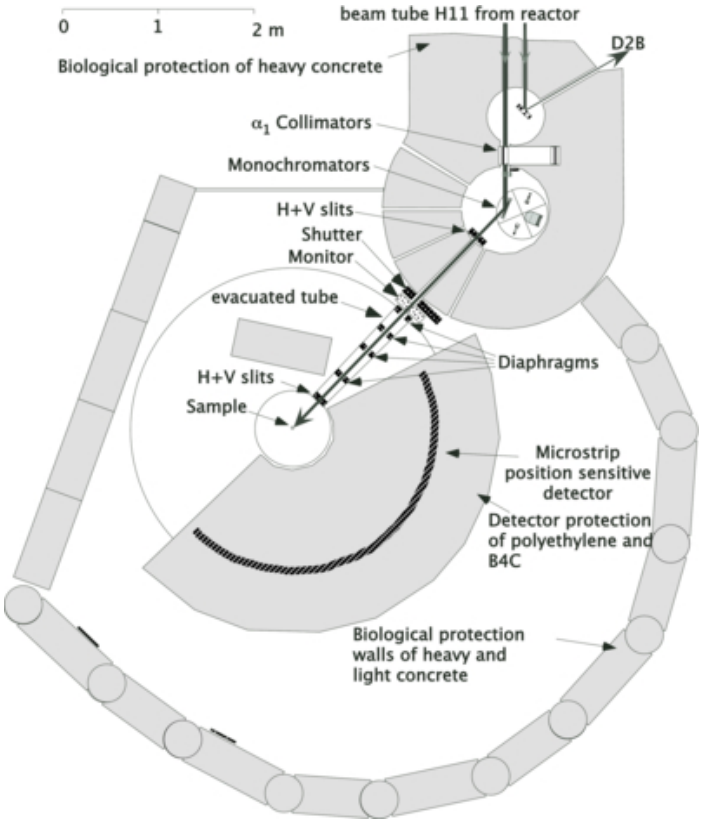

Figure 3.4: The different components comprising the $D20$ instrument profile at the ILL are shown in this schematic. This figure was reprinted from the article *The D20 instrument at the ILL: a versatile high-intensity two-axis neutron diffractometer, from Measurement Science and Technology, Volume 19, Number 3 (2008).*. Permission was obtained from Thomas Hansen to reuse this figure. Copyright 2020 by IOP Publishing.

$D20$ is a medium to high resolution two-axis neutron instrument located at the ILL. The instrument is fed neutrons via the high flux H11 beam tube which originates in the reflector vessel containing D_2O. The schematic showing the layout of the instrument (from above) is shown in Figure 3.4. As the neutrons arrive via the H11 guide, the beam of neutrons gets collimated before arriving at the monochromator, which is located 17.5 m from the neutron source. This collimator is known as the

α_1 collimators and is a revolving stage enabling different configurations so that the horizontal divergence of the neutron beam striking the monochromator is defined at the desired setting. The different α_1 collimation settings include the positions $27'$, $20'$, $10'$ and closed [2]. The "white" beam further travels to the monochromator shielding or "casemate", which houses four monochromators. The monochromator is selected based on the desired incident energy of the experiment. In our experiments we utilized a pyrolytic graphite monochromator with a take-off angle of 42° in order to achieve an incident neutron wavelength of 2.41 Å. In this configuration, the neutron flux at sample position is optimized compared with other common monochromator combinations which are typically employed at $D20$ as shown in Table 3.1. Downstream of the monochromator are the $H + V$ slits which are used to define the beam further, a secondary beam shutter and a beam monitor. The diaphragms in the evacuated tube serve to reduce the background count. There are a second set of $H + V$ slits which are located about 50 cm and 60 cm upstream of the sample. The sample is located 3.2 m from the monochromator and has maximum beam dimensions of $50\,mm$ (height) $\times\, 30\,mm$ (width). After the incident neutrons are scattered from the sample, they are detected by a one-dimensional position sensitive detector which is based on a 'microstrip' gas chamber technology (MSGC) [3]. $D20$ detectors contain 1536 detection cells which afford a 2θ coverage of 153.6° over a total solid angle of 0.27 sr. The normal positioning of the beamstop downstream of the sample limits the minimum useful diffraction angle to 5°.

Monochromator reflection	Neutron Wavelength (Å)	Flux on sample ($10^7 \cdot s^{-1} \cdot cm^{-2}$)
Cu(200) at 26°	0.82	3.4
Cu(200) at 30°	0.94	5.9
Cu(200) at 42°	1.30	9.8
Pyrolytic Graphite at 42°	2.41	4.2
Ge(115) at 120°	1.88	1.0

Table 3.1: A summary of the neutron flux achieved at the sample position given different monochromator and neutron wavelength combinations are illustrated in this table .

3.3 Time-of-flight technique at *SEQUOIA*

The time-of-flight (TOF) inelastic neutron scattering technique is a very powerful probe of direct low-lying excitations in condensed matter systems. The details of this technique will be discussed in relation to the chopper spectrometer, *SEQUOIA, BL-16*, which is located at the Spallation Neutron Source (SNS) at Oak Ridge National Laboratory in Oak Ridge, Tennessee [4].

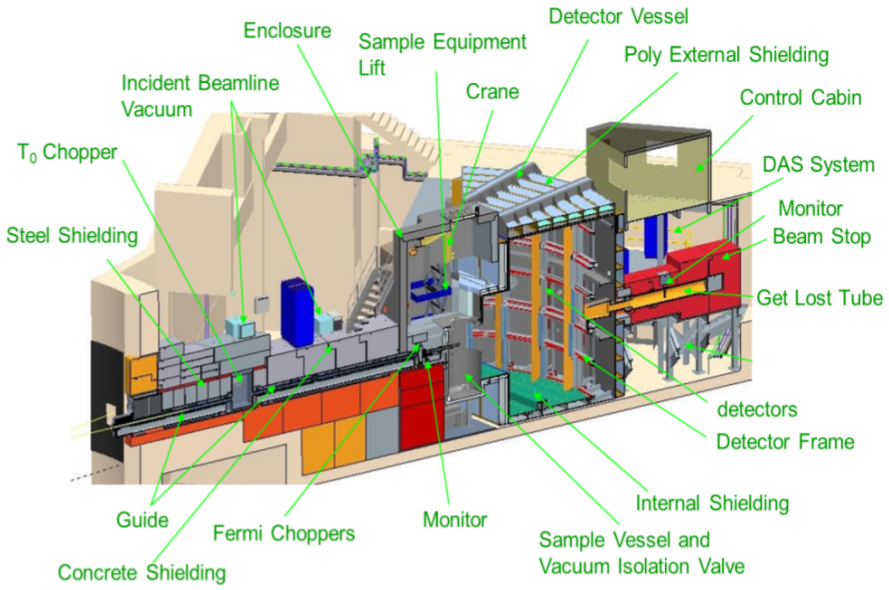

Figure 3.5: The components comprising the indirect geometry time-of-flight spectrometer, *SEQUOIA* is shown. This figure was reprinted from the open access article (also Ref. [4]) *SEQUOIA: A Newly Operating Chopper Spectrometer at the SNS.* Permission was obtained from Garrett E. Granroth to reuse this figure.

As *SEQUOIA* is a thermal neutron spectrometer, decoupled ambient temperature H_2O is utilized to reduce neutron energies coming from the moderator to $E \sim 100$ meV to 2 eV. The time at which the neutrons emerge from the moderator is referred to as $t = 0$. Thereafter, the neutrons encounter the T_0 chopper as seen in Figure 3.5 which is specifically designed to block the prompt fast pulse of neutrons and the gamma flash which is produced when the H^+ ions strike the moderator. The T_0 chopper is a thick propeller blade which is made of inconel, and deflects fast neutrons into the surrounding shielding. At the next stage, the Fermi choppers are utilized to monochromate the neutron pulses. Fermi choppers are effectively heavy rotating

drums armed with a slit package. The slit package is comprised of curved, spaced slats, which are made of a neutron absorbing material. The rotation speed of the chopper is selected so that neutrons of the appropriate incident energy are transmitted through the channels of the slit package, as seen in Figure 3.6. The resolution of the measurement is also defined by spacings in the slit package. Neutrons of the desired energy are then delivered to the sample, and scatter in different directions thereafter. The position, recorded as a scattering angle, and the time of arrival, t_a of the neutrons are recorded by the large bank of ^{3}He position sensitive detectors. All information gathered at the detector banks are recorded in a timing histogram.

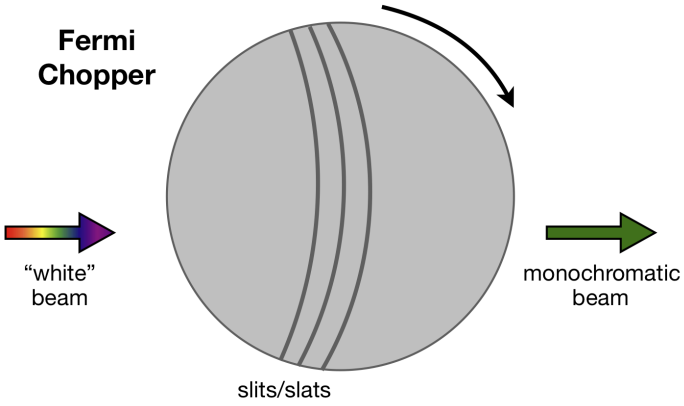

Figure 3.6: This bird's eye view of the rotating Fermi chopper shows the alternating slits/slats which transmit/absorb neutrons of the correct/wrong incident energy. The "white neutron beam" is made monochromatic after passing through the Fermi chopper.

As the incident energy of the neutrons, E, the arrival time t_a and travel distances are accurately known, it is possible to determine the final velocity v' and final energy $'$ of the neutron by simple kinematics. The quantity $\Delta E = E' - E$ characterizes the energy which the neutron exchanges with the sample. Coupling final energy of the neutron, E', with the final position of the neutron, the final wave vector of the neutron $\mathbf{k}'$ can also be obtained. The full spectrum of the scattered neutron intensity $S(\mathbf{Q}, \omega)$ can therefore be deduced, resulting in the production of a $4D$ data set - the energy exchanged with the sample ΔE and three directions of the scattering vector $\vec{\boldsymbol{\kappa}}$. As measurements were taken on polycrystalline samples at $SEQUOIA$, it is appropriate to image the neutron scattering in two-dimensions i.e. ΔE, and the magnitude of the scattered wavevector $|\vec{\boldsymbol{\kappa}}|$.

Bibliography

[1] Gerry Lander and Albert-José Dianoux. *Neutron Data Booklet*. 628 North Second Street, Philadelphia, PA 19123 USA: Old City Publishing Group, 2003.

[2] Thomas C. Hansen, Paul F. Henry, Henry E. Fischer, Jacques Torregrossa, and Pierre Convert. "The D20 instrument at the ILL: a versatile high-intensity two-axis neutron diffractometer". In: *Measurement Science and Technology* 19 (2008), p. 034001.

[3] A. Oed. "Position Sensitive Detector With Microstrip Anode For Electron Multiplication With Gases". In: *Nucl. Instrum. Methods A* 263 (1988), pp. 351–359.

[4] G. E. Granroth, A. I. Kolesnikov, T. E. Sherline, J. P. Clancy, K. A. Ross, J. P. C. Ruff, B. D. Gaulin, and S. E. Nagler. "SEQUOIA: A Newly Operating Chopper Spectrometer at the SNS". In: *Journal of Physics: Conference Series* 251 (2010), p. 012058.

4

Crystal field excitations from Yb^{3+} ions at defective sites in highly stuffed $Yb_2Ti_2O_7$

This chapter incorporates the article *"Crystal field excitations from Yb^{3+} ions at defective sites in highly stuffed $Yb_2Ti_2O_7$"*, which has been published in Physical Review B. Reproduced from with permission, copyrighted by the American Physical Society 2020. The full reference is given below:

G. Sala, D. D. Maharaj, M. B. Stone, H. A. Dabkowska, and B. D. Gaulin. Physical Review B 97, 224409 (2018).

This work presents a time-of-flight inelastic neutron scattering and powder diffraction studies of the crystal-field levels of Yb^{3+} ions in highly stuffed samples of $Yb_2Ti_2O_7$. Two single-crystal samples of stuffed $Yb_2Ti_2O_7$ were produced with concentrations x = 0.12 and x = 0.19 where the chemical formula of the stuffed samples is given by $Yb_{(2+x)}Ti_{(2-x)}O_{7-y}$. For the first time, the crystal-field scheme associated with Yb^{3+} ions at the B-site, and Yb^{3+} ions at the A-site in the presence of an oxygen deficient environment, were determined. Our studies also confirmed findings in earlier work done on pure $Yb_2Ti_2O_7$ and a lightly stuffed sample (on the $\sim$ 2% level) which showed the systematic broadening of the crystal-field excitations associated with the A site as a function of increasing stuffing. Ultimately, the measurement of the crystal-field levels of these defective sites enabled the determination of the crystal-field parameters associated with the crystal-field Hamiltonians as well as the ground state anisotropy of the Yb^{3+} ions at these defective sites.

PHYSICAL REVIEW B **97**, 224409 (2018)

Crystal field excitations from Yb^{3+} ions at defective sites in highly stuffed $Yb_2Ti_2O_7$

G. Sala,[1,2,*] D. D. Maharaj,[2] M. B. Stone,[1] H. A. Dabkowska,[3] and B. D. Gaulin[2,3,4,†]

[1]*Neutron Scattering Division, Oak Ridge National Laboratory, Oak Ridge, Tennessee 37831, USA*
[2]*Department of Physics and Astronomy, McMaster University, Hamilton, Ontario, Canada L8S 4M1*
[3]*Brockhouse Institute for Materials Research, McMaster University, Hamilton, Ontario, Canada L8S 4M1*
[4]*Canadian Institute for Advanced Research, 661 University Avenue, Toronto, Ontario, Canada M5G 1M1*

(Received 18 October 2017; revised manuscript received 23 February 2018; published 11 June 2018)

The pyrochlore magnet $Yb_2Ti_2O_7$ has been proposed as a quantum spin ice candidate, a spin liquid state expected to display emergent quantum electrodynamics with gauge photons among its elementary excitations. However, $Yb_2Ti_2O_7$'s ground state is known to be very sensitive to its precise stoichiometry. Powder samples, produced by solid-state synthesis at relatively low temperatures, tend to be stoichiometric, while single crystals grown from the melt tend to display weak "stuffing" wherein ∼2% of the Yb^{3+}, normally at the A site of the $A_2B_2O_7$ pyrochlore structure, reside as well at the B site. In such samples Yb^{3+} ions should exist in defective environments at low levels and be subjected to crystalline electric fields very different from those at the stoichiometric A sites. Neutron scattering measurements of Yb^{3+} in four compositions of $Yb_{2+x}Ti_{2-x}O_{7-y}$ show the spectroscopic signatures for these defective Yb^{3+} ions and explicitly demonstrate that the spin anisotropy of the Yb^{3+} moment changes from XY-like for stoichiometric Yb^{3+} to Ising-like for "stuffed" B site Yb^{3+} or for A site Yb^{3+} in the presence of oxygen vacancies.

DOI: 10.1103/PhysRevB.97.224409

I. INTRODUCTION

Exotic magnetic ground states of cubic pyrochlore magnets, with the composition $A_2B_2O_7$, are of great topical interest, as the pyrochlore lattice is one of the canonical architectures supporting geometrical frustration in three dimensions [1,2]. Magnetism can reside at either the A^{3+} site or the B^{4+} site, and the magnetic moments' anisotropy and the interactions between the moments conspire to give rise to rich ground-state selection. Among the states and materials that have been of recent interest are the classical spin ice states in Dy and Ho titanate pyrochlores [3–7], spin liquid and spin glass states in molybdate pyrochlores [8], and spin fragmentation in Nd-based zirconate pyrochlores [9]. The possibility that a quantum analog of the spin ice ground state, i.e., quantum spin ice (QSI), may exist in certain low-moment pyrochlore magnets, including $Yb_2Ti_2O_7$ and $Pr_2Zr_2O_7$, has generated much excitement [10–23].

At low temperatures $Yb_2Ti_2O_7$ displays two magnetic heat capacity anomalies: a broad one near 2 K and a sharp anomaly signifying a thermodynamic phase transition near $T_C = 0.26$ K [24–28]. The thermodynamic phase transition near $T_C = 0.26$ K is generally thought to be to a splayed ferromagnet, with moments pointing close to 100 directions [29–32]. However, surprising sample variability has been reported in this phase transition, with some studies not seeing direct evidence for the ferromagnetic ordered state [16,33–39]. Using the sharp anomaly in C_P as the figure of merit for the phase transition, interesting systematics have been observed [27,28,40,41]. Powder samples produced by solid-state synthesis at relatively low temperatures show a sharp C_P anomaly and a high T_C, usually ∼0.26 K [27,28,40]; however, most single-crystal studies display broader thermodynamic anomalies at much lower temperatures, often with T_C around and below 0.2 K [29,30,42,43].

Crystallographic studies of the powder and single-crystal samples have revealed that the powder samples are stoichiometric $Yb_2Ti_2O_7$, while the single crystals are "lightly stuffed" [27]. They are characterized by the composition $Yb_{2+x}Ti_{2-x}O_{7-y}$, with $x \sim 0.05$ [27]. That is, a small excess of Yb^{3+} ions, nominally at the crystallographic 16d or A site, is "stuffed" onto the 16c or B site where nonmagnetic Ti^{4+} ions are located in pure $Yb_2Ti_2O_7$, as schematically indicated in Fig. 1. It is remarkable that such a small change in stoichiometry could so strongly affect the ground-state selection of a simple ordered state in a three-dimensional magnetic insulator. A related phenomenon has also recently been observed in the effect of hydrostatic pressure on stoichiometric $Yb_2Ti_2O_7$ samples, where ambient pressure conditions show no sign of a muon spin rotation (μSR) signal for the transition, but a minimal 1 kbar (and above) applied pressure results in a clear signal for a transition near $T_C \sim 0.26$ K [44].

With weak stuffing able to suppress this phase transition by as much as ∼25% [27–30,40] in this topical material, it is important to understand precisely what is at play in its ground-state selection. One thing that is clear is that most single crystals of $Yb_2Ti_2O_7$ likely have Yb^{3+} ions occupying not only the stoichiometric A sites but also B sites. They also possess A sites with missing oxygen neighbors. These Yb^{3+} ions in defective environments are expected to experience very different crystal field effects than those at stoichiometric A sites [45]. As the spin anisotropy and size of Yb^{3+} moment are determined by

*salag@ornl.gov
†bruce.gaulin@gmail.com

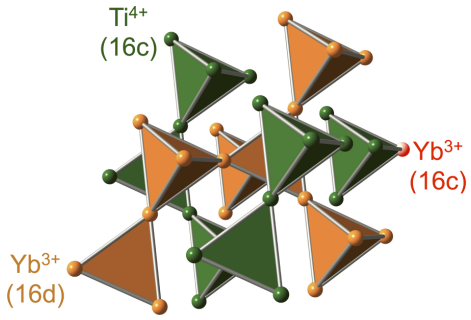

FIG. 1. The pyrochlore lattice, displayed by $A_2B_2O_7$ compounds, belongs to the $Fd\bar{3}m$ space group and consists of two interpenetrating networks of corner-sharing tetrahedra. In stoichiometric $Yb_2Ti_2O_7$, the A sublattice is occupied by rare-earth magnetic Yb^{3+} ions (orange spheres), and the B sublattice is occupied by a nonmagnetic Ti^{4+} site (green spheres). In stuffed $Yb_{2+x}Ti_{2-x}O_{7-y}$, a small fraction of Yb^{3+} ions (in red) also occupy the B sites, and they experience a different crystalline electric field due to the different local environment of surrounding ligands at the B site compared with the A site.

such crystal field effects, it is possible that the defective Yb^{3+} moments and their anisotropy are very different from those of stoichiometric Yb^{3+}; indeed, a prediction from point-charge calculations of the crystal field effects on Yb^{3+} has already suggested that this is the case [45].

The eigenvalues and eigenfunctions associated with crystal field states can be determined using inelastic neutron spectroscopy, and indeed, these have been determined for stoichiometric $Yb_2Ti_2O_7$ and several other rare-earth-based pyrochlore magnets [45–48]. However, the equivalent measurements on Yb^{3+} in defective environments in $Yb_{2+x}Ti_{2-x}O_{7-y}$ are much more difficult, as the environments occur at low density in these materials. Additionally, as we will see, the eigenvalues associated with the defective environments tend to extend to much higher energies. These difficulties necessitated the use of the most modern neutron sources and instrumentation to tackle this problem.

II. EXPERIMENTAL TECHNIQUES

For clarity, we shall refer to the $x = 0$ and $x = 0.05$ samples as the stoichiometric and lightly stuffed samples, respectively. The newly synthesized samples with stuffing levels of $x = 0.12$ and $x = 0.19$ will be referred to as the highly stuffed samples henceforth. It should be noted that all "stuffed samples" are crushed single crystals, and they will be collectively described as such in this work. The sample preparation and characterization of the stoichiometric ($x = 0$) and lightly stuffed ($x = 0.05$) samples of $Yb_{2+x}Ti_{2-x}O_{7-y}$ are described elsewhere [27]. Two rods of $Yb_{2+x}Ti_{2-x}O_{7-y}$ with composition $x = 0.12$ and $x = 0.19$ and dimensions $50 \times 6 \times 6\,mm^3$ were prepared by solid-state reaction between pressed powders of Yb_2O_3 and TiO_2 which were sintered at 450 °C for 15 h with warming and cooling rates of 100 °C/h. The purity of the starting powders of Yb_2O_3 and TiO_2 was close to 99.999%. To produce highly stuffed samples of $Yb_{2+x}Ti_{2-x}O_{7-y}$, a higher ratio of Yb_2O_3 to TiO_2 was used in comparison to what is conventionally used in order to produce stoichiometric samples of $Yb_2Ti_2O_7$. The two single crystals were grown from these rods at McMaster University by utilizing the floating-zone image furnace technique, which is described elsewhere [49]. The growths were conducted in O_2 gas with no overpressure, and the growth rates were 7 and 8 mm/h for the $x = 0.12$ and $x = 0.19$ samples, respectively. Each of the single-crystal samples was then crushed with a mortar and subsequently pulverized using a Pulverisette 2 mortar grinder for 30 min to produce the highly stuffed powder samples. The resulting samples were ≈4 g each. The chemical compositions of these two highly stuffed powders were fully characterized using the neutron powder diffractometer POWGEN [50] located at the Spallation Neutron Source at Oak Ridge National Laboratory (ORNL). The crystallographic refinement was performed using JANA2006 [51] and FULLPROF [52] crystallographic refinement software. Our best refinement of these powder diffraction data gives $x = 0.122(4)$ and $0.192(3)$, with oxygen vacancies located preferentially on the O(1) sites of the pyrochlore lattice, in agreement with Ref. [53].

Inelastic neutron scattering measurements were performed on these highly stuffed samples. We studied their crystal electric field (CEF) excitations using the direct geometry time-of-flight spectrometer SEQUOIA [54] at ORNL. The highly stuffed powder samples were loaded into aluminum flat plates with dimensions $50 \times 50 \times 1\,mm^3$ and were sealed with indium wires under He atmosphere in a glove box. An empty aluminum flat plate with the same dimensions was prepared in a similar manner and employed for background measurements. The empty plate together with the two highly stuffed powder samples were loaded on a three-sample changer in a closed-cycle refrigerator. Measurements were performed at $T = 5$ and 200 K, with incident energies of $E_i = 150$, 250, and 500 meV. The corresponding chopper settings selected for the T_0 chopper, which blocks fast neutrons, and the fine-resolution chopper, FC_2, selected at these energies were $T_0 = 150$ Hz and $FC_2 = 600$ Hz, $T_0 = 120$ Hz and $FC_2 = 600$ Hz, and $T_0 = 150$ Hz and $FC_2 = 600$ Hz, respectively. The data were reduced with MANTID [55] and analyzed using DAVE [56] software, while we employed custom software to refine the CEF spectrum of the highly stuffed powder samples.

III. POWDER DIFFRACTION REFINEMENT

We first discuss the results of our refinement for neutron powder diffraction data collected at POWGEN [50] at $T = 300$ K. The Rietveld refinements of the POWGEN data sets were done independently using JANA2006 [51] and FULLPROF [52]. The starting structural model assumed in the refinements was that of the stoichiometric compound, $Yb_2Ti_2O_7$, and this model has been found to yield poor agreement with the data sets. A second model was then used to permit occupancy of Yb ions at the 16*c* Ti site according to the formula $Yb_{2+x}Ti_{2-x}O_{7-y}$, and the best solutions according to this model were found using both JANA2006 and FULLPROF. The resulting solutions for each of the compounds from JANA2006 were put into FULLPROF and vice versa and were further refined. The resulting best-fit parameters were found to be the same within error, confirming the robustness of

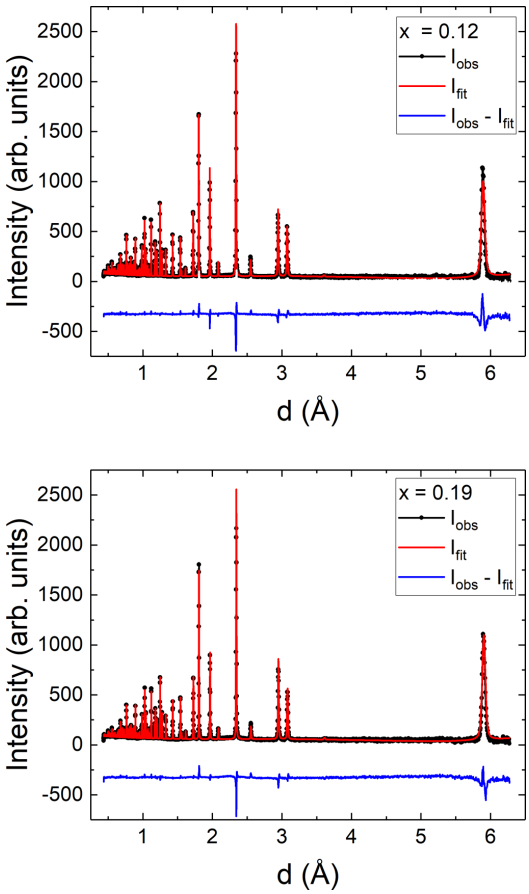

FIG. 2. Rietveld powder neutron diffraction refinements of the $Yb_{2+x}Ti_{2-x}O_{7-y}$ stuffed crystals: The refined chemical formulas for the two compounds are $Yb_{2.122}Ti_{1.878}O_{6.939}$ and $Yb_{2.192}Ti_{1.808}O_{6.904}$, giving $x = 0.12$ and $x = 0.19$, respectively, consistent with the approximate stoichiometry of the starting materials in the crystal growth. As can be seen, the refinement agrees well with the experimental data with $R = 4.6$ and $R = 4.3$ obtained for the two highly stuffed samples, $x = 0.12$ and $x = 0.19$, respectively.

the fits conducted on these samples. The resulting fits for $x = 0.12$ and $x = 0.19$ are shown in Fig. 2 and agree well with the data, with R factors of 4.6 and 4.3, respectively. These R factors compare well with previous refinements done on stuffed ytterbium titanate pyrochlores [27,57]. The high-quality neutron powder diffraction refinements shown in Fig. 2 give unit cell parameters of $a = 10.061(2)$ Å for the $x = 0.12$ sample and of $a = 10.079(3)$ Å for the $x = 0.19$ sample. The fact that the length of the unit cell gets bigger as the stuffing x increases is a direct consequence of the oxygen vacancies; the Coulomb repulsion of the cations left unshielded by the vacancy tends to push all the ions away from each other, increasing the size of the unit cell. Moreover,

TABLE I. Summary of the Rietveld refinement results obtained from neutron powder diffraction experiments conducted at POWGEN on the two highly stuffed samples of $Yb_2(Ti_{2-x}Yb_x)O_{7-y}$ with $x = 0.12$ and $x = 0.19$ at $T = 300$ K.

Atom	x	y	z	Site	Occupancy
		$x = 0.12$ sample			
Yb	0.625	0.125	0.125	16*d*	1
Ti	0.125	0.125	0.125	16*c*	0.939(2)
Yb	0.125	0.125	0.125	16*c*	0.061(2)
O(2)	0.456(8)	0.25	0.25	48*f*	0.992(11)
O(1)	0.5	0.5	0.5	8*b*	0.927(6)
		$x = 0.19$ sample			
Yb	0.625	0.125	0.125	16*d*	1
Ti	0.125	0.125	0.125	16*c*	0.904(2)
Yb	0.125	0.125	0.125	16*c*	0.096(2)
O(2)	0.458(10)	0.25	0.25	48*f*	0.987(12)
O(1)	0.5	0.5	0.5	8*b*	0.910(7)

our refinement showed that these vacancies are mainly located on the O(1) sites of the pyrochlore lattice, confirming the analysis in Ref. [53]. The refined chemical formulas for the two highly stuffed powders are $Yb_{2.122}Ti_{1.878}O_{6.939}$ and $Yb_{2.192}Ti_{1.808}O_{6.904}$, giving a stuffing level of $x = 0.12$ and $x = 0.19$, respectively, in agreement with the approximate stoichiometry of the starting materials used in the crystal growth (see Tables I and II). Note that the stoichiometric ($x = 0$) and lightly stuffed ($x = 0.05$) samples have previously been characterized by powder diffraction techniques by Ross *et al.* [27].

IV. CRYSTAL FIELD ANALYSIS OF INELASTIC NEUTRON SPECTROSCOPY

Inelastic neutron scattering spectra taken at $T = 5$ K on all four powder samples of $Yb_{2+x}Ti_{2-x}O_{7-y}$ studied are shown in Figs. 3 and 4. Figure 3 shows relatively low energy data taken with $E_i = 150$ meV, while Fig. 4 shows relatively high energy data taken with $E_i = 500$ meV. Most of the spectral weight at these high energies is due to CEF excitations from the ground-state doublet appropriate for Yb^{3+} as the lowest CEF excitation is at ∼76 meV and the highest-energy

TABLE II. Results from Rietveld refinement for the degree of stuffing x and the lattice parameter a for the four compounds of $Yb_2(Ti_{2-x}Yb_x)O_{7-y}$ studied. The values for the pure and lightly stuffed compounds, $x = 0.000(1)$ and $x = 0.046(4)$, were refined at $T = 250$ K and were retrieved from Ref. [34]. The values of the lattice parameter obtained for $x = 0.122(4)$ and $x = 0.192(3)$ were those obtained for the $T = 300$ K neutron diffraction data reported in Table I.

Degree of stuffing x	a (Å)
0.000(1)	10.020(3)
0.046(4)	10.029(4)
0.122(4)	10.061(2)
0.192(3)	10.079(3)

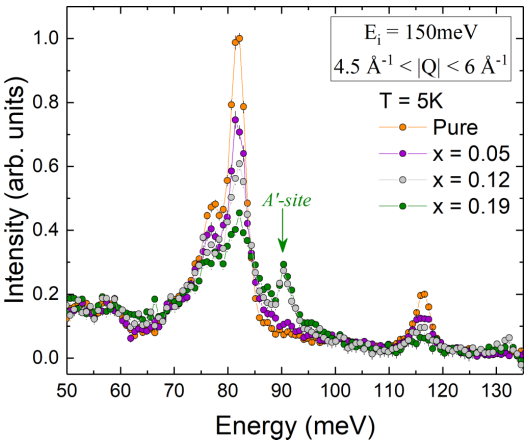

FIG. 3. The measured neutron scattering intensity obtained from $E_i = 150$ meV data sets for four powder samples of $Yb_{2+x}Ti_{2-x}O_{7-y}$ is shown. An empty-can data set has been subtracted from all data. The difference between the CEF intensities of the four samples is evident. In the stoichiometric compound (orange points) there are only three visible levels at ∼76, 81, and 116 meV; their intensities decrease as the system is stuffed (as x increases), and a new CEF level at ∼90 meV appears. The intensities have been scaled in proportion to the actual sample masses.

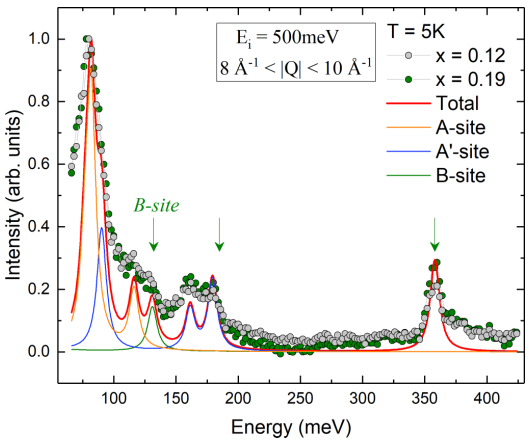

FIG. 4. The measured neutron scattering intensity obtained from $E_i = 500$ meV data sets for two highly stuffed samples of $Yb_{2+x}Ti_{2-x}O_{7-y}$ are shown. An empty-sample-can subtraction has been employed. The calculated spectrum (red line) shows good agreement with the experimental data (gray and green dots for the $x = 0.12$ and $x = 0.19$ samples, respectively). The three different contributions to the total spectrum are highlighted in orange for the stoichiometric A sites, blue for the oxygen-deficient A' sites, and green for stuffed Yb^{3+} ions at the B sites. The total calculated intensity from all three sites is shown in red.

phonons in this pyrochlore family are known to extend to only 100 meV [58]. Inelastic neutron scattering data for the highly stuffed samples ($x = 0.12$ and $x = 0.19$) are shown in Fig. 5 as a function of temperature at both $T = 5$ K [Figs. 5(a) and 5(b)] and $T = 200$ K [Figs. 5(c) and 5(d)].

CEF excitations have several important characteristics: as single-ion properties, the CEFs tend to be dispersionless, and the $|Q|$ dependence of their intensities is largely determined by the magnetic form factor of the magnetic ion involved. They also display temperature dependence that reflects the population distribution of the CEF levels. Given that the lowest-energy CEF excited state is at ∼76 meV for all temperatures below room temperature, we expect no excited states to be thermally populated. These features can be used to distinguish the CEF levels from the background and from other elementary excitations, particularly phonons.

As the temperature is increased, the spectrum becomes broader in energy, in agreement with previous observations by Gaudet *et al.* [45]. This is not a thermal population effect but the result of the CEFs acquiring finite lifetimes due to interactions with other excitations, notably phonons. With the exception of the A site Yb^{3+} CEF excitations, the normalized intensity of the inelastic features in the spectrum is stronger for the $x = 0.19$ sample than for the $x = 0.12$ sample, as expected, reflecting the higher level of stuffing.

Crystal field refinement

In order to analyze the neutron scattering data and fit the CEF excitations, we developed a calculation based on the point-charge model [59] using Stevens's formalism [60]. The former neglects the overlap between the orbitals and any relativistic corrections, while the latter is a mathematical tool to write an expansion of the Coulomb potential of the crystal based on the symmetries of the environment that surrounds

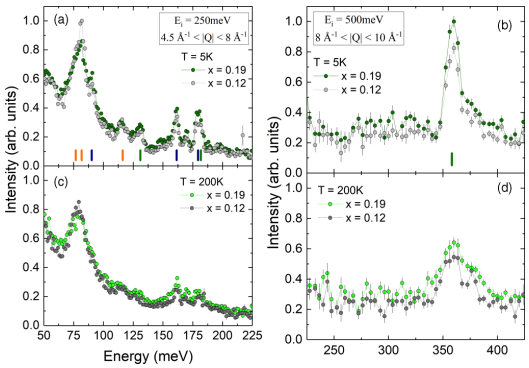

FIG. 5. Comparison of the normalized intensities of the inelastic neutron spectrum at $T = 5$ K (top panels) and $T = 200$ K (bottom panels) for incident energies $E_i = 250$ meV and $E_i = 500$ meV. The inelastic peak at ∼358 meV arises due to Yb^{3+} at B sites. The calculated energy eigenvalues associated with all three of the A, A', and B Yb^{3+} sites are shown as the fiducial lines at the bottom of (a) and (b). The color scheme used for the fiducial lines is the same as in Fig. 4, and we see that the CEF model describes the inelastic spectra below 400 meV very well.

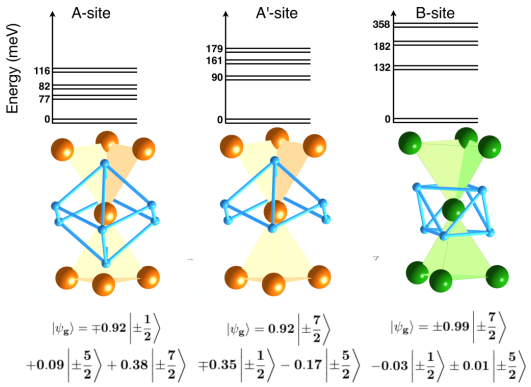

FIG. 6. Left: At the stoichiometric A sites, the ligands are located on the vertex of a scalenohedron, a cube distorted along the diagonal. The blue spheres represent the six O(2) ions and two O(1) ions around the A site Yb^{3+}. The O(1) sites are located along the axis connecting the centers of two tetrahedra. Middle: The A' sites correspond to A sites with one O(1) vacancy that breaks the symmetry of the scalenohedron. Right: At the B sites, the environment is a trigonal antiprism made of six O(2) ions; green spheres represent the position of Ti^{4+} ions or the position of the stuffed Yb^{3+} ions. The top panels show the corresponding energy eigenvalues associated with each environment. Note that the energy scale is approximate and serves only to guide the eye for comparison of the CEF excitation energies. The bottom panels give the three largest contributions to the ground-state energy eigenfunctions associated with each environment.

the magnetic ion. In our samples, the magnetic rare-earth ion is assumed to be sitting in three different environments: stoichiometric A sites, oxygen deficient A' sites, and B sites (see Fig. 6). Notice that we have rotated the reference system in order to align the local $\langle 111\rangle$ direction along $\hat{z}$.

In general the Coulomb potential of the crystal can be expressed using a linear combination of tesseral harmonics as follows:

$$V(x,y,z) = \frac{q_j}{4\pi\epsilon_0}\sum_{n=0}^{\infty}\frac{r^n}{R_j^{(n+1)}}\left\{\sum_m \frac{4\pi}{(2n+1)} \times Z_{nm}(x_j,y_j,z_j)Z_{nm}(x,y,z)\right\}. \quad (1)$$

Here q_j is the charge of the ligand, R_j is the position of the ligand, and $Z_{nm}(x_j,y_j,z_j)$ is the tesseral harmonic [59]. If we center our reference system on the magnetic ion, we can rewrite the previous equation in the following way:

$$V(x,y,z) = \frac{1}{4\pi\epsilon_0}\sum_n^{\infty}\sum_m r^n \gamma_{nm} Z_{nm}(x,y,z), \quad (2)$$

where, for k ligands,

$$\gamma_{nm} = \sum_{j=1}^{k}\frac{q_j}{R_j^{(n+1)}}\frac{4\pi}{2n+1}Z_{nm}(x_j,y_j,z_j). \quad (3)$$

Equation (3) gives the coefficients of the linear combination of the tesseral harmonics. For every point group, only a few terms in the expansion are nonzero (see, e.g., Ref. [61]), and these terms coincide with the number of Stevens operators we use in our Hamiltonian.

The point group of both the scalenohedron at the A site and the trigonal antiprism at the B site is D_{3d}, and thus, following Prather's convention [62], only the terms $Z_{20}, Z_{40}, Z_{43}, Z_{60}, Z_{63}$, and Z_{66} survive in our expansion. This convention states that the highest rotational C_3 axis of the system must be rotated along $\hat{z}$ and one of the C_2 axis must be rotated along $\hat{y}$, ensuring in this way that we have the minimum number of terms in the Coulomb expansion.

Finally, we can use the so-called Stevens operators equivalence method to evaluate the matrix elements of the crystalline potential between coupled wave functions specified by one particular value of the total angular momentum J. This method states that, if $f(x,y,z)$ is a Cartesian function of given degree, then to find the operator equivalent to such a term one replaces x, y, z with J_x, J_y, J_z, respectively, keeping in mind the commutation rules between these operators. This is done by replacing products of x, y, z by the appropriate combinations of J_x, J_y, J_z, divided by the total number of combinations. Note that, although it is conventional to use J or L in the equivalent-operator method, all factors of $\hbar$ are dropped when evaluating the matrix elements.

As we are studying the ground state of a rare-earth system, without an external magnetic field applied, S^2, L^2, J^2, and J_z are good quantum numbers. Thus, the CEF Hamiltonian can now be written as

$$H_{\mathrm{CEF}} = \mathrm{const}\sum_{nm}\left[\frac{e^2}{4\pi\epsilon_0}\gamma_{nm}\langle r^n\rangle\theta_n\right]O_n^m = \sum_{nm}\underbrace{\left[A_n^m\langle r^n\rangle\theta_n\right]}_{B_{nm}}O_n^m = \sum_{nm}B_{nm}O_n^m, \quad (4)$$

where γ_{nm} is the same coefficient as in Eq. (3), e is the electron charge, ϵ_0 is the vacuum permittivity, $\langle r^n\rangle$ is the expectation value of the radial part of the wave function, θ_n is a numerical factor that depends on the rare-earth ion [59], const is a constant to normalize the tesseral harmonics, and O_n^m are the Stevens operators.

The terms $A_n^m\langle r^n\rangle\theta_n$ are commonly called crystal field parameters, and they coincide with the parameters we fit in our calculation. A general form of the Hamiltonian for our system is therefore

$$H_{\mathrm{CEF}} = B_{20}O_2^0 + B_{40}O_4^0 + B_{43}O_4^3 + B_{60}O_6^0 + B_{63}O_6^3 + B_{66}O_6^6. \quad (5)$$

These equations are nonlinear, so we cannot write a closed system to solve the problem and identify a unique solution. We thus decided to use our Hamiltonian as a function of the six CEF parameters and to simultaneously fit these to experimental quantities of interest: the energy of the CEF excitations and the relative intensities of the transitions between the CEF levels. The resulting refined CEF parameters are then used to calculate the inelastic neutron spectrum for a direct comparison with the data set. Table III shows the best CEF parameters which were found minimize χ^2 in the fitting procedure along with

TABLE III. Refinement of the CEF parameters and energy eigenvalues at each of the three Yb^{3+} sites from fits to the inelastic spectra data set at the three sites and relative energy levels. All energy eigenvalues are doublets (d), as required by Kramers's theorem.

A Site	*A′* Site	*B* Site
Crystal field parameters (meV)		
$B_2^0 = 1.1$	$B_2^0 = -3.9860$	$B_2^0 = -4.8744$
$B_4^0 = -0.0591$	$B_4^0 = -0.002186$	$B_4^0 = -0.1407$
$B_4^3 = 0.3258$	$B_4^3 = 1.0655$	$B_4^3 = 1.47542$
$B_6^0 = 0.00109$	$B_6^0 = 0.001533$	$B_6^0 = -0.004862$
$B_6^3 = 0.0407$	$B_6^3 = 0.049192$	$B_6^3 = -0.1117$
$B_6^6 = 0.00727$	$B_6^6 = 0.01666$	$B_6^6 = 0$
Calculated spectrum (meV)		
0.0(*d*)	0.0(*d*)	0.0(*d*)
76.72(*d*)	90.17(*d*)	130.98(*d*)
81.76(*d*)	161.38(*d*)	181.79(*d*)
116.15(*d*)	179.36(*d*)	358.14(*d*)

the energy eigenvalues corresponding to the CEF excitations of Yb^{3+} ions out of the ground state at the *A*, *A′*, and *B* sites.

V. RESULTS AND DISCUSSION

The CEFs originate primarily from the "cage" of O^{2-} ions surrounding the cations, lifting the $(2J+1)$-fold degeneracy of the $J = 7/2$ ground-state manifold appropriate for Yb^{3+}. The case for Yb^{3+} is relatively straightforward as its odd number (13) of $4f$ electrons means that it satisfies Kramers's theorem, and all the CEF states are at least doubly degenerate, so with $J = 7/2$ there can be at most three CEF transitions from the ground state.

We considered the three local Yb^{3+} environments shown in Fig. 6. These are Yb^{3+} in an *A*-site environment with a full complement of eight neighboring O^{2-} ions, Yb^{3+} in an *A*-site environment with one O^{2-} vacancy (referred to as an *A′* site), and a Yb^{3+} ion in a *B*-site environment with a full complement of six neighboring O^{2-} ions. The *A* site O^{2-} environment consists of a cube distorted along the local [111] directions. Six O(2) ions are located on a plane perpendicular to this direction and a threefold rotation axis. Two additional O(1) ions are located along the local [111] axis. In other titanate pyrochlores, the O(1) sites are known to have a higher probability of hosting vacancies than the O(2) sites [53], a result which we confirmed here for $Yb_{2+x}Ti_{2-x}O_{7-y}$ using powder neutron diffraction. By contrast, the environment at the *B* site is a trigonal antiprism made of six O(2) oxygen ions. Additional local Yb^{3+} environments, such as an *A* site Yb^{3+} with an O(2) vacancy or with two vacancies, were assumed to be unlikely at the stuffing levels considered here.

The unpolarized neutron partial differential magnetic cross section can be written within the dipole approximation as [63]

$$\frac{d^2\sigma}{d\Omega dE'} = C\frac{k_f}{k_i}F(|Q|)S(|Q|,\omega), \quad (6)$$

where Ω is the scattered solid angle, $\frac{k_f}{k_i}$ is the ratio of the scattered and incident momentum of the neutron, C is a constant, and $F(|Q|)$ is the magnetic form factor of the magnetic

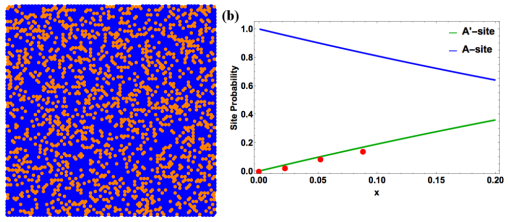

FIG. 7. Preponderance of *A* and *A′* sites within the pyrochlore lattice as a function of stuffing: (a) Projection of the $64 \times 64 \times 64$ supercell used in the Monte Carlo simulation. The orange dots represent oxygen ions removed from the calculation. (b) Histogram showing the distribution of *A* (blue line) and *A′* sites (green line) in the lattice as a function of the stuffing. The red points represents the experimental intensities of the 90 meV CEF level extrapolated using the pure compound as background. This agreement confirms that this 90 meV CEF transition originates from an *A′* site.

Yb^{3+} ion. The scattering function $S(|Q|,\hbar\omega)$ gives the relative scattered intensity due to transitions between different CEF levels. At constant temperature and wave vector $|Q|$, we have

$$S(|Q|,\hbar\omega) = \sum_{i,i'} \frac{\left(\sum_\alpha |\langle i|J_\alpha|i'\rangle|^2\right)e^{-\beta E_i}}{\sum_j e^{-\beta E_j}} F(\Delta E + \hbar\omega), \quad (7)$$

where $\alpha = x,y,z$ and $F(\Delta E + \hbar\omega) = F(E_i - E_{i'} + \hbar\omega)$ is a Lorentzian function which ensures energy conservation as the neutron induces transitions between the CEF levels $i \rightarrow i'$ that possess a finite-energy width or inverse lifetime.

Figure 3 shows a comparison of the data from the four powder $Yb_{2+x}Ti_{2-x}O_{7-y}$ samples at relatively low energies, using incident neutrons with $E_i = 150$ meV. The intensity scale has been normalized to sample mass. The stoichiometric, $x = 0$, and lightly stuffed, $x = 0.05$, samples show only the three *A* site CEF transitions at ∼76, 81, and 116 meV, as previously reported [45]. We clearly observe the growth of a new CEF at ∼91 meV, which we will attribute to *A′*-site Yb^{3+}, as a function of increasing stuffing x. This is quantitatively borne out by a Monte Carlo simulation which shows that its normalized intensity scales in proportion to x. Assuming that oxygen atoms are removed at random, we performed a simple Monte Carlo simulation to calculate the relative preponderance of *A* to *A′* sites in the lattice as a function of the stuffing level x. Assuming that each *A* and *A′* site contributes independently to the intensity of the spectrum, we can argue that the intensity of the transition at 91 meV should be proportional to this ratio.

For this calculation we created a supercell consisting of $64 \times 64 \times 64$ unit cells filled with random vacancies located only at the O(1) position. Due to the symmetry of the pyrochlore lattice each Yb^{3+} ion at an *A* site has only two O(1) ions as the first-nearest neighbor; thus, we calculated how many ions have no vacancies and how many have a single vacancy. The calculation was repeated for 10 000 realizations of disorder. Figure 7 shows the results of this analysis, with the conclusion that the transition at 91 meV originates from *A′* sites, and its intensity is directly proportional to the number of vacancies in the system.

The CEF spectrum at energies above 100 meV is shown in Fig. 4 for the highly stuffed ($x = 0.12$ and 0.19) samples, as measured with $E_i = 500$ meV neutrons. One observes clear excitations above the 116 meV CEF excitation associated with the stoichiometric A site's most energetic CEF level. Of particular note is the well-isolated CEF excitation at 358 meV which we associate with Yb^{3+} at the B site, whose intensity scales between the two highly stuffed samples, $x = 0.12$ and 0.19, in proportion to x. The stoichiometric ($x = 0$) and lightly stuffed ($x = 0.05$) samples were measured at high energies with $E_i = 700$ meV neutrons, and the 358 meV CEF excitation is not visible for either.

The energies and relative intensities of all the CEF excitations measured below ∼400 meV were fit as described above, assuming the CEF parameters previously established for the stoichiometric sample ($x = 0$) [45]. The new CEF parameters and energies for the A' site and B site are tabulated along with those for the A site Yb^{3+} in Table III. The results for both the CEF intensities and the CEF energy eigenvalues are shown as the solid lines in Fig. 4 for the highly stuffed ($x = 0.12$ and $x = 0.19$) samples at base temperature, $T = 5$ K. Figure 5 shows higher-energy-resolution, inelastic neutron scattering below 225 meV energy transfer, obtained with $E_i = 250$ meV, as well as the same $E_i = 500$ meV data for the highly stuffed samples ($x = 0.12$ and $x = 0.19$) at $T = 5$ K [Figs 5(a) and 5(b)] and at $T = 200$ K [Figs. 5(c) and 5(d)]. For reference, the energies associated with the nine CEF transitions from the A, A', and B sites, as calculated in our fit, are shown as fiducial lines in Figs. 5(a) and 5(b). One can see that virtually all inelastic features in the range from 75 to 400 meV can be identified using this model, and these excitations decrease in intensity and broaden somewhat in energy on warming to $T = 200$ K, shown in Figs. 5(c) and 5(d), as expected for CEF excitations. The description of all CEF levels below ∼400 meV is therefore very good, and the resulting CEF energy eigenvalues are shown for the A-, A'-, and B-site Yb^{3+} in the top panel of Fig. 6. The bandwidth of the CEF excitations is much larger for Yb^{3+} in the defective environments, with the defective B site environment giving the largest bandwidth, consistent with this Yb^{3+} ion experiencing the largest electric fields and their gradients.

The determination of the CEF parameters allows a determination of the g-tensor characterizing the anisotropy, as well as the moment size associated with the ground-state doublet of Yb^{3+} at the A, A', and B sites. The resulting eigenfunctions within the Yb^{3+} ground-state doublets are shown in the bottom panel of Fig. 6. The corresponding anisotropic g-tensor values are $g_\perp = 3.69 \pm 0.15$, $g_z = 1.92 \pm 0.20$ for Yb^{3+} at the A site; $g_\perp = 1.5 \pm 0.2$, $g_z = 6.8 \pm 0.7$ for Yb^{3+} at the A' site; and $g\perp = 0.07 \pm 0.03$, $g_z = 8.0 \pm 0.8$ for Yb^{3+} at the B site. The A-site Yb^{3+} moment was previously known to display XY anisotropy [45]. These results show both the A'-site and B-site Yb^{3+} moments to possess Ising-like anisotropies, with the B-site Yb^{3+} Ising anisotropy being stronger than that associated with the A' site. Such a change in anisotropy between the A site and the defective B and A' Yb^{3+} sites was predicted on the basis of point-charge calculations [45] but has now been directly verified with these measurements. The ground-state moments associated with the A, A', and B sites are found to be $\mu = 2.07\mu_B$, $\mu = 3.5\mu_B$, and $\mu = 4.0\mu_B$, respectively [45]. While dipolar interactions are expected to be relatively weak in $Yb_2Ti_2O_7$ due to the low moment size, they scale as the square of the moment, and thus, larger defective moments would tend to produce a strong, random perturbation on the dipole sum.

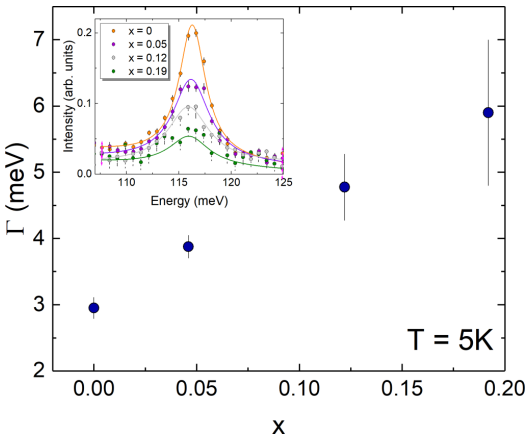

FIG. 8. The systematic broadening of the CEF intrinsic energy width which is observed with increased stuffing x in $Yb_{2+x}Ti_{2-x}O_{7-y}$, as obtained from the Lorentzian line-shape analysis discussed in the text. The inset shows the inelastic neutron scattering near the ∼116 meV CEF transition and the resulting fits performed with a Lorentzian line shape.

It is also clear that the A-site CEF transitions develop significant energy broadening with increasing stuffing. This can be broadly appreciated in Fig. 3 and is examined quantitatively in Fig. 8, where attention is focused on the ∼116 meV A-site Yb^{3+} CEF transition, which is well separated in energy from any other transition for all powder samples. The energy width of the CEF excitations can be examined by fitting the data, shown in the inset of Fig. 8, utilizing a damped harmonic oscillator (DHO) line shape for the 116 meV CEF transitions. At the energy transfers and temperatures of interest, the DHO can be approximated by a single Lorentzian, the form of which is given by

$$L(E) = \frac{1}{\pi} \frac{\frac{\Gamma_{\text{obs}}}{2}}{(E - \Delta E)^2 + (\frac{\Gamma_{\text{obs}}}{2})^2}. \quad (8)$$

This is a Lorentzian function of energy with width Γ_{obs} centered on the energy of the CEF transition. This form convolutes both the intrinsic energy width and that arising from the instrumental resolution, which are assumed to add in quadrature. The intrinsic energy width or inverse lifetime of the 116 meV CEF excitation for each of the four powder samples was extracted from this analysis and is plotted as a function of stuffing x in Fig. 8.

Figure 8 clearly shows the CEF excitations at low temperatures in the crushed single-crystal samples display much larger energy widths than that of the stoichiometric sample. The trend for low-temperature CEF inverse lifetimes to systematically increase with stuffing, previously reported for the stoichiometric ($x = 0$) and lightly stuffed ($x = 0.05$) samples [45], is seen to extend to the largest stuffing level studied, $x = 0.19$.

VI. CONCLUSION

In conclusion, time-of-flight neutron spectroscopy allows the possibility of detecting and distinguishing CEF excitations in complex real materials with relatively low levels of defective environments, and we have demonstrated this for the quantum spin ice candidate pyrochlore magnet $Yb_{2+x}Ti_{2-x}O_{7-y}$. Such detailed information is particularly important for the case of $Yb_2Ti_2O_7$, as its ground state displays unusually strong sensitivity to stoichiometry. Our results specifically show Yb^{3+} moments in stuffed and oxygen-deficient environments display Ising anisotropy, rather than the XY local anisotropy displayed by the stoichiometric moments. Such defective Yb^{3+} moments are also considerably larger than their stoichiometric counterparts, and these, at a minimum, would tend to randomize dipolar interactions. Both of these manifestations of stuffing can be important for ground-state selection in real samples of $Yb_{2+x}Ti_{2-x}O_{7-y}$ and may underlie the ground state's extreme sensitivity to stoichiometry in this family of quantum magnets.

Note added. Recently, we became aware of two papers that discuss the role of stuffing in iridate pyrochlores [64], and atomic and electronic structure in stuffed $Yb_2Ti_2O_7$ [65].

ACKNOWLEDGMENTS

Research conducted at McMaster University was supported by the Natural Sciences and Engineering Research Council of Canada (NSERC). We acknowledge useful discussions with A. Aczel, C. Balz, L. Balents, G. Ehlers, M. D. Lumsden, S. E. Nagler, and K. A. Ross. We are very grateful for the instrument and sample environment support provided during our inelastic neutron scattering measurements. The experiments which were performed at the Spallation Neutron Source at Oak Ridge National Laboratory were sponsored by the US Department of Energy, Office of the Basic Energy Sciences, Scientific User Facilities Division.

[1] C. Lacroix, P. Mendels, and F. Mila, *Introduction to Frustrated Magnetism* (Springer, Berlin, 2011).
[2] J. S. Gardner, M. J. P. Gingras, and J. E. Greedan, Rev. Mod. Phys. **82**, 53 (2010).
[3] M. J. Harris, S. T. Bramwell, D. F. McMorrow, T. Zeiske, and K. W. Godfrey, Phys. Rev. Lett. **79**, 2554 (1997).
[4] A. P. Ramirez, A. Hayashi, R. J. Cava, R. Siddharthan, and B. S. Shastry, Nature (London) **399**, 333 (1999).
[5] B. C. den Hertog and M. J. P. Gingras, Phys. Rev. Lett. **84**, 3430 (2000).
[6] S. T. Bramwell and M. J. P. Gingras, Science **294**, 1495 (2001).
[7] C. Castelnovo, R. Moessner, and S. L. Sondhi, Nature (London) **451**, 42 (2008).
[8] L. Clark, G. J. Nilsen, E. Kermarrec, G. Ehlers, K. S. Knight, A. Harrison, J. P. Attfield, and B. D. Gaulin, Phys. Rev. Lett. **113**, 117201 (2014).
[9] S. Petit, E. Lhotel, B. Canals, M. Ciomaga Hatnean, J. Ollivier, H. Mutka, E. Ressouche, A. R. Wildes, M. R. Lees, and G. Balakrishnan, Nat. Phys. **12**, 746 (2016).
[10] K. A. Ross, L. Savary, B. D. Gaulin, and L. Balents, Phys. Rev. X **1**, 021002 (2011).
[11] N. R. Hayre, K. A. Ross, R. Applegate, T. Lin, R. R. P. Singh, B. D. Gaulin, and M. J. P. Gingras, Phys. Rev. B **87**, 184423 (2013).
[12] J. D. Thompson, P. A. McClarty, H. M. Rønnow, L. P. Regnault, A. Sorge, and M. J. P. Gingras, Phys. Rev. Lett. **106**, 187202 (2011).
[13] R. Applegate, N. R. Hayre, R. R. P. Singh, T. Lin, A. G. R. Day, and M. J. P. Gingras, Phys. Rev. Lett. **109**, 097205 (2012).
[14] O. Benton, O. Sikora, and N. Shannon, Phys. Rev. B **86**, 075154 (2012).
[15] L. Savary and L. Balents, Phys. Rev. Lett. **108**, 037202 (2012).
[16] R. M. D'Ortenzio, H. A. Dabkowska, S. R. Dunsiger, B. D. Gaulin, M. J. P. Gingras, T. Goko, J. B. Kycia, L. Liu, T. Medina, T. J. Munsie, D. Pomaranski, K. A. Ross, Y. J. Uemura, T. J. Williams, and G. M. Luke, Phys. Rev. B **88**, 134428 (2013).
[17] J. D. Thompson, P. A. McClarty, and M. J. P. Gingras, J. Phys.: Condens. Matter **23**, 164219 (2011).
[18] L. Savary and L. Balents, Phys. Rev. B **87**, 205130 (2013).
[19] K. Kimura, S. Nakatsuji, J.-J. Wen, C. Broholm, M. B. Stone, E. Nishibori, and H. Sawa, Nat. Commun. **4**, 1934 (2013).
[20] M. J. P. Gingras and P. A. McClarty, Rep. Prog. Phys. **77**, 056501 (2014).
[21] L. D. Pan, S. W. Kim, A. Ghosh, C. M. Morris, K. A. Ross, E. Kermarrec, B. D. Gaulin, S. M. Koohpayeh, O. Tchernyshyov, and N. P. Armitage, Nat. Commun. **5**, 4970 (2014).
[22] L. D. Pan, N. J. Laurita, K. A. Ross, B. D. Gaulin, and N. P. Armitage, Nat. Phys. **12**, 361 (2016).
[23] N. Hamachi, Y. Yasui, K. Araki, S. Kittaka, and T. Sakakibara, AIP Adv. **6**, 055707 (2016).
[24] H. Blöte, R. Wielinga, and W. Huiskamp, Physica **43**, 549 (1969).
[25] P. Dalmas de Réotier, V. Glazkov, C. Marina, A. Yaouanc, P. C. M. Gubbens, S. Sakarya, P. Bonville, A. Amato, C. Baines, and P. J. C. King, Phys. B (Amsterdam, Neth.) **374-375**, 145 (2006).
[26] A. Yaouanc, P. Dalmas de Réotier, C. Marin, and V. Glazkov, Phys. Rev. B **84**, 172408 (2011).
[27] K. A. Ross, Th. Proffen, H. A. Dabkowska, J. A. Quilliam, L. R. Yaraskavitch, J. B. Kycia, and B. D. Gaulin, Phys. Rev. B **86**, 174424 (2012).
[28] A. M. Hallas, J. Gaudet, and B. D. Gaulin, Annu. Rev. Condens. Matter Phys. **9**, 105 (2018).
[29] Y. Yasui, M. Soda, S. Iikubo, M. Ito, M. Sato, N. Hamaguchi, T. Matsushita, N. Wada, T. Takeuchi, N. Aso, and K. Kakurai, J. Phys. Soc. Jpn. **72**, 3014 (2003).
[30] L.-J. Chang, S. Onoda, Y. Su, Y. J. Kao, K. D. Tsuei, Y. Yasui, K. Kakurai, and M. R. Lees, Nat. Commun. **3**, 992 (2012).
[31] J. Gaudet, K. A. Ross, E. Kermarrec, N. P. Butch, G. Ehlers, H. A. Dabkowska, and B. D. Gaulin, Phys. Rev. B **93**, 064406 (2016).
[32] A. Scheie, J. Kindervater, S. Säubert, C. Duvinage, C. Pfleiderer, H. J. Changlani, S. Zhang, L. Harriger, K. Arpino, S. M. Koohpayeh, O. Tchernyshyov, and C. Broholm, Phys. Rev. Lett. **119**, 127201 (2017).
[33] K. A. Ross, J. P. C. Ruff, C. P. Adams, J. S. Gardner, H. A. Dabkowska, Y. Qiu, J. R. D. Copley, and B. D. Gaulin, Phys. Rev. Lett. **103**, 227202 (2009).

[34] K. A. Ross, L. R. Yaraskavitch, M. Laver, J. S. Gardner, J. A. Quilliam, S. Meng, J. B. Kycia, D. K. Singh, Th. Proffen, H. A. Dabkowska, and B. D. Gaulin, Phys. Rev. B **84**, 174442 (2011).

[35] J. A. Hodges, P. Bonville, A. Forget, A. Yaouanc, P. Dalmas de Réotier, G. André, M. Rams, K. Królas, C. Ritter, P. C. M. Gubbens, C. T. Kaiser, P. J. C. King, and C. Baines, Phys. Rev. Lett. **88**, 077204 (2002).

[36] A. Yaouanc, P. Dalmas de Réotier, P. Bonville, J. A. Hodges, P. C. M. Gubbens, C. T. Kaiser, and S. Sakarya, Phys. B (Amsterdam, Neth.) **326**, 456 (2003).

[37] J. S. Gardner, G. Ehlers, N. Rosov, R. W. Erwin, and C. Petrovic, Phys. Rev. B **70**, 180404 (2004).

[38] S. Bhattacharjee, S. Erfanifam, E. L. Green, M. Naumann, Z. Wang, S. Granovsky, M. Doerr, J. Wosnitza, A. A. Zvyagin, R. Moessner, A. Maljuk, S. Wurmehl, B. Büchner, and S. Zherlitsyn, Phys. Rev. B **93**, 144412 (2016).

[39] P. Bonville, J. A. Hodges, E. Bertin, J. P. Bouchaud, P. Dalmas de Réotier, L. P. Regnault, H. M. Rønnow, J. P. Sanchez, S. Sosin, and A. Yaouanc, Hyperfine Interact. **156**, 103 (2004).

[40] K. E. Arpino, B. A. Trump, A. O. Scheie, T. M. McQueen, and S. M. Koohpayeh, Phys. Rev. B **95**, 094407 (2017).

[41] A. Mostaed, G. Balakrishnan, M. R. Lees, Y. Yasui, L.-J. Chang, and R. Beanland, Phys. Rev. B **95**, 094431 (2017).

[42] J. D. Thompson, P. A. McClarty, D. Prabhakaran, I. Cabrera, T. Guidi, and R. Coldea, Phys. Rev. Lett. **119**, 057203 (2017).

[43] E. Lhotel, S. R. Giblin, M. R. Lees, G. Balakrishnan, L. J. Chang, and Y. Yasui, Phys. Rev. B **89**, 224419 (2014).

[44] E. Kermarrec, J. Gaudet, K. Fritsch, R. Khasanov, Z. Guguchia, C. Ritter, K. A. Ross, H. A. Dabkowska, and B. D. Gaulin, Nat. Commun. **8**, 14810 (2017).

[45] J. Gaudet, D. D. Maharaj, G. Sala, E. Kermarrec, K. A. Ross, H. A. Dabkowska, A. I. Kolesnikov, G. E. Granroth, and B. D. Gaulin, Phys. Rev. B **92**, 134420 (2015).

[46] S. Rosenkranz, A. P. Ramirez, A. Hayashi, R. J. Cava, R. Siddharthan, and B. S. Shastry, J. Appl. Phys. **87**, 5914 (2000).

[47] A. Bertin, Y. Chapuis, P. Dalmas de Réotier, and A. Yaouanc, J. Phys.: Condens. Matter **24**, 256003 (2012).

[48] J. Gaudet, A. M. Hallas, A. I. Kolesnikov, and B. D. Gaulin, Phys. Rev. B **97**, 024415 (2018).

[49] H. A. Dabkowska and A. B. Dabkowski, in *Springer Handbook of Crystal Growth*, edited by G. Dhanaraj, K. Byrappa, V. Prasad, and M. Dudley (Springer, Berlin, 2010), p. 367.

[50] A. Huq, J. P. Hodges, O. Gourdon, and L. Heroux, Z. Kristallogr. Proc. **1**, 127 (2011).

[51] V. Petricek, M. Dusek, and L. Palatinus, Z. Kristallogr. **229**, 345 (2014).

[52] J. Rodriguez-Carvajal, Phys. B (Amsterdam, Neth.) **192**, 55 (1993).

[53] G. Sala, M. J. Gutmann, D. Prabhakaran, D. Pomaranski, C. Mitchelitis, J. B. Kycia, D. G. Porter, C. Castelnovo, and J. P. Goff, Nat. Mater. **13**, 488 (2014).

[54] G. E. Granroth, A. I. Kolesnikov, T. E. Sherline, J. P. Clancy, K. A. Ross, J. P. Ruff, B. D. Gaulin, and S. E. Nagler, J. Phys. Conf. Ser. **251**, 12058 (2010).

[55] O. Arnold, J. C. Bilheux, J. M. Borreguero, A. Buts, S. I. Campbell, L. Chapon, M. Doucet, N. Draper, R. Ferraz Leal, M. A. Gigg, V. E. Lynch, A. Markvardsen, D. J. Mikkelson, R. L. Mikkelson, R. Miller, K. Palmen, P. Parker, G. Passos, T. G. Perring, P. F. Peterson, S. Ren, M. A. Reuter, A. T. Savici, J. W. Taylor, R. J. Taylor, R. Tolchenov, W. Zhou, and J. Zikovsky, Nucl. Instrum. Methods Phys. Res., Sect. A **764**, 156 (2014).

[56] R. T. Azuah, L. R. Kneller, Y. Qiu, P. L. W. Tregenna-Piggott, C. M. Brown, and J. R. D. Copley, and R. M. Dimeo, J. Res. Natl. Inst. Stand. Technol. **114**, 341 (2009).

[57] V. Peçanha-Antonio, E. Feng, Y. Su, V. Pomjakushin, F. Demmel, L.-J. Chang, R. J. Aldus, Y. Xiao, M. R. Lees, and T. Brückel, Phys. Rev. B **96**, 214415 (2017).

[58] M. Ruminy, M. N. Valdez, B. Wehinger, A. Bosak, D. T. Adroja, U. Stuhr, K. Iida, K. Kamazawa, E. Pomjakushina, D. Prabakharan, M. K. Haas, L. Bovo, D. Sheptyakov, A. Cervellino, R. J. Cava, M. Kenzelmann, N. A. Spaldin, and T. Fennell, Phys. Rev. B **93**, 214308 (2016).

[59] M. T. Hutchings, in *Solid State Physics*, edited by F. Seitz and D. Turnbull, Advances in Research and Applications Vol. 16 (Academic, New York, 1964), pp. 227–273.

[60] K. W. H. Stevens, Proc. Phys. Soc. A **65**, 209 (1952).

[61] U. Walter, J. Phys. Chem. Solids **45**, 401 (1984).

[62] J. L. Prather, *Atomic Energy Levels in Crystals*, NBS Monograph 19 (National Bureau of Standards, Washington, DC, 1961).

[63] G. L. Squires, *Introduction to the Theory of Thermal Neutron Scattering* (Cambridge University Press, Cambridge, 1978).

[64] P. Telang, K. Mishra, A. K. Sood, and S. Singh, Phys. Rev. B **97**, 235118 (2018).

[65] S. S. Ghosh and E. Manousakis, Phys. Rev. B **97**, 245117 (2018).

5

Spin gaps in the ordered states of La_2LiXO_6 (X = Ru, Os) and their relation to distortion of the cubic double perovskite structure in $4d^3$ and $5d^3$ magnets

> "Man muss noch Chaos in sich haben, um einen tanzenden Stern gebären zu können." — *Friedrich Nietzsche*

This chapter incorporates the article *"Spin gaps in the ordered states of La_2LiXO_6 (X = Ru, Os) and their relation to the distortion of the cubic double perovskite structure in $4d^3$ and $5d^3$ magnets"*, which has been published in Physical Review B. Reproduced from with permission, copyrighted by the American Physical Society 2020. The full reference is given below:

D. D. Maharaj, G. Sala, C. A. Marjerrison, M. B. Stone, J. E. Greedan, and B. D. Gaulin. Physical Review B 98, 104434 (2018).

The following chapter discloses our studies of the monoclinic $5d^3$ and $4d^3$ double perovskite systems, La_2LiOsO_6 and La_2LiRuO_6, which were investigated via time-of-flight inelastic neutron scattering techniques. This study is comparative in nature as it seeks to address the effect of lattice distortions on the magnetic ground state of d^3 double perovskites. To this end, our full analysis includes *spinW* calculations which were performed to model the spin excitation spectra of La_2LiOsO_6, La_2LiRuO_6, Ba_2YOsO_6, Ba_2YRuO_6 and Sr_2ScOsO_6. Notable trends in the physical properties and anisotropic spin Hamiltonians are highlighted in these d^3 magnets.

PHYSICAL REVIEW B **98**, 104434 (2018)

Spin gaps in the ordered states of La_2LiXO_6 (X= Ru, Os) and their relation to the distortion of the cubic double perovskite structure in $4d^3$ and $5d^3$ magnets

D. D. Maharaj,[1,*] G. Sala,[1,2] C. A. Marjerrison,[1] M. B. Stone,[2] J. E. Greedan,[3,4] and B. D. Gaulin[1,4,5]

[1]*Department of Physics and Astronomy, McMaster University, Hamilton, Ontario L8S 4M1, Canada*
[2]*Neutron Scattering Division, Oak Ridge National Laboratory, Oak Ridge, Tennessee 37831, USA*
[3]*Department of Chemistry and Chemical Biology, McMaster University, Ontario L8S 4M1, Canada*
[4]*Brockhouse Institute for Materials Research, McMaster University, Hamilton, Ontario L8S 4M1, Canada*
[5]*Canadian Institute for Advanced Research, 661 University Avenue, Toronto, Ontario M5G 1M1, Canada*

(Received 15 May 2018; revised manuscript received 11 August 2018; published 28 September 2018)

Time-of-flight inelastic neutron scattering measurements have been carried out on polycrystalline samples of the $4d^3$ and $5d^3$ double pervoskite antiferromagnets La_2LiRuO_6 and La_2LiOsO_6. These reveal the development of an inelastic spin gap in La_2LiRuO_6 and La_2LiOsO_6 of ∼1.8(8) and 6(1) meV, below their respective ordering temperatures T_N, ∼23.8 and 30 K. The bandwidths of the spin excitations are shown to be ∼5.7(9) and 12(1) meV, respectively, at low temperatures. Spin gaps are surprising in such magnets as the t_{2g} levels of Ru^{5+} or Os^{5+} are expected to be half-filled, resulting in an anticipated orbital singlet for both materials. We compare these results in monoclinic double perovskites La_2LiRuO_6 and La_2LiOsO_6 with those in cubic Ba_2YRuO_6 and Ba_2YOsO_6 as well as with those in other monoclinic La_2NaRuO_6, La_2NaOsO_6, and Sr_2ScOsO_6 and model the inelastic magnetic scattering with linear spin-wave theory using minimal anisotropic exchange interactions. We discuss the possible role of the distortion of the face-centered-cubic double perovskite structure on the spin gap formation and geometric frustration in these materials and show that T_N scales with the top of the spin-wave band in all members of these families that display long-range order.

DOI: 10.1103/PhysRevB.98.104434

I. INTRODUCTION

Double perovskite antiferromagnets display a diverse set of quantum magnetic ground states due to the confluence of geometrical frustration and strong spin-orbit coupling, two topical trends in contemporary condensed matter physics [1]. Their low temperature phase behavior has been the subject of much recent study—both experimental and theoretical in nature [2–15]. Double perovskites are characterized by a chemical formula of the form $A_2BB'O_6$, where the B and B' ions reside on octahedral sites and form two interpenetrating face-centered-cubic (fcc) lattices, provided that the overall structure is cubic. This is schematically shown in Fig. 1(a). If only one of the B or B' sites is magnetic, such a sublattice forms a single magnetic fcc lattice, and in this configuration the magnetic moments decorate a network of edge-sharing tetrahedra as seen in Fig. 1(b). This generates one of the canonical architectures supporting geometrical frustration in three dimensions [16].

These materials are such a rich platform for the study of quantum magnetism as the double perovskite structure is very flexible, and many magnetic and nonmagnetic ions can occupy the B and B' sublattices. The overall crystal symmetry can be lower than cubic [17], and, independently, the B and B' sublattices can mix at some low (∼5%) level. Monoclinic symmetries typically arise due to correlated rotations of BO_6 and $B'O_6$ octahedra as is shown in Fig. 1(c). Both B-B' site mixing and distortions to structures with symmetries lower than cubic are controlled by the charge and ionic size difference between B and B' ions within the $A_2BB'O_6$ structure [17]. In this regard, the study of families of double perovskite systems can enable systematic investigations of magnetic materials where the size of the moment, its quantum nature, as well as the role of spin-orbit coupling can be varied systematically within or among the many families of these materials. Strong spin-orbit coupling in $5d$ systems is already known to induce a Mott instability in $5d^5$ iridate compounds, leading to an effective total angular momentum $J_{\text{eff}} = \frac{1}{2}$ state, distinct from the $S = 1/2$ localized state of conventional Mott insulators [18] and is hence a route to novel quantum states of matter at low temperatures.

The $Ba_2YB'O_6$ family of double perovskites illustrates well the diversity of magnetic ground states that can be realized when the magnetic B' ion is occupied by different $4d$ or $5d$ transition metal ions. This family has been of particular recent interest as its structure remains cubic at low temperatures, enabling the realization of the perfect frustrated fcc magnetic sublattice. The family is also well ordered chemically with only low levels (∼1%) of B-B' site mixing observed [19–21]. Specific members of this family studied to date include Ba_2YMoO_6 ($4d^1$), which exhibits a gapped collective spin-singlet ground state at low temperatures [2], Ba_2YReO_6 ($4d^2$) which shows an anomalous spin-glass state below $T \sim 35$ K [6], and Ba_2YRuO_6 ($4d^3$) and Ba_2YOsO_6 ($5d^3$), which both form the same type-I antiferromagnetic (AF) structure below $T_N \sim 36$ and 69 K, respectively [3,4]. The structural and thermodynamic properties of Ba_2YIrO_6 ($5d^4$) have also been

*maharadd@mcmaster.ca

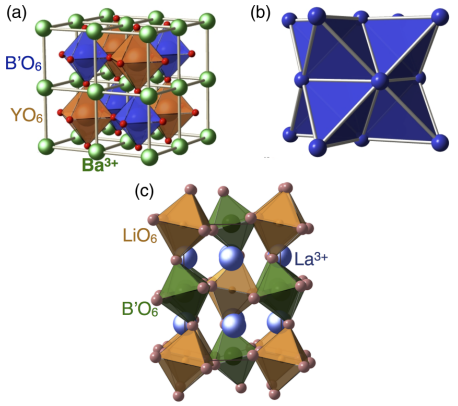

FIG. 1. The fcc double perovskite structure exhibited by Ba_2YXO_6 ($X = Ru, Os$) and the lower symmetry structure of La_2LiXO_6 are shown in panels (a) and (c), respectively. In each structure the nonmagnetic and magnetic B and B' ions coordinate with six oxygen atoms forming a lattice of interpenetrating octahedra. The Ba^{3+} and La^{3+} atoms are distributed within this network. Panel (b) shows the frustrated fcc network of edge-sharing tetrahedra of the B' site magnetic moments that are generated in the high symmetry Ba_2YXO_6 ($X = Ru, Os$) cubic structure.

studied and this system has been found to remain paramagnetic down to 0.4 K [11].

Here we consider the $4d^3$ and $5d^3$ double perovskites La_2LiRuO_6 and La_2LiOsO_6 with weak monoclinic distortions and compare these new inelastic neutron scattering (INS) results to those previously obtained on the cubic d^3 systems Ba_2YRuO_6 and Ba_2YOsO_6 as well as the monoclinic d^3 systems Sr_2ScOsO_6 and La_2NaRuO_6. The degree of distortion away from a cubic double perovskite structure can be parametrized by the average of the bond angle $\angle B\text{-}O\text{-}B'$ in monoclinic systems and subsequently compared to the cubic case where $\angle B\text{-}O\text{-}B' = 180^\circ$. This figure of merit indicates that the Sr_2ScXO_6 ($X = Ru, Os$) family is least distorted; with greater distortion in the La_2LiXO_6 family whereas the La_2NaXO_6 family is most distorted.

Like Ba_2YRuO_6 and Ba_2YOsO_6, La_2LiRuO_6 and La_2LiOsO_6 are expected to have the same half-filling of their t_{2g} levels and thus display the same orbital singlet. La_2LiRuO_6 and La_2LiOsO_6 are also expected to differ from each other primarily through the strength of the spin-orbit coupling displayed by $4d^3$ ions compared to $5d^3$ ions. Earlier INS measurements on cubic Ba_2YRuO_6 and Ba_2YOsO_6 revealed spin gaps within their ordered states of ∼5 and 17 meV, respectively [3,4] with the gap of the $5d^3$ system being ∼3 times larger than that in the $4d^3$ system [4]. The values of the free ion spin orbit coupling parameters λ for Ru^{5+} and Os^{5+}, as extrapolated from work done by Ma *et al.* [22], roughly scale in the same manner where $\lambda_{Os}/\lambda_{Ru} \sim 3.4$, making a compelling argument that spin-orbit coupling stabilizes the d^3 spin gaps.

We have carried out a series of INS measurements on La_2LiRuO_6 and La_2LiOsO_6 in polycrystalline form. The form of the inelastic magnetic scattering above and below their respective T_N's is seen to be qualitatively similar to that observed in Ba_2YRuO_6 and Ba_2YOsO_6 in that the spin gaps develop coincident with T_N and again scale roughly in proportion to expectations from atomic spin-orbit coupling factors. We can quantitatively account for the ground state spin excitation spectra using classical linear spin-wave theory and a minimal microscopic spin Hamiltonian involving near-neighbor anisotropic exchange. We see that we get a very good description of the spin excitation spectra from all four d^3 double perovskite materials, that is, for the new INS data from monoclinic La_2LiRuO_6 and La_2LiOsO_6 and from our earlier data on cubic Ba_2YRuO_6 and Ba_2YOsO_6. This then allows us to make systematic comparisons between the microscopic spin Hamiltonian parameters so estimated in these systems and to formulate an understanding of how the ordering temperatures T_N are related to each other and to their Hamiltonians.

II. EXPERIMENTAL DETAILS

Time-of-flight INS measurements were performed using the direct geometry chopper spectrometer SEQUOIA, BL-17, located at the Spallation Neutron Source of Oak Ridge National Laboratory [23]. Powder samples weighing 10 g of each of La_2LiRuO_6 and La_2LiOsO_6 were packed in aluminum foil and placed in identical aluminum annular cans ∼3 cm in diameter. The two sample cans as well as an empty sample can (used to obtain background measurements) were sealed in a glovebox containing a He atmosphere to improve thermalization of the samples at low temperatures. The three cans were loaded on a three-sample carousel mounted to a closed-cycle refrigerator which produced a base temperature of 7 K.

INS measurements were carried out on each sample using incident energies of $E_i = 40$ and 11 meV, which were both selected with chopper settings of $T_0 = 120$ and $FC_2 = 60$ Hz. The elastic energy resolution associated with these INS measurements is ∼2% of E_i, giving elastic energy resolutions of ∼0.8 and 0.22 meV for $E_i = 40$ and 11 meV, respectively. These measurements were performed at a variety of temperatures above and below the respective Néel temperatures of La_2LiOsO_6 ($T_N = 30$ K) and La_2LiRuO_6 ($T_N = 23.8$ K). The data sets were reduced using MANTID [24] and analyzed using the neutron scattering software DAVE [25].

III. NEUTRON SCATTERING RESULTS AND CALCULATIONS

A. Experimental results and analysis

Representative plots of the neutron scattering intensity as a function of energy transfer $\hbar\omega$ and wave vector transfer $|Q|$, appropriate for the powder samples of La_2LiRuO_6 and La_2LiOsO_6 are shown in Figs. 2 and 3, respectively, for several temperatures near and below T_N. Figure 2 shows data taken on La_2LiRuO_6 using $E_i = 11$ meV incident neutrons, whereas Fig. 3 shows data taken on La_2LiOsO_6 using $E_i = 40$ meV incident neutrons. In both cases an empty sample can data set has been subtracted as a background. For both materials it is clear that a spin gap begins to develop near T_N, where $T_N = 23.8$ K for La_2LiRuO_6 and $T_N = 30$ K for La_2LiOsO_6. The spin gaps are well developed by $\frac{2}{3} \times T_N$ and fully formed by our base temperature of $T = 7$ K. The intensity

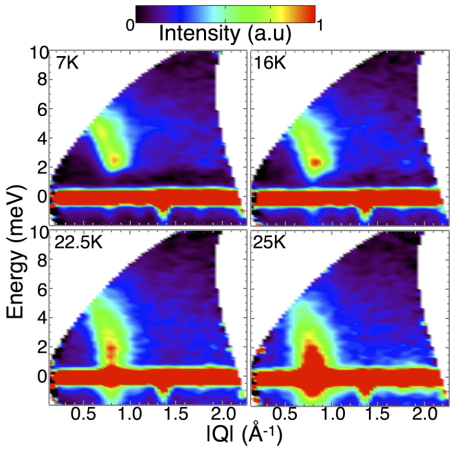

FIG. 2. Contour plots showing the INS intensity as a function of energy transfer $\hbar\omega$ and wave vector transfer $|Q|$ for La_2LiRuO_6 using $E_i = 11$ meV neutrons. Above $T_N = 23.8$ K there is an excess of quasielastic magnetic spectral weight centered near the (100) magnetic Bragg position at $|Q| = 0.8$ Å^{-1}. Below T_N, a spin gap develops and is fully formed by $T = 7$ K. An empty sample cell data set at $T = 7$ K has been subtracted from all displayed data sets.

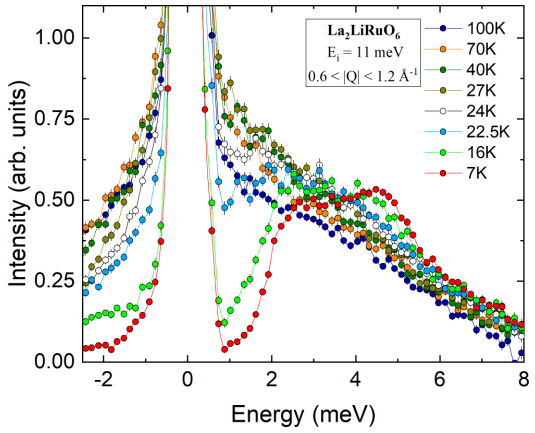

FIG. 4. $|Q|$-integrated [$|Q| = (0.6, 1.2)$ Å^{-1}] cuts of the INS data shown in Fig. 2, showing the 1.8 meV spin gap in La_2LiRuO_6. Above $T_N = 23.8$ K, quasielastic magnetic spectral weight is observed. At low temperatures, by $T = 7$ K, it is suppressed at energies low compared with the spin gap, and spectral weight shifts to higher energies where it is evident in a bimodal distribution of spin excitations with a total energy bandwidth of ∼5.7 meV.

scales for Figs. 2 and 3 are chosen to highlight the relatively weak inelastic scattering. The much stronger elastic scattering saturates the scale in both figures, but clear Bragg peaks are observed to develop below T_N at the 100 and 110 Bragg positions near 0.8 and 1.15 Å^{-1} as reported in a separate account of the magnetic elastic scattering and structure [5]. For convenience, we employ the pseudocubic reciprocal lattice vector notations here and in the remainder of the paper.

Detailed cuts through the two-dimensional data sets in the $\hbar\omega$-$|Q|$ maps of Figs. 2 and 3, are shown in Figs. 4 and 5 for La_2LiRuO_6 and La_2LiOsO_6, respectively. These cuts

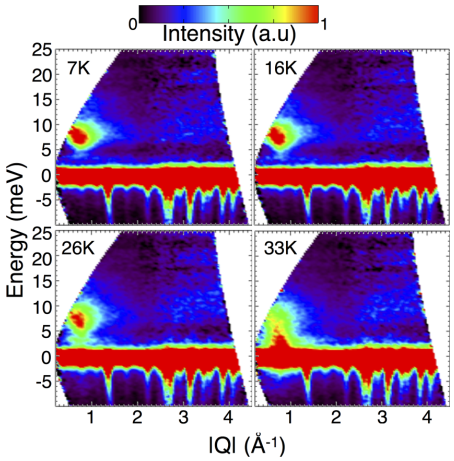

FIG. 3. Contour plots showing the INS intensity as a function of energy transfer $\hbar\omega$ and wave vector transfer $|Q|$ are shown above for La_2LiOsO_6 using the $E_i = 40$ meV neutron data set. Above $T_N = 30$ K there is an excess of quasielastic magnetic spectral weight centered near the magnetic (100) Bragg position $|Q| = 0.8$ Å^{-1}. Below T_N, a spin gap develops and is fully formed by $T = 7$ K. An empty sample cell data set at $T = 7$ K has been subtracted from all displayed data sets.

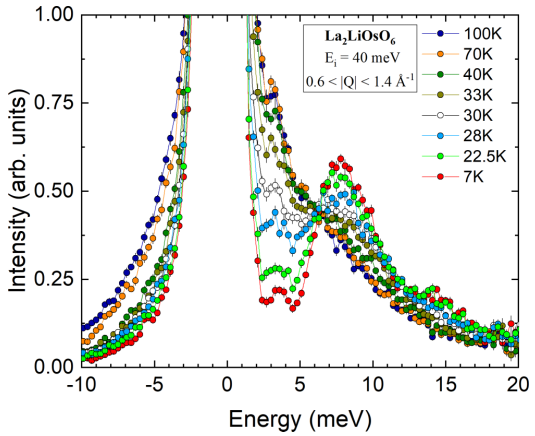

FIG. 5. $|Q|$-integrated [$|Q| = (0.6, 1.4)$ Å^{-1}] cuts showing the 6 meV spin gap in La_2LiOsO_6 at low temperatures. Above $T_N =$ 30 K, quasielastic magnetic spectral weight is observed. Again the low energy scattering is suppressed below the spin gap below T_N. At $T = 7$ K a well developed spin gap is evident with spectral weight transferred to energies above the gap. The total energy bandwidth of the spin excitations is ∼12 meV.

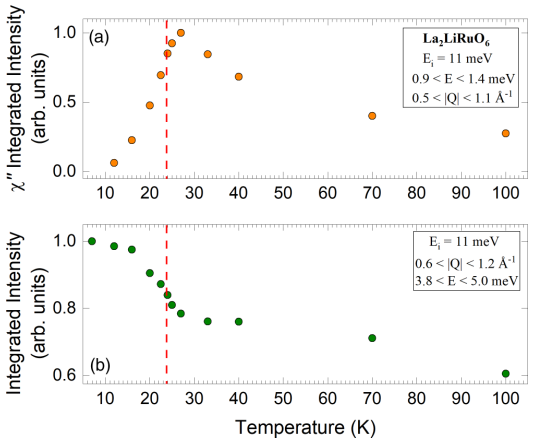

FIG. 6. The temperature dependence of χ'' for La_2LiRuO_6 is shown in panel (a) where the integration of the intensity was performed in the range of $|Q| = (0.5, 1.1)$ Å^{-1} and $E = (0.9, 1.4)$ meV $< \Delta$. Data taken at $T = 7$ K have been used as a background. This is derived from integrals of the data presented in Fig. 2. A complementary plot of the scattered intensity obtained from integrating $|Q| = (0.6, 1.2)$ Å^{-1} and $E = (3.8, 4.9)$ meV $> \Delta$ is shown in (b). T_N is shown as the vertical dashed line in both panels.

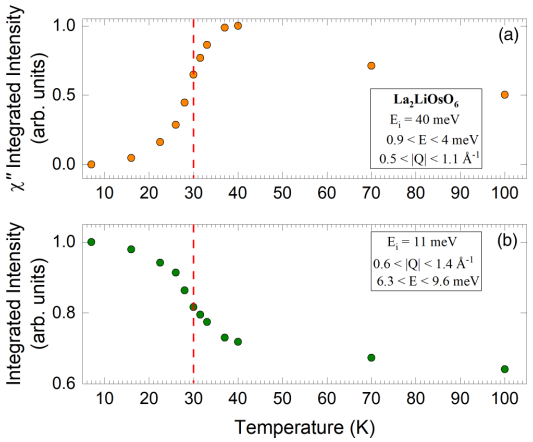

FIG. 7. The temperature dependence of χ'' for La_2LiOsO_6 is shown in (a) where the integration of the intensity was performed in the range of $|Q| = (0.5, 1.1)$ Å^{-1} and $E = (0.9, 4)$ meV $< \Delta$. Data taken at $T = 7$ K have been used as a background. This is derived from integrals of the data presented in Fig. 3. A complementary plot of the scattered intensity obtained by integrating $|Q| = (0.6, 1.4)$ Å^{-1} and $E = (6.3, 9.6)$ meV $> \Delta$ is shown in (b). T_N is shown as the vertical dashed line in both panels.

are taken by integrating around the 100 and 110 positions in $|Q|$; $0.6 < |Q| < 1.2$ Å^{-1} for La_2LiRuO_6 with $E_i = 11$ meV neutrons in Fig. 4 and $0.6 < |Q| < 1.4$ Å^{-1} for La_2LiOsO_6 with $E_i = 40$ meV neutrons in Fig. 5. At our base temperature of $T = 7$ K, we clearly identify a spin gap of 1.8(8) meV for La_2LiRuO_6 and 6(1) meV for La_2LiOsO_6. In both cases the spectral weight of the gapped magnetic scattering rises sharply from zero near the spin gap energy and extends out with an energy bandwidth of ∼5.9 meV for La_2LiRuO_6 and ∼12 meV for La_2LiOsO_6. The inelastic magnetic spectral weight in La_2LiRuO_6 appears to be bimodal with the higher energy peak just below ∼5 meV as can be seen in the low temperature data in Fig. 4. For La_2LiOsO_6 in Fig. 5, one observes an extended high energy tail to the magnetic spectral weight above the spin gap at low temperatures. This is similar phenomenology to that displayed by the cubic double perovskites Ba_2YRuO_6 and Ba_2YOsO_6 where their low temperature magnetic spectral weight above their larger spin gaps are a factor of 1.5–2 larger in bandwidth than those observed in La_2LiRuO_6 and La_2LiOsO_6.

Figures 4 and 5 show in detail how the spin gap collapses in La_2LiRuO_6 and La_2LiOsO_6 and how the magnetic spectral weight fills in at low energies as the temperature moves towards and beyond their respective ordering temperatures. This is shown more quantitatively in Figs. 6 and 7 where the temperature dependence of an integration of both the inelastic scattering $S(|Q|, \omega)$ for energies above the spin gap and the dynamic susceptibility χ'' for energies below the spin gap is shown as a function of temperature for La_2LiRuO_6 and La_2LiOsO_6.

χ'' is related to the measured INS intensity by

$$\Delta S(|Q|, \omega) = \frac{\chi''(|Q|, \hbar\omega)}{1 - e^{-\hbar\omega/k_BT}}. \quad (1)$$

Consideration of χ'' allows the temperature dependence from detailed balance, contained in the Bose factor $1 - e^{-\hbar\omega/k_BT}$ to be removed so that attention can focus on the physics of the system in question. However this analysis depends on a good understanding of the background. Assuming that there is no inelastic scattering at energies well below the spin gap at low temperatures, we can use a low temperature data set as the background $T = 7$ K and isolate χ'' as a function of temperature. The temperature dependence of this low energy χ'' is shown in Figs. 6(a) and 7(a) for La_2LiRuO_6 and La_2LiOsO_6, respectively. At energies above the spin gap, the inelastic magnetic scattering is never zero, and we look instead at the detailed temperature dependence of $S(|Q|, \omega)$ for La_2LiRuO_6 and La_2LiOsO_6 in Figs. 6(b) and 7(b), respectively.

Examination of Figs. 6 and 7 shows that T_N occurs at the inflection points of either the growth of χ'' below the spin gap or the fall of $S(|Q|, \omega)$ above the spin gap, indicating that the formation of the spin gap is central to the magnetic phase transitions. For both La_2LiRuO_6 and La_2LiOsO_6 materials χ'' peaks at temperatures of ∼10–20% above T_N and then slowly decreases as temperature increases towards their respective Curie-Weiss (CW) temperatures ~ -204 and -154 K, respectively.

The $|Q|$ dependence of χ'' at low energies within the spin gap is shown for La_2LiRuO_6 and La_2LiOsO_6 in Fig. 8. The energy integrations are performed over different ranges for La_2LiRuO_6 and La_2LiOsO_6 as the sizes of the spin gaps differ by a factor of ∼3.3. The La_2LiRuO_6 data employ an

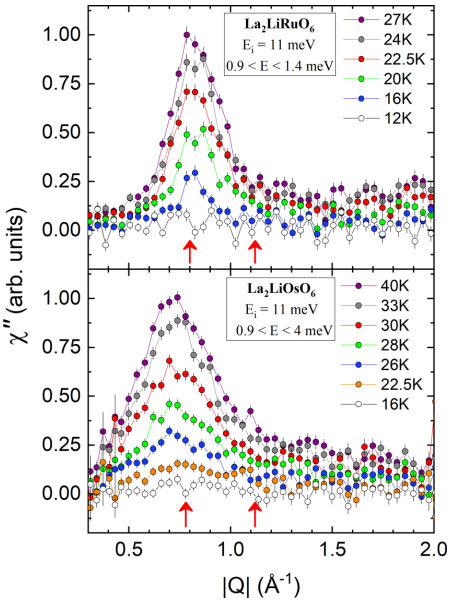

FIG. 8. (a) The temperature dependence of χ'' for La_2LiRuO_6 is shown where integrations were performed with $|Q| = (0.5, 1.1)$ Å^{-1} and $E = (0.9, 1.4)$ meV $< \Delta$. Data taken at $T = 7$ K have been used as a background. This shows the $|Q|$ dependence of χ'' ($|Q|$, $E < \Delta$) and how it evolves as a function of temperature for temperatures below and just above T_N. (b) The temperature dependence of low energy cuts of χ'' taken in the range of $E = (0.9, 4)$ meV for La_2LiOsO_6 are shown. This shows the $|Q|$ dependence of χ'' ($|Q|$, $E < \Delta$) and how it evolves as a function of temperature for temperatures below and just above T_N. In both panels, the red fiducial arrows indicate the positions of the (100) and (110) magnetic Bragg positions.

energy integration from 0.9 meV $< E <$ 1.4 meV and Fig. 8(a) shows this $|Q|$ dependence as a function of temperature for temperatures below and above $T_N = 23.8$ K. A very similar analysis is performed for La_2LiOsO_6 and the resulting $|Q|$ dependence of its low energy χ'' is shown in Fig. 8(b) for temperatures below and above its $T_N = 30$ K. In this case the energy is integrated over a larger range from 0.9 meV $< E <$ 4.0 meV.

The trends in the $|Q|$ dependence of low-energy χ'' as a function of temperature are similar for the two materials. The $|Q|$ values appropriate to the (100) and (110) ordering wave vectors are denoted with vertical red fiduciaries in both panels of Fig. 8. One can see that χ'' ($|Q|$, $\hbar\omega < \Delta$) is centered primarily on the (100) ordering wave vector, and this peak rises in intensity as the temperature approaches T_N. The $|Q|$ dependence of χ'' ($|Q|$, $\hbar\omega < \Delta$) for La_2LiOsO_6 is, however, clearly broader than that of La_2LiRuO_6. This is likely a reflection of the different (1/2 1/2 0) magnetic ordering wave vector that La_2LiOsO_6 displays, compared with the (100) type I AF ordering that La_2LiRuO_6 displays. The relative structure factor for the (110) magnetic Bragg intensity compared with the (100) magnetic Bragg intensity is stronger for the (1/2 1/2 0) structure displayed by La_2LiOsO_6 than for the (100) structure displayed by La_2LiRuO_6. A natural explanation for the increased breath in $|Q|$ for La_2LiOsO_6 is that the dynamic spectral weight is also relatively stronger at (110) and this extends the $|Q|$ dependence in χ'' from (100) to (110), therefore out to larger $|Q|$'s. As will be discussed below in the context of linear spin-wave theory applied to these systems, the observed magnetic scattering in both systems falls off anomalously quickly with $|Q|$, likely related to the covalency of the 4 and 5*d* electrons, which implies a magnetic form factor corresponding to more extended *d*-electron wave functions. This effect also tends to concentrate the inelastic scattering shown in Fig. 8 to smaller $|Q|$ than would otherwise be the case.

B. Linear spin-wave theory calculations

Linear spin-wave theory calculations were carried out in order to estimate the microscopic spin Hamiltonian for the double perovksite systems La_2LiRuO_6, La_2LiOsO_6, Ba_2YRuO_6, and Ba_2YOsO_6. The calculations were performed using the SPINW software package [26], and these were benchmarked against the ground state INS data for La_2LiRuO_6 at $T =$ 7 K in Fig. 2, for La_2LiOsO_6 at $T = 7$ K in Fig. 3, and using the corresponding data for Ba_2YRuO_6, Ba_2YOsO_6, and La_2NaRuO_6, taken from previous studies performed by Carlo *et al.* [3], Kermarrec *et al.* [4], and Aczel *et al.* [8], respectively.

The linear spin-wave theory employed a minimal model for an anisotropic exchange Hamiltonian, which reproduces the type I AF ordered state displayed by La_2LiRuO_6, Ba_2YRuO_6, and Ba_2YOsO_6 at low temperatures and which also produces a gap in the low-energy magnetic inelastic spectrum,

$$\mathcal{H} = -\left(J_1 \sum_{NN} \mathbf{S}_i \mathbf{S}_j + K_1 \sum_{NN} S_{i,x} S_{j,x} \right), \qquad (2)$$

where the J_1 term represents an isotropic near-neighbor exchange interaction, related to the bandwidth of the spin excitations. The K_1 term generates the spin gap in these systems and an additional coupling of a particular component of spin, hence anisotropic exchange. J_1 and K_1 are defined such that positive values are ferromagnetic and negative values are antiferromagnetic. Near-neighbor anisotropic exchange interactions were previously identified as the likely cause for the spin gap observed in these d^3 systems [4,10], and a similar spin-wave theory analysis was carried out by Taylor *et al.* [10] to model the spin excitation spectrum of the related monoclinic d^3 double perovskite Sr_2ScOsO_6. The spin-wave theory calculations were performed equivalently for both the cubic and the monoclinic systems despite the slight distortion in the monoclinic systems La_2LiOsO_6 and La_2LiRuO_6. These distortions are relatively weak, and their INS spectra are remarkably similar to their cubic counterparts. The Os^{5+} magnetic form factor, obtained from the work of Kobayashi *et al.* [27], was employed in our spin-wave theory calculations. To our knowledge, the magnetic form factor for Ru^{5+} is not reported in the literature, and as such, the Os^{5+} form factor was

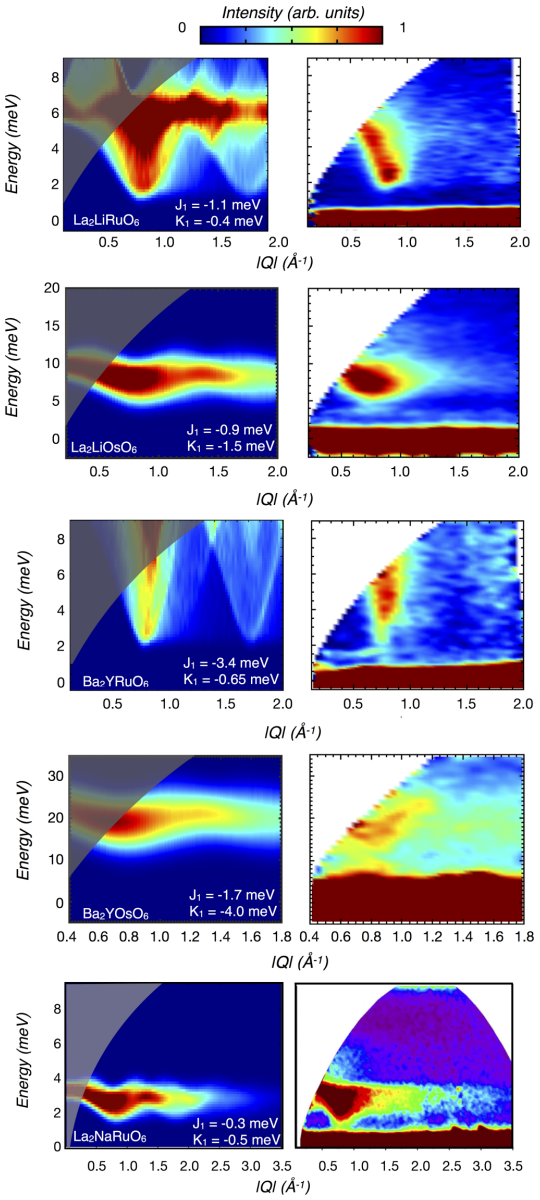

FIG. 9. The calculated spin-wave spectra, performed with SPINW for the double perovskites La_2LiRuO_6, La_2LiOsO_6, Ba_2YRuO_6, Ba_2YOsO_6, and La_2NaRuO_6 are presented in the left panels, and the corresponding experimentally obtained INS spectra obtained at base temperatures are provided on the right. All experimental data sets are background subtracted. Appropriate Gaussian broadening of the calculated spin-wave spectra was applied to each case in order to account for experimental resolution.

TABLE I. Microscopic exchange parameters relevant to each double perovskite system resulting from SPINW fits to the experimental spectra are shown. J_1, K_1, and D represent isotropic nearest-neighbor exchange, anisotropic nearest-neighbor exchange, and single-ion Ising-like anisotropy, respectively.

System	J_1 (meV)	K_1 (meV)	D (meV)	$\frac{K_1}{J_1}$	$\frac{\lvert D\rvert}{J_1}$
Ba_2YRuO_6	−3.4	−0.65	1.3	0.2	0.4
Ba_2YOsO_6	−1.7	−4.0	8.0	2.4	4.7
La_2LiRuO_6	−1.1	−0.4	0.8	0.4	0.7
La_2LiOsO_6	−0.9	−1.5	2.9	1.7	3.2
Sr_2ScOsO_6	−4.4	−3.8	7.5	0.9	1.7
La_2NaRuO_6	−0.3	−0.5	1.0	1.7	3.3

also used in the spin wave calculations for the Ru^{5+} systems [28].

The spectra obtained from calculations using Eq. (2) are shown in Fig. 9, and the resulting fit parameters are presented in Table I. The parameters provide good phenomenological descriptions of the observed spectra at low temperatures. The primary difference between the observed spectra and the calculated spectra is that the intensity of the magnetic excitations drops off more rapidly as a function of $|Q|$ in the former case. This can be explained in terms of metal-ligand covalency effects between the d orbitals of the B' ions and the p orbitals of the neighboring O^{2-} ions [4,8,10]. Thus the magnetic form factor for both Os^{5+} and Ru^{5+} should reflect more extended d-electron wave functions and thus drop off more sharply with $|Q|$.

The spin-wave theory calculations were carried out, adjusting the two parameters in the spin Hamiltonian J_1 and K_1 using the INS for La_2LiRuO_6, La_2LiOsO_6, Ba_2YRuO_6, and Ba_2YOsO_6 as benchmarks, until a good description of the data was achieved. For comparison, literature data for La_2NaRuO_6 were also fit in this manner. Our best efforts resulted in the comparison between theory and experiment shown in Fig. 9. The resulting "best-fit" parameters for J_1 and K_1 are shown both in the appropriate panels of Fig. 9 and in Table I for all five double perovskites as well as for Sr_2ScOsO_6 using the literature results from Taylor *et al.* [10]. Comparing now between the Ba_2YXO_6 and the La_2YLiXO_6 families, it is clear that all the energy scales are higher in cubic Ba_2YXO_6 compared with La_2LiXO_6, consistent with the θ_{CW} values being higher in the cubic Ba_2YXO_6 family. Looking across the J_1 and K_1 parameters for the six double perovskites listed in Table I, we see that the anisotropic exchange values K_1 are relatively consistent, ~ -0.5 meV for the ruthenates and from -1.5 to -4 meV for the osmates. There is greater variation in the isotropic exchange parameter J_1 ranging from -0.3 meV for La_2NaRuO_6, which displays an incommensurate magnetic structure, to -4.4 meV for Sr_2ScOsO_6, which displays the highest temperature phase transition $T_N = 92$ K to a type I AF structure. Where the comparison can be made, in the Ba_2YXO_6

and La_2LiXO_6 families, the anisotropic near-neighbor exchange K_1 is much stronger in the osmate members of each family relative to the ruthenate members. This latter effect is responsible for the much higher spin gaps in the osmate members of the families compared to the ruthenates and is consistent with spin-orbit coupling being ∼3.2 times stronger in $5d^3$ Os^{5+} compared to $4d^3$ Ru^{5+} configurations.

The INS spectra can also be effectively reproduced using a spin Hamiltonian with isotropic near-neighbor exchange and single-ion anisotropy as

$$\mathcal{H} = -\left(J_1 \sum_{NN} \mathbf{S}_i \mathbf{S}_j + D \sum_i S_{i,x}^2\right). \quad (3)$$

The quality of the comparison between experiment and theory using this spin Hamiltonian is equivalent to that using an anisotropic exchange term as described by Eq. (2) and hence this comparison is not reproduced here. The best fits to the inelastic spectra for La_2LiRuO_6, La_2LiOsO_6, Ba_2YRuO_6, Ba_2YOsO_6, as well as Sr_2ScOsO_6 and La_2NaRuO_6 are listed in Table I where the same J_1 value is relevant to best fits with either single-ion anisotropy [Eq. (2)] or anisotropic exchange [Eq. (1)].

IV. DISCUSSION

The gapped magnetic excitation spectrum in the weakly monoclinic double perovskite family La_2LiRuO_6 and La_2LiOsO_6 bears a striking resemblance to that observed in their corresponding cubic counterparts Ba_2YRuO_6 and Ba_2YOsO_6, despite the fact that La_2LiRuO_6, Ba_2YRuO_6, and Ba_2YOsO_6 share a common magnetic structure below their respective ordering temperatures (T_N), while La_2LiOsO_6 displays a different AF structure [5]. It is therefore useful to make a quantitative comparison between the figures of merit for the magnetic properties and energy scales in these two families of double perovskites. This is what is shown in Table II. We will also discuss these trends in light of the microscopic spin Hamiltonians we have determined using spin-wave theory and shown in Table I.

Table II shows the measured T_N, ordered moment size, CW constants (θ_{CW}), spin-wave bandwidths, and spin gaps for the cubic double perovskite family Ba_2YXO_6 and for the monoclinic double perovskite families La_2LiXO_6 and La_2NaXO_6, where X = Ru and Os. The ratio of the observed spin gaps within a particular Ru^{5+} and Os^{5+} family is also listed where possible, and, as previously discussed, it is as expected from atomic spin-orbit coupling ∼3.4.

One can see that a consistent picture emerges for the energy scales of the monoclinic La_2LiRuO_6 and La_2LiOsO_6 family relative to those of the cubic Ba_2YXO_6 family, wherein all energy scales in the monoclinic family are smaller than those corresponding to the cubic family by factors of between 2 and 3. Note here that the CW constants for the cubic double perovskites Ba_2YRuO_6 and Ba_2YOsO_6 are well above room temperature and thus difficult to accurately determine as the high temperature regime of validity of such an analysis is not easily accessible. Nonetheless, the conclusion remains that the θ_{CW} values for Ba_2YRuO_6 and Ba_2YOsO_6 are substantially larger than their monoclinic counterparts La_2LiRuO_6 and La_2LiOsO_6.

For this comparison we also include results from related monoclinic double perovskite systems: La_2NaRuO_6 and La_2NaOsO_6 and Sr_2ScRuO_6 and Sr_2ScOsO_6, which have all been recently studied [7–10,29]. To characterize the degree of the distortion of these monoclinic structures in relation to undistorted fcc structures, e.g., those exhibited by Ba_2YOsO_6 and Ba_2YRuO_6, we ascribe the average of the angle $\angle B\text{-}O\text{-}B'$. For fcc double perovskites with a single oxygen site, the $B\text{-}O\text{-}B' = 180°$. For monoclinic double perovskites, however, $B\text{-}O\text{-}B' < 180°$, and a smaller $\angle B\text{-}O\text{-}B'$ corresponds to more severe distortion from the fcc structures. The energy scales of the La_2NaRuO_6 and La_2NaOsO_6 family with relatively large distortion away from the fcc structures are all suppressed relative to the less distorted La_2LiXO_6 and Ba_2YXO_6 families; so much so that La_2NaOsO_6 does not order to temperatures

TABLE II. A summary of the key properties of d^3 double perovskites considered in this comparison are shown in this table. Please note that: (a) INS studies have not been performed on the Ru-based compound Sr_2ScRuO_6, and as such, Δ_{Os}/Δ_{Ru} is not reported for this family of double perovskites, (b) numerical values for T_N, μ, f, and Δ are not quoted for La_2NaOsO_6 as it fails to develop long-range order as determined in studies by Aczel and co-workers [7,8], (c) the values quoted for Δ in this table are the values which have been defined using the convention described earlier in Sec. III B and will not correspond to the reported values in the original work on these materials [3,4,8,10], and (d) the bond angles $\angle B\text{-}O\text{-}B'$ were retrieved from published crystallographic studies outlined in the footnotes at the bottom of this table.

System	T_N (K)	μ	θ_{CW} (K)	Bandwidth (meV)	$\angle B\text{-}O\text{-}B'$ (deg)	f ($\equiv \lvert\theta_{CW}\rvert/T_N$)	Δ (meV)	Δ_{Os}/Δ_{Ru}	Reference
Ba_2YRuO_6	36	$2.2(1)\mu_B$	−399(2)	11(2)	180	11	4(2)	3.8	[3]
Ba_2YOsO_6	69	$1.65(6)\mu_B$	−717(5)	16(3)	180	11	15(3)		[4]
La_2LiRuO_6	23.8	$2.2(2)\mu_B$	−185(5)	5.7(9)	155.1(4)[a]	9	1.8(8)	3.3	[5], This paper
La_2LiOsO_6	30	$1.8(2)\mu_B$	−154(2)	12(1)	153.5(5)[b]	6	6(1)		[5], This paper
La_2NaRuO_6	15(1)	$1.87(7)\mu_B$	−57(1)	2.0(3)	146.00(22)[c]	4	1.8(2)		[7,8]
La_2NaOsO_6			−74(1)		145.4(5)[d]				[7,8]
Sr_2ScRuO_6	60	$1.97(2)\mu_B$	−242		178.7(6)	4			
Sr_2ScOsO_6	92(1)	$1.6(1)\mu_B$	−677	20(4)	165.5(6)	7.4	14(4)		[9,10]

[a]P. D. Battle, C. P. Grey, M. Hervieu, C. Martin, C. A. Moore, and Y. Paik, J. Solid State Chem. **175**, 20 (2003).
[b]W. R. Gemmill, M. D. Smith, and H.-C. zur Loye, J Solid State Chem. **179**, 1750 (2006).
[c]W. R. Gemmill, M. D. Smith, and H.-C. zur Loye, J Solid State Chem. **177**, 3560 (2004).
[d]W. R. Gemmill, M. D. Smith, R. Prozorov, and H.-C. zur Loye, Inorg. Chem. **44**, 2639 (2005).

as low as 7 K, while La_2NaRuO_6 orders into an unusual incommensurate structure below $T_N \sim 15$ K [7]. This incommensurate structure is unique among these d^3 systems and has been attributed to the considerable tilting of the NaO_6 and Os/RuO_6 octahedra implied by the low $\angle B\text{-}O\text{-}B'$ values they display. This is argued to randomize the strength of near-neighbor exchange interactions such that they are, on average, weaker. This could also lead to competition between near-neighbor J_1 interactions and next-near-neighbor J_2 interactions [9] leading to incommensurate magnetic structures. Sr_2ScOsO_6 and Sr_2ScRuO_6 are interesting comparators as these structures are more weakly distorted than either of La_2LiXO_6 or La_2NaXO_6, and they exhibit the highest T_N's and highest θ_{CW}'s of these three families of monoclinic double perovskites. In fact Sr_2ScOsO_6 exhibits $T_N = 92$ K, which is 1/3 higher than the $T_N = 69$ K exhibited by fcc Ba_2YOsO_6 and a spin gap roughly the same as Ba_2YOsO_6, $\Delta = 14(4)$ meV.

This comparison suggests that the tilting of the BO_6 and $B'O_6$ octahedra systematically weakens the interaction energy scales in these families of double perovskites, but it is not the only factor. Indeed first principles density-functional theory calculations show that, for a series of compounds, $Sr_2ScB'O_6$ where $B' = (Y, In, Sc)$, Sc is the strongest mediator of magnetic exchange interactions due to the overlap in energy between the Os-5*d* and the Y/In/Sc-*d* states, even though the same magnetic ion and same magnetic ground state is involved [12]. The relative strengths of Y^{3+} and Sc^{3+} in mediating the exchange is also consistent with Sr_2YOsO_6 ordering at $T_N = 53$ K [30] whereas Sr_2ScOsO_6 orders at $T_N = 92$ K [9], which in turn is larger than the $T_N = 69$ K of fcc Ba_2YOsO_6 [4].

The wide variation in T_N observed in the d^3 systems is considered in Fig. 10, and an excellent linear relationship between T_N and $S(J_1 + 2K_1)$, going through the origin, is observed. This is consistent with the observation that T_N scales according to the top of the spin-wave band in all these double perovskite magnets. Figure 11 demonstrates how K_1 generates the spin gap (as does single-ion anisotropy D). J_1 generates the spin-wave bandwidth, whereas both the bandwidth and the spin gap scale as the moment size S. Hybridization of the *d*-electron orbitals is stronger for the 5*d* osmates compared to the 4*d* ruthenates, and this appears to result in a lower ordered moment S in the osmates compared to the ruthenates. K_1 is empirically observed to be twice as effective at increasing the gap as J_1 is to increasing the bandwidth. Both contribute equally to the energy of the top of the spin-wave band, and this then gives the relation that T_N is expected to increase as $S(J_1 + 2K_1)$ as Fig. 10 illustrates.

Table II shows that the frustration index f, defined as the ratio of θ_{CW} to T_N, is highest for the cubic double perovskites ~10 as expected. The high symmetry of the face-centered-cubic structure allows the most competition among equivalent interactions. This condition is expected to be relaxed somewhat as the symmetry is lowered to monoclinic. We see that the cubic double perovskites display frustration indices of ~10, which is about 30% greater than those displayed by the monoclinic double perovskites in this comparator group. A frustration index of 10 is large, comparable to those exhibited, for example, by the $4d^2$ pyrochlore antiferromagets $Y_2Mo_2O_7$ and $Lu_2Mo_2O_7$, both of which exhibit frozen spin-glass states at

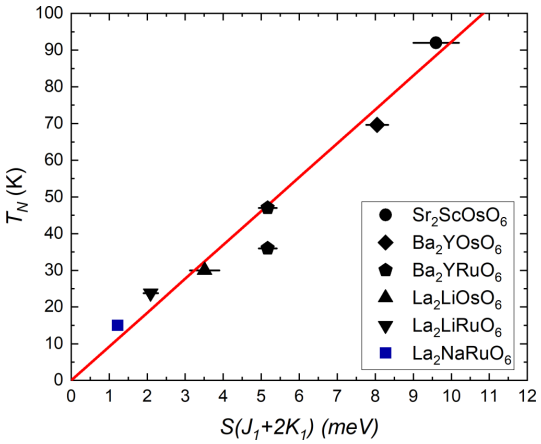

FIG. 10. The correlation between $S(J_1 + 2K_1)$ versus ordering temperature T_N is shown for La_2LiRuO_6, La_2LiOsO_6, Ba_2YRuO_6, Ba_2YOsO_6, Sr_2ScOsO_6, and La_2NaRuO_6. The straight line is a fit to the data, constrained to go through the origin. Both transition temperatures reported by Carlo *et al.* [3] for Ba_2YRuO_6 are included in this plot, and the higher of the two temperatures T^* is employed in the fit. (The fit is better using $T^* \sim 47$ K rather than $T_N = 36$ K, although both support the trend.) Please note that: (i) The error bars associated with $S(J_1 + 2K_1)$ are due to S and as such, we expect this to be a lower limit on the estimate of the error in this quantity. (ii) The data point corresponding to La_2NaRuO_6 is highlighted in blue to emphasize that a $k = (0, 0, 0)$ type I AF magnetic structure was utilized for simplicity in the SPINW calculation. In actuality, the material exhibits an unusual incommensurate magnetic structure as reported in the original work by Aczel *et al.* [8].

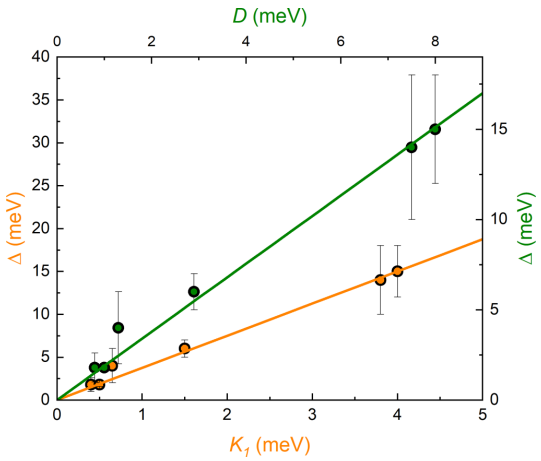

FIG. 11. The variation of the measured spin gap Δ with the anisotropic exchange parameter K_1 (in orange) and single-ion anisotropy D (in green) which are responsible for generating spin gaps within the model Hamiltonians.

sufficiently low temperatures. However these f values are not as large as those found in quasi-two-dimensional $3d^9$ kagome antiferromagnets, such as herbertsmithite $ZnCu_3(OH)_6Cl_2$, where f exceeds 200.

V. CONCLUSIONS

To conclude, we have studied the inelastic magnetic scattering and corresponding spin gaps in the weakly monoclinic double perovskite antiferromagnets La_2LiRuO_6 and La_2LiOsO_6 using time-of-flight INS techniques. We observe the spin gaps to collapse on passing through T_N. The spin gaps themselves 1.8(8) meV for La_2LiRuO_6 and 6(1) meV for La_2LiOsO_6 scale with the strength of the atomic spin-orbit coupling parameter λ, appropriate for $4d^3$ Ru^{5+} and $5d^3$ Os^{5+}. Such a spin gap is naively unanticipated for a d^3 system due to the orbital singlet expected from half-filled t_{2g} levels. The magnetic spectral weights in La_2LiRuO_6 and La_2LiOsO_6 below their respective T_N's are well described by linear spin-wave theory, based on near-neighbor anisotropic exchange, as is the low temperature magnetic spectral weight in the cubic double perovskites Ba_2YRuO_6 and Ba_2YOsO_6, which were previously measured.

A similar spin wave analysis was carried out earlier for Sr_2ScOsO_6, and the T_N's for this family of five double perovskite antiferromagnets scales very well with $S(J_1 + 2K_1)$, which characterizes the energy of the top of the spin-wave band in all of these materials. The magnitude of the spin-wave gap is controlled by the near-neighbor anisotropic exchange strength K_1, and together these are strong evidence for the gapped spectrum arising due to anisotropic exchange, which itself is generated by spin-orbit coupling. We hope that these new measurements and their analysis in the context of spin dynamics in other d^3 double perovskites can guide a full understanding of the nature of their ordered states and counterintuitive spin gaps.

ACKNOWLEDGMENTS

Research at McMaster University was supported by NSERC of Canada. This work was supported, in part, by the National Science Foundation under Grant No. PHYS-1066293 and the hospitality of the Aspen Center for Physics. We also acknowledge the hospitality of the Telluride Science Research Center. We gratefully acknowledge useful conversations with A. Taylor, R. F. Fishman, and S. Calder. We are very grateful for the instrument and sample environment support provided during our INS experiment at SEQUOIA. The experiment which was performed at the Spallation Neutron Source at Oak Ridge National Laboratory was sponsored by the U.S. Department of Energy, Office of the Basic Energy Sciences, Scientific User Facilities Division.

[1] W. Witczak-Krempa, G. Chen, Y. B. Kim, and L. Balents, Annu. Rev. Condens. Matter Phys. **5**, 57 (2014).
[2] J. P. Carlo, J. P. Clancy, T. Aharen, Z. Yamani, J. P. C. Ruff, J. J. Wagman, G. J. Van Gastel, H. M. L. Noad, G. E. Granroth, J. E. Greedan, H. A. Dabkowska, and B. D. Gaulin, Phys. Rev. B **84**, 100404 (2011).
[3] J. P. Carlo, J. P. Clancy, K. Fritsch, C. A. Marjerrison, G. E. Granroth, J. E. Greedan, H. A. Dabkowska, and B. D. Gaulin, Phys. Rev. B **88**, 024418 (2013).
[4] E. Kermarrec, C. A. Marjerrison, C. M. Thompson, D. D. Maharaj, K. Levin, S. Kroeker, G. E. Granroth, R. Flacau, Z. Yamani, J. E. Greedan, and B. D. Gaulin, Phys. Rev. B **91**, 075133 (2015).
[5] C. M. Thompson, C. A. Marjerrison, A. Z. Sharma, C. R. Wiebe, D. D. Maharaj, G. Sala, R. Flacau, A. M. Hallas, Y. Cai, B. D. Gaulin, G. M. Luke, and J. E. Greedan, Phys. Rev. B **93**, 014431 (2016).
[6] C. M. Thompson, J. P. Carlo, R. Flacau, T. Aharen, I. A. Leahy, J. R. Pollichemi, T. J. S. Munsie, T. Medina, G. M. Luke, J. Munevar, S. Cheung, T. Goko, Y. J. Uemura, and J. E. Greedan, J. Phys.: Condens. Matter **26**, 306003 (2014).
[7] A. A. Aczel, D. E. Bugaris, L. Li, J.-Q. Yan, C. de la Cruz, H.-C. zur Loye, and S. E. Nagler, Phys. Rev. B **87**, 014435 (2013).
[8] A. A. Aczel, P. J. Baker, D. E. Bugaris, J. Yeon, H.-C. zur Loye, T. Guidi, and D. T. Adroja, Phys. Rev. Lett. **112**, 117603 (2014).
[9] A. E. Taylor, R. Morrow, D. J. Singh, S. Calder, M. D. Lumsden, P. M. Woodward, and A. D. Christianson, Phys. Rev. B **91**, 100406 (2015).
[10] A. E. Taylor, R. Morrow, R. S. Fishman, S. Calder, A. I. Kolesnikov, M. D. Lumsden, P. M. Woodward, and A. D. Christianson, Phys. Rev. B **93**, 220408 (2016).
[11] T. Dey, A. Maljuk, D. V. Efremov, O. Kataeva, S. Gass, C. G. F. Blum, F. Steckel, D. Gruner, T. Ritschel, A. U. B. Wolter, J. Geck, C. Hess, K. Koepernik, J. van den Brink, S. Wurmehl, and B. Büchner, Phys. Rev. B **93**, 014434 (2016).
[12] S. Kanungo, B. Yan, C. Felser, and M. Jansen, Phys. Rev. B **93**, 161116 (2016).
[13] F.-Y. Li, Y.-D. Li, Y. Yu, A. Paramekanti, and G. Chen, Phys. Rev. B **95**, 085132 (2017).
[14] G. Chen, R. Pereira, and L. Balents, Phys. Rev. B **82**, 174440 (2010).
[15] G. Chen and L. Balents, Phys. Rev. B **84**, 094420 (2011).
[16] C. Lacroix, P. Mendels, and F. Mila, *Introduction to Frustrated Magnetism* (Springer-Verlag, Berlin, Heidelberg, 2011).
[17] M. T. Anderson, K. B. Greenwood, G. A. Taylor, and K. R. Poeppelmeier, Prog. Solid State Chem. **22**, 197 (1993).
[18] B. J. Kim, H. Ohsumi, T. Komesu, S. Sakai, T. Morita, H. Takagi, and T. Arima, Science **323**, 1329 (2009).
[19] T. Aharen, J. E. Greedan, F. Ning, T. Imai, V. K. Michaelis, S. Kroeker, H. Zhou, C. R. Wiebe, and L. M. D. Cranswick, Phys. Rev. B **80**, 134423 (2009).
[20] T. Aharen, J. E. Greedan, C. A. Bridges, A. A. Aczel, J. Rodriguez, G. MacDougall, G. M. Luke, T. Imai, V. K. Michaelis, S. Kroeker, H. Zhou, C. R. Wiebe, and L. M. D. Cranswick, Phys. Rev. B **81**, 224409 (2010).
[21] T. Aharen, J. E. Greedan, C. A. Bridges, A. A. Aczel, J. Rodriguez, G. MacDougall, G. M. Luke, V. K. Michaelis, S. Kroeker, C. R. Wiebe, H. Zhou, and L. M. D. Cranswick, Phys. Rev. B **81**, 064436 (2010).
[22] C.-G. Ma and M. G. Brik, J. Lumin. **145**, 402 (2014).

[23] G. E. Granroth, A. I. Kolesnikov, T. E. Sherline, J. P. Clancy, K. A. Ross, J. P. Ruff, B. D. Gaulin, and S. E. Nagler, J. Phys.: Conf. Ser. **251**, 12058 (2010).

[24] O. Arnold, J. C. Bilheux, J. M. Borreguero, A. Buts, S. I. Campbell, L. Chapon, M. Doucet, N. Draper, R. Ferraz Leal, M. A. Gigg, V. E. Lynch, A. Markvardsen, D. J. Mikkelson, R. L. Mikkelson, R. Miller, K. Palmen, P. Parker, G. Passos, T. G. Perring, P. F. Peterson, S. Ren, M. A. Reuter, A. T. Savici, J. W. Taylor, R. J. Taylor, R. Tolchenov, W. Zhou, and J. Zikovsky, Nucl. Instrum. Methods Phys. Res., Sect. A **764**, 156 (2014).

[25] R. T. Azuah, L. R. Kneller, Y. Qiu, P. L. W. Tregenna-Piggott, C. M. Brown, J. R. D. Copley, and R. M. Dimeo, J. Res. Natl. Inst. Stand. Technol. **114**, 341 (2009).

[26] S. Tóth and B. Lake, J. Phys.: Condens. Matter **27**, 166002 (2015).

[27] K. Kobayashi, T. Nagao, and M. Ito, Acta Crystallogr., Sect. A: Found Crystallogr. **67**, 473 (2011).

[28] The $\langle j_0 \rangle$ parameters for $4d$ and $5d$ magnetic form factors corresponding to the same number of d electrons, e.g., W^{+} and Mo^{+} differ little as do the form factors associated with Os^{4+}, Os^{5+}, and Os^{6+}. We therefore consider the Os^{5+} form factor a good proxy for that of Ru^{5+}. Consideration of the weak $\langle j_2 \rangle$ contribution extends the form factor to higher $|Q|$'s, which is opposite to the effect of covalency between the $4/5d$ orbitals of the magnetic ion and the $2p$ orbitals of the O^{2-} ion.

[29] P. Kayser, S. Injac, B. Ranjbar, B. J. Kennedy, M. Avdeev, and K. Yamaura, Inorg. Chem. **56**, 9009 (2017).

[30] A. K. Paul, A. Sarapulova, P. Adler, M. Reehuis, S. Kanungo, D. Mikhailova, W. Schnelle, Z. Hu, C. Kuo, V. Siruguri, S. Rayaprol, Y. Soo, B. Yan, C. Felser, L. H. Tjeng, and M. Jansen, Z. Anorg. Allg. Chem. **641**, 197 (2015).

6 Multipolar vs Néel Order in Cubic $5d^2$ double perovskites

> "It ain't what you don't know that gets you into trouble. It's what you know for sure that just ain't so." — *Anon*

This chapter incorporates the article *"Octupolar versus Néel Order in Cubic $5d^2$ Double Perovskites"*, which has been published in Physical Review Letters. Reproduced from with permission, copyrighted by the American Physical Society 2020. The full reference is given below:

D. D. Maharaj, G. Sala, M. B. Stone, E. Kermarrec, C. Ritter, F. Fauth, C. A. Marjerrison, J. E. Greedan, A. Paramekanti, and B. D. Gaulin. Physical Review Letters 124, 087206 (2020).

In this work we explore the case of d^2 ions on the B' site, with effective $J = 2$ moments. We combine time-of-flight inelastic neutron scattering, neutron powder diffraction, and x-ray synchrotron diffraction techniques to characterize the ground states exhibited by the $5d^2$ double perovskites Ba_2CaOsO_6, Ba_2MgOsO_6 and Ba_2ZnOsO_6. Our measurements find the co-existence of strong spin excitations in the absence of magnetic Bragg peaks, which would otherwise indicate magnetic long-range order in Ba_2CaOsO_6, Ba_2MgOsO_6 and Ba_2ZnOsO_6. These findings were puzzling at first as previous results from muon spin relaxation, heat capacity and magnetization experiments suggested that Ba_2CaOsO_6 and Ba_2MgOsO_6 host a type I antiferromagnetic ground state. To reconcile these seemingly disparate properties, we account for the

effect of spin-orbit coupling along with an effective crystal-field applied to the two-electron ground state multiplet. In this framework, we provide a compelling case that Ba_2CaOsO_6, Ba_2MgOsO_6 and Ba_2ZnOsO_6 form a novel octupolar ordered ground state which has hitherto only been observed in f electron magnets.

PHYSICAL REVIEW LETTERS **124,** 087206 (2020)

Octupolar versus Néel Order in Cubic $5d^2$ Double Perovskites

D. D. Maharaj,[1,*] G. Sala,[1,2] M. B. Stone,[2] E. Kermarrec,[1,3] C. Ritter,[4] F. Fauth,[5] C. A. Marjerrison,[6] J. E. Greedan,[6,7] A. Paramekanti,[8] and B. D. Gaulin[1,6,9]

[1]*Department of Physics and Astronomy, McMaster University, Hamilton, Ontario L8S 4M1, Canada*
[2]*Neutron Scattering Division, Oak Ridge National Laboratory, Oak Ridge, Tennessee 37831, USA*
[3]*Université Paris-Saclay, CNRS, Laboratoire de Physique des Solides, 91405 Orsay, France*
[4]*Institut Laue-Langevin, Boîte Postale 156, 38042 Grenoble Cédex, France*
[5]*CELLS-ALBA Synchrotron, Carrer de la Llum 2-26, 08290 Cerdanyola del Vallès, Barcelona, Spain*
[6]*Brockhouse Institute for Materials Research, McMaster University, Hamilton, Ontario L8S 4M1, Canada*
[7]*Department of Chemistry and Chemical Biology, McMaster University, Ontario L8S 4M1, Canada*
[8]*Department of Physics, University of Toronto, 60 St. George Street, Toronto, Ontario M5S 1A7, Canada*
[9]*Canadian Institute for Advanced Research, 661 University Avenue, Toronto, Ontario M5G 1M1, Canada*

(Received 6 September 2019; accepted 30 January 2020; published 27 February 2020)

We report time-of-flight neutron spectroscopy and neutron and x-ray diffraction studies of the $5d^2$ double perovskite magnets, Ba_2MOsO_6 ($M = Zn, Mg, Ca$). These materials host antiferromagnetically coupled $5d^2$ Os^{6+} ions decorating a face-centered cubic (fcc) lattice and are found to remain cubic down to the lowest temperatures. They all exhibit thermodynamic anomalies consistent with a single phase transition at a temperature T^*, and a gapped magnetic excitation spectrum with spectral weight concentrated at wave vectors typical of type-I antiferromagnetic orders. However, while muon spin resonance experiments show clear evidence for time-reversal symmetry breaking below T^*, we observe no corresponding magnetic Bragg scattering signal. These results are shown to be consistent with ferro-octupolar symmetry breaking below T^*, and are discussed in the context of other $5d$ double perovskite magnets and theories of exotic orders driven by multipolar interactions.

DOI: 10.1103/PhysRevLett.124.087206

Introduction.—Ordered double perovskite magnets, with the chemical formula $A_2BB'O_6$, provide a fascinating avenue to study the interplay of geometric frustration with strong spin-orbit coupling [1]. Here, B and B' sublattices individually form a fcc lattice of edge-sharing tetrahedra, an archetype for geometric frustration in three dimensions. Furthermore, the flexibility of the double perovskite lattice to host heavy ions at the B' site allows the study of spin-orbit driven physics, as the strength of spin-orbit coupling scales $\sim Z^2$, where Z is the atomic number of the magnetic ion [2]. This interplay of spin-orbit coupling and frustration in double perovskites is predicted to yield exotic ground states [3–6].

The single-particle t_{2g} levels in an octahedral crystal field are split by strong spin-orbit coupling, resulting in a quartet $j = 3/2$ ground state and a doublet $j = 1/2$ excited state. Famously, for a d^5 electronic configuration, as occurs for Ir^{4+} or Ru^{3+}, this results in a single $j = 1/2$ hole, leading to extreme quantum magnetism, and Kitaev exchange interactions in appropriate geometries [7–13]. On the other hand, ions with d^1 and d^2 configurations are, respectively, expected to form $j = 3/2$ or total $J = 2$ moments [3,4,6]. Theoretical studies incorporating intersite orbital repulsion between such ions argue for wide regimes of quadrupolar order on the fcc lattice [3,4,6] which may coexist with dipolar antiferromagnetic or valence bond orders [14]. Recent experiments on $5d^1$ oxides, Ba_2NaOsO_6 with Os^{7+} [15,16] and Ba_2MgReO_6 with Re^{6+} [17], have found evidence for two transitions associated with these distinct broken symmetries: quadrupolar ordering at T_Q and onset of coexisting dipolar antiferromagnetic order below a lower transition temperature T_N.

In this Letter, we explore the case of d^2 ions on the B' site, with effective $J = 2$ moments. We report new magnetic neutron powder diffraction, inelastic neutron scattering, and high angular resolution synchrotron x-ray diffraction results on three cubic double perovskites: Ba_2MOsO_6, with $M = Zn$, Mg, Ca (respectively referred to henceforth as BZO, BMO, and BCO). In contrast to d^1 double perovskites, these materials display clear thermodynamic signatures of a *single* phase transition [18–20] at $T^* \sim 30$–50 K, which is associated with time-reversal symmetry breaking based on oscillations observed in zero field muon spin relaxation (μSR) [20]. Our inelastic neutron scattering results show strong, gapped, magnetic spectral weight at wave vectors typical of type-I antiferromagnetic order, but we detect no clear signature of an ordered antiferromagnetic moment in the diffraction data, leading us to place an upper limit between 0.13 and $0.06\mu_B$ per B' site. Furthermore, our neutron powder diffraction

and x-ray diffraction results show no deviation from cubic symmetry, thus ruling out quadrupolar order. We propose that these striking and unexpected results may be understood via the emergence of time-reversal symmetry breaking ferro-octupolar order below T^*.

Multipolar orders have been extensively studied in heavy fermion f-electron compounds [21]. Examples include NpO_2 [22–25], where experiments suggest a primary rank-5 magnetic multipolar order driving secondary quadrupolar order, the "hidden order" state of URu_2Si_2 [26–28], and recent discoveries of quadrupolar and octupolar orders in PrX_2Al_{20} ($X = \mathrm{Ti}, \mathrm{V}$) [29–31]. In stark contrast, multipolar orders in d-electron systems are less explored [15–17,32–34]; our work appears to be the first reported candidate for d-orbital octupolar order.

BZO, BMO, and BCO have been previously studied in powder form. In all three materials, neutron powder diffraction and x-ray diffraction confirm that they remain in the cubic $Fm\bar{3}m$ space group down to the lowest temperature. They all display Curie-Weiss-like magnetic susceptibilities (χ) at high temperatures, with large antiferromagnetic Curie-Weiss constants ($\Theta_{\mathrm{CW}} \sim 130\,\mathrm{K}$), and anomalies at T^* in the form of a splitting between field-cooled and zero-field-cooled results. They all exhibit peaks in their heat capacity, or in the related measure $d(\chi T)/dT$, at $T^* \sim 50$ K (BMO, BCO) or $T^* \sim 30$ K (BZO), indicating a phase transition [18,20]. These findings are summarized in Table I.

The entropy released up to $\sim 2T^*$ in all three materials appears to be $\sim R\ln(2)$ per mole, as explicitly shown for BZO and BMO in the Supplemental Material [35,36]. This is much smaller than the $R\ln(5)$ expected for an effective $J = 2$ moment [18–20], and it points to part of the entropy being quenched at $T \gg T^*$ (i.e., above ~200 K). This is in contrast to the $\sim R\ln(5)$ entropy released up to $\sim 2T_N$ for the tetragonal counterpart Sr_2MgOsO_6, which has a high Néel ordering temperature $T_N \sim 100$ K [37].

These three cubic samples have also been previously studied using μSR techniques [18,20], and it is primarily on the basis of these zero longitudinal field μSR oscillations for $T < T^*$, indicative of a time-reversal broken state, that the transition at T^* was associated with antiferromagnetic order. However, no magnetic neutron diffraction peaks could be identified in this earlier study at low temperatures, with a sensitivity to ordered moment of $\sim 0.7\ \mu_B$. In the present work, we *significantly* improve on this bound, still finding no evidence of magnetic Bragg peaks.

TABLE I. Summary of experimental results for the three cubic double perovskites studied. T^* denotes the peak in the heat capacity indicating a thermodynamic phase transition [18,20]. θ_{CW} is the Curie-Weiss temperature extracted from high temperature susceptibility data [18,20]. μ_{ord} is the upper limit on the ordered dipolar moment associated with type-I antiferromagnetic order, as determined from neutron diffraction in this work.

System	T^*	θ_{CW}	a (Å)	Reference	μ_{ord}
Ba_2CaOsO_6	49	−156.2(3)	8.3456	[18]	$<0.13\ \mu_B$
Ba_2MgOsO_6	51	−120(1)	8.0586	[20]	$<0.11\ \mu_B$
Ba_2ZnOsO_6	30	−149.0(4)	8.0786	[20]	$<0.06\ \mu_B$

The corresponding $5d^3$ osmium-based double perovskites, both cubic Ba_2YOsO_6 and monoclinic Sr_2ScOsO_6 and La_2LiOsO_6, show clear Néel transitions to antiferromagnetic ordered states, with large ordered moments $\sim 1.7\mu_B$ [19,38–41]. These observed ordered moments are reduced from the $3\mu_B$ value expected for an orbitally quenched moment, pointing to strong spin-orbit coupling effects, or covalency, or both. Nonetheless, magnetic Bragg scattering at the (100) and (110) positions is easily observed, along with strong, gapped inelastic magnetic scattering centered at these two ordering wave vectors. Previously studied $5d^2$ double perovskites such as monoclinic Sr_2MgOsO_6 and cubic Ba_2LuReO_6 (with Re^{5+}) also show transitions to type-I antiferromagnetic order, as seen via neutron diffraction, albeit with much smaller ordered moments, 0.6(2) and 0.34(4) μ_B, respectively [37,42].

Below we present our experimental findings on powder samples of the cubic systems, BZO, BMO, and BCO. Details of experimental methods and analysis are in the Supplemental Material [35], which includes Refs. [43–47]. Our new neutron powder diffraction measurements on D20 [48,49] at the Institut Laue Langevin (ILL) have ~10–20 times more sensitivity to magnetic Bragg scattering as compared with previous neutron powder diffraction measurements taken at the C2 instrument of the Chalk River Laboratories. No magnetic Bragg scattering is observed at 10 K, factors of 3–5 below T^* for any of these materials. We do, however, observe gapped, inelastic magnetic spectral weight centered on wave vectors characteristic of type-I antiferromagnetic order. We thus conclude that the dominant broken symmetry below T^* in these three cubic double perovskite d^2 magnets must involve multipolar ordering.

Results.—Time-of-flight inelastic neutron scattering measurements from SEQUOIA [50] are shown in Fig. 1. Figures 1(a)–1(c) show the inelastic neutron scattering spectra well below (top panel) and above (bottom panel) T^* for BZO, BMO, and BCO, respectively. Figures 1(d)–1(f) show cuts through this data as a function of energy, integrating all $|Q| < 1.15$ Å^{-1}, and as a function of temperature, again for BZO, BMO, and BCO respectively.

The datasets for all three samples in Fig. 1 are similar, with gapped magnetic spectral weight at low $|Q|$'s, typical of the 100 (0.78 Å^{-1}) and 110 (1.1 Å^{-1}) Bragg positions. The full bandwidth of the magnetic excitation spectrum appears to be ~6 meV. From Figs. 1(b), 1(c), 1(e), and 1(f), this magnetic spectral weight overlaps in energy with strong phonon scattering near ~18 and 14 meV for BMO and BCO, respectively. Even though our low $|Q|$ integration favors magnetic scattering at the expense of

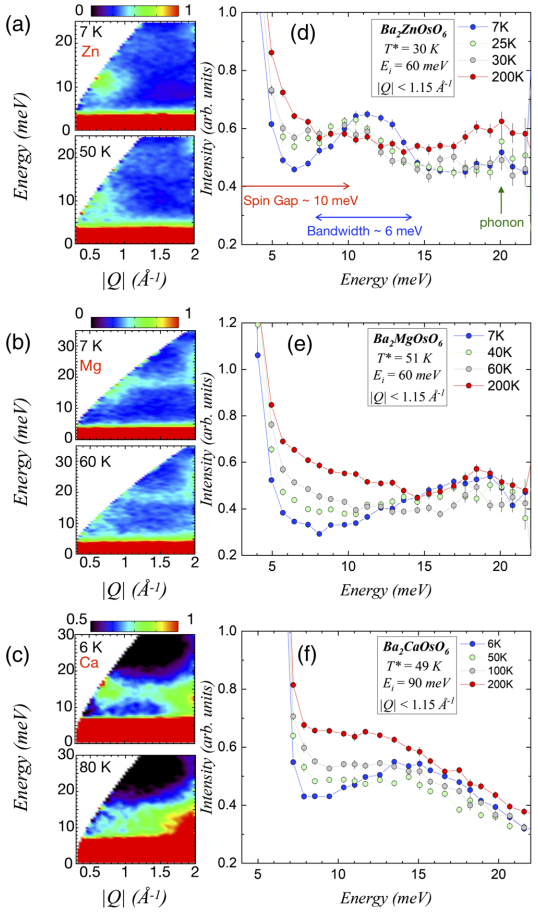

FIG. 1. (a)–(c) Neutron scattering intensity contour plots for BZO, BMO, and BCO shown as a function of energy transfer E and momentum transfer $|Q|$ at base temperature (top) and at $T > T^*$ (bottom), respectively. Below T^*, clear gapped magnetic inelastic spectral weight develops around (100) and (110) wave vectors (~0.78 Å^{-1}) and 110 (1.1 Å^{-1}) in each case. (d),(e) Low $|Q|$ integrated cuts of the neutron scattering intensity as a function of energy transfer E as a function of temperature for BZO, BMO, and BCO, respectively. A gap in the magnetic excitation spectrum is clearly revealed for each compound for $T < T^*$.

scattering from phonons, whose intensity tends to go like $|Q|^2$, we still pick up a sizable contribution from this high phonon density of states (DOS), especially at high temperatures where the thermal population of the phonons is large. The observed redshift in the peak of the phonon DOS from ~17 meV in BMO to ~14 meV for BCO is expected since Ca^{2+} is isoelectronic to Mg^{2+} but heavier. While the Zn^{2+} in BZO is heavier still than Ca^{2+}, it is not isoelectronic, instead possessing a filled $3d$ shell. This might lead to its higher energy phonon.

As the high phonon DOS is well separated from the magnetic spectral weight in BZO, shown in Figs. 1(a) and 1(d), this is where the nature of the gapped magnetic scattering is most easily appreciated. The energy cuts in Fig. 1(d) clearly show a well developed gap of ~10 meV and a bandwidth of ~6 meV. This structure collapses by 25 K, where $T^* = 30$ K for BZO, at which point the gap has largely filled in and only a vestige of an overdamped spin excitation at ~10 meV remains. This is very similar to what occurs in the d^3 double perovskites on the approach to their T_N's, *except* that there is no obvious temperature dependent Bragg scattering at the 100 or 110 positions, as would be expected for type-I antiferromagnetic order.

The absence of evidence for magnetic Bragg scattering is seen in Fig. 2. Figure 2(a) shows neutron diffraction data taken at $T = 10$ K, well below $T^* = 30$ K in BZO, using the D20 diffractometer at the ILL [48]. These data and the corresponding neutron powder diffraction data on BMO and BCO refine in the cubic $Fm\bar{3}m$ space group at all temperatures measured. Figures 2(b)–2(d) then show a subtraction of high temperature (50 K for BZO, 70 K for BMO and BCO) datasets from low temperature data sets for each of BZO, BCO, and BMO, respectively. A calculated neutron diffraction profile appropriate for a type-I antiferromagnetic structure below T^* is shown as the red line in Figs. 2(b)–2(d), where the assumed ordered moment in the calculation is $0.06\mu_B$ for BZO [Fig. 2(b)], $0.11\mu_B$ for BMO [Fig. 2(c)], and $0.13\mu_B$ for BCO [Fig. 2(d)]. Taking the case where the evidence *against* long-range magnetic order below T^* is most stringent, BZO, we can eliminate conventional type-I antiferromagnetic order of magnetic dipoles with an ordered moment greater than $\sim 0.06\mu_B$. This upper limit for magnetic dipole order is a factor of ~12 more stringent than previous limits on magnetic Bragg scattering for this family of cubic double perovskite materials. This upper bound for μ_{ord} in BCO is ~35% lower than the value, $0.2\mu_B$, previously extracted from a comparison of the μSR internal fields of BCO and Ba_2YRuO_6 [18,51].

Competing multipolar orders.—Our study shows that all or most of the static $5d^2$ moment of Os^{6+} in BZO, BMO, and BCO is not visible to neutron diffraction below T^*. Nonetheless, strong inelastic magnetic scattering is easily observed at all temperatures, and it is most clearly gapped at $T \ll T^*$. One scenario to explain these results is that the ground state has dominant quadrupolar ordering, accompanied by weak dipolar ordering [3,4,6]. A quadrupolar ordering transition at $T \gg T^*$ can partially quench the $R\ln(5)$ entropy, with the residual $\sim R\ln(2)$ entropy being quenched by antiferromagnetic dipolar ordering at T^* which breaks time-reversal symmetry. The quadrupolar order can also pin the direction of the ordered dipole moment, explaining the spin gap, and if the ordered dipole moment is weak, it may escape detection in a neutron powder diffraction experiment. However, the orbital

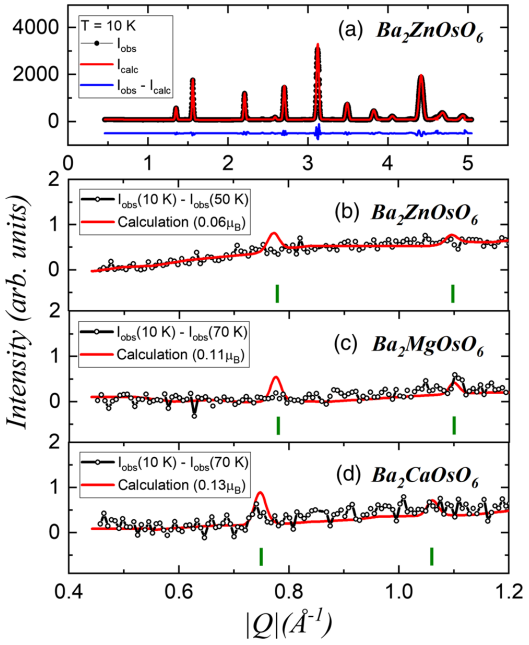

FIG. 2. (a) Neutron powder diffraction measurements on BZO for $T = 10$ K with the experimental dataset in black and the fit to the refined $Fm\bar{3}m$ structure in red. (b) Subtraction of the 50 K dataset from the 10 K dataset. The red line shows the calculated magnetic diffraction pattern for BZO with an Os^{6+} ordered moment of 0.06 μ_B, which we establish as the upper limit for an ordered dipole moment in BZO. Green fiducial lines indicate the locations of the magnetic peaks expected for type-I antiferromagnetic order. Panels (c) and (d) show the same comparison for BMO and BCO. These establish upper limits on an ordered Os^{6+} dipole moment of 0.11 and 0.13 μ_B, respectively.

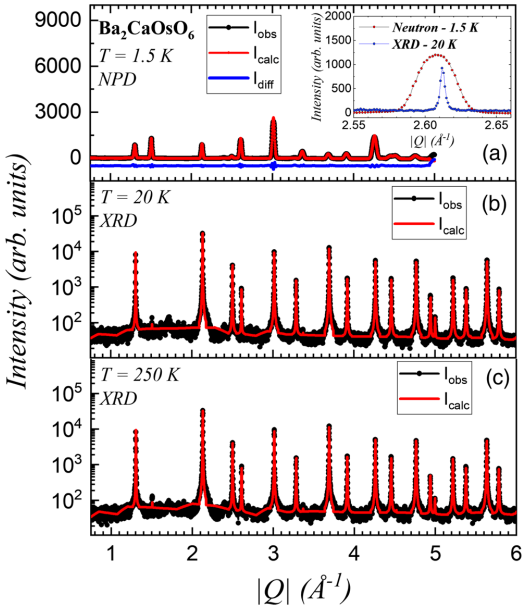

FIG. 3. (a) The neutron powder diffraction profile for BCO is shown at $T = 1.5$ K in the main panel, while the inset shows a comparison of neutron powder diffraction versus synchrotron x-ray diffraction data taken on BCO at 20 K. Panels (b) and (c) show synchrotron x-ray diffraction data on BCO at T = 20 K (b) and T = 250 K (c), along with corresponding cubic structural refinements, in red.

selection accompanying such a quadrupolar order would lower the crystal symmetry, at odds with our high resolution neutron powder diffraction data shown for BCO in Fig. 2(a). We have carried out even higher resolution x-ray diffraction measurements on BCO, the family member which best exhibits undamped zero field μSR oscillations. These measurements were conducted at the high angular resolution diffraction instrument $BL04 - MSPD$, beam line 8 of the ALBA Synchrotron Light facility (Barcelona, Spain) [52]. The sensitivity of these measurements to possible weak splittings of the cubic Bragg peaks is ~10 times greater than the neutron powder diffraction measurements; see Fig. 3(a) inset. These x-ray diffraction results, in Figs. 3(b)–3(d), show no splitting or broadening of the cubic Bragg peaks, yielding an upper limit on local distortions $< 0.1\%$ (see Supplemental Material [35]). This confirms that BCO remains cubic even for $T \ll T^*$, ruling out quadrupolar ordering. We contrast this with the $5d^1$ osmate Ba_2NaOsO_6 which exhibits measurable ~0.5%–0.7% local distortions associated with quadrupolar ordering [53].

Here, we propose a distinct scenario, an octupolar ordered ground state, that provides the most promising vehicle to explain all the salient observations. For an effective $J = 2$ moment, a residual octahedral crystal field Hamiltonian is $H_{CEF'} = -V_{eff}(\mathcal{O}_{40} + 5\mathcal{O}_{44})$, where the Steven's operators (dropping constant terms) are

$$\mathcal{O}_{40} = 35J_z^4 - [30J(J+1) - 25]J_z^2, \quad (1)$$

$$\mathcal{O}_{44} = \frac{1}{2}(J_+^4 + J_-^4). \quad (2)$$

$V_{eff} > 0$ results in a non-Kramers ground state doublet and an excited triplet with a gap $\Delta = 120V_{eff}$, as shown in Fig. 4 (details in Supplemental Material [35]). This naturally accounts for partial entropy quenching for $T \lesssim \Delta$, without a phase transition, with the residual $R\ln(2)$ entropy being quenched by ordering within the doublet sector at T^*. In the $|J_z = m\rangle$ basis, the ground state wave functions are $|\psi_{g,\uparrow}\rangle = |0\rangle$ and $|\psi_{g,\downarrow}\rangle = (1/\sqrt{2})(|2\rangle + |-2\rangle)$, with excited triplet

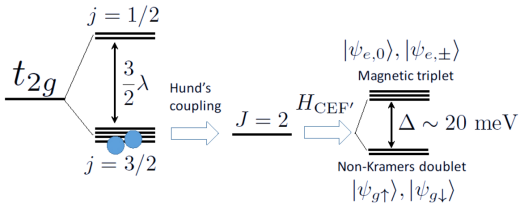

FIG. 4. Schematic level diagram showing single-particle t_{2g} orbitals split by spin-orbit coupling (λ) and interactions (Hund's coupling) leading to a $J = 2$ ground state. Residual crystal field $H_{\mathrm{CEF}'}$ splits this $J = 2$ manifold into a non-Kramers doublet ground state and an excited magnetic triplet (see text for details).

wave functions $|\psi_{e,\pm}\rangle = |\pm 1\rangle$ and $|\psi_{e,0}\rangle = (1/\sqrt{2})(|2\rangle - |-2\rangle)$. The ground state manifold has vanishing matrix elements for the dipole operators $\vec{J}$, precluding dipolar order. However, $\vec{J}$ can induce transitions into the excited triplet, accounting for the spin gap in inelastic neutron scattering. Defining pseudospin-1/2 operators $\vec{\tau}$ within the ground doublet, the quadrupolar operators are $(J_x^2 - J_y^2) \equiv 2\sqrt{3}\tau_x$, $(3J_z^2 - J^2) \equiv -6\tau_z$, while the octupolar operator $\overline{J_x J_y J_z} \equiv -\sqrt{3}\tau_y$ (overline denoting symmetrization). Octupolar order, with $\langle\tau_y\rangle \neq 0$, leads to broken time-reversal symmetry below T^* while preserving cubic symmetry. A mean field calculation with $\langle\tau_y\rangle \neq 0$ qualitatively captures the observed entropy and magnetic susceptibility (see Supplemental Material [35]). Further implications of this proposal are studied in Ref. [54].

To conclude, the low temperature phases of the cubic $5d^2$ double perovskites BZO, BMO, and BCO are best described as arising from octupolar order within a non-Kramers ground state doublet. This exotic ground state appears to require the perfect fcc structure as noncubic d^2 double perovskites, such as Sr_2MgOsO_6 [37], display conventional antiferromagnetic ground states. In noncubic systems like Sr_2MgOsO_6, the non-Kramers degeneracy is broken and antiferromagnetic exchange is stronger. Further structural studies, using dilatometry and total x-ray scattering on single crystals, and probes such as magnetostriction or Raman scattering [55], may provide smoking gun signatures of octupolar order in these $5d^2$ materials.

This work was supported by the Natural Sciences and Engineering Research Council of Canada. It was also supported in part by the National Science Foundation under Grant No. PHYS-1066293 and the hospitality of the Aspen Center for Physics. We also acknowledge the hospitality of the Telluride Science Research Center. We gratefully acknowledge useful conversations with G. M. Luke and G. Chen. We are very grateful for the instrument and sample environment support provided during our inelastic neutron scattering measurements at SEQUOIA. The experiments which were performed at the Spallation Neutron Source at Oak Ridge National Laboratory were sponsored by the U.S. Department of Energy, Office of the Basic Energy Sciences, Scientific User Facilities Division. The authors would also like to acknowledge ILL for beam time allocation experiment code 5-31-2577. We acknowledge the BL04-MSPD staff of ALBA for the x-ray synchrotron powder diffraction data collection.

*maharadd@mcmaster.ca

[1] W. Witczak-Krempa, G. Chen, Y. B. Kim, and L. Balents, Annu. Rev. Condens. Matter Phys. **5**, 57 (2014).
[2] K. V. Shanavas, Z. S. Popović, and S. Satpathy, Phys. Rev. B **90**, 165108 (2014).
[3] G. Chen, R. Pereira, and L. Balents, Phys. Rev. B **82**, 174440 (2010).
[4] G. Chen and L. Balents, Phys. Rev. B **84**, 094420 (2011).
[5] C. Svoboda, M. Randeria, and N. Trivedi, Phys. Rev. B **95**, 014409 (2017).
[6] C. Svoboda, M. Randeria, and N. Trivedi, arXiv:1702.03199.
[7] J. Chaloupka, G. Jackeli, and G. Khaliullin, Phys. Rev. Lett. **105**, 027204 (2010).
[8] Y. Singh, S. Manni, J. Reuther, T. Berlijn, R. Thomale, W. Ku, S. Trebst, and P. Gegenwart, Phys. Rev. Lett. **108**, 127203 (2012).
[9] K. W. Plumb, J. P. Clancy, L. J. Sandilands, V. V. Shankar, Y. F. Hu, K. S. Burch, H.-Y. Kee, and Y.-J. Kim, Phys. Rev. B **90**, 041112(R) (2014).
[10] S. Hwan Chun, J.-W. Kim, J. Kim, H. Zheng, C. C. Stoumpos, C. D. Malliakas, J. F. Mitchell, K. Mehlawat, Y. Singh, Y. Choi, T. Gog, A. Al-Zein, M. M. Sala, M. Krisch, J. Chaloupka, G. Jackeli, G. Khaliullin, and B. J. Kim, Nat. Phys. **11**, 462 (2015).
[11] A. Banerjee, C. A. Bridges, J. Q. Yan, A. A. Aczel, L. Li, M. B. Stone, G. E. Granroth, M. D. Lumsden, Y. Yiu, J. Knolle, S. Bhattacharjee, D. L. Kovrizhin, R. Moessner, D. A. Tennant, D. G. Mandrus, and S. E. Nagler, Nat. Mater. **15**, 733 (2016).
[12] S. M. Winter, A. A. Tsirlin, M. Daghofer, J. van den Brink, Y. Singh, P. Gegenwart, and R. Valentí, J. Phys. Condens. Matter **29**, 493002 (2017).
[13] Y. Kasahara, T. Ohnishi, Y. Mizukami, O. Tanaka, S. Ma, K. Sugii, N. Kurita, H. Tanaka, J. Nasu, Y. Motome, T. Shibauchi, and Y. Matsuda, Nature (London) **559**, 227 (2018).
[14] J. Romhányi, L. Balents, and G. Jackeli, Phys. Rev. Lett. **118**, 217202 (2017).
[15] L. Lu, M. Song, W. Liu, A. P. Reyes, P. Kuhns, H. O. Lee, I. R. Fisher, and V. F. Mitrović, Nat. Commun. **8**, 14407 (2017).
[16] W. Liu, R. Cong, E. Garcia, A. Reyes, H. Lee, I. Fisher, and V. Mitrovi, Physica (Amsterdam) **536B**, 863 (2018).
[17] D. Hirai and Z. Hiroi, J. Phys. Soc. Jpn. **88**, 064712 (2019).
[18] C. M. Thompson, J. P. Carlo, R. Flacau, T. Aharen, I. A. Leahy, J. R. Pollichemi, T. J. S. Munsie, T. Medina, G. M. Luke, J. Munevar, S. Cheung, T. Goko, Y. J. Uemura, and J. E. Greedan, J. Phys. Condens. Matter **26**, 306003 (2014).

[19] E. Kermarrec, C. A. Marjerrison, C. M. Thompson, D. D. Maharaj, K. Levin, S. Kroeker, G. E. Granroth, R. Flacau, Z. Yamani, J. E. Greedan, and B. D. Gaulin, Phys. Rev. B **91**, 075133 (2015).

[20] C. A. Marjerrison, C. M. Thompson, A. Z. Sharma, A. M. Hallas, M. N. Wilson, T. J. S. Munsie, R. Flacau, C. R. Wiebe, B. D. Gaulin, G. M. Luke, and J. E. Greedan, Phys. Rev. B **94**, 134429 (2016).

[21] P. Santini, S. Carretta, G. Amoretti, R. Caciuffo, N. Magnani, and G. H. Lander, Rev. Mod. Phys. **81**, 807 (2009).

[22] P. Santini and G. Amoretti, Phys. Rev. Lett. **85**, 2188 (2000).

[23] J. A. Paixão, C. Detlefs, M. J. Longfield, R. Caciuffo, P. Santini, N. Bernhoeft, J. Rebizant, and G. H. Lander, Phys. Rev. Lett. **89**, 187202 (2002).

[24] A. Kiss and P. Fazekas, Phys. Rev. B **68**, 174425 (2003).

[25] Y. Tokunaga, D. Aoki, Y. Homma, S. Kambe, H. Sakai, S. Ikeda, T. Fujimoto, R. E. Walstedt, H. Yasuoka, E. Yamamoto, A. Nakamura, and Y. Shiokawa, Phys. Rev. Lett. **97**, 257601 (2006).

[26] K. Haule and G. Kotliar, Nat. Phys. **5**, 796 (2009).

[27] H.-H. Kung, R. E. Baumbach, E. D. Bauer, V. K. Thorsmølle, W.-L. Zhang, K. Haule, J. A. Mydosh, and G. Blumberg, Science **347**, 1339 (2015).

[28] H.-H. Kung, S. Ran, N. Kanchanavatee, V. Krapivin, A. Lee, J. A. Mydosh, K. Haule, M. B. Maple, and G. Blumberg, Phys. Rev. Lett. **117**, 227601 (2016).

[29] A. Sakai and S. Nakatsuji, J. Phys. Soc. Jpn. **80**, 063701 (2011).

[30] T. J. Sato, S. Ibuka, Y. Nambu, T. Yamazaki, T. Hong, A. Sakai, and S. Nakatsuji, Phys. Rev. B **86**, 184419 (2012).

[31] M. Tsujimoto, Y. Matsumoto, T. Tomita, A. Sakai, and S. Nakatsuji, Phys. Rev. Lett. **113**, 267001 (2014).

[32] L. Fu, Phys. Rev. Lett. **115**, 026401 (2015).

[33] J. W. Harter, Z. Y. Zhao, J.-Q. Yan, D. G. Mandrus, and D. Hsieh, Science **356**, 295 (2017).

[34] S. Hayami, H. Kusunose, and Y. Motome, Phys. Rev. B **97**, 024414 (2018).

[35] See Supplemental Material at http://link.aps.org/supplemental/10.1103/PhysRevLett.124.087206 for experiment details (Part I), time-of-flight inelastic neutron scattering (Part I A), high intensity neutron powder diffraction (Part I B), high angular resolution x-ray diffraction (Part I C), theory (Part II), and the single-site model, multipole moments (Part II A).

[36] K. Yamamura, M. Wakeshima, and Y. Hinatsu, J. Solid State Chem. **179**, 605 (2006).

[37] R. Morrow, A. E. Taylor, D. J. Singh, J. Xiong, S. Rodan, A. U. B. Wolter, S. Wurmehl, B. Büchner, M. B. Stone, A. I. Kolesnikov, A. A. Aczel, A. D. Christianson, and P. M. Woodward, Sci. Rep. **6**, 32462 (2016).

[38] D. D. Maharaj, G. Sala, C. A. Marjerrison, M. B. Stone, J. E. Greedan, and B. D. Gaulin, Phys. Rev. B **98**, 104434 (2018).

[39] A. E. Taylor, R. Morrow, D. J. Singh, S. Calder, M. D. Lumsden, P. M. Woodward, and A. D. Christianson, Phys. Rev. B **91**, 100406(R) (2015).

[40] C. M. Thompson, C. A. Marjerrison, A. Z. Sharma, C. R. Wiebe, D. D. Maharaj, G. Sala, R. Flacau, A. M. Hallas, Y. Cai, B. D. Gaulin, G. M. Luke, and J. E. Greedan, Phys. Rev. B **93**, 014431 (2016).

[41] A. A. Aczel, D. E. Bugaris, L. Li, J.-Q. Yan, C. de la Cruz, H. C. zur Loye, and S. E. Nagler, Phys. Rev. B **87**, 014435 (2013).

[42] J. Xiong, J. Yan, A. A. Aczel, and P. M. Woodward, J. Solid State Chem. **258**, 762 (2018).

[43] R. T. Azuah, L. R. Kneller, Y. Qiu, P. L. W. Tregenna-Piggott, C. M. Brown, J. R. D. Copley, and R. M. Dimeo, J. Res. Natl. Inst. Stand. Technol. **114**, 341 (2009).

[44] O. Arnold *et al.*, Nucl. Instrum. Methods Phys. Res., Sect. A **764**, 156 (2014).

[45] J. Rodriguez-Carvajal, Physica (Amsterdam) **192B**, 55 (1993).

[46] K. Kobayashi, T. Nagao, and M. Ito, Acta Crystallogr. Sect. A **67**, 473 (2011).

[47] P. J. van der Linden, M. Moretti Sala, C. Henriquet, M. Rossi, F. Ohgushi, K. Fauth, L. Simonelli, C. Marini, E. Fraga, C. Murray, J. Potter, and M. Krisch, Rev. Sci. Instrum. **87**, 115103 (2016).

[48] T. C. Hansen, P. F. Henry, H. E. Fischer, J. Torregrossa, and P. Convert, Meas. Sci. Technol. **19**, 034001 (2008).

[49] E. Kermarrec, B. D. Gaulin, M. Dalini, and R. Clemens, *Magnetic Ordering and Ground State Selection in the Frustrated 5d2 and 5d1 FCC Double Perovskites A2BB'O6 with Neutron Diffraction* (Institut Laue-Langevin, 2018), https://doi.ill.fr/10.5291/ILL-DATA.5-31-2577.

[50] G. E. Granroth, A. I. Kolesnikov, T. E. Sherline, J. P. Clancy, K. A. Ross, J. P. C. Ruff, B. D. Gaulin, and S. E. Nagler, J. Phys. Conf. Ser. **251**, 012058 (2010).

[51] J. P. Carlo, J. P. Clancy, K. Fritsch, C. A. Marjerrison, G. E. Granroth, J. E. Greedan, H. A. Dabkowska, and B. D. Gaulin, Phys. Rev. B **88**, 024418 (2013).

[52] F. Fauth, I. Peral, C. Popescu, and M. Knapp, Powder Diffr. **28**, S360 (2013).

[53] W. Liu, R. Cong, A. P. Reyes, I. R. Fisher, and V. F. Mitrović, Phys. Rev. B **97**, 224103 (2018).

[54] A. Paramekanti, D. D. Maharaj, and B. D. Gaulin, companion paper, Phys. Rev. B **101**, 054439 (2020).

[55] A. S. Patri, A. Sakai, S. Lee, A. Paramekanti, S. Nakatsuji, and Y. B. Kim, Nat. Commun. **10**, 4092 (2019).

Supplemental Material: Octupolar vs Néel Order in Cubic $5d^2$ Double Perovskites

D. D. Maharaj,[1,*] G. Sala,[1,2] M. B. Stone,[2] E. Kermarrec,[1,3] C. Ritter,[4] F. Fauth,[5] C. A. Marjerrison,[6] J. E. Greedan,[6,7] A. Paramekanti,[8] and B. D. Gaulin[1,6,9]

[1]*Department of Physics and Astronomy, McMaster University, Hamilton, ON L8S 4M1 Canada*
[2]*Neutron Scattering Division, Oak Ridge National Laboratory, Oak Ridge, Tennessee 37831, USA*
[3]*Université Paris-Saclay, CNRS, Laboratoire de Physique des Solides, 91405 Orsay, France*
[4]*Institut Laue-Langevin, Boîte Postale 156, 38042 Grenoble Cédex, France*
[5]*CELLS-ALBA Synchrotron, Carrer de la Llum 2-26, 08290 Cerdanyola del Vallès, Barcelona, Spain*
[6]*Brockhouse Institute for Materials Research, McMaster University, Hamilton, ON L8S 4M1 Canada*
[7]*Department of Chemistry and Chemical Biology, McMaster University, ON, L8S 4M1, Canada*
[8]*Department of Physics, University of Toronto, 60 St. George Street, Toronto, ON, M5S 1A7 Canada*
[9]*Canadian Institute for Advanced Research, 661 University Ave., Toronto, ON M5G 1M1 Canada*

(Dated: February 21, 2020)

Details relevant to both experimental and theoretical aspects of the main paper are discussed in this supplemental material. Experimental methods for the time-of-flight inelastic neutron scattering (INS), neutron powder diffraction (NPD) and high angular resolution x-ray powder diffraction (XRD) measurements are fully explained in section I., parts A, B and C. An outline of the calculations which were performed in order to estimate the upper bound on the ordered magnetic moment in Ba_2CaOsO_6 (BCO), Ba_2MgOsO_6 (BMO), and Ba_2ZnOsO_6 (BZO) is provided in section I B. part 2. Section I. C, parts 1 - 2 contain a detailed analysis of the XRD data sets for BCO which were collected over a range of temperatures from 200K down to 20K. Section II provides details regarding the theoretical argument for the ground and excited state wavefunctions for the two-electron system in $5d^2$ ions, arising from the cubic crystal-field splitting of the renormalized two-electron wavefunction.

I. EXPERIMENT DETAILS

A. Time-of-flight Inelastic Neutron Scattering

Methods – The INS measurements were conducted using the direct geometry chopper spectrometer SEQUOIA, which is located at the Spallation Neutron Source[1] of Oak Ridge National Laboratory. Powder samples weighing 8 grams of BMO, BZO, and BCO were packed tightly in aluminum foil and loaded in identical annular cans, 3 cm in diameter. An identical empty can was also prepared for background measurements. The sample cans and empty can were sealed in a glove box containing helium gas to improve thermalization of samples at low temperatures. The cans were loaded on a three-sample carousel mounted in a closed-cycle refrigerator with a base temperature of 7 K. Inelastic neutron scattering (INS) measurements were carried out on BMO and BZO at a variety of temperatures above and below T^*, using an incident energy of $E_i = 60$ meV while in the case of BCO, the incident energy chosen was $E_i = 90$ meV. The chopper settings utilized for both incident energies were the same. The chopper settings selected for the fast neutron chopper (T_0) and the high flux fermi chopper (FC_1) were $T_0 = 240$ Hz, and $FC_1 = 120$ Hz, respectively. Empty can background data sets were collected at base temperature, and $T = 200\,K$, and correspondingly subtracted from the data sets. The data sets were reduced using Mantid[2] and analyzed using neutron scattering software DAVE[3].

B. High Intensity Neutron Powder Diffraction

1. Methods

NPD data were collected on the two-axis high intensity diffractometer D20 (Institut Laue Langevin, Grenoble, France)[4] using a wavelength of $\lambda = 2.41$ Å selected by a Graphite monochromator using a take-off angle of 42°. The powder samples of BCO and BMO were those utilized for the INS measurements while a new sample of BZO was synthesized for the NPD measurements. Measurements were taken at a base temperature of 10 K for 10 hrs on BZO for 11 hrs on BMO and at 1.5 K for 11 hrs on BCO. A higher base temperature was selected for the former compounds to avoid probing any features which could arise from the ferromagnetic ordering of the impurity phase $Ba_{11}Os_4O_{24}$ which was reported to be present at low levels in these compounds[5]. High temperature data sets with the same statistics were taken at T = 50 K for BZO and at T = 70 K for both BMO and BCO. Data analysis was performed using the Rietveld refinement program FULLPROF[6] and the resulting refinement parameters are shown in Table I.

2. Magnetic Neutron Profile Calculations

The NPD measurements performed at D20 show no evidence for magnetic order of the Os^{6+} ions in BCO,

TABLE I. The table shows results from Rietveld refinements of the low temperature and high temperature neutron powder diffraction data sets obtained from D20 at the ILL, assuming $Fm\bar{3}m$ symmetry. The refined atomic parameters, site occupancies (i.e. chemical occupancy × site multiplicity), lattice parameter a, volume of the unit cell V, goodness of fit R_{Bragg} and overall thermal parameter B_{ov} are quoted.

Low Temperature Structural Refinements with $Fm\bar{3}m$ Symmetry					
	Atom	x	y	z	*Site Occupancy*
Ba_2ZnOsO_6					
$(T = 10K)$	Ba	0.25	0.25	0.25	0.042
$a = 8.07858(32)$Å	Zn	0.5	0.5	0.5	0.021
$V = 527.236(36)$Å^3	Os	0.00	0.00	0.00	0.021
$R_{Bragg} = 1.18$	O(1)	0.23936(19)	0.00	0.00	0.125
$B_{ov} = 0.15383$Å^2					
Ba_2MgOsO_6					
$(T = 10K)$	Ba	0.25	0.25	0.25	0.042
$a = 8.05861(41)$Å	Mg	0.5	0.5	0.5	0.021
$V = 523.336(46)$Å^3	Os	0.00	0.00	0.00	0.021
$R_{Bragg} = 1.82$	O(1)	0.23956(26)	0.00	0.00	0.125
$B_{ov} = 0.00110$Å^2					
Ba_2CaOsO_6					
$(T = 1.5K)$	Ba	0.25	0.25	0.25	0.042
$a = 8.34558(35)$Å	Ca	0.5	0.5	0.5	0.021
$V = 581.258(42)$Å^3	Os	0.00	0.00	0.00	0.021
$R_{Bragg} = 2.38$	O(1)	0.22897(16)	0.00	0.00	0.125
$B_{ov} = 0.04292$Å^2					
High Temperature Structural Refinements with $Fm\bar{3}m$ Symmetry					
	Atom	x	y	z	*Site Occupancy*
Ba_2ZnOsO_6					
$(T = 50K)$	Ba	0.25	0.25	0.25	0.042
$a = 8.07908(32)$Å	Zn	0.5	0.5	0.5	0.021
$V = 527.334(36)$Å^3	Os	0.00	0.00	0.00	0.021
$R_{Bragg} = 1.18$	O(1)	0.23932(19)	0.00	0.00	0.125
$B_{ov} = 0.16554$Å^2					
Ba_2MgOsO_6					
$(T = 70K)$	Ba	0.25	0.25	0.25	0.042
$a = 8.05972(40)$Å	Mg	0.5	0.5	0.5	0.021
$V = 523.552(45)$Å^3	Os	0.00	0.00	0.00	0.021
$R_{Bragg} = 1.85$	O(1)	0.23950(26)	0.00	0.00	0.125
$B_{ov} = 0.01855$Å^2					
Ba_2CaOsO_6					
$(T = 70K)$	Ba	0.25	0.25	0.25	0.042
$a = 8.34719(35)$Å	Ca	0.5	0.5	0.5	0.021
$V = 581.96(42)$Å^3	Os	0.00	0.00	0.00	0.021
$R_{Bragg} = 2.30$	O(1)	0.22904(16)	0.00	0.00	0.125
$B_{ov} = 0.08909$Å^2					

BMO and BZO. A limit for the upper bound on the magnetic moment potentially present at low temperatures in these materials can still be performed, and used for comparison with other double perovskites. This involves assuming a magnetic structure, and we employed a simple type 1 AF structure, as is observed in a variety of d^3 double perovskites. FULLPROF was utilized to calculate the diffraction pattern due to the assumed magnetic structure alone, for each compound. Each calculation was performed utilizing the lattice parameters determined from fits to the low temperature data sets for each compound. The magnetic form factor for Os^{6+} was also included in this calculation, using parameters extracted from previous work done by Kobayashi *et al*[7]. The result from this calculation was then compared with the plots showing the difference between the high temperature data set from the low temperature data set. This calculation produced a strong magnetic Bragg peak near ~ 0.76 Å^{-1}, corresponding to the type I AF structure, whose intensity depended on the size of the ordered moment in the structure. The ordered moment was then adjusted until this magnetic peak was just observable above background, thus setting the upper bound to the size of a possible ordered magnetic moment in these materials. Upper bounds for the ordered Os^{6+} moments of $0.13\mu_B$, $0.11\mu_B$, and $0.06\mu_B$ were obtained for BCO, BMO and BZO, respectively. The difference data sets are shown for all compounds in the low $|Q|$ range, $|Q| < 3$ Å^{-1} in Fig. 1.

C. High Angular Resolution X-ray Diffraction

Methods – Synchrotron X-ray diffraction experiments were performed on the powder diffraction station of the BL04-MSPD beamline[8] of the ALBA Synchrotron Light facility (Barcelona, Spain). Data were collected in transmission mode using the 13 channel multi-analyzer (MAD) setup (220 Bragg reflection of silicon crystal) which offers the highest possible instrumental angular resolution ($\Delta 2\theta = 0.005°$). In order to minimize absorption, the patterns were recorded at a short wavelength, $\lambda = 0.31713$ Å, with the sample filled in a 0.5 mm diameter borosilicate capillary. Data were recorded in the temperature range between 20 K and 250 K using the liquid Helium flow cryostat Dynaflow[9]. The resulting refinement parameters are shown in Table 2.

1. *Bragg Peak Widths as a Function of Temperature*

As the presence/absence of *local* distortions in the double perovskite lattice do not manifest as a global symmetry lowering of the compound, this detail must be investigated by analysing the width and lineshape of the nuclear Bragg peaks. If present, local distortions will lead to progressive broadening of the nuclear Bragg peaks below the transition temperature of BCO ($T^* = 50\,K$). To illustrate this, raw data for two different Bragg reflections, the (660) and (800) are shown at three temperatures T = 20 K, 70 K and 250 K in Figure 2. These data sets have had their peak positions in $|Q|$ recentered to correct for thermal expansion. It is clear that these nuclear Bragg peaks do not broaden appreciably with decreasing

TABLE II. The table shows results from Rietveld refinements of the synchrotron x-ray data sets obtained at the BL04-MSPD beamline at ALBA[8] at all measured temperatures, assuming $Fm\bar{3}m$ symmetry. Only the refined atomic parameter for $O(1)$ is provided. The special positions of the are omitted to avoid repetitive details (see Table I for the special positions of Ba, Ca and Os, for example). The site occupancies (i.e. chemical occupancy × site multiplicity), lattice parameter a, volume of the unit cell V, goodness of fit R_{Bragg} and overall thermal parameter B_{ov} are quoted.

Refined Parameters for Ba_2CaOsO_6 Synchrotron Data							
	$20K$	$50K$	$70K$	$100K$	$150K$	$200K$	$250K$
O1(x)	0.23164(8)	0.23102(81)	0.23215(84)	0.23241(83)	0.23122(83)	0.23181(84)	0.23108(86)
a(Å)	8.33198(2)	8.33291(1)	8.33361(1)	8.33494(1)	8.33781(1)	8.34121(1)	8.34492(1)
V(Å^3)	578.422(1)	578.616(1)	578.761(1)	579.038(1)	579.637(1)	580.346(1)	581.121(1)
R_{Bragg} (%)	1.97	2.06	1.95	2.08	1.86	1.82	2.01
B_{ov}(Å^2)	0.02	0.02	0.02	0.02	0.02	0.02	0.02

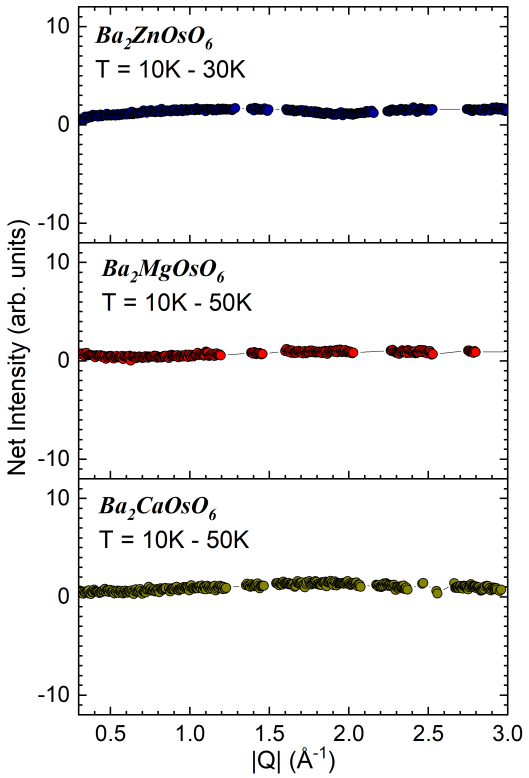

FIG. 1. The temperature difference plots for Ba_2ZnOsO_6, Ba_2MgOsO_6 and Ba_2CaOsO_6 are shown for the range $|Q| < 3\,\text{Å}^{-1}$ for reference. Data in regions of $|Q|$ overlapping with allowed nuclear Bragg peaks have been omitted. Flat profiles are obtained exhibiting the absence of magnetic Bragg peaks indicative of magnetic long-range order at any low $|Q|$ position.

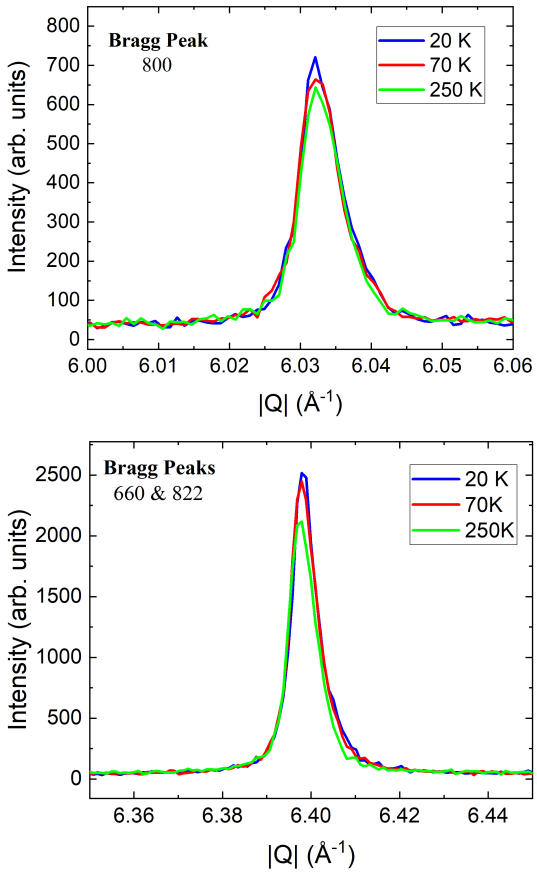

FIG. 2. The evolution of the measured XRD lineshapes for Ba_2CaOsO_6 of the 800 (top) and 660 (bottom) Bragg peaks are shown as a function of temperature.

temperature, providing no evidence for local distortions.

2. *Simulated Distortions of Cubic Ba_2CaOsO_6*

To illustrate the limits of our ability to detect global distortions of the double perovskite lattice in BCO, we have performed simulations using FULLPROF. In these simulations, we calculate diffraction profiles for slightly distorted versions of BCO. To simulate this distortion, we hypothetically consider a distortion of the $Fm\bar{3}m$ cubic lattice to $I4/m$ symmetry. The c-axis is stretched at the 0.1 % and 0.5 % level and the results compared against the raw data profiles obtained from our XRD measurements on BCO as shown in Figure 3. As it can be seen, our high resolution XRD measurements can set a strict upper limit of $\frac{\Delta a}{a} < 0.1\%$, for such a putative tetragonal distortion.

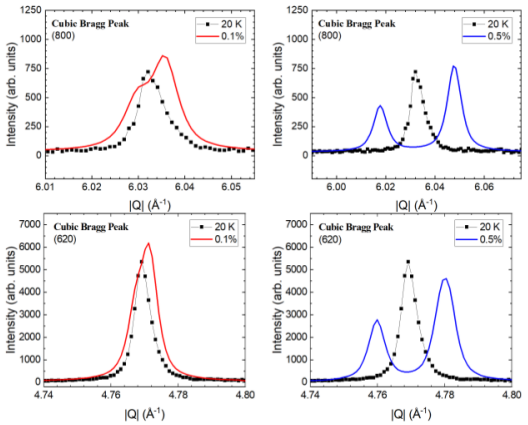

FIG. 3. Simulated distortions of the Ba_2CaOsO_6 structure to the lower $I4/m$ symmetry are compared with the raw data sets. In the presence of a global symmetry lowering of the structure, the splitting would be clearly visible down to at least the 0.1% level.

3. *Entropy Released at T^**

As discussed in the main paper, the entropy released in all three of BCO, BZO, and BMO up to $\sim 2T^*$ is $\sim R\ln(2)$ per mole = 5.75 J/mole·K, much smaller than the $R\ln(5)$ per mole = 13.37 J/mole·K expected for a J = 2 moment. A calculation of the magnetic entropy released around T^* in BCO is not available, because the original reference does not contain a correct estimate for the magnetic heat capacity since the lattice contribution to the heat capacity could not be reliably estimated[10]. However, an explicit estimation can be obtained for BZO and BMO. We perform this explicit calculation based on earlier heat capacity measurements by Marjerrison *et al*[5] and these are shown in Fig. 4. The result is that the entropy released around T^* is $\sim$ 6.3 and 4.8 J/mole·K in BZO and BMO respectively, both roughly consistent with $R\ln(2)$ and much less than $R\ln(5)$.

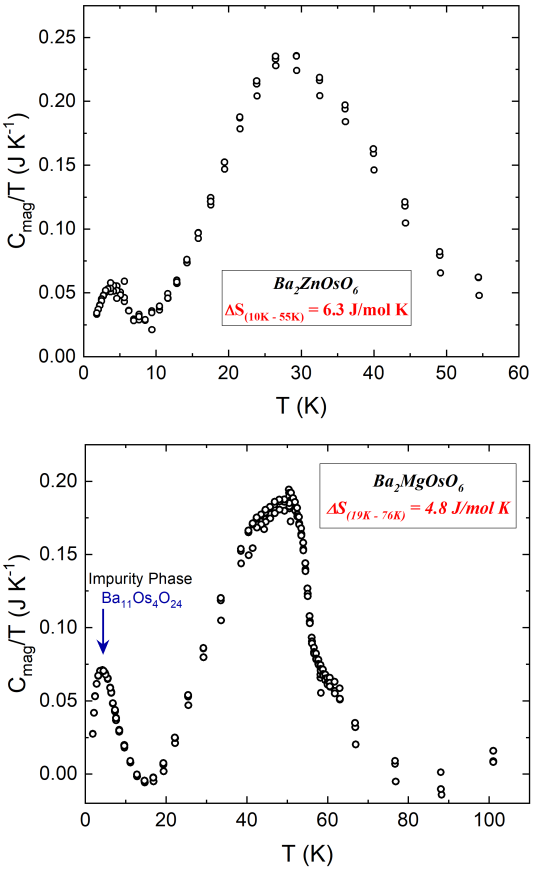

FIG. 4. The experimental entropy loss for Ba_2ZnOsO_6 and Ba_2MgOsO_6 between $T > T^*$ to $T < T^*$ are shown in top and bottom panels respectively. As it can be seen, the entropy loss is close to $R\ln(2)$, which is much less than what is expected $R\ln(5)$ in the absence of the crystal-field splitting of the renormalized two-electron levels.

II. THEORY

A. Single-site model, multipole moments

We begin with an effective $J = 2$ moment and incorporate the impact of a residual octahedral crystal field via

$$H_{\mathrm{CEF}'} = -V_{\mathrm{eff}}(\mathcal{O}_{40} + 5\mathcal{O}_{44}), \qquad (1)$$

where the Steven's operators

$$\mathcal{O}_{40} = 35J_z^4 - (30J(J+1) - 25)J_z^2 + 3J^2(J+1)^2 - 6J(J+1) \quad (2)$$

$$\mathcal{O}_{44} = \frac{1}{2}(J_+^4 + J_-^4), \quad (3)$$

For $V_{\rm eff} > 0$, we find that the $J = 2$ multiplet splits into a ground doublet and an excited triplet with a gap $\Delta = 120V_{\rm eff}$. Choosing $V_{\rm eff} = 0.2\,$meV, for example, leads to a doublet-triplet gap $\Delta \sim 24\,$meV.

The ground state wavefunctions in the $|m\rangle$ basis are

$$|\psi_{g,\uparrow}\rangle = |0\rangle \quad (4)$$

$$|\psi_{g,\downarrow}\rangle = \frac{1}{\sqrt{2}}(|2\rangle + |-2\rangle) \quad (5)$$

while the excited state wavefunctions are given by

$$|\psi_{e,\pm}\rangle = |\pm 1\rangle \quad (6)$$

$$|\psi_{e,0}\rangle = \frac{1}{\sqrt{2}}(|2\rangle - |-2\rangle) \quad (7)$$

This sequence of level splittings for the $5d^2$ configuration is schematically described in Fig. 5. The rightmost level scheme results from the familiar splitting of the $5d$ levels in an octahedral crystal electric field (CEF). Strong spin orbit coupling (SOC) then splits the t_{2g} levels into an higher energy $j = 1/2$ doublet and a lower energy quartet, corresponding to $j = 3/2$. The two d electrons then occupy the $j = 3/2$ levels, and combine to give a $J_{\rm eff} = 2$ degree of freedom. A residual crystal field, arising from electron-interaction induced change in the CEF splitting (denoted as CEF') gives the final non-Kramers doublet ground state with octupolar and quadrupolar moments (discussed below), and an excited state triplet, some 15 to 30 meV above the octupolar doublet.

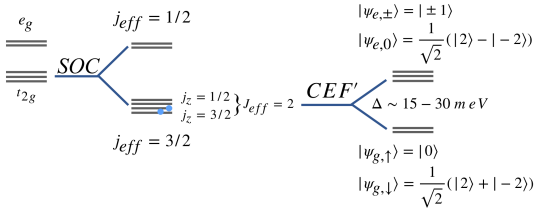

FIG. 5. The splitting of the energy levels of the $5d^2$ Os^{6+} ion is schematically illustrated. The $5d$ levels are acted on by the octahedral crystal-electric field (CEF) of the lattice, strong spin-orbit coupling (SOC), and finally a residual cubic CEF due to electron-interaction induced change in the CEF splitting (denoted here as CEF') that results in a non-Kramers doublet ground state with quadrupolar and octupolar moments, and a weakly split off triplet of excited states some 15-30 meV higher in energy. The ground state and excited state wavefunctions of the d^2 ion are explicity stated in the figure.

It is clear that the ground state manifold has vanishing matrix elements for the dipolar vector operators $\vec{J}$. However, $\vec{J}$ can induce transitions between the ground doublet and the excited triplet. We thus attribute the observed spin gap to this doublet-triplet gap Δ.

Defining the pseudospin-1/2 operators $\vec{\tau}$ within the ground state doublet, we find that the quadrupolar operators $(J_x^2 - J_y^2) \equiv 2\sqrt{3}\tau_x$, $(3J_z^2 - J^2) \equiv -6\tau_z$, while the octupolar operator $\overline{J_xJ_yJ_z} \equiv -\sqrt{3}\tau_y$ where the overline denotes symmetrization.

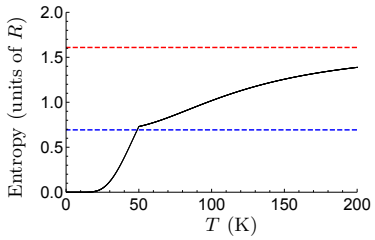

FIG. 6. Entropy of the single-site model (solid) line in units of R as a function of temperature, showing the quenching of the entropy from $R\ln(5)$ at high temperature to $\ll R\ln(5)$ (dashed lines denote $R\ln(5)$ and $R\ln(2)$) for $T \sim 100\,$K, which is further quenched by octupolar ordering at $T^* = 50\,$K.

In the single-site limit, we can easily compute the following results for the entropy and the magnetic susceptibility. Here, we pick $V_0 = 0.2\,$meV as above, and include a local octupolar symmetry breaking field, in the spirit of mean field theory, via

$$H = H_{\rm CEF} - \phi(T)\ \overline{J_xJ_yJ_z}. \quad (8)$$

As an illustrative example, we choose the symmetry breaking field $\phi(T)$ to be given by the simple form $\phi(T < T^*) = T^*\sqrt{1 - T/T^*}$ and $\phi(T > T^*) = 0$.

The entropy, shown in Fig. 6, starts at $R\ln(5)$ at high temperature, before decreasing to $\ll R\ln(5)$ for $T \lesssim 100\,$K. This residual low temperature entropy of near $R\ln(2)$ is quenched by ordering of the doublet states induced by intersite interactions for $T < T^*$.

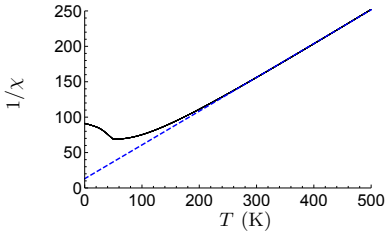

FIG. 7. Plot of the inverse susceptibility $1/\chi$ of the single-site model as a function of temperature, showing its apparent 'Curie-Weiss' like behavior at high temperature (indicated by the dashed fit) and its eventual saturation at low temperature, arising from the spin-gap, with the kink denoting the octupolar transition.

The inverse spin susceptibility, in units where a free spin-S leads to the Curie susceptibility $S(S+1)/3T$, is shown in Fig. 7. It is clear that the spin gap induces an effective 'antiferromagnetic Curie-Weiss' type behavior, with an intercept at $T \approx -30\,\mathrm{K}$. The larger Curie-Weiss temperature $\Theta_{\mathrm{CW}} \approx -150\,\mathrm{K}$ inferred from experiments must thus stem from residual intersite interactions.

* maharadd@mcmaster.ca

[1] G. E. Granroth, A. I. Kolesnikov, T. E. Sherline, J. P. Clancy, K. A. Ross, J. P. C. Ruff, B. D. Gaulin, and S. E. Nagler, Journal of Physics: Conference Series **251**, 012058 (2010).

[2] O. Arnold, J. Bilheux, J. Borreguero, A. Buts, S. Campbell, L. Chapon, M. Doucet, N. Draper, R. F. Leal, M. Gigg, V. Lynch, A. Markvardsen, D. Mikkelson, R. Mikkelson, R. Miller, K. Palmen, P. Parker, G. Passos, T. Perring, P. Peterson, S. Ren, M. Reuter, A. Savici, J. Taylor, R. Taylor, R. Tolchenov, W. Zhou, and J. Zikovsky, Nuclear Instruments and Methods in Physics Research Section A: Accelerators, Spectrometers, Detectors and Associated Equipment **764**, 156 (2014).

[3] R. T. Azuah, L. R. Kneller, Y. Qiu, P. L. W. Tregenna-Piggott, C. M. Brown, J. R. D. Copley, and R. M. Dimeo, J. Res. Natl. Inst. Stand. Technol. **114**, 341 (2009).

[4] T. C. Hansen, P. F. Henry, H. E. Fischer, J. Torregrossa, and P. Convert, Measurement Science and Technology **19**, 034001 (2008).

[5] C. A. Marjerrison, C. M. Thompson, A. Z. Sharma, A. M. Hallas, M. N. Wilson, T. J. S. Munsie, R. Flacau, C. R. Wiebe, B. D. Gaulin, G. M. Luke, and J. E. Greedan, Phys. Rev. B **94**, 134429 (2016).

[6] J. Rodriguez-Carvajal, Physica B **192**, 55 (1993).

[7] K. Kobayashi, T. Nagao, and M. Ito, Acta Crystallographica Section A **67**, 473 (2011).

[8] F. Fauth, I. Peral, C. Popescu, and M. Knapp, Powder Diffr. **28**, S360 (2013).

[9] P. J. van der Linden, M. Moretti Sala, C. Henriquet, M. Rossi, F. Ohgushi, K. Fauth, L. Simonelli, C. Marini, E. Fraga, C. Murray, J. Potter, and M. Krisch, Rev. Sci. Instrum. **87**, 115103 (2016).

[10] K. Yamamura, M. Wakeshima, and Y. Hinatsu, Journal of Solid State Chemistry **179**, 605 (2006).

7 Conclusions and Outlook

"All's well that ends well" — *John Heywood*

The effect of stuffing in $Yb_2Ti_2O_7$

In this thesis, neutron scattering studies were conducted on a series of magnetic oxides which are based on frustrated tetrahedral architectures. Two stuffed samples of the rare-earth titanate, $Yb_2Ti_2O_7$, were investigated to discern the effect of stuffing on the ground state anisotropy of Yb^{3+} ions at defective sites in the $R_2Ti_2O_7$ lattice. The $4d$ and $5d$ double perovskite magnets which were investigated exhibit exotic ground states which are stabilized by spin-orbit coupling. The monoclinic d^3 double perovskite magnets, La_2LiOsO_6 and La_2LiRuO_6, were found to host the same type I antiferromagnetic long-range ordered ground state which related cubic d^3 systems possess. Significantly, the d^2 double perovskites systems Ba_2CaOsO_6, Ba_2MgOsO_6 and Ba_2ZnOsO_6 have been classified as candidates to exhibit exotic octupolar order.

Chapter 4 describes our neutron scattering measurements which were conducted on two stuffed samples of $Yb_2Ti_2O_7$. These samples are described by the chemical formula $Yb_{(2+x)}Ti_{(2-x)}O_7$, with concentrations x = 0.11 and x = 0.19. This study was conducted to probe the crystal-field excitations associated with the Yb^{3+} ions at the B site and A site in the presence of oxygen vacancies. The complete crystal-field spectra were measured in each case enabling the determination of the ground state anisotropy of the Yb^{3+} ions at the two defective sites. The anisotropic g-tensor values for the Yb^{3+} moments were found to be $g_\perp = 3.69 \pm 0.15$, $g_z = 1.92 \pm 0.20$ at the A site, $g_\perp$

$= 1.5 \pm 0.2$, gz $= 6.8 \pm 0.7$ at the A' site and $g_\perp = 0.07 \pm 0.03$, $g_z = 8.0 \pm 0.8$ at the B site. It is well-known that Yb^{3+} ions at their nominal A site possess an XY like anisotropy. As it can be seen here however, the Yb^{3+} moments at the two defective sites posses Ising-like anisotropy. Another key result of our crystal-field study is that the defective Yb^{3+} moments possess a significantly larger moment with $\mu = 3.5\mu_B$ at the A' site and $\mu = 4.0\mu_B$ at the B site. This should be compared with the magnetic moment of the A site Yb^{3+} ions which is $\mu = 2.07\mu_B$. The unusually strong sensitivity of $Yb_2Ti_2O_7$'s ground state to sample stoichiometry can be attributed to the effect of defective Yb^{3+} Ising moments in randomizing dipolar interactions, which are well understood to be of great influence on the nature of the ground state exhibited by $R_2Ti_2O_7$ compounds.

An additional avenue in the research of stuffed $Yb_2Ti_2O_7$ can involve the investigation of a mixed compound with formula $Yb_{(2-x)}Y_xTi_2O_7$. Introduction of weak chemical disorder via nonmagnetic yttrium at random A sites would weaken dipolar interactions between the regular Yb^{3+} ions at the A site. A full characterization of these materials via heat capacity, magnetization and subsequently, neutron scattering techniques can highlight the effect of disrupting dipolar interactions in stoichiometric $Yb_2Ti_2O_7$.

The d^3 Double Perovskite Magnets - La_2LiRuO_6 and La_2LiOsO_6

We now turn our attention to the neutron scattering studies presented in Chapter 5 on the monoclinic double perovskite systems La_2LiOsO_6 and La_2LiRuO_6. This study was conducted in an effort to determine the effect of lattice distortion on the magnetic ground state of d^3 double perovskites containing osmium and ruthenium. Cubic d^3 magnets like Ba_2YOsO_6, Ba_2YRuO_6 and Sr_2ScOsO_6 were previously found to exhibit a spin-gap, which is unexpected for ions with a quenched orbital moment. Coincident with the development of the spin gaps in these cubic materials is the formation of a type I antiferromagnetic long-range ordered state.

Our studies show that these properties are preserved in the slightly distorted systems La_2LiOsO_6 and La_2LiRuO_6. La_2LiOsO_6 and La_2LiRuO_6 both develop spin gaps of size 5.7(9) meV and 12(1) meV upon cooling through their respective transition temperatures of $T_N = 24$ K and 30 K, respectively. Like in cubic Ba_2YOsO_6, the inelastic and elastic magnetic spectral weight appears at $|Q| = 0.76\text{Å}^{-1}$ and $|Q| = 1.1\text{Å}^{-1}$. Analysis of the elastic scattering from these materials confirm that these

systems enter the same type I antiferromagnetic long-range ordered state which characterizes the ordered states of Ba_2YRuO_6, Ba_2YOsO_6 and Sr_2ScOsO_6. To generate a meaningful comparison among these monoclinic and cubic d^3 systems based on Ru and Os, two phenomenological spin Hamiltonians were utilized to model the bandwidth of the spin excitations and the size of the spin gap in a La_2LiOsO_6, La_2LiRuO_6, Ba_2YRuO_6 and Ba_2YOsO_6. Both models included antiferromagnetic nearest neighbour interactions and a term which provides a source of anisotropy in these systems. The first model employed a term involving the parameter D, which highlights the strength of single-ion anisotropy while the second model utilized a term involving the parameter K which highlights the strength of anisotropic exchange interactions. This analysis allows us to extract systematics exhibited by five d^3 doubles perovskites. In particular, T_N was found to scale as $S(J1 + 2K_1)$, which characterizes the top of the spin wave band in all the materials. This provides strong evidence that the origin of the gapped spectrum arises due to anisotropic exchange, which itself is generated by spin-orbit coupling. Our studies therefore provide an excellent benchmark for understanding $4d^3$ and $5d^3$ double perovskite magnets.

These studies considered along with the numerous research efforts surrounding the study of double perovskite magnets highlight the importance of single-crystal samples of double perovskite materials. Neutron scattering studies of single-crystals of d^3 double perovskites can enable an unambiguous determination of their spin Hamiltonians, leading to a full understanding of the physics governing the exotic ground states in these materials.

Octupolar Order in Ba_2CaOsO_6, Ba_2MgOsO_6 and Ba_2ZnOsO_6

A deeper understanding of the d^2 double perovskites Ba_2CaOsO_6, Ba_2MgOsO_6 and Ba_2ZnOsO_6 was established through our neutron scattering and x-ray diffraction studies which were presented in Chapter 6. Ba_2CaOsO_6, Ba_2MgOsO_6 and Ba_2ZnOsO_6 are all shown to exhibit spin gaps of $\sim$ 12 meV, $\sim$ 15 meV and $\sim$ 10 meV, respectively. Our high flux neutron powder diffraction studies enabled us to place an upper bound for the ordered moment in Ba_2CaOsO_6, Ba_2MgOsO_6 and Ba_2ZnOsO_6 of 0.13 μ_B, 0.11 μ_B and 0.06 μ_B, respectively. As these small ordered moments cannot account for the prominent spin excitations measured in these systems, this brought into question their origin. We sought to improve the theoretical description of d^2 moments in cubic double perovskite magnets. Applying a residual crystal-field effect on the spin-orbit coupled

$J = 2$ ground state multiplet leads to a non-Kramers octupolar ground state doublet and an excited triplet with a gap $\Delta \sim 20$ meV. The ground state wavefunctions are given by $|\psi_{g,\uparrow}\rangle = |0\rangle$ and $|\psi_{g,\downarrow}\rangle = \frac{1}{\sqrt{2}}(|2\rangle + |-2\rangle)$ while the excited wavefunctions are given by $|\psi_{e,\pm}\rangle = |\pm 1\rangle$ and $|\psi_{e,0}\rangle = \frac{1}{\sqrt{2}}(|2\rangle - |-2\rangle)$.

This description accounts for many salient features which are showcased by these double perovskite magnets. One clear result is that dipolar order is forbidden as the ground state manifold has vanishing matrix elements for the dipole operators $\vec{J}$. This would then explain why neutron diffraction does not detect this order while muon spin relaxation is sensitive to it. Our theory also accounts for the significantly reduced $R \ln(2)$ entropy which is released up to $\sim 2T^*$ in Ba_2MgOsO_6 and Ba_2ZnOsO_6, compared with $R \ln(5)$ which is expected for $J = 2$ moments.

To test the robustness of the model we have developed, future work on these systems with Raman scattering can be conducted. Octupolar order can be detected in a Raman scattering experiment by the appearance of an additional mode at $2\mathcal{B}_{oct} = 0.1\Delta$, where $\mathcal{B}_{oct}$ is the ferro-octupolar Weiss field utilized in the model to develop our theory. This mode physically arises from the transition between the two doublet states which are split by octupolar order. This would qualify as the smoking gun signature of this octupolar order. However, this study necessitates the use of single-crystal samples and this fact further highlights the importance of single-crystal studies of double perovskite magnets.

8 Appendix

This appendix incorporates the article *"Octupolar order in d-orbital Mott insulators"*, which has been published in Physical Review B. This paper provides a complete description of the theoretical framework which was developed for the description of the quantum magnetism of spin-orbit coupled $J = 2$ ions which is realized in the double perovskite lattice. This article was reproduced from with permission, copyrighted by the American Physical Society 2020. This has been added for ease of reference and the full reference is given below:

A. Paramekanti, D. D. Maharaj, and B. D. Gaulin. Physical Review B 101, 054439 (2020).

PHYSICAL REVIEW B **101**, 054439 (2020)

Octupolar order in *d*-orbital Mott insulators

A. Paramekanti,[1,2,*] D. D. Maharaj,[3] and B. D. Gaulin[3,4,5]

[1]*Department of Physics, University of Toronto, 60 St. George Street, Toronto, Ontario, Canada M5S 1A7*
[2]*International Centre for Theoretical Sciences, Tata Institute of Fundamental Research, Bengaluru 560089, India*
[3]*Department of Physics and Astronomy, McMaster University, Hamilton, Ontario, Canada L8S 4M1*
[4]*Brockhouse Institute for Materials Research, McMaster University, Hamilton, Ontario, Canada L8S 4M1*
[5]*Canadian Institute for Advanced Research, 661 University Ave., Toronto, Ontario, Canada M5G 1M1*

(Received 6 September 2019; accepted 23 December 2019; published 27 February 2020)

Motivated by experimental and theoretical interest in realizing multipolar orders in d-orbital materials, we discuss the quantum magnetism of $J = 2$ ions which can be realized in spin-orbit coupled oxides with $5d^2$ transition metal ions. Based on the crystal-field environment, we argue for a splitting of the $J = 2$ multiplet, leading to a low-lying non-Kramers doublet which hosts quadrupolar and octupolar moments. We discuss a microscopic mechanism whereby the combined perturbative effects of orbital repulsion and antiferromagnetic Heisenberg spin interactions leads to ferro-octupolar coupling between neighboring sites, and stabilizes ferro-octupolar order for a face-centered cubic lattice. This same mechanism is also shown to disfavor quadrupolar ordering. We show that studying crystal field levels via Raman scattering in a magnetic field provides a probe of octupolar order. We study spin dynamics in the ferro-octupolar state using a slave-boson approach, uncovering a gapped and dispersive magnetic exciton. For sufficiently strong magnetic exchange, the dispersive exciton can condense, leading to conventional type-I antiferromagnetic (AFM) order which can preempt octupolar order. Our proposal for ferrooctupolar order, with specific results in the context of a model Hamiltonian, provides a comprehensive understanding of thermodynamics, μSR, x-ray diffraction, and inelastic neutron-scattering measurements on a range of cubic $5d^2$ double perovskite materials including Ba_2ZnOsO_6, Ba_2CaOsO_6, and Ba_2MgOsO_6. Our proposal for exciton condensation leading to type-I AFM order may be relevant to materials such as Sr_2MgOsO_6.

DOI: 10.1103/PhysRevB.101.054439

I. INTRODUCTION

Multipolar symmetry-breaking orders have been extensively discussed in f-orbital-based lanthanide and actinide compounds, which host ions where spin-orbit coupling (SOC) is a dominant energy scale [1]. For instance, the "hidden order" state of URu_2Si_2 has been extensively investigated as potentially arising from complex multipolar symmetry breaking [2–4]. Another well-known example is cubic NpO_2 [5–8], where a large body of experiments have been reconciled in terms of a primary antiferro-triakontadipolar rank-five magnetic multipolar) symmetry breaking which drives secondary antiferro-quadrupolar order. In certain pyrochlore magnets, all-in all-out magnetic order has been proposed to lead to "effective octupoles" on tetrahedra [9]. Ongoing experimental [10–12] and theoretical investigations [13–16] of $PrTi_2Al_{20}$ and PrV_2Al_{20} have also uncovered quadrupolar and ferro-octupolar orders.

Recently, unconventional multipolar orders have also been proposed in d-orbital metals to occur as Pomeranchuk instabilities of spin-orbit-coupled Fermi surfaces [17]. Specifically, metallic oxides which have d-orbital ions with large SOC, such as $LiOsO_3$ and $Cd_2Re_2O_7$, have been proposed as potential candidates to realize this physics [17]. Experiments have indeed discovered an odd-parity nematic metal in $Cd_2Re_2O_7$ below $T_c \sim 200$ K via optical second-harmonic generation [18]. Other proposed materials for hosting multipolar orders include A_2OsO_4 (with A = K, Rb, Cs) [19]. However, to the best of our knowledge, there have been no clear d-orbital candidates for hosting octupolar orders. Indeed, there appears to be no microscopic understanding of what the key ingredients are to potentially stabilize such octupolar phases.

In this paper, we consider spin-orbit-coupled Mott insulators having transition-metal ions with total angular momentum $J = 2$. We show that such Mott insulators can exhibit competing multipolar orders and discuss a microscopic mechanism which stabilizes a ferro-octupolar state on the face-centered cubic (FCC) lattice. We show how nonresonant Raman scattering may probe the octupolar order and compute the dynamic spin structure factor which can be measured using neutron-scattering experiments. Our work in this paper is directly motivated by a series of recent experiments on cubic double perovskite (DP) magnets and we discuss how our results apply to these materials.

II. BACKGROUND REVIEW

Ordered DP materials, with chemical formula $A_2BB'O_6$, are of great interest in the context of frustrated magnetism since the B and B′ sublattices individually form networks of edge-sharing tetrahedra. When only one of these ions (say, B′) is magnetically active, it results in quantum magnetism on

*arunp@physics.utoronto.ca

the FCC lattice, a prototypical setting for exploring geometric frustration in Mott insulators. Such DP Mott insulators have been studied for various electronic fillings d^1-d^5, and we briefly review some key results below.

For d-orbitals in an octahedral crystal field, the t_{2g} single-particle levels associated with the magnetic B' ion are split by SOC, resulting in a fourfold degenerate, $j_{\rm eff} = 3/2$, ground state and a doubly degenerate, $j_{\rm eff} = 1/2$, excited state. The physics of such materials then depends strongly on the electronic filling, d^1-d^5, of these t_{2g} states. For the most well-studied d^5 electronic configuration (e.g., for Ir^{4+} or Ru^{3+} ions), this results in a single hole in a $j_{\rm eff} = 1/2$ state [20,21]. Recent experimental and theoretical studies on the DP Ba_2CeIrO_6, which hosts such a $j_{\rm eff} = 1/2$ Mott insulator on the FCC lattice, have found evidence of magnetic ordering with a strong frustration parameter, suggesting proximity to a quantum spin-liquid state [22,23]. Stepping down to a d^4 configuration, strong SOC favors a total $J_{\rm eff} = 0$ singlet ground state, with a gap to all excitations [24], which appears to be realized in Ba_2YIrO_6 [25–28]. However, if intersite exchange competes with SOC, it can lead to magnetic ordering from exciton condensation [24,29]; clear experimental candidates for such an exciton condensate are yet to be found. Further down, a d^3 configuration would naively be expected to form an orbital singlet state with spin $S = 3/2$; however, neutron scattering and resonant inelastic x-ray scattering experiments have found that $5d$ transition metal oxides bely this expectation, finding magnetically ordered states with large spin gaps which clearly reveal the dominance of SOC over Hund's coupling [30–32]. Skipping to d^1 ions, we are led to a $j_{\rm eff} = 3/2$ angular momentum state. Theoretical studies of such moments on the FCC lattice have shown that incorporating important intersite orbital repulsion can lead to complex multipolar exchange interactions, stabilizing wide regimes of quadrupolar order in the phase diagram [33–35] which may coexist with conventional dipolar magnetic order, or valence bond orders [36]. Indeed, recent experiments on $5d^1$ oxides, Ba_2NaOsO_6 with Os^{7+} [37,38] and Ba_2MgReO_6 with Re^{6+} [39], have found clear evidence for multiple transitions associated with these distinct broken symmetries, with a higher temperature quadrupolar ordering transition followed by dipolar ordering at a lower temperature.

Finally, we turn to the topic of our work: d^2 ions with an effective $J_{\rm eff} = 2$ angular momentum state. In this case, previous theoretical work has found intricate multipolar couplings as for d^1 filling and broad swaths of quadrupolar orders in the phase diagram [33–35]. In this paper, in contrast to previous work, we make the case that $J_{\rm eff} = 2$ quantum magnets in a cubic environment may instead support ground states with ferro-octupolar order. We show that this can lead to a consistent understanding of a large body of experimental data on the family of cubic DP materials Ba_2MOsO_6 (with $M =$ Zn, Mg, Ca), including specific heat, magnetic susceptibility, x-ray diffraction, powder neutron diffraction, muon spin relaxation (μSR), and inelastic neutron scattering. We present a microscopic mechanism which leads to ferro-octupolar coupling, make predictions for how Raman scattering might uncover octupolar order, and compute the dynamic spin structure factor which shows a gapped magnetic exciton. Our results point to Ba_2MOsO_6 DPs as rare examples of octupolar order in d-orbital systems.

III. EFFECTIVE LOCAL MODEL

We start from an effective $J = 2$ local moment, as appropriate for d^2 ions arising from coupling total $L = 1$ and $S = 1$ for two electrons. The most general form of the octahedral crystal field Hamiltonian for $J = 2$ ions is given by [40]

$$H_{\rm CEF} = -V_{\rm eff}(\mathcal{O}_{40} + 5\mathcal{O}_{44}). \tag{1}$$

Here, the Steven's operators are given by

$$\mathcal{O}_{40} = 35J_z^4 - (30J(J+1) - 25)J_z^2 + 3J^2(J+1)^2 - 6J(J+1), \tag{2}$$

$$\mathcal{O}_{44} = \tfrac{1}{2}(J_+^4 + J_-^4). \tag{3}$$

For $V_{\rm eff} > 0$, this results in a non-Kramers ground-state doublet and an excited triplet with a gap $\Delta = 120V_{\rm eff}$. As shown in a parallel publication [40], working in the $|J_z = m\rangle$ basis leads to ground-state wave functions,

$$|\psi_{g,\uparrow}\rangle = |0\rangle, \quad |\psi_{g,\downarrow}\rangle = \frac{1}{\sqrt{2}}(|2\rangle + |-2\rangle), \tag{4}$$

and excited state wave functions,

$$|\psi_{e,\pm}\rangle = |\pm 1\rangle; \quad |\psi_{e,0}\rangle = \frac{1}{\sqrt{2}}(|2\rangle - |-2\rangle). \tag{5}$$

The ground-state manifold has vanishing matrix elements for the dipole operators $(J^z, J^\pm)$, precluding any dipolar order stemming from the low-energy doublet manifold. However, $\vec{J}$ can induce transitions between the ground doublet and the excited triplet, which will lead to a spin-gap Δ in the excitation spectrum. As discussed below, incorporating intersite AFM exchange would convert this local mode into a dispersing gapped "magnetic exciton."

We have previously shown (see Supplemental Material of Ref. [40]) that this simple model can reasonably account for the measured entropy and magnetic susceptibility in the $5d^2$ DP Mott insulators Ba_2MOsO_6 (with $M =$ Zn, Mg, Ca). Defining pseudospin-1/2 operators $\vec{\tau}$ within the ground-state doublet, we find that the e_g quadrupolar operators $(J_x^2 - J_y^2) \equiv 2\sqrt{3}\tau_x$, $(3J_z^2 - J^2) \equiv -6\tau_z$, while the octupolar operator $\overline{J_xJ_yJ_z} \equiv -\sqrt{3}\tau_y$ (where overline denotes symmetrization). Thus, the ground doublet can lead to time-reversal invariant quadrupolar symmetry breaking from ordering in the (τ_x, τ_z) plane, which would also cause noncubic distortions due to accompanying orbital order. Alternatively, octupolar ordering with $\langle\tau_y\rangle \neq 0$ will lead to spontaneously broken time-reversal symmetry without noncubic distortions. Finally, if the gapped magnetic exciton is sufficiently dispersive, with a bandwidth larger than the spin gap, it can Bose condense and lead to dipolar magnetic order.

IV. ORIGIN OF FERROOCTUPOLAR COUPLING

We next consider projecting microscopic intersite interactions into the low-energy doublet sector described by the

pseudospin-1/2 operators $\vec{\tau}$. We have two types of interactions to consider here: type-I couplings have nonzero weight in the doublet sector can be directly projected into this subspace, while type-II operators which mix the doublet and triplet sectors will contribute within perturbation theory.

Examples of type-I interactions may be illustrated by considering a pair of neighboring sites in the xy plane which will have interactions between the e_g quadrupolar charge densities $(J_x^2 - J_y^2)$ or $(3J_z^2 - J^2)$ at the two sites. These interactions may be directly projected into the doublet sector as

$$H^{(1)}_{\text{eff},xy} = \sum_{\langle ij\rangle_{xy}} (-\gamma_0 \tau_{ix}\tau_{jx} + \gamma_1 \tau_{iz}\tau_{jz}), \tag{6}$$

with $\gamma_0, \gamma_1 > 0$. (The effective Hamiltonian for nearest neighbors in other planes can be obtained using symmetry transformations.)

Examples of type-II interactions for a pair of neighboring spins in the xy plane include the conventional AFM exchange $\gamma_m \vec{J}_i \cdot \vec{J}_j$ with $\gamma_m > 0$, where $\vec{J}$ denotes the $J = 2$ spin. In addition, they include t_{2g} quadrupolar interactions of the form $\gamma_2 \rho_{i,xy}\rho_{j,xy}$, where $\rho_{i,xy} = (J_{ix}J_{iy} + J_{iy}J_{ix})/2$ and $\gamma_2 > 0$. In this case, neither $\vec{J}_i$ nor $\rho_{i,xy}$ have matrix elements in the low-energy doublet space $|L\rangle$, but they instead mix $|L\rangle$ into the high-energy triplet subspace $|H\rangle$, with an energy cost 2Δ since both sites (i, j) get excited into the triplet sector. We find that the effective Hamiltonian for such neighboring spins in the xy plane is given, in second-order perturbation theory, by

$$H^{(2)}_{\text{eff},xy} = -\frac{1}{2\Delta} \sum_{\langle ij\rangle_{xy}} (\gamma_m \vec{J}_i \cdot \vec{J}_j + \gamma_2 \rho_{i,xy}\rho_{j,xy})^2. \tag{7}$$

Projecting these operators to the doublet sector, we find

$$H^{(2)}_{\text{eff},xy} = -\frac{1}{2\Delta} \sum_{\langle ij\rangle_{xy}} \Big[12\gamma_m\gamma_2 \tau_{iy}\tau_{jy} + \Big(6\gamma_m^2 + \frac{9}{4}\gamma_2^2\Big)\tau_{iz}\tau_{jz} + \big(6\gamma_m^2 - 12\gamma_m\gamma_2\big)\tau_{ix}\tau_{jx}\Big]. \tag{8}$$

This equation is one of the key results of our paper. The first term shows that the second-order perturbation theory produces a ferro-octupolar coupling with strength $6\gamma_m\gamma_2/\Delta$ from the cross-coupling of γ_2 and γ_m. Furthermore, assuming a hierarchy $\gamma_m \ll \gamma_2$, we see that the net quadrupolar interaction, after including the terms in Eq. (6), involves direct and perturbative contributions which come with opposite signs,

$$H^{\text{Quad}}_{xy} = \sum_{\langle ij\rangle_{xy}} \Big[\Big(-\gamma_0 + 6\frac{\gamma_m\gamma_2}{\Delta}\Big)\tau_{ix}\tau_{jx} + \Big(\gamma_1 - \frac{9}{8}\frac{\gamma_2^2}{\Delta}\Big)\tau_{iz}\tau_{jz}\Big]. \tag{9}$$

This partial cancellation of quadrupolar couplings may cause suppression of quadrupolar order, allowing for the ferro-octupolar coupling to dominate. We thus identify the key microscopic mechanism underlying ferrooctupolar ordering. A complete theory starting from an electronic hopping model with interactions, along the lines of calculations presented in Refs. [19,33–35,41], is left for future work.

V. RAMAN SCATTERING AS A PROBE OF OCTUPOLAR ORDER

We next turn to magnetic Raman scattering [42] in such systems given its usefulness as a probe of crystal field levels and quadrupolar order in heavy fermion compounds [43]. We show that Raman scattering in a nonzero magnetic field strikingly leads to additional modes in the presence of octupolar order.

Our work builds on a recent study by Patri *et al.* [16], which revealed an unusual magnetoelastic coupling between the strain and the octupolar order induced by a magnetic field, which leads to linear-in-field magnetostriction as a hallmark of octupolar order. They argued that octupolar ordering may also lead to a softening of certain phonon modes in the presence of a magnetic field, which may be detectable by Raman scattering. Here, by contrast, we focus on the impact of octupolar ordering on the crystal-field levels themselves.

The nonresonant Raman scattering intensity is given by the expression [42]

$$\mathcal{I}_{\mu\nu}(\omega) = \sum_{i,f} \mathcal{P}_i \, |\langle f|R_{\mu\nu}|i\rangle|^2 \, \delta(E_f - E_i - \hbar\omega), \tag{10}$$

where i, f refer to initial and final states, with corresponding energies E_i, E_f, and $\mathcal{P}_i$ is the (thermal) occupation probability of the initial state. The Raman operator $R_{\mu\nu}$ depends on the polarizations $\hat{\varepsilon}$ of the incoming and outgoing photons which differ in frequency by $\hbar\omega$. Here, we will focus on the specific Raman operator corresponding to $\hat{\varepsilon}_{\text{in}} \parallel \hat{x}$ and $\hat{\varepsilon}_{\text{out}} \parallel \hat{y}$, which, on symmetry grounds, is given by $R_{xy} = (J_xJ_y + J_yJ_x)/2$.

To explore the crystal-field levels of the $J = 2$ ion in the presence of octupolar order and a nonzero magnetic field $B\hat{z}$, we modify the crystal-field Hamiltonian in Eq. (1) as

$$H_{\text{loc}} = H_{\text{CEF}} - \mathcal{B}_{\text{oct}} \sum_i \tau_{iy} - B \sum_i J_{i,z}, \tag{11}$$

where $\mathcal{B}_{\text{oct}}$ is the ferro-octupolar Weiss field in the symmetry broken phase. This Weiss field does not impact the excited triplet wave functions which cost energy Δ, but splits the non-Kramers doublet to form eigenstates

$$|\phi_\pm\rangle = \frac{1}{\sqrt{2}}(|\psi_{g,\uparrow}\rangle \pm i|\psi_{g,\downarrow}\rangle), \tag{12}$$

which have their energies shifted, respectively, by $\mp\mathcal{B}_{\text{oct}}$. We focus here on the zero temperature behavior of the Raman spectrum in this local limit.

For $B = 0$, it is easy to show that the Raman operator R_{xy} has no matrix elements in the low-energy sector $\{|\phi_\pm\rangle\}$. Instead, at zero temperature, it induces transitions between the octupolar ground state $|\phi_+\rangle$ and the excited crystal-field state $|\psi_{e,0}\rangle$ at energy $\Delta + \mathcal{B}_{\text{oct}}$. The main panel of Fig. 1 depicts this mode, which is obtained by diagonalizing H_{loc} and computing $\mathcal{I}_{xy}(\omega)$. Here, we have artificially introduced a broadening $\sim 0.02\Delta$ to mimic resolution effects.

Switching on $B \neq 0$ mixes the doublet and triplet wave functions at $\mathcal{O}(B/\Delta)$, so we must work with perturbed low-energy doublet eigenstates

$$|\phi'_\pm\rangle = |\phi_\pm\rangle \pm i\sqrt{2}\frac{B}{\Delta \pm \mathcal{B}_{\text{oct}}}|\psi_{e,0}\rangle. \tag{13}$$

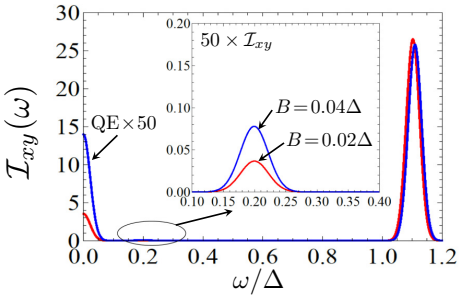

FIG. 1. Main panel: Raman intensity $\mathcal{I}_{xy}(\omega)$ as a function of frequency ω in units of the doublet-triplet gap Δ, in the presence of an octupolar Weiss field $\mathcal{B}_{\rm oct} = 0.1\Delta$, for magnetic field $B\hat{z}$ with $B = 0.02\Delta$ (red) and $B = 0.04\Delta$ (blue). The dominant peak is at $\omega = \Delta + \mathcal{B}_{\rm oct}$, while QE refers to the B-induced quasielastic part in the presence of octupolar order, which we have scaled up by a factor of 50. Inset: Rescaled $\mathcal{I}_{xy}$ zoomed in at small low nonzero frequency, showing an additional mode emerging for $B \neq 0$ at a frequency $\omega \sim 2\mathcal{B}_{\rm oct}$, corresponding to the transition between the two doublet states split by octupolar order.

In addition to a weak renormalization of the above crystal-field transition, this leads to two effects. First, we find that

$$\langle\phi'_+|R_{xy}|\phi'_+\rangle = -2\sqrt{3}\frac{B}{\Delta+\mathcal{B}_{\rm oct}}, \tag{14}$$

which is closely tied to the linear-in-field magnetostriction explored by Patri *et al.* [16] and should lead to a quasielastic Raman signal with strength $|\langle\phi'_+|R_{xy}|\phi'_+\rangle|^2 \propto B^2/(\Delta+\mathcal{B}_{\rm oct})^2$. Remarkably, a striking parallel of such a quasielastic field-induced mode was discussed long ago in the context of (resonant) B_{2g} Raman scattering to probe uniform scalar spin chirality in insulating square lattice antiferromagnets [44,45]. The spin chirality breaks time reversal but preserves spin-rotation symmetry, being similar, in this sense, to octupolar order.

In addition, we uncover a Raman mode corresponding to a $|\phi'_+\rangle \to |\phi'_-\rangle$ transition at an energy $\approx 2\mathcal{B}_{\rm oct}$. For $B \ll \Delta - \mathcal{B}_{\rm oct}$, the intensity of this mode scales $\propto B^2\mathcal{B}_{\rm oct}^2/(\Delta^2 - \mathcal{B}_{\rm oct})^2$. The inset of Fig. 1 depicts this mode, which is obtained by diagonalizing $H_{\rm loc}$ and computing $\mathcal{I}_{xy}(\omega)$.

The quasielastic signal and the mode at $2\mathcal{B}_{\rm oct}$ are unambiguous signatures of octupolar order. Both features lie well within the spin gap Δ. Temporally modulating B, or comparing the Raman intensity in a field relative to the zero field spectrum, might enable one to potentially search for these signals; however, their weak intensities render this a potentially challenging experiment.

VI. MAGNETIC EXCITONS AND DYNAMIC SPIN-STRUCTURE FACTOR

To explore, in more detail, the spin-excitation spectrum at energy scales on the order of the spin gap Δ, we use a slave boson approach [46–48]. The ensuing results can then be compared with existing inelastic neutron-scattering results on Ba_2MOsO_6 [40]. We define the ground and excited states of the low-energy doublet via

$$|\psi_{g,\sigma}\rangle = b^\dagger_\sigma|{\rm vac}\rangle, \tag{15}$$

$$|\psi_{e,\alpha}\rangle = d^\dagger_\alpha|{\rm vac}\rangle, \tag{16}$$

where $\sigma = \uparrow, \downarrow$, $\alpha = 0, \pm$, and $|{\rm vac}\rangle$ denotes the boson vacuum. This requires a local constraint:

$$\sum_{\sigma=\pm} b^\dagger_\sigma b_\sigma + \sum_{\alpha=0,\pm} d^\dagger_\alpha d_\alpha = 1. \tag{17}$$

Excitations out of the low-energy space contain at least one b boson; we thus get

$$J^+ = \sqrt{6}(b^\dagger_\uparrow d_- + d^\dagger_+ b_\uparrow) + \sqrt{2}(b^\dagger_\downarrow d_+ + d^\dagger_- b_\downarrow), \tag{18}$$

$$J^z = 2(d^\dagger_0 b_\downarrow + b^\dagger_\downarrow d_0). \tag{19}$$

Going beyond the simple local Hamiltonian, we model the dispersion of the gapped spin excitations using a nearest-neighbor Heisenberg exchange $\gamma_m \sum_{\langle ij\rangle} \vec{J}_i \cdot \vec{J}_j$. We supplement this, in the ferro-octupolar symmetry broken phase, by a uniform octupolar Weiss field: $-\mathcal{B}_{\rm oct}\sum_i \tau_{iy}$. Here, $\tau_y \equiv -i(b^\dagger_\uparrow b_\downarrow - b^\dagger_\downarrow b_\uparrow)$, and, without loss of generality, we can set $\mathcal{B}_{\rm oct} > 0$. The total Hamiltonian we study is thus

$$H_{\rm spin} = H_{\rm CEF} + \gamma_m \sum_{\langle ij\rangle} \vec{J}_i \cdot \vec{J}_j - \mathcal{B}_{\rm oct} \sum_i \tau_{iy}. \tag{20}$$

The Weiss field favors a ground-state Bose condensate $b_\uparrow \approx 1/\sqrt{2}$ and $b_\downarrow \approx i/\sqrt{2}$, resulting in the simplified expressions

$$J^+ \approx \sqrt{3}(d^\dagger_+ + d_-) - i(d_+ - d^\dagger_-), \tag{21}$$

$$J^z \approx i\sqrt{2}(d^\dagger_0 - d_0). \tag{22}$$

Using these and accounting for the local doublet-triplet gap, we transform to momentum space, so the full Hamiltonian for describing the magnetic excitons is given by

$$H_{\rm exc} = (\Delta + \mathcal{B}_{\rm oct})\sum_{\mathbf{k}\alpha} d^\dagger_{\mathbf{k},\alpha} d_{\mathbf{k},\alpha} + \frac{\gamma_m}{2}\sum_{\mathbf{k}} \eta_{\mathbf{k}} J^+_{\mathbf{k}} J^-_{-\mathbf{k}} - \gamma_m \sum_{\mathbf{k}} \eta_{\mathbf{k}} (d^\dagger_{\mathbf{k},0} - d_{-\mathbf{k},0})(d^\dagger_{-\mathbf{k},0} - d_{\mathbf{k},0}), \tag{23}$$

where $J^+_{\mathbf{k}} \equiv \sqrt{3}(d^\dagger_{\mathbf{k},+} + d_{-\mathbf{k},-}) - i(d_{-\mathbf{k},+} - d^\dagger_{\mathbf{k},-})$, $J^-_{-\mathbf{k}} \equiv (J^+_{\mathbf{k}})^\dagger$, and $\eta_{\mathbf{k}} = \sum_\delta e^{i\mathbf{k}\cdot\delta}$ with δ labeling the 12 nearest-neighbor vectors on the FCC lattice. This leads to a threefold degenerate magnetic exciton with energy dispersion given by

$$\lambda(\mathbf{k}) = \sqrt{(\Delta + \mathcal{B}_{\rm oct})(\Delta + \mathcal{B}_{\rm oct} + 4\gamma_m\eta_{\mathbf{k}})}. \tag{24}$$

We find that the exciton energy $\lambda(\mathbf{k})$ is largest at the Γ point, and is softest at the typical FCC lattice type-I AF ordering wave vector $\mathbf{K}$.

We expect the exciton dispersion will have temperature dependence through the temperature dependence of the octupolar order parameter, which enters via the Weiss field $\mathcal{B}_{\rm o}(T)$, softening somewhat as we heat up toward the octupolar ordering transition. A plot of the dispersion along a high-symmetry path in the FCC Brillouin zone, for a choice $\mathcal{B}_{\rm oct}/\Delta = 0.1$ and $\gamma_m/\Delta = 0.05$, is shown in Fig. 2. For sufficiently large

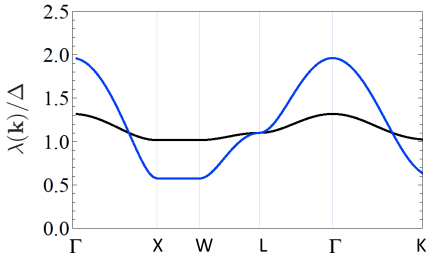

FIG. 2. Magnetic exciton dispersion $\lambda(\mathbf{k})$ (in units of Δ) along high-symmetry path in the FCC lattice Brillouin zone, for a choice of octupolar Weiss field $\mathcal{B}_{\rm oct} = 0.1\Delta$ and two different choices for the Heisenberg coupling: (i) $\gamma_m = 0.01\Delta$ (black) and (ii) $\gamma_m = 0.05\Delta$ (blue). The exciton mode clearly softens with increasing γ_m.

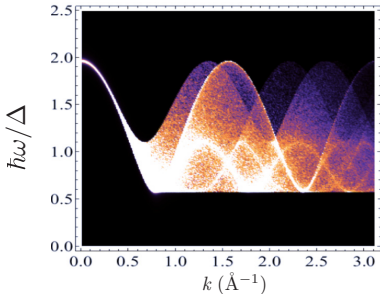

FIG. 3. Powder-averaged dynamic spin structure factor (arbitrary units) including the Os^{6+} form factor, showing the gapped magnetic exciton, as a function of momentum transfer k (in Å^{-1}, for a lattice constant $a = 4$ Å) and energy $\hbar\omega$ (in units of Δ). We have set the Heisenberg exchange coupling $\gamma_m = 0.05\Delta$ and octupolar Weiss field $\mathcal{B}_o = 0.1\Delta$.

exchange coupling γ_m, the magnetic exciton can potentially condense, leading to coexistence of dipolar and octupolar orders. The dipolar order can even preempt octupolar order if $\gamma_m > \Delta/16$, leading to conventional type-I AFM order.

VII. EXPERIMENTAL IMPLICATIONS

The cubic osmates Ba_2MOsO_6 (with M = Zn, Mg, Ca) potentially provide a realization of $J = 2$ ions on the FCC lattice. They all exhibit a single phase transition at $T^* \sim$ 30-50 K, across which the entropy release is only $\sim \ln(2)$ per Os, suggesting that the full ln(5) entropy is partially quenched for $T \lesssim 100$ K [49–51] without any phase transition. Indeed, the structure appears to be perfectly cubic, in the $Fm\bar{3}m$ space group, at all temperatures; both neutron diffraction and high resolution XRD measurements find no signs of any noncubic distortions [40]. This suggests that the entropy quenching above the phase transition at T^* must arise from symmetry-allowed crystal field effects, as discussed in our theory with a non-Kramers ground-state doublet.

Below the phase transition at T^*, neutron diffraction sees no ordered moment, even for $T \ll T^*$, instead placing tight upper bounds on the ordered dipolar moment, $\lesssim$0.06–0.13μ_B, depending on the material [40]. At the same time, μSR measurements have found evidence for zero-field oscillations, showing spontaneous breaking of time-reversal symmetry [49]. Since neutron diffraction strongly hints at the absence of dipolar magnetic order, and the cubic structure appears inconsistent with quadrupolar order, we argue that octupolar ordering within the doublet, which preserves cubic crystal symmetry and breaks time-reversal symmetry, provides the simplest explanation for the data. (Unlike for the Γ_5 multipoles in NpO_2 [1], which undergo triple-$\mathbf{Q}$ ordering, the ferro-octupolar ordering here is not symmetry constrained to induce secondary quadrupolar order.)

Inelastic neutron-scattering experiments [40] find a spin gap ∼10–15 meV, which we interpret as arising from the doublet-triplet gap of the crystal-field levels. We assume the local gap $\Delta \sim 25$ meV, since this yields a reasonable temperature scale below which the single-site entropy saturates to ln(2). This value of Δ is somewhat larger than the above quoted spin gap, seen using neutrons, near the (100) wave vector, but we attribute this difference to the dispersion of the magnetic exciton.

While the measured magnetic susceptibility [49–51] for $T \lesssim 300$ K in these materials hints at a Curie-Weiss temperature scale ~ -150 K, we have shown that the true $\Theta_{\rm CW}$ must be shifted by $\sim 0.1\Delta$ due to the local spin gap, so we estimate $\Theta_{\rm CW} \sim -120$ K; dividing this by zJ^2, with the FCC coordination number $z = 12$ and moment size $J = 2$, we crudely estimate $\gamma_m \sim 0.25$ meV.

Next, to explain T^* for the Ising octupolar symmetry breaking, we must estimate the octupolar coupling constant in Eq. (8). We do not have any microscopic estimate for γ_2. Assuming $\gamma_2 \ll \Delta$, so this inte-site coupling is weaker than the on-site CEF splitting Δ, if we set $\gamma_2 \sim 5$ meV, we find the Ising ferro-octupolar exchange $6\gamma_m\gamma_2/\Delta \sim 7$ K. Using a classical FCC Ising model to describe the ferrooctupolar order, the known results for the Ising transition temperature [52], lead us to estimate an ordering temperature $T^* \sim 70$ K, somewhat larger than the experimental result. (We note that although we have explored the detailed consequences for $\gamma_2 > 0$, we are unable to rule out the possibility that $\gamma_2 < 0$, which would favor antiferro-octupolar order. In this case, a larger value of $|\gamma_2| \sim 50$ meV would be necessary to explain the octupolar ordering temperature T^*; however, it is not then clear why the $\tau_x\tau_x$ coupling in Eq. (9) would not cause a leading quadrupolar instability. Moreover, we do not have a microscopic explanation for such an antiferro-octupolar coupling.)

Turning to the measured exciton gap from inelastic neutron scattering, if we assume a Weiss field $\mathcal{B}_{\rm oct} \sim 2.5$ meV (which is $\sim T^*/2$), then using the above Δ, γ_m, we find $\lambda(\mathbf{K}) \sim$ 25 meV, larger than the measured exciton gap at $\mathbf{K}$. Choosing a larger $\gamma_m \sim 1$ meV leads to $\lambda(\mathbf{K}) \sim 14$ meV, in better agreement with the data. These uncertainties in γ_m might reflect the possibility that other magnetic exchange terms could be important, beyond a single isotropic Heisenberg coupling. Figure 3 shows the dynamical spin structure factor

$$\mathcal{S}(\mathbf{k},\omega) \propto \sqrt{\frac{\mathcal{B}_{\rm oct}+\Delta}{\mathcal{B}_{\rm oct}+\Delta+4\gamma_m\eta_{\mathbf{k}}}}\,\delta(\hbar\omega-\lambda(\mathbf{k})), \qquad (25)$$

plotted after powder averaging, and including the Os^{6+} form factor. We find a high intensity gapped band in an energy window $\sim(0.5\Delta, \Delta)$, with the largest intensity concentrated at $k = \pi/a$, which corresponds to type-I ordering wave vector $\mathbf{K} = (\pi/a, 0, 0)$. We have assumed the Os-Os distance to be $a\sqrt{2}$, with $a = 4$ Å as the typical cubic lattice constant for such perovskite crystals.

We finally note that for a smaller gap Δ and stronger intersite exchange, the octupolar order can coexist with dipolar order or even be totally preempted by Bose condensation of the magnetic exciton. The resulting conventional type-I AFM state can have a small ordered moment if it is close to the exciton condensation transition. We propose this scenario for Sr_2MgOsO_6, which appears to have a smaller Δ (based on its entropy) and a larger γ_m (based on its Curie-Weiss temperature), and exhibits a type-I AFM ground state with an ordered moment $\sim 0.6\mu_B$, much smaller than the moment size $\sim 1.88\mu_B$ inferred from high temperature susceptibility measurements [53]. Weak tetragonal deformation in Sr_2MgOsO_6 will split the non-Kramers doublet and partially the triplet. In this case, the magnetic exciton condensation proposed here might still be of some relevance. However, we note that strong deformation may partially suppress the contribution of the orbital angular momentum, and drive the system closer to an orbitally quenched $S = 1$ magnet.

VIII. SUMMARY

We have presented arguments in this work in favor of octupolar ordering of $J = 2$ ions on the FCC lattice which is relevant to a family of complex $5d^2$ oxides, and identified a microscopic mechanism for generating ferro-octupolar coupling. Further theoretical and experimental work, perhaps using magnetostriction as discussed in Ref. [16] or magnetic Raman scattering as explored here, is needed to provide smoking gun signatures of the ferro-octupolar symmetry breaking. For Raman scattering, our illustrative field scale $B = 0.04\,\Delta$ corresponds to $\sim$10 Tesla. Such experiments may require single crystals of suitable sizes. It may also be useful to carry out more detailed microscopic calculations to compute the sign of the octupolar exchange; as noted above, the possibility of antiferro-octupolar order is not ruled out by our work. Another interesting experimental direction would be to apply pressure on the cubic DPs discussed here in an attempt to induce Bose condensation of the magnetic excitons. Our finding of a perturbative microscopic mechanism to induce octupolar couplings via excited crystal field levels through the combination of intersite orbital repulsion and Heisenberg spin exchange is general enough to be applicable to other lattice geometries. However, the specific competition between quadrupolar and octupolar orders will depend on details of the crystal structure. Finally, this mechanism we have identified may also be of potential importance in heavy fermion compounds, where underlying intersite orbital repulsion and spin exchange interactions needed to drive ferrooctupolar exchange can be induced via coupling to conduction electrons.

ACKNOWLEDGMENTS

This work was supported by the Natural Sciences and Engineering Research Council of Canada. A.P. also acknowledges support from a Simons Foundation Targeted Grant to ICTS-TIFR.

[1] P. Santini, S. Carretta, G. Amoretti, R. Caciuffo, N. Magnani, and G. H. Lander, Rev. Mod. Phys. **81**, 807 (2009).
[2] K. Haule and G. Kotliar, Nat. Phys. **5**, 796 (2009).
[3] H.-H. Kung, R. E. Baumbach, E. D. Bauer, V. K. Thorsmølle, W.-L. Zhang, K. Haule, J. A. Mydosh, and G. Blumberg, Science **347**, 1339 (2015).
[4] H.-H. Kung, S. Ran, N. Kanchanavatee, V. Krapivin, A. Lee, J. A. Mydosh, K. Haule, M. B. Maple, and G. Blumberg, Phys. Rev. Lett. **117**, 227601 (2016).
[5] P. Santini and G. Amoretti, Phys. Rev. Lett. **85**, 2188 (2000).
[6] J. A. Paixão, C. Detlefs, M. J. Longfield, R. Caciuffo, P. Santini, N. Bernhoeft, J. Rebizant, and G. H. Lander, Phys. Rev. Lett. **89**, 187202 (2002).
[7] A. Kiss and P. Fazekas, Phys. Rev. B **68**, 174425 (2003).
[8] Y. Tokunaga, D. Aoki, Y. Homma, S. Kambe, H. Sakai, S. Ikeda, T. Fujimoto, R. E. Walstedt, H. Yasuoka, E. Yamamoto, A. Nakamura, and Y. Shiokawa, Phys. Rev. Lett. **97**, 257601 (2006).
[9] T.-h. Arima, J. Phys. Soc. Jpn. **82**, 013705 (2013).
[10] A. Sakai and S. Nakatsuji, J. Phys. Soc. Jpn. **80**, 063701 (2011).
[11] T. J. Sato, S. Ibuka, Y. Nambu, T. Yamazaki, T. Hong, A. Sakai, and S. Nakatsuji, Phys. Rev. B **86**, 184419 (2012).
[12] M. Tsujimoto, Y. Matsumoto, T. Tomita, A. Sakai, and S. Nakatsuji, Phys. Rev. Lett. **113**, 267001 (2014).
[13] K. Hattori and H. Tsunetsugu, J. Phys. Soc. Jpn. **85**, 094001 (2016).
[14] F. Freyer, J. Attig, S. B. Lee, A. Paramekanti, S. Trebst, and Y. B. Kim, Phys. Rev. B **97**, 115111 (2018).
[15] S. B. Lee, S. Trebst, Y. B. Kim, and A. Paramekanti, Phys. Rev. B **98**, 134447 (2018).
[16] A. S. Patri, A. Sakai, S. B. Lee, A. Paramekanti, S. Nakatsuji, and Y. B. Kim, Nat. Commun. **10**, 4092 (2019).
[17] L. Fu, Phys. Rev. Lett. **115**, 026401 (2015).
[18] J. W. Harter, Z. Y. Zhao, J.-Q. Yan, D. G. Mandrus, and D. Hsieh, Science **356**, 295 (2017).
[19] S. Hayami, H. Kusunose, and Y. Motome, Phys. Rev. B **97**, 024414 (2018).
[20] B. J. Kim, H. Jin, S. J. Moon, J.-Y. Kim, B.-G. Park, C. S. Leem, J. Yu, T. W. Noh, C. Kim, S.-J. Oh, J.-H. Park, V. Durairaj, G. Cao, and E. Rotenberg, Phys. Rev. Lett. **101**, 076402 (2008).
[21] K. W. Plumb, J. P. Clancy, L. J. Sandilands, V. V. Shankar, Y. F. Hu, K. S. Burch, H.-Y. Kee, and Y.-J. Kim, Phys. Rev. B **90**, 041112(R) (2014).
[22] A. A. Aczel, J. P. Clancy, Q. Chen, H. D. Zhou, D. Reig-i-Plessis, G. J. MacDougall, J. P. C. Ruff, M. H. Upton, Z. Islam, T. J. Williams, S. Calder, and J.-Q. Yan, Phys. Rev. B **99**, 134417 (2019).
[23] A. Revelli, C. C. Loo, D. Kiese, P. Becker, T. Fröhlich, T. Lorenz, M. Moretti Sala, G. Monaco, F. L. Buessen, J. Attig,

M. Hermanns, S. V. Streltsov, D. I. Khomskii, J. van den Brink, M. Braden, P. H. M. van Loosdrecht, S. Trebst, A. Paramekanti, and M. Grüninger, Phys. Rev. B **100**, 085139 (2019).
[24] G. Khaliullin, Phys. Rev. Lett. **111**, 197201 (2013).
[25] T. Dey, A. Maljuk, D. V. Efremov, O. Kataeva, S. Gass, C. G. F. Blum, F. Steckel, D. Gruner, T. Ritschel, A. U. B. Wolter, J. Geck, C. Hess, K. Koepernik, J. van den Brink, S. Wurmehl, and B. Büchner, Phys. Rev. B **93**, 014434 (2016).
[26] K. Pajskr, P. Novák, V. Pokorný, J. Kolorenč, R. Arita, and J. Kuneš, Phys. Rev. B **93**, 035129 (2016).
[27] Q. Chen, C. Svoboda, Q. Zheng, B. C. Sales, D. G. Mandrus, H. D. Zhou, J.-S. Zhou, D. McComb, M. Randeria, N. Trivedi, and J.-Q. Yan, Phys. Rev. B **96**, 144423 (2017).
[28] A. Paramekanti, D. J. Singh, B. Yuan, D. Casa, A. Said, Y.-J. Kim, and A. D. Christianson, Phys. Rev. B **97**, 235119 (2018).
[29] C. Svoboda, M. Randeria, and N. Trivedi, Phys. Rev. B **95**, 014409 (2017).
[30] A. E. Taylor, S. Calder, R. Morrow, H. L. Feng, M. H. Upton, M. D. Lumsden, K. Yamaura, P. M. Woodward, and A. D. Christianson, Phys. Rev. Lett. **118**, 207202 (2017).
[31] A. E. Taylor, R. Morrow, M. D. Lumsden, S. Calder, M. H. Upton, A. I. Kolesnikov, M. B. Stone, R. S. Fishman, A. Paramekanti, P. M. Woodward, and A. D. Christianson, Phys. Rev. B **98**, 214422 (2018).
[32] D. D. Maharaj, G. Sala, C. A. Marjerrison, M. B. Stone, J. E. Greedan, and B. D. Gaulin, Phys. Rev. B **98**, 104434 (2018).
[33] G. Chen, R. Pereira, and L. Balents, Phys. Rev. B **82**, 174440 (2010).
[34] G. Chen and L. Balents, Phys. Rev. B **84**, 094420 (2011).
[35] C. Svoboda, M. Randeria, and N. Trivedi, arXiv:1702.03199.
[36] J. Romhányi, L. Balents, and G. Jackeli, Phys. Rev. Lett. **118**, 217202 (2017).
[37] L. Lu, M. Song, W. Liu, A. P. Reyes, P. Kuhns, H. O. Lee, I. R. Fisher, and V. F. Mitrović, Nat. Commun. **8**, 14407 (2017).
[38] W. Liu, R. Cong, E. Garcia, A. P. Reyes, H. O. Lee, I. R. Fisher, and V. F. Mitrović, Physica B **536**, 863 (2018).
[39] D. Hirai and Z. Hiroi, J. Phys. Soc. Jpn. **88**, 064712 (2019).
[40] D. D. Maharaj, G. Sala, M. B. Stone, E. Kermarrec, C. Ritter, F. Fauth, C. A. Marjerrison, J. E. Greedan, A. Paramekanti, and B. D. Gaulin, Phys. Rev. Lett. **124**, 087206 (2020).
[41] K. Kubo and T. Hotta, Phys. Rev. B **95**, 054425 (2017).
[42] T. P. Devereaux and R. Hackl, Rev. Mod. Phys. **79**, 175 (2007).
[43] M. Ye, H.-H. Kung, P. F. S. Rosa, E. D. Bauer, Z. Fisk, and G. Blumberg, Phys. Rev. Mater. **3**, 065003 (2019).
[44] B. S. Shastry and B. I. Shraiman, Phys. Rev. Lett. **65**, 1068 (1990).
[45] The work by Shastry and Shraiman [44] focused on resonant Raman scattering for the two-photon Raman process to sense the three-site spin chirality.
[46] S. Sachdev and R. N. Bhatt, Phys. Rev. B **41**, 9323 (1990).
[47] F.-Y. Li and G. Chen, Phys. Rev. B **100**, 045103 (2019).
[48] S. Das, D. Nafday, T. Saha-Dasgupta, and A. Paramekanti, Phys. Rev. B **100**, 140408 (2019).
[49] C. M. Thompson, J. P. Carlo, R. Flacau, T. Aharen, I. A. Leahy, J. R. Pollichemi, T. J. S. Munsie, T. Medina, G. M. Luke, J. Munevar, S. Cheung, T. Goko, Y. J. Uemura, and J. E. Greedan, J. Phys.: Condens. Matter **26**, 306003 (2014).
[50] E. Kermarrec, C. A. Marjerrison, C. M. Thompson, D. D. Maharaj, K. Levin, S. Kroeker, G. E. Granroth, R. Flacau, Z. Yamani, J. E. Greedan, and B. D. Gaulin, Phys. Rev. B **91**, 075133 (2015).
[51] C. A. Marjerrison, C. M. Thompson, A. Z. Sharma, A. M. Hallas, M. N. Wilson, T. J. S. Munsie, R. Flacau, C. R. Wiebe, B. D. Gaulin, G. M. Luke, and J. E. Greedan, Phys. Rev. B **94**, 134429 (2016).
[52] J. W. Essam and M. E. Fisher, J. Chem. Phys. **38**, 802 (1963).
[53] R. Morrow, A. E. Taylor, D. J. Singh, J. Xiong, S. Rodan, A. U. B. Wolter, S. Wurmehl, B. Büchner, M. B. Stone, A. I. Kolesnikov, A. A. Aczel, A. D. Christianson, and P. M. Woodward, Sci. Rep. **6**, 32462 (2016).